Title
An Investigation into the evolution of damage and residual stresses in Ti6Al4V-Al_3Ti metal intermetallic laminate (MIL) composites

Author
Li, Tiezheng

Publication Date
2006

Peer reviewed|Thesis/dissertation

UNIVERSITY OF CALIFORNIA, SAN DIEGO

SAN DIEGO STATE UNIVERSITY

An Investigation into the Evolution of Damage and Residual Stresses in Ti6Al4V-Al_3Ti Metal Intermetallic Laminate (MIL) Composites

A dissertation submitted in partial satisfaction of the

requirements for the degree of Doctor of Philosophy in

Engineering Science (Applied Mechanics)

by

Tiezheng Li

Committee in charge:

University of California, San Diego
Professor Marc A. Meyers, Co-Chair
Professor David J. Benson
Professor M. Lea Rudee

San Diego State University
Professor Eugene A. Olevsky, Chair
Professor Satchi Venkataraman

2006

The dissertation of Tiezheng Li is approved, and it is acceptable in quality and form for publication on microfilm:

____

Co-Chair

Chair

University of California, San Diego
San Diego State University
2006

To my parents

TABLE OF CONTENTS

LIST OF FIGURES

LIST OF TABLES

ACKNOWLEDGEMENTS

First, I would like to thank my advisors, Professors M.A. Meyers and E.A. Olevsky, for giving me the opportunity to conduct research on this fascinating topic, and for their support, guidance and encouragement throughout. The collaboration with the group of Professor K.S. Vecchio, and in particular, the help provided by Dr. Jiang, Dr. A. Rohatgi, Dr. Ma, Ms. Cai, Tom Phillips and Evelyn York (Scripps Institution of Oceanography) and Mr. K. Harvey, are greatly appreciated. Dr. A. Rohatgi processed the materials. Dr. Ma, Dr. Jiang, Jing Cai, Tom Phillips and Evelyn York (Scripps Institution of Oceanography) helped in specimen preparation, mechanical tests and SEM. Mr. K. Harvey carried out the measurements of residual stresses. I also thank Dr. R. Schwarz for the resonant ultrasonic spectroscopy (RUS) measurements at Los Alamos National Laboratory.

I would also like to thank my committee members, Professor David J. Benson, Professor M. Lea Rudee and Professor Satchi Venkataraman, for their time, comments and suggestions.

The support of DARPA through contract No. DAAD 19-00-1-0511 and the financial support from the Joint Doctorial Program between SDSU and UCSD are gratefully appreciated.

VITA

2001	B.S.E. in Mechanical Engineering, Tsinghua University, Beijing, China.
2001 – 2006	Teaching Assistant, College of Engineering, San Diego State University
2006	Ph.D. in Engineering Science / Applied Mechanics, University of California, San Diego and San Diego State University

ABSTRACT OF THE DISSERTATION

An Investigation into the Evolution of Damage and Residual Stresses in Ti6Al4V-Al_3Ti Metal Intermetallic Laminate (MIL) Composites

by

Tiezheng Li

Doctor of Philosophy in Engineering Science (Applied Mechanics)

University of California, San Diego, 2006

San Diego State University, 2006

Professor Eugene A. Olevsky, Chair

Professor Marc A. Meyers, Co-Chair

A systematic investigation of the evolution of damage and the residual stresses in Ti6Al4V-Al_3Ti metal-intermetallic laminate (MIL) composites were carried out. Crack morphology and density of as-processed MIL composites were quantified, and quasi-static and dynamic compression tests were conducted on pure Al_3Ti, as well as on MIL composites, with different volume fractions of Ti6Al4V (14%, 20% and 35%) under different loading directions (perpendicular and parallel directions to laminate plane), to different strains (~1%, ~2%, ~3%), and at different strain rates (0.0001/s and 800-2000/s). Crack densities and distributions were measured, and the differences in crack propagation and damage evolution in MIL composites under

quasi-static (0.0001/s) and dynamic (800-2000/s) deformation were observed and discussed. The fracture stresses under different testing conditions do not exhibit significant strain-rate sensitivity, which is indicative of the dominance of microcracking processes in determining strength. The crack density after dynamic deformation is higher than that after quasi-static deformation. This is attributed to the decreased time for crack interaction in high-strain rate deformation. The effect of crack density, quantified by a damage parameter, on elastic modulus were quantified and the results were compared with experimental results. The principal damage evolution mechanisms were identified.

The elastic properties and anisotropy of the laminates were calculated and successfully compared with Resonant Ultrasonic Spectroscopy (RUS) measurements. The residual stress in MIL composites was evaluated from the differences in the thermal expansion coefficients of Ti6Al4V and Al_3Ti. The residual stress evolution during cooling process was modeled by incorporating two stress release mechanisms: creep and crack propagation, and implemented through analytical modeling and finite element simulation. The obtained results indicate good agreements with the X-ray measurements. The fracture toughness of MIL composites was modeled as a combination of the crack initiation toughness and the stress intensity, and the calculation predicts the maximum fracture toughness occurs at 57% volume fraction of Ti6Al4V.

CHAPTER 1

INTRODUCTION

Ti6Al4V-Al_3Ti metal intermetallic laminate (MIL) composites have been fabricated from elemental titanium and aluminum foils by the self-propagating high-temperature synthesis (SHS) by Vecchio and co-workers [1 - 5]. The resulting layered structure of alternating ductile Ti6Al4V and brittle intermetallic Al_3Ti is designed to utilize the unique properties of the constituent components, providing the composites the high strength, high stiffness and high toughness.

Al_3Ti, as most intermetallics, has good high-temperature strength, high resistance to oxidation and corrosion, high melting point, high stiffness, good creep resistance, and relatively low material density. However, the low tensile ductility and poor fracture resistance at ambient temperature restrict the applications of intermetallics in many cases. To improve their toughness at room temperature, considerable efforts have been devoted to toughen intermetallics with ductile reinforcements, in the form of particles, fibers, and layers. The production of Ti6Al4V-Al_3Ti metal intermetallic laminate (MIL) composites is one such effort.

There are two primary objectives of this research. The first objective is to investigate the crack morphology and damage evolution in Ti6Al4V-Al_3Ti MIL composites, to better understand its responses under different testing conditions. To achieve this objective, compression tests were conducted on Ti6Al4V-Al_3Ti MIL composites and on pure Al_3Ti produced in the same fashion, with different loading directions, strains, strain rates and volume fraction of Ti6Al4V. Optical microscopy and scanning electron microscopy (SEM) were employed to characterize the crack morphology of MIL composites before and after tests. Crack density was measured and converted to a damage parameter, which was used to study the effect of damage on the elastic modulus and stress strain relations. Based on experiments, physical models were developed to capture the dynamics of the crack propagation in Ti6Al4V-Al_3Ti MIL composites. The second objective of this research is to study the evolution of residual stress during cooling and its effect on fracture toughness of MIL composites. The mismatch of thermal expansion coefficients between Ti6Al4V and Al_3Ti introduces the residual stress during the processing and its magnitude depends upon the stiffness of the components and the change in temperature. The proper prediction of residual stress can help us better understand damage initiation during cooling in processing and during thermal cycling experienced in service. The residual stress was elastically analyzed, and stress release mechanisms were identified and employed to quantify the residual stress evolution. To take into consideration of the finite size of the composite, finite element simulation was preformed using ABAQUS, including both creep and cracking mechanisms, to study the magnitude as well as distribution of residual stress during cooling. The residual stress analysis was later incorporated into the modeling of fracture toughness of MIL composites. These studies enable us to better understand the behavior of Ti6Al4V-Al_3Ti MIL composites during the processing and during service, and lead us one step forward towards the development of optimal materials for structural and aerospace applications.

Chapter 2 reviews the background of intermetallics and ductile reinforced intermetallic composites. The benefits and the disadvantages of intermetallics are discussed, as well as various ductile reinforcement methods. Technological issues in producing ductile reinforced intermetallic composites are also addressed. Previous work in ductile reinforced intermetallic laminate composites is reviewed, and the toughening mechanisms and several laminate composite systems are described. Ti6Al4V-Al_3Ti MIL composites, as well as its specific properties, are briefly discussed at the end the chapter.

Chapter 3 describes the research objectives and scientific originality of this research. The research objectives and tasks needed to accomplish them are discussed in details.

Chapter 4 describes the experimental procedures in this research. The quasi-static and dynamic compression tests conducted on Ti6Al4V-Al_3Ti MIL composite and pure Al_3Ti are detailed. The preparation and characterization of composite and pure Al_3Ti on crack density and crack morphology by optical microscopy and scanning electron microscopy are also described.

Chapter 5 presents and discusses the results of mechanical testing and characterization of Ti6Al4V-Al_3Ti MIL composites. Crack morphology of the as-processed MIL composites was characterized by optical microscopy: three types of cracks were observed, parallel cracks, perpendicular cracks and 45^0 angled cracks, with respect to the interface. Photomicrographs were taken for MIL composite specimens and were assembled in montages. The crack length, crack orientations and crack locations were measured, and the crack densities were calculated and compared for different concentration of Ti6Al4V. Quasi-static and dynamic compression tests are conducted on pure Al_3Ti and the maximum compressive stress was obtained. Scanning electron microscopy (SEM) analysis shows two types of the crack modes in pure Al_3Ti, intergranular and transgranular cracks, the form of which have little dependence on the strain rates. Quasi-static and dynamic compression tests were conducted and SEM was employed to analyze different failure modes of MIL composites under different loading directions, strains, strain rates and volume fraction of Ti6Al4V. The effect of crack density, as quantified by a damage parameter, on elastic modulus and stress-strain relation were calculated and compared with experimental results. The physical models of damage evolution in MIL composites were developed to capture the dynamics of crack propagation.

Chapter 6 describes the theoretical modeling of the elastic properties, residual stress and the fracture toughness of Ti6Al4V-Al_3Ti MIL composites. Elastic properties of MIL composite, such as Young's modulus, shear modulus and Poisson's ratio, were calculated as a function of volume fraction of Ti6Al4V and orientations, and were successfully compared with the experimental results obtained by Resonant Ultrasonic Spectroscopy (RUS) carried out by Dr. R. Schwarz at Los Alamos National Laboratory. Residual stresses due to the mismatch of thermal expansion coefficients of Ti6Al4V and Al_3Ti, were analyzed. Two stress release mechanisms, creep and crack propagation mechanisms were identified and implemented in the analytical modeling and finite element simulations. The analytical modeling employed the critical stress criterion to determine the onset of the crack propagation, and a Matlab code was developed to conduct the computation. The finite element simulation took into consideration of composite boundary and took the advantage of symmetry to simulate one eighth of the MIL sample, The J-integral at crack tips was used to determine the onset of the crack propagation. Results from both analytical modeling and finite element simulation compare well with the experimental results. The effect of residual stress on the fracture toughness of MIL composite was modeled as a combination of the crack-initiation toughness and the stress intensity influenced by the residual stresses, and the calculation predicts the maximum stress intensity at 57% volume fraction of Ti6Al4V.

Chapter 7 summarizes the conclusions drawn from this research and suggests the future work.

Appendix lists the Matlab code developed for the analytical modeling in the evolution of residual stress in MIL composites, with creep and/or cracking mechanism involved.

CHAPTER 2

BACKGROUND

2.1 Intermetallics

Intermetallics are phases or compounds formed from constituent metals whose crystal structure is different from the individual metals, typically in an ordered atomic distribution or superlattice where the different atomic species occupy different regular lattice sites. As a distinct class of materials, intermetallics have good high-temperature strength, high resistance to oxidation and corrosion, high melting point, high stiffness, good creep resistance, and relatively low density. Most intermetallics, however, exhibit brittle fracture and low tensile ductility at ambient temperature, because of limited dislocation mobility, insufficient number of slip or twinning systems, and very low surface energy resulting in little to no plastic deformation at the crack tip. Their usefulness as engineering materials is, therefore, restricted in many cases by the poor fracture resistance and limited fabricability. In addition, a number of them are sensitive to moisture in the environment at lower temperatures. For the past several decades, considerable efforts have been devoted to the research and development of intermetallics. While many researchers have focused on the deformation mechanisms and the brittle fracture properties of intermetallics, others have concentrated on improving its mechanical and fracture properties by controlling microstructures, adding additional reinforcement phases, and optimizing the processing variables. As a result of those intense efforts, a number of new intermetallics based on nickel, iron and titanium and enhanced by reinforcement phases in the form of particles, fibers or platelets have been developed. Many of them provide very attractive mechanical and fracture properties for structural and aerospace applications.

Table 1 lists some of the most promising intermetallics with their physical and mechanical properties.

Table 1 Physical and mechanical properties of candidate intermetallics.

	Density (g/cm^3)	Young's Modulus (GPa)	Coefficients of thermal expansion ($\times 10^{-6} / {}^0C$)	Tensile yield stress (MPa)	Melting point (${}^0C$)
Al_3Ti	3.4-4.0	215	12-15	120-425	1350
TiAl	3.8-4.0	160-175	11.7	400-775	1480
Ti_3Al	4.1-4.7	120	12	700-900	1680
$MoSi_2$	6.1	380-440	8.1-8.5	200-400	2020
Ni_3Al	7.4-7.7	180-200	14-16	200-900	1397
NiAl	5.9	177-190	14-16	175-300	1638
Fe_3Al	6.7	140-170	19	600-1350	N/A
Ni_5Si_3	7.2	340	N/A	550	N/A
FeAl	5.6-5.8	160-250	21.5	500-700	N/A

2.2 Toughening intermetallics

2.2.1 Overview of ductile toughening methods

Because of the brittleness and low ductility of intermetallics, many efforts have been made to improve their toughness at lower temperature by modifying their intrinsic fracture properties and by reinforcing intermetallics with ductile phases in the form of particles [6 - 8], fibers [9 - 11], and layer [12 - 18]. Several metallurgical and processing modifications have been used to improve the intrinsic fracture properties, including refinement of grain structures, controlling the grain shapes, alloying with chromium, and processing with surface protection layers. Although nominal improvements in toughness have been achieved by transformation toughening [19], more efforts have been devoted to ductile reinforcement [20 - 26] . Many reinforced intermetallics have showed promising low temperature fracture toughness along with their high temperature strength. Among the existing fabrication methods are traditional solidification techniques [27 , 28], pressure-aided consolidation of pre-alloyed intermetallic powders mixed with the ductile reinforcement [29-30], a reaction between elemental powders mixed with metal fibers or foils [31,32], thin foil hot pressing [33], and self propagating high temperature synthesis [3 - 5]

By introducing the ductile phase in intermetallics, toughness can be improved by crack deflection, crack bridging and energy absorbing mechanisms. The idea behind crack deflection and crack bridging is that the reinforcement-matrix interface needs to provide a path of relatively easy crack extension or deflection, which leads to the belief that the interface needs to be weak. The energy absorbing mechanism, on the other hand, utilizes the plastic deformation of the ductile phases to increase energy dissipation and thus increases the toughness of the intermetallic composites [34].

Figure 2-1 shows the schematic depiction of the different types of reinforcement in intermetallics (adapted from Clyne and Withers [35]).

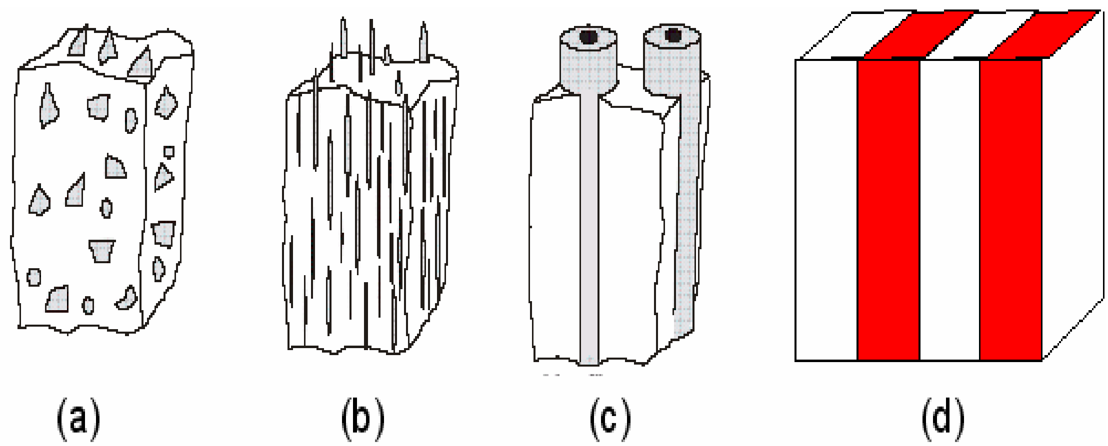

Figure 2-1 The schematic depiction of the different types of reinforcement in intermetallics: (a) particle reinforcement; (b) short fiber reinforcement; (c) long fiber reinforcement; (d) layer/platelet reinforcement.

2.2.2 Technological issues in producing ductile reinforced intermetallic composites

Several fundamental requirements must be satisfied to produce desirable ductile phase reinforced intermetallic composites. They reflect the challenges to successfully engineer the ductile reinforced intermetallic composites for structural and aerospace applications: simultaneously achieving both high-temperature strength and room temperature fracture toughness. Some of the most important technological issues are discussed in this section.

Chemical compatibility between the reinforcement and the intermetallic matrix is the first concern when producing ductile reinforced intermetallics composites. To avoid unacceptable alteration of the matrix microstructure and properties or degradation of the reinforcement during processing and service at elevated temperature, chemical compatibility between the matrix and reinforcement has to be considered, either thermodynamically or kinetically. Chemical compatibility determines the maximum temperature range of the composite and also imposed limitations on the fabrication method. For most fiber reinforced intermetallic composites, a relatively weak fiber-matrix bond is desirable in order to enhance room temperature toughness by promoting energy absorbing delamination and fiber pull-out. Fiber pull-out occurs when fibers fracture away from the main fracture plane and subsequently pull out from the matrix as the crack opening increases. This can increase the fracture strength both by absorbing energy during frictional sliding between the fibers and the matrix and by providing bridging behind the crack front, which will carry load, and consequently reduce the stress concentration near the crack tip.

The high strength and low toughness of most ceramic reinforcements make them extremely susceptible to even small amounts of chemical interaction with the matrix. For example, a surface flaw less than 1 mm deep on a SiC monofilament reinforcement can reduce its failure strength by over 50% [36]. However, because of the additional requirements for obtaining designed properties of the composites, thermodynamic compatibility is not often achieved. Thus, in practice, strength, stiffness, and availability are the principal considerations in the selection of reinforcement-matrix combinations, and the chemical compatibility is achieved through other means, such as application of a sacrificial coating and often at a price by sacrificing the control of reinforcement volume fraction and morphology and the interface properties. Although such systems are thermodynamically stable, coarsening may also rise as a problem.

Another concern while reinforcing intermetallics with ductile phases is the mismatch in coefficient of thermal expansion. The difference in coefficient of thermal expansion between the reinforcement phases and the intermetallic matrix introduces the residual stresses during the processing and during the service. The magnitude of the residual stress depends upon the stiffness of the components and the change in temperature. Research shows [37] that residual stresses as high as 300 MPa were measured by asymmetrical X-ray diffraction in Nb-Nb_5Si_3 composites when cooling from 1500K.

Since intermetallic matrices typically have limited plasticity below one-half of their absolute melting temperature, residual stresses generated cannot be relieved by plastic deformation. As a result, the selection of a reinforcement-matrix combination must carefully consider the coefficient of thermal expansion of each component to avoid the introduction of damage during cooling in processing and from thermal cycling experienced during service. Therefore, it is essential that existing residual stresses can be correctly anticipated and managed during heat treatment and machining. Figure 2-2 shows the coefficients of thermal expansion of a number of candidate reinforcements and intermetallic matrices (adapted from Miracle [38] and

Ward-Close [39]).

Other issues such as environmental resistance are also concerns for ductile reinforced intermetallic composites. Many intermetallic alloys are susceptible to environmental embrittlement and failure strains are very low under tensile testing in air environment [40]. Intense spallation of the oxide is driven by the poor adhesion and large volume increase of the oxide phase. Mo-silicide intermetallics can suffer from a "pest" phenomenon at intermediate temperatures that attacks materials which are not fully dense. Both solid (SiO_2) and vapor (MoO_3) oxides may form, and when these form in small cracks or voids, stresses generated by the volume expansion causes parts of the Mo-silicide to spall. Cracks and pores are often present in the as-processed material, but even if these could be avoided, cracks can easily form from applied mechanical and thermal loads, so that avoidance of this degradation mechanism is difficult. Finally, refractory metals are often used as ductile phase reinforcements. These phases (elements or alloys of Nb, Mo, Ta, and W) are only effective when they bridge cracks, and generally have very poor oxidation resistance. Thus, the ability to maintain toughening may be seriously compromised.

The final technological concern is to develop the consolidation and processing techniques and methodologies that can provide complete densification without damaging the reinforcements, and that can provide control over the matrix composition and microstructure and the distribution of reinforcements.

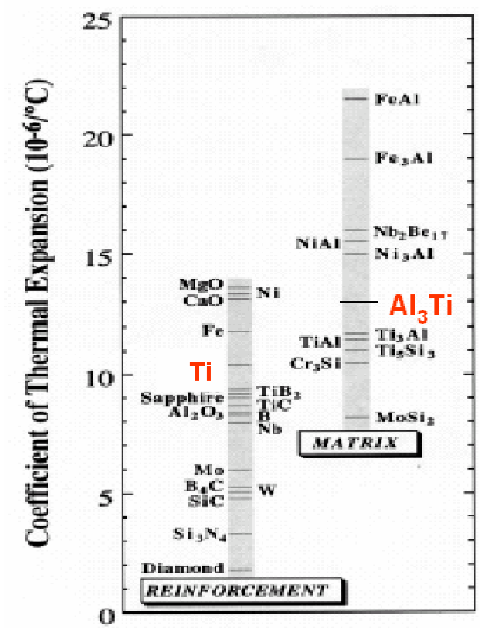

Figure 2-2 The coefficients of thermal expansion for candidate intermetallic matrix compounds and reinforcements. The coefficients of thermal expansion are averaged from room temperature to 1000 ^{0}C .

2.2.3 Fiber reinforcement toughening

Ceramic particulate reinforcements are available in a broad range of materials (including oxides, borides, carbides, and nitrides), morphologies (including particles, plates, and whiskers), and sizes. Although particulate reinforcements can provide improvements in stiffness, in practice, they are generally not capable to provide required levels of high-temperature strength or toughness at room temperature.

By comparison, fiber reinforcements have better performances providing improvements in stiffness and strength and continuous long fiber reinforcements are especially suitable at the highest operational temperatures. In addition, long fiber reinforcements can provide higher toughness and fracture resistance for the composites than the discontinuous short fiber reinforcement composites. However, to develop and produce a desirable reinforcement fiber, a great number of technological obstacles have to be overcome [41].

Since many ceramic fiber reinforcement materials are sensitive to processing defects, very fine grain sizes are desired in those fibers. For large diameter fibers, chemical vapor deposition (CVD) is most often used, while small diameter fibers are generally produced in tows and are produced by spinning a sol, followed by drying and crystallization at high temperature.

To minimize damage during processing and to provide chemical compatibility between fiber reinforcement and intermetallic matrix, fiber coatings are often necessary, and the three components of the final composites – intermetallic matrix, fiber reinforcement and the coating – comprise, on their own, a micro-composite system. Therefore, the chemical compatibility is the most important factor to be taken into consideration. Further, the residual stress generated during the processing and during the service may jeopardize the properties of the composites as a whole.

As a result of the technological problems discussed above, only a limited number of continuous fibers are commercially available for use in intermetallics and they are listed in Table 2. The first four fibers – boron, molybdenum, niobium and tungsten – are metal fibers, and the rest of them are ceramic fibers. Although metal fibers have been developed for intermetallics, comparing with ceramics fibers, they are chemically instable with many intermetallic matrices, and have high density and low strength at high temperature. Therefore, even if metal fibers can be produced more cost effectively, more researches have to be conducted to overcome their deficiencies.

Among the commercially available fibers, SiC monofilament reinforced Ti aluminide intermetallic composites have demonstrated outstanding performance in both high temperature strength and room temperature fracture toughness. These SiC/Ti-aluminide intermetallic composites not only compete with existing materials systems, but far exceed current capabilities, providing a materials technology that has enabled the revolutionary design of ring rotors, which dramatically reduce the rotating mass required for compressor stages. In addition, these materials enable significantly higher operating temperature, which further improves the efficiency of gas turbine engines.

Table 2 Characteristics of commercially available fibers.

Fiber	Density (g/cm^3)	Modulus (GPa)	Coefficient of thermal expansion ($\times 10^{-6}/{}^0C$)	Diameter (μm)	Coating
Boron (Borsic)	2.34	380	8.3		none/SiC
Molybdenum	10.4	325	6.5	variable	none
Niobium	8.6	100	7.9	variable	none
Tungsten	19.3	415	4.6	104	none
SiC (Textron SCS-6)	3.0	380 - 400	4.5	142	C (33 mm)/C+SiC (4 mm)
SiC (DERA Sigma 1140+)	3.4	410 – 430	4.5	100	W (14 mm)/C (5 mm)
SiC (Trimarc)	3.4	410 - 430	4.5	127	W (12.5 mm)/C+SiC (4 mm)
SiC (Textron Ultra SCS)	3.0	370	n/a	142	C (33 mm)/C+Si (4 mm)
Sapphire (a-Al_2O_3 (Saphikon)	3.97	410	8.3 – 9.0	150	none
Al_2O_3 tow (DuPont FP)	3.92	380	9.1	18 - 20	none
Al_2O_3 tow (3M Nextel 610)	3.9	380	7.9	11.5	none
Al_2O_3+20% ZrO_2 tow (DuPont PRD-166)	4.2	380	9.4	20	None
Mullite+2% B_2O_3 tow (3M Nextel 480)	3.05	224	n/a	10 - 12	None

2.3 Ductile reinforced intermetallic laminate composites

2.3.1 Development of ductile reinforced intermetallic laminate composites and toughening mechanisms

Ductile reinforced intermetallic laminate composites comprise of alternating layers of ductile reinforcements, usually metals, and intermetallic layers, manufactured by tape casting or sintering techniques [42]. By optimizing the constituent properties in the layered structure, ductile reinforced intermetallic laminate composites improve the ductility necessary for intermetallics at low temperature, and in general, provide the maximum toughening efficiency among other forms of ductile reinforcements [43]. Figure 2-3 shows the schematics of the increase in toughness in the composites for different forms of reinforcement, from particle, short fiber, and continuous fiber to laminates morphology.

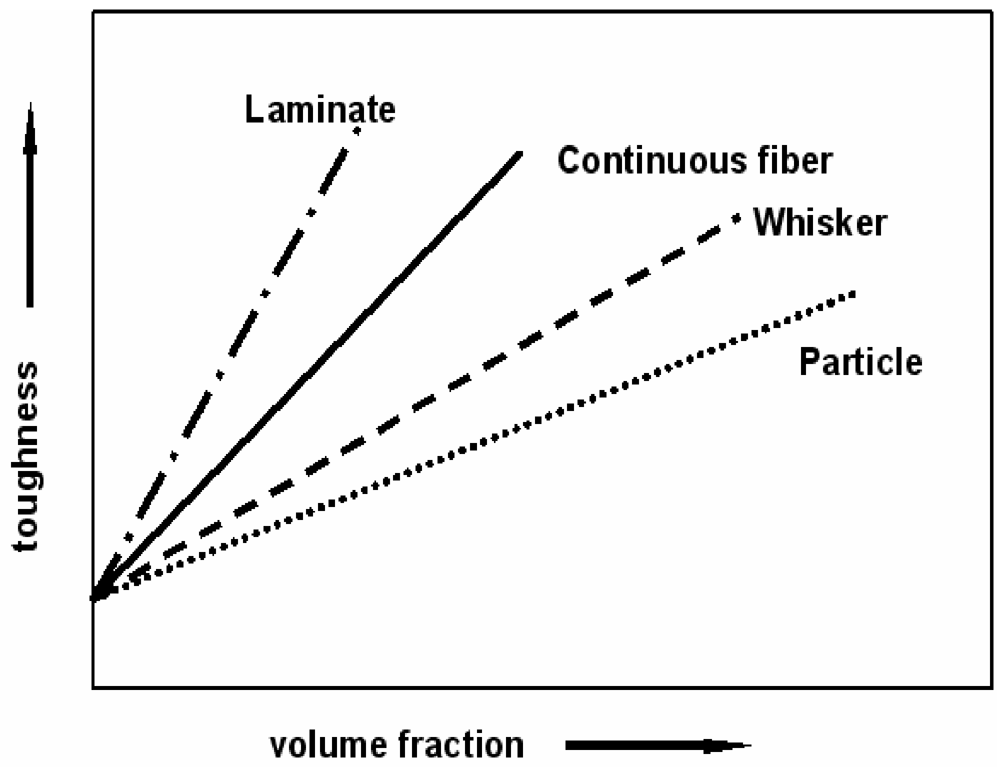

Figure 2-3 The schematics of the increase in toughness in the composites for different forms of reinforcement, from particle, short fiber, continuous fiber to laminates morphology.

By layering a ductile phase with the brittle intermetallic, the resulting laminate composites are toughened by reducing the local stress intensity at the crack tip and the local crack growth driving force. The mechanisms involved have been studied in two crack growth orientations, as shown schematically in Figure 2-4.

In the crack arrester orientation, a crack grows sequentially in the direction perpendicular to the ductile and brittle layers of the laminate composites. In the crack divider orientation, crack grows simultaneously through all the layers in the direction parallel to the layer faces [44]. Six major toughening mechanisms have been identified in the ductile reinforced intermetallic laminate composites, and they are briefly discussed below.

Crack deflection occurs when layer delamination happens ahead of an advancing crack or when a crack encounters an interface. Large crack deflection, up to 90° in the crack-arrester orientation, can reduce the Mode I component of the local stress intensity and causes the crack to move away from the planes of maximum stress. Crack blunting occurs when a crack encounters a ruptured region and is consequently, deflected and blunted. Further crack growth requires re-nucleation, i.e. a significant amount of energy absorption, resulting in an increase in toughness.

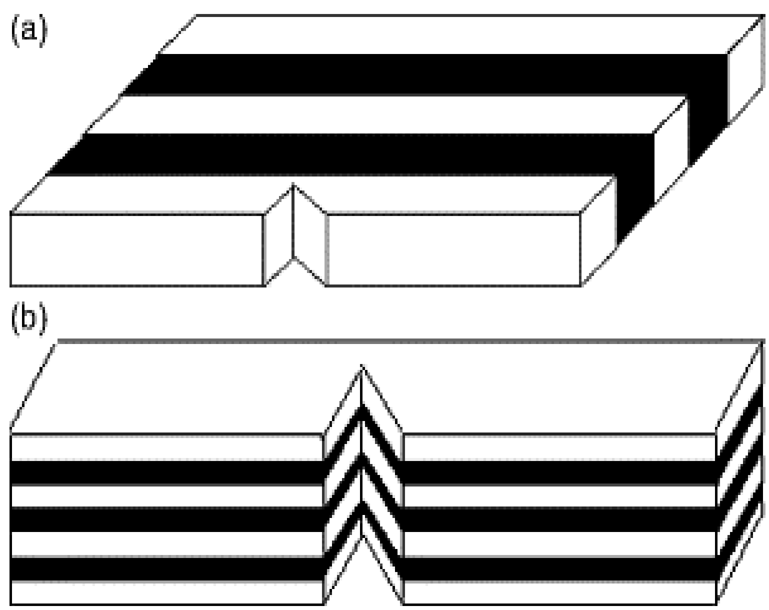

Figure 2-4 Schematic diagrams of (a) crack arrester orientation and (b) crack divider orientation in the ductile reinforced intermetallic laminate composites.

In crack bridging toughening mechanism, unbroken ductile layers span the wake of the crack and crack-growth requires stretching of the bridging ligaments which must have sufficient ductility to avoid fracture at or ahead of the crack tip. In the stress redistribution mechanism, delaminations in the layers ahead of the crack tip result in a reduction and redistribution of the local stress. For the crack front convolution, the composite comprised of layers with dissimilar ductility and tested in the divider orientation, and the crack front in the less ductile component leads the crack in the more ductile component. The resulting crack front is highly convoluted and can result in delamination at the interfaces. Thus, crack growth is slowed and reduced by the plastic tearing required for crack propagation in the more ductile layer. The last toughening mechanism is the change in the local deformation mode. In the divider orientation, substantial deformation at the crack-tip may change the deformation mode of individual layers from plane strain to plane stress. This change in the deformation mode causes the layers to fail in shear rather than flat fracture and, consequently, increases the stress required for crack growth.

2.3.2 Existing ductile reinforced intermetallic laminate composites

Over the past decade, a number of diverse brittle intermetallics have been toughened with various ductile metal laminates [45, 46], including Ti6Al4V-Al_3Ti, Nb-Cr_2Nb [16], Nb-Nb_3Al [16, 47], TiAl-TiNb [48], FeAl-Tic [49], Al-Al_2O_3 [50 - 53], Al_2O_3-Cu [54,55], Al-NiAl [56], Mo-NiAl [57].

Enoki [33, 58] studied Nb/Nb-aluminide and $Nb/Nb_3Al/Nb_2Al/NbAl_3$, laminate composite system, manufactured from pure Nb and Al sheets, by thin foil hot pressing process. Microvickers hardness demonstrates the formation of various phases, and the hardness values decrease with increasing Al-Nb atomic ratio. It is also shown that tensile strength of the laminate composite is affected by the thickness and volume fraction of metal layer. Chisel edge fracture was observed in the fracture surface after tensile test that are related to the thickness of the metal and the intermetallic compound layers. The laminate composites demonstrate high ductility (6.6–14.5%) and fracture toughness (9.7–12.4 $MPa\sqrt{m}$) due to strong bonding at the interface between the metal and the intermetallic compound layers interface.

Odette [59] investigated the γ-TiAl-TiNb laminate composites, produced by hot pressing the TiNb foils (thickness of 1500 μm) between lapped γ-TiA1 plates at 1066 ^0C at 10 MPa for 4 hours. The resulting laminate composites were composed of alternating layers of brittle γ-TiA1 of 80% volume fraction and ductile TiNb reinforcements of 20% volume fraction. Two toughening mechanisms, crack renucleation and bridging mechanisms, have identified and yielded a steep resistance curve and effective toughness more than ten times higher than the matrix.

Kajuch [60] and Rigney [61] studied the effects of contamination, imposed constraints and temperature on the mechanical properties of the Nb reinforced Nb-Nb_5Si_3 laminate composites, which were manufactured in a vacuum hot press at 1473K for 5 hours with 10 MPa pressure. Shang [37] investigated the residual stresses and bending stresses in both flat and curved Nb/Nb_5Si_3 microlaminates.

Residual stress as high as $300\,MPa$ and bending stress as high as $673\,MPa$ were obtained by asymmetrical X-ray diffraction.

Pickard [62] studied the mechanical properties at the interface between NiAl intermetallic and Mo ductile phase in the laminated structure, under a variety of stress states involving primarily shear. A microstructural investigation of the interfacial reaction zone and the shear failure path was conducted to identify failure mechanisms. The residual stress was measured by debonding the Mo interlayer from the NiAl matrix over a large length of interface, over 10 mm long, and measuring directly the extension of the metal when the residual strain was released. The mechanical strain due to coefficients of thermal expansion mismatch is 0.083% and the upper limit residual stress of $380\,MPa$ was estimated for the biaxial residual stress state in the laminate.

Xiao [63] investigated the effects of interfacial coatings on the fracture toughness of Nb-$MoSi_2$ laminate composites. Because of the chemical incompatibility of niobium with $MoSi_2$, different oxide coatings, Al_2O_3 and ZrO_2, have been applied to niobium reinforcement for high-temperature structural applications. Bloyer [20, 21, 22] studied the effects of layer thickness and orientation on the fracture toughness of Nb-Nb_3Al. Increasing the layer thickness improves fracture toughness of Nb/Nb_3Al laminates, and the influence of coarsening the scale of Nb reinforcement was more apparent in the crack-divider than the crack arrester orientation.

2.4 Ti6Al4V–Al_3Ti metal intermetallic laminate (MIL) composites

Ti6Al4V–Al_3Ti metal intermetallic laminate (MIL) composites, produced from elemental titanium and aluminum foils by a novel one-step process utilizing a controlled reaction at elevated temperature and pressure, have been extensive studied recently. Ti6Al4V–Al_3Ti MIL composites possess a combination of high strength, toughness and stiffness at a lower density than monolithic titanium [64]. Further, since Al is relatively inexpensive compared to Ti, the Ti6Al4V–Al_3Ti MIL composites is economically more attractive than monolithic titanium. Although Ti6Al4V–Al_3Ti MIL composites have been fabricated earlier by several researchers [65 - 68], the Ti6Al4V–Al_3Ti MIL composites in this study was able to be synthesized in open air by Vecchio and co-workers [1, 2]. This represents a great technological advantage, since it enables industrial production at significant cost reduction.

The intermetallics Al_3Ti formed during fabrication is one of the three titanium aluminides that interest people for a long time. The early interest in titanium aluminides can be traced back as early as 1980s from the efforts to design and build advanced gas turbine engines [69 - 71] with revolutionary performance improvements [72 - 76]. The reason was that specific weight of these materials [77,78] is only half of that of the presently used steels and nickel based alloys while their mechanical properties [79] especially at high temperatures come close to the traditional materials [80 , 81 , 82]. Moreover, these intermetallics retain a good dimensional stability [83] and good thermal conductivities. Titanium aluminides Al_3Ti, AlTi and $AlTi_3$ offer potential for increased temperature range and enhanced high temperature strength, stiffness and oxidation resistance compared with conventional titanium alloys.

Among the possible formation in the Ti-Al system, Al_3Ti is thermodynamically and kinetically favored over the formation of other aluminides when reacting Al directly with Ti. In addition, it has higher Young's modulus (216 GPa), oxidation resistance, and lower density (3.3 g/cm^3) than that of the other titanium aluminides such as Ti_3Al and TiAl. However, its extremely brittleness at room temperature and low fracture toughness (up to $2\,MPa\sqrt{m}$) limit its potential applications and ductile reinforcement is needed to improve its toughness before the industrial use.

For structural applications, materials should typically have high strength, high toughness and low density. A comparison of the specific compressive strength (i.e. compressive strength divided by density) as a function of specific Young's modulus (i.e. Young's modulus divided by the density) of Ti6Al4V–Al_3Ti MIL composites and a variety of engineering materials is shown in Figure 2-5. It is seen that the Ti6Al4V–Al_3Ti MIL composites have both higher specific compressive strength and higher specific modulus than the most conventional metals.

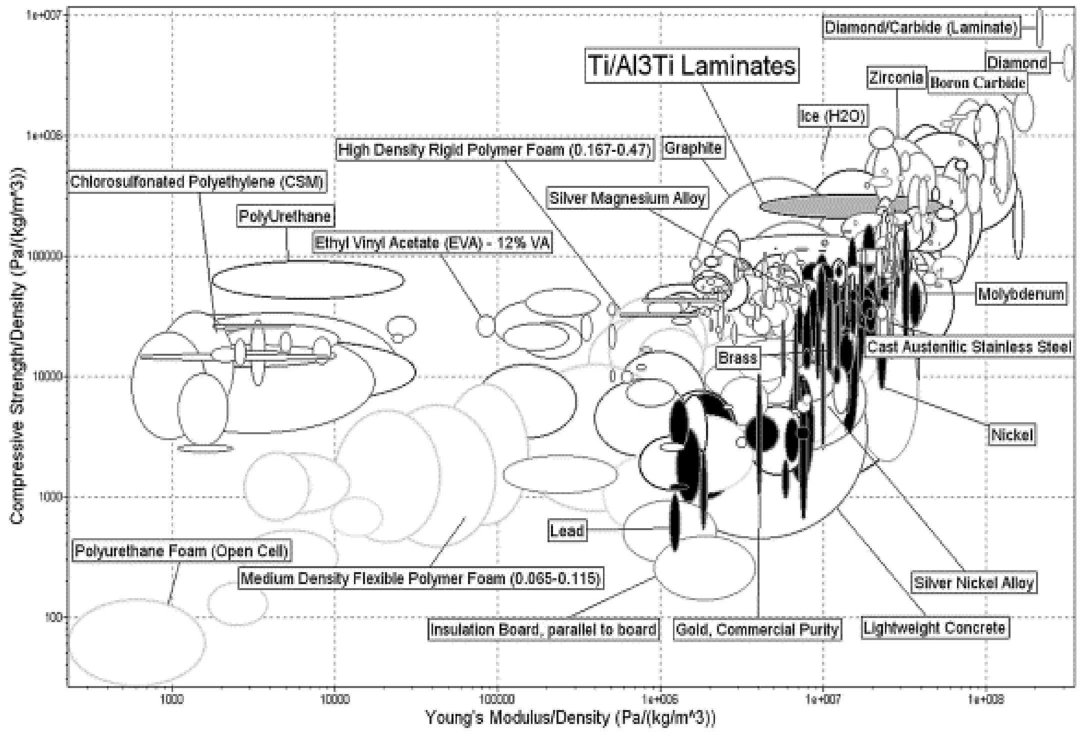

Figure 2-5 Plot of specific compressive strength vs. specific modulus of Ti6Al4V–Al_3Ti laminates relative to other engineering materials [2].

Figure 2-6 is an Ashby property map of Ti6Al4V–Al3Ti MIL composites and other laminate systems, metals, alloys and composites [2]. Specific fracture toughness, fracture toughness divided by the density, is shown as a function of specific Young's modulus. It can be seen that the Ti6Al4V–Al3Ti MIL composites have higher specific toughness than other laminate systems. It is seen that the MIL composites are extremely promising materials for structural applications that require high compressive strength and high stiffness.

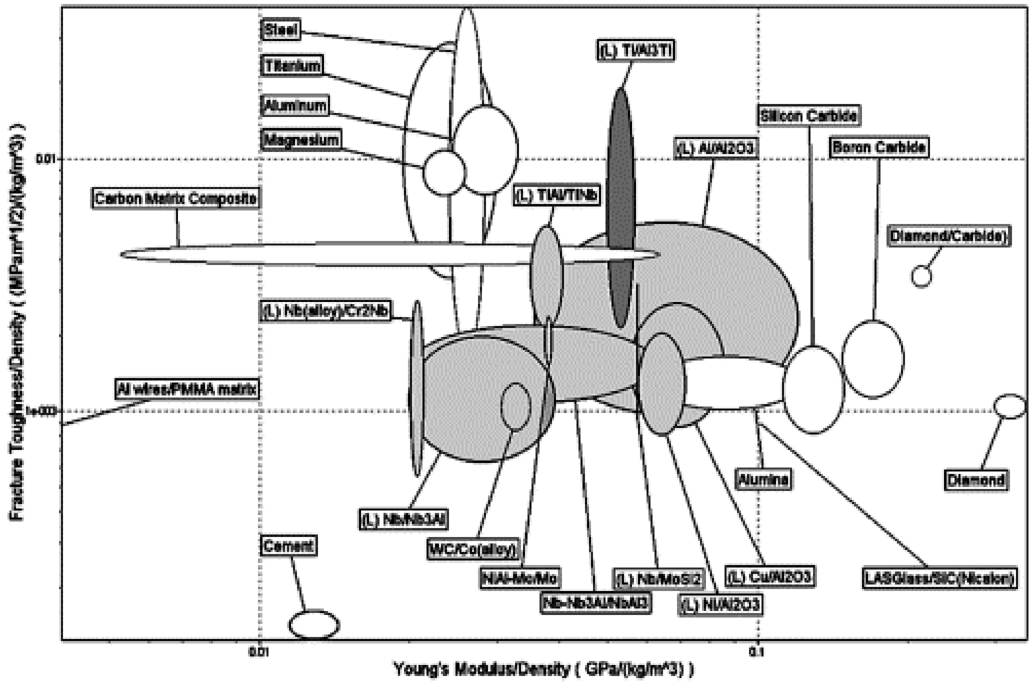

Figure 2-6 Property map of Ti6Al4V–Al_3Ti laminates (colored dark gray) and other laminate systems, metals, alloys and composites, showing specific fracture toughness as a function of specific Young's modulus [2].

CHAPTER 3

RESEARCH OBJECTIVES

3.1 Research objectives and tasks

The objective of this study is to investigate the evolution of damage and residual stress in the Ti6Al4V-Al_3Ti metal intermetallic laminate composite. This includes the modeling of its mechanical and fracture properties.

The goals and the tasks of this investigation are described as follows:

1. Investigate the crack morphology of as-processed Ti6Al4V-Al_3Ti MIL composites (section 1.1). Tasks needed to accomplish this goal are:

a) Employ optical microscopy to determine the crack locations, crack lengths, crack orientations, and crack distributions of as-processed MIL composites.

b) Calculate and compare the crack density of as-processed MIL composites.

2. Investigate the crack morphology of pure Al_3Ti after compression tests (section 5.2). Tasks needed to accomplish this goal are:

a) Conduct quasi-static and dynamic compression tests on pure Al_3Ti.

b) Employ SEM to characterize the crack morphology of pure Al_3Ti after quasi-static and dynamic compression tests.

c) Determine the effects of strain rates on the crack morphology.

3. Investigate the crack morphology of Ti6Al4V-Al_3Ti MIL composites after compression tests (section 5.3). Tasks needed to accomplish this goal are:

a) Conduct quasi-static and dynamic compression tests on MIL composites, with different volume fraction of Ti6Al4V, loading directions, strains and strain rates.

b) Employ optical microscope and SEM to characterize the crack morphology and quantify the crack density of MIL composites after perpendicular and parallel compression tests.

c) Evaluate the effects of volume fraction of Ti6Al4V, loading directions, strains, and strain rates on damage evolution in MIL composites.

d) Quantify the effect of damage evolution on the elastic modulus and compare with experimental results.

e) Establish physical models of crack propagation in MIL composites.

4. Investigate the elastic properties of Ti6Al4V- Al_3Ti MIL composites (section 6.1). Tasks needed to accomplish this goal are:

a) Evaluate the elastic properties of MIL composites as a function of volume fraction of Ti6Al4V and orientation, and compare with the experimental measurements.

5. Investigate the evolution of residual stress in Ti6Al4V- Al_3Ti MIL composites (section 6.2). Tasks needed to accomplish this goal are:

a) Evaluate the residual stress by elastic analysis.

b) Evaluate the residual stress by creep release mechanisms.

c) Evaluate the residual stress by crack propagation release mechanisms.

d) Evaluate the residual stress distribution by finite element simulation.

6. Investigate the effect of residual stress on the fracture toughness of Ti6Al4V-

Al_3Ti MIL composites (section 6.4). Tasks needed to accomplish this goal are:

a) Evaluate the apparent fracture toughness as the combination of the crack initiation toughness and the stress intensity due to the existence of residual stress, and compare with the experimental measurements.

Figure 3-1 shows the schematics of the research tasks and inter-connections.

3.2 Scientific originality

This study has the following scientific novelties:

1. The analytical modeling, finite element simulation and experiments have been combined to provide a general framework to study the evolution of damage and residual stress in Ti6Al4V-Al_3Ti MIL composites.

2. The crack distributions and crack density (section 1.1), as well as the patterns of damage evolution in MIL composites were studied through a series of controlled compression tests, and the damage effect on elastic modulus was quantified and compared with experimental results. The physical models of damage evolution were developed based on the experimental observation (section 5.3, 5.4 and 5.5).

3. Analytical modeling incorporated creep and crack release mechanisms, which were introduced in a Matlab code developed to quantify the evolution of the average residual stress in Ti6Al4V-Al_3Ti MIL composites (section 6.2).

4. Finite element simulation complemented the analytical modeling by verifying its solution and providing the distribution of the residual stress in Ti6Al4V-Al_3Ti MIL composites (section 6.3).

5. The effect of residual stress on fracture toughness was studied and an analytical model was established to quantify the fracture toughness of Ti6Al4V-Al_3Ti MIL composites as a function of volume fraction of Ti6Al4V (section 6.4).

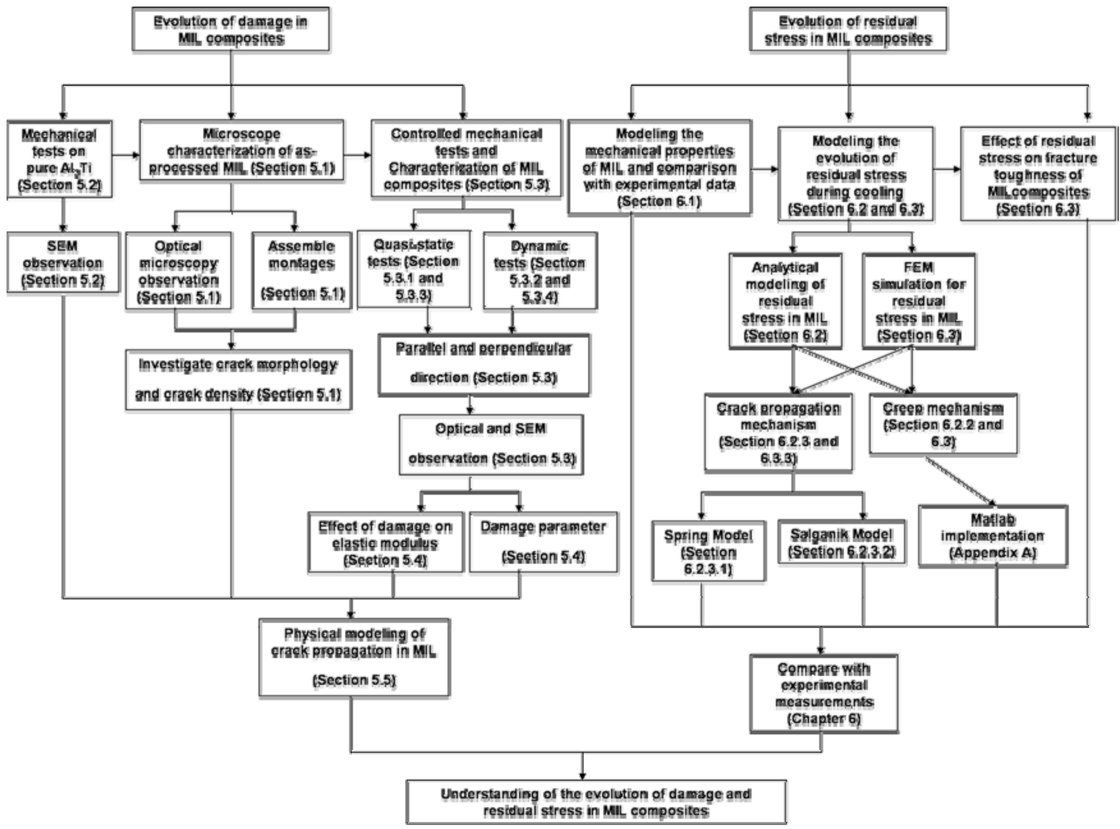

Figure 3-1 The schematics of research tasks and inter-connections.

CHAPTER 4

EXPERIMENTAL PROCEDURE

4.1 Specimen preparation

4.1.1 Starting materials

The foil materials used in this study are Ti6Al4V alloy and 1100-0 aluminum foils obtained from Supra Alloys Inc. and National Electronic Alloy Inc. Chemical composition and mechanical properties are listed in Table 3.

Table 3 Chemical composition and mechanical properties of foil materials.

Materials	Chemical composition %	Mechanical properties
Titanium Ti-6Al-4V	Ti: 89.57 Al: 6.13 C: 0.01 Fe: 0.1 H: 0.008 O: 0.16 N: 0.007 V: 4.01 Y: 0.005	Ultimate: 1035 *MPa* Yield: 950 *MPa*
Aluminum Al-1100-0	Al: 99 Cu: 0.05-0.2 Zn: 0.1 Mn: 0.05 Si&Fe: 0.95 All others: 0.05	Ultimate: 90 *MPa*

4.1.2 Processing of Ti6Al4V-Al_3Ti MIL composites and pure Al_3Ti

The processing was developed by Dr. K.S. Vecchio and co-workers. After cleaning, the foils were stacked in alternating layers of Ti6Al4V and aluminum with Ti6Al4V on the top and bottom. Ti6Al4V-Al_3Ti metal intermetallic laminate composites were then fabricated in the synthesis apparatus with controlled temperature and pressure by a novel one step process in the open air [1, 2]. The thickness of the initial Al and Ti alloy sheets is selected in such a manner that aluminum is completely consumed in forming the intermetallic compound Al_3Ti with alternating layers of partially unreactedTi6Al4Vmetal.

Pure Al_3Ti is produced in the same manner as the MIL composites and the only difference is that the starting thickness ofTi6Al4Vand Al is chosen in such a way that all the Ti6Al4V and aluminum are consumed in the reaction to form Al_3Ti and the final product consists only of Al_3Ti intermetallic compound.

4.2 Characterization of Ti6Al4V-Al_3Ti MIL composites and pure Al_3Ti

4.2.1 Optical microscopy

Samples of 10mm x 8.5mm x 7.5mm (LxWxH) and 80 mm x 18 mm x 8 mm (LxWxH) were ground from 220 to 4000 grit, and then polished by 0.05 micron Al_2O_3 to final polish. No etching was necessary to distinguish between the metal and intermetallic layers. Nikon Ephiphot optical microscope and Image-Pro Plus image analysis software was used to film and digitally store the images. The volume fraction of Ti6Al4V was calculated as:

$$\frac{t_{Ti}}{t_{Al_3Ti} + t_{Ti}} \tag{4.1}$$

where t_{Ti} and t_{Al_3Ti} refer to the thickness of the Ti6Al4V and the Al_3Ti layer, respectively.

4.2.2 Scanning electron microscopy (SEM)

Scanning electron microscopy was performed on a FEI Quanta 600 scanning electron microscope with secondary and backscattered imaging mode. Cracking and damage evolutions were characterized in both MIL composites and pure Al_3Ti. The layer thickness of Ti6Al4V-Al_3Ti metal intermetallic laminate composites was verified.

4.2.3 Mechanical testing

4.2.3.1 Quasi-static compression tests

The mechanical tests were conducted on rectangular samples with typical dimensions of 10mm x 8.5mm x 7.5mm (LxWxH). Each resulting curve represents the average of three to four tests. Samples were tested at room temperature at a strain rate of 10^{-4} /second on a SATEC testing frame, in both perpendicular and parallel direction to the interface. Figure 4-1 show the perpendicular and parallel loading configurations. The designation refers to the orientation between loading direction and plane of laminates.

4.2.3.2 Dynamic tests

Dynamic tests were performed at strain rates in the range of 800~2000/second in a split Hopkinson pressure bar. The mechanical tests were conducted in both perpendicular and parallel directions to the interfaces. A striker bar of suitable length, determined by the required strain and strain rate, was accelerated by compressed gas. The striker impacted the incident bar and generated a pressure pulse, which then travels down the incident bar and impacts the sample. A portion of the incident pulse impacting the sample is reflected and the remainder is transmitted into the transmission bar. The striker, incident, and transmission bars were all 19.1 mm diameter 350 maraging steel.

4.2.4 Crack density measurements

Nikon Ephiphot optical microscope and Image-Pro Plus image analysis software were used to digitally store and analysis the images. Images of the whole sample were recovered and crack length, locations and orientations were measured and recorded.

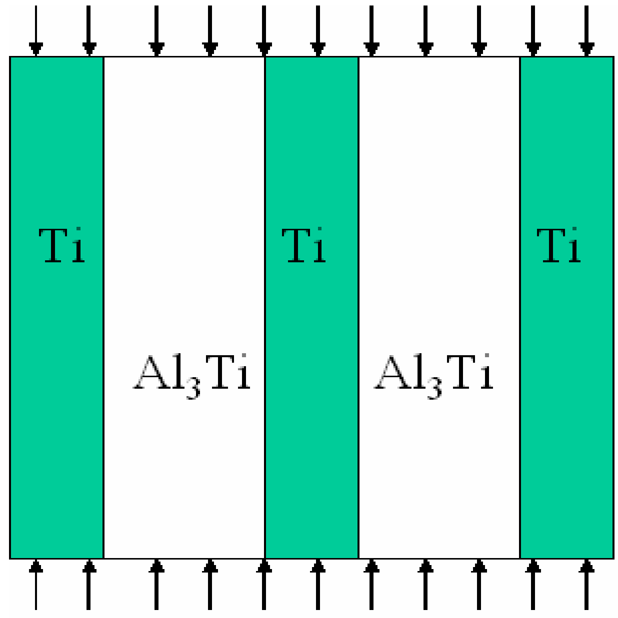

(a)

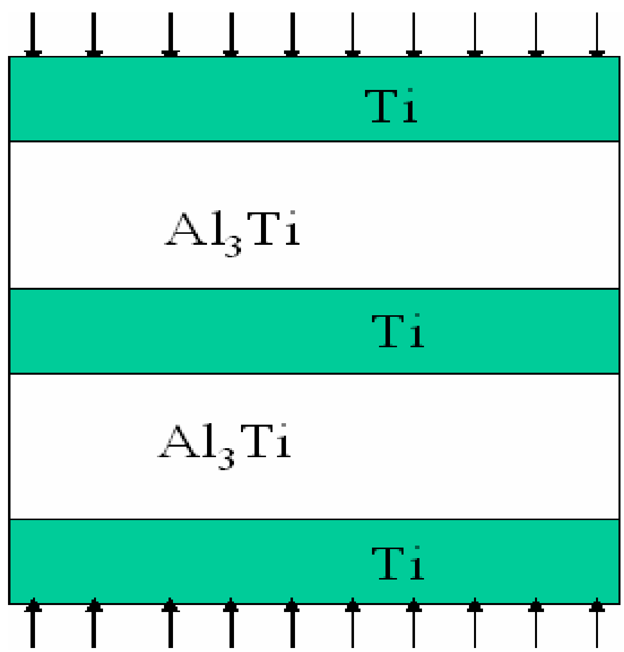

(b)

Figure 4-1 Loading configuration: (a) compression loading perpendicular to the laminate plane; (b) compression loading parallel to the laminate plane.

CHAPTER 5

EXPERIEMENTAL RESULTS AND DISCUSSION

5.1 Crack morphology and crack density in the as-processed Ti6Al4V-Al_3Ti MIL composites

Optical microscopy was performed to investigate the crack morphology and crack density in Ti6Al4V-Al_3Ti MIL composites. A rectangular Ti6Al4V-Al_3Ti MIL composite bar specimen of 80 mm x 18 mm x 8 mm was used to minimize the edge effect on the crack distribution and ensure the statistic validity.

5.1.1 Crack morphology

Figure 5-1 (a) shows a typical optical picture of the as-processed Ti6Al4V-Al_3Ti MIL composite. The darker phase is Ti6Al4V and the lighter is Al_3Ti. Cracks were observed in Al_3Ti layers were classified into three categories: parallel to the interface, perpendicular to the interface and 45^0 angled to the interface.

Figure 5-1 (b) - (d) show the optical pictures of those three typical configurations. Most cracks observed are perpendicular cracks, and the parallel cracks appear mostly in the middle of Al_3Ti layers.

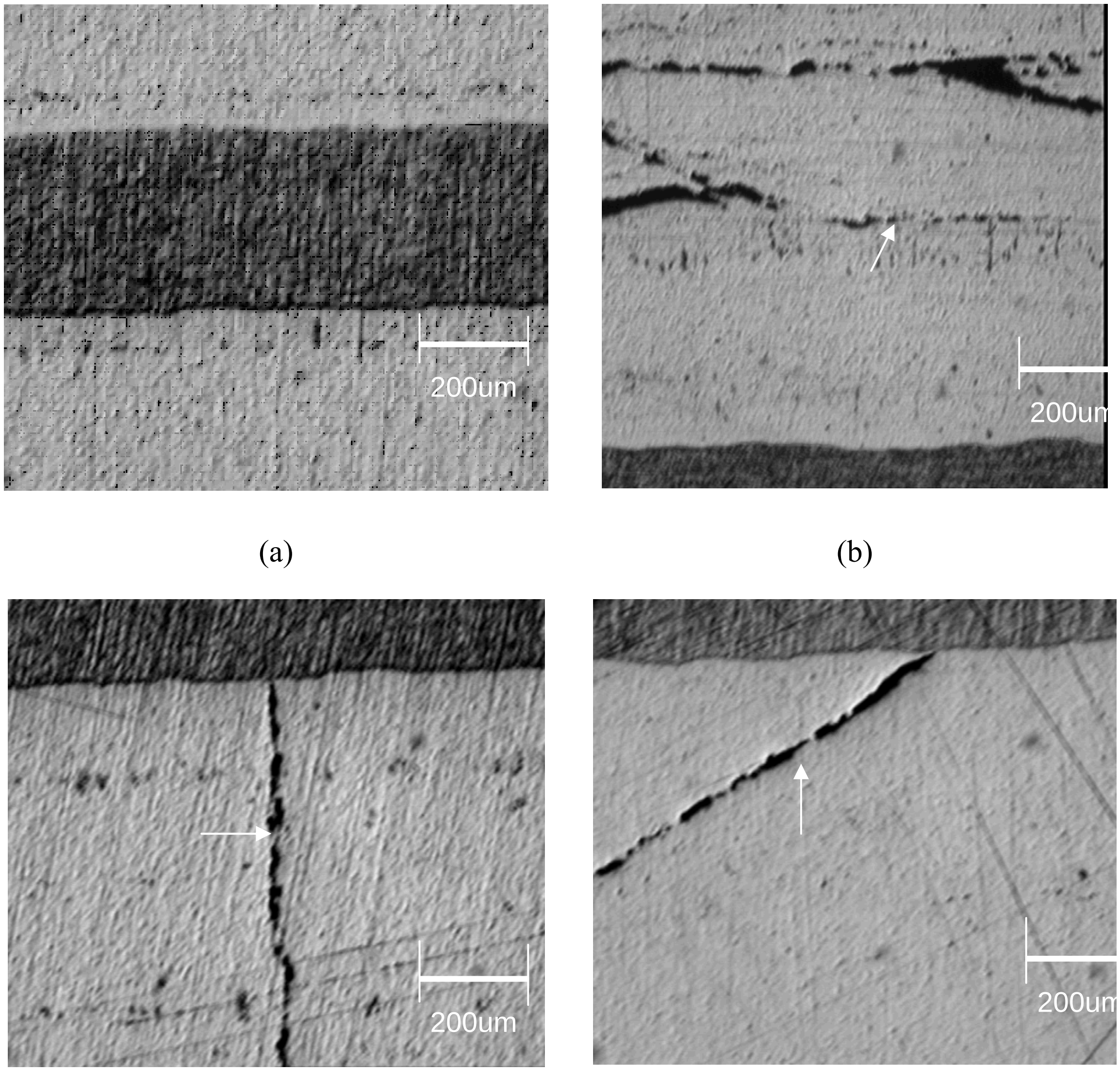

(a) (b)

(c) (d)

Figure 5-1 (a) A typical optical picture of Ti6Al4V-Al_3Ti MIL composite; (b) parallel crack; (c) perpendicular crack; (d) crack inclined 45^0 to the interface.

Photomicrographs were taken for the entire specimen and assembled in montages. Figure 5-2, Figure 5-3 and Figure 5-4 show the montages for different volume fractions of Ti6Al4V: 14%, 20% and 35%. All cracks (parallel, perpendicular and inclined (~45^0) to the interface) were measured for the three composites. It is seen that most cracks are located in the top part of the specimen which may be the result that during the cooling that part has faster cooling rate than the rest of the specimen so that larger residual stress was generated, which led to more cracking in that part.

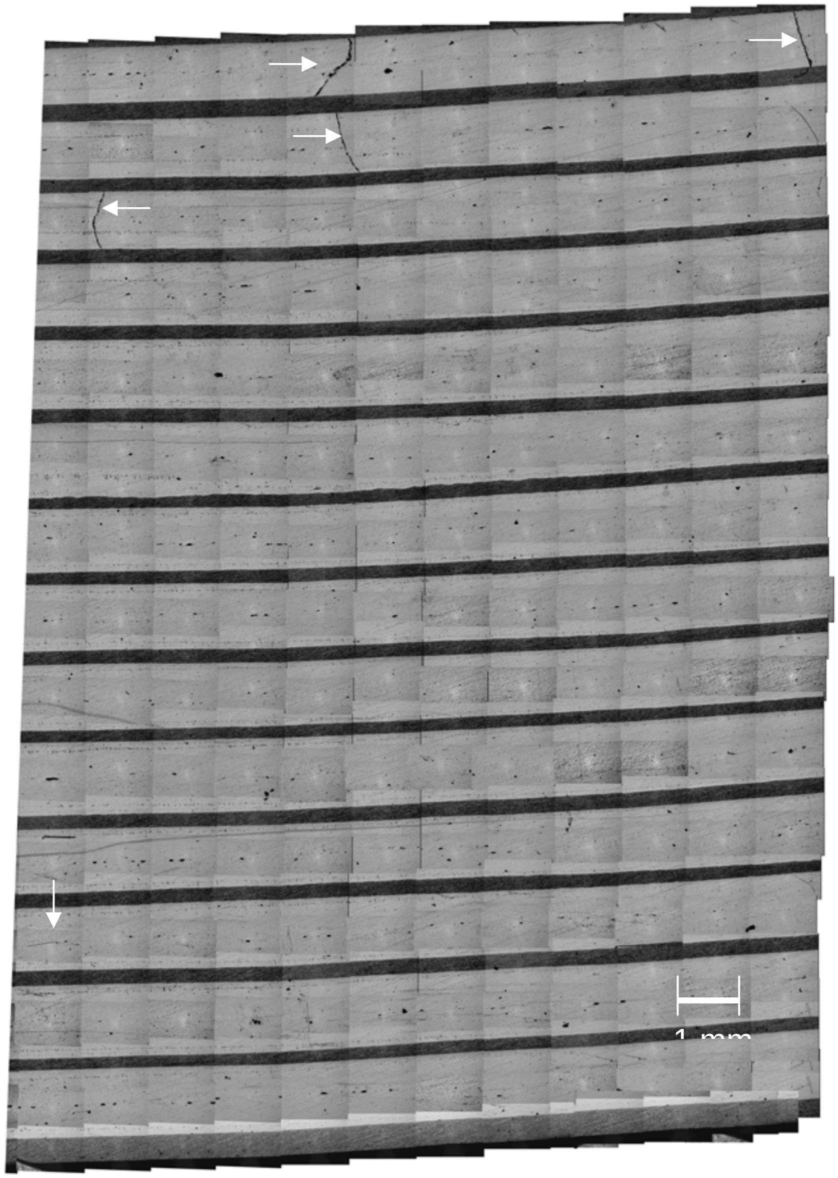

Figure 5-2 A montage of part of the cross-section of as-processed 14% Ti6Al4V MIL composite (cracks marked by arrows).

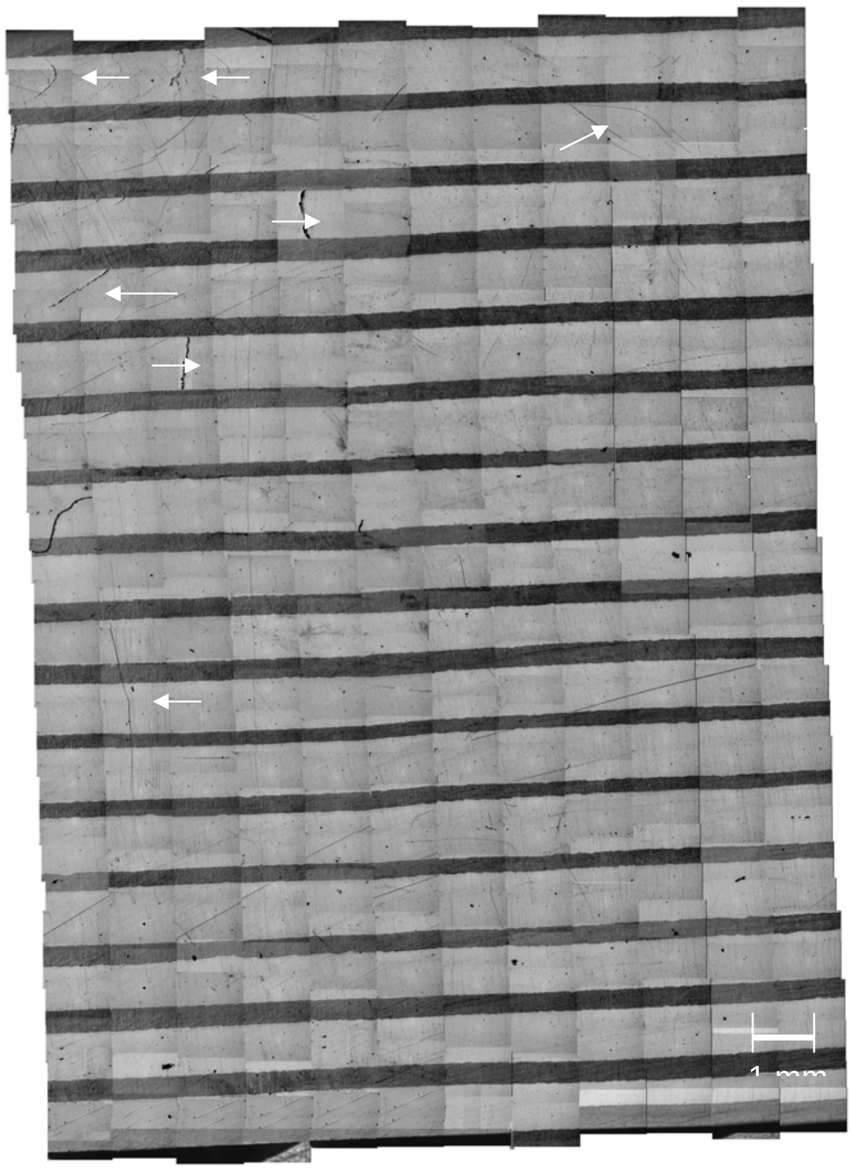

Figure 5-3 A montage of part of the cross-section of as-processed 20% Ti6Al4V MIL composite (cracks marked by arrows).

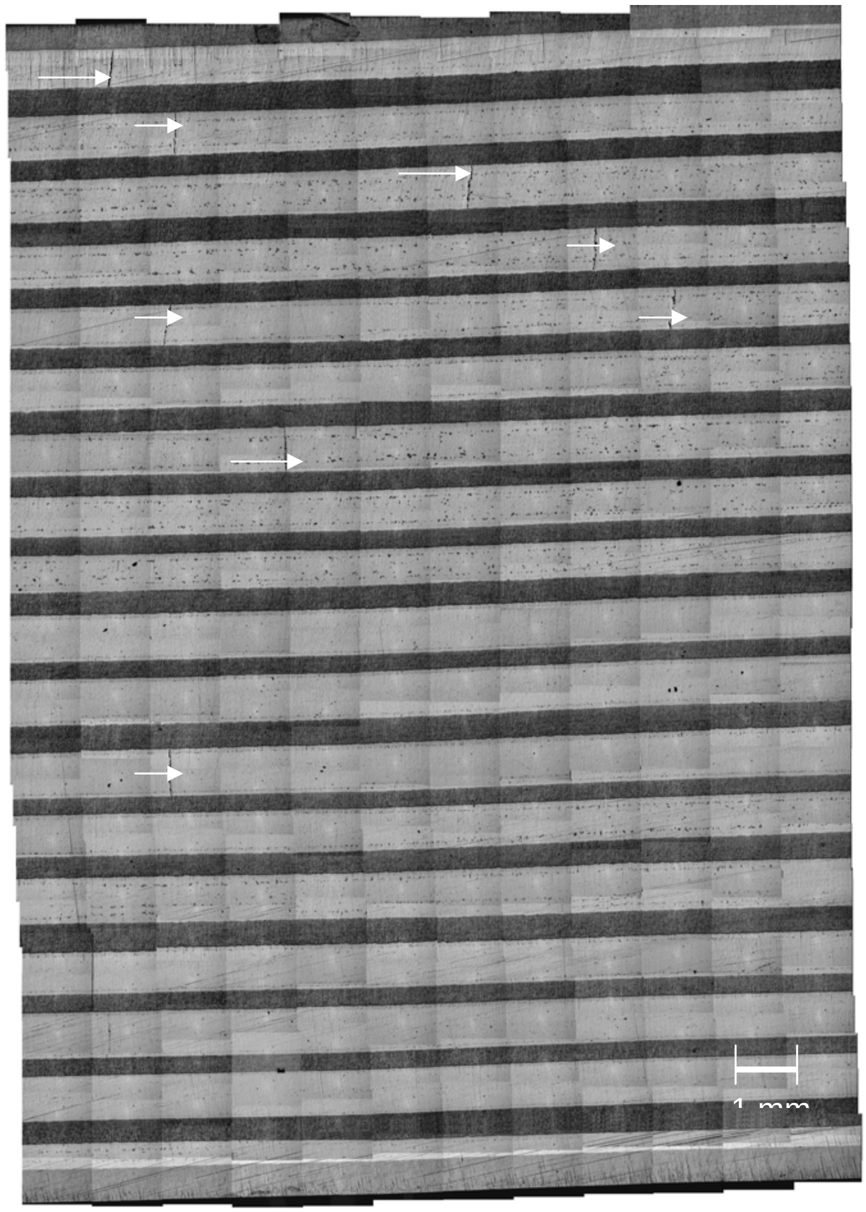

Figure 5-4 A montage of part of the cross-section of as-processed 35% Ti6Al4V MIL composite (cracks marked by arrows).

5.1.2 Crack density

Figure 5-5, Figure 5-6 and Figure 5-7 show the crack distribution for the three as-processed MIL composites. In all cases, the length of perpendicular cracks is close to the average thickness of Al_3Ti layers, and the length of inclined cracks is close to $\sqrt{2}$ times of the average Al_3Ti layer. Table 4 and Table 5 summarize the crack distribution and crack density measurements.

Table 4 Crack sizes and density in as-processed MIL composites

	Perpendicular (μm)	Inclined (μm)	Al_3Ti thickness (μm)	Crack density (mm/mm^2)
14% Ti6Al4V	900 - 1150	1400	1000	0.321
20% Ti6Al4V	660 – 740	1000	700	0.255
35% Ti6Al4V	340 – 480	600	450	0.137

Table 5 Crack distribution in as-processed MIL composites

	Perpendicular	Inclined	Parallel
14% Ti6Al4V	49%	31%	20%
20% Ti6Al4V	59%	19%	22%
35% Ti6Al4V	72%	7%	21%

The crack density, ρ_{crack} was calculated by dividing the total length of cracks, ℓ, by the total surface area they are located, A.

$$\rho_{crack} = \frac{\ell}{A} \tag{5.1}$$

The second dimension of the crack is not known and is assumed to be equal to the thickness of the specimen, t. The crack density, represented as the area of cracks per unit volume, is

$$\rho_{crack} = \frac{\ell t}{At} = \frac{\ell t}{V} \tag{5.2}$$

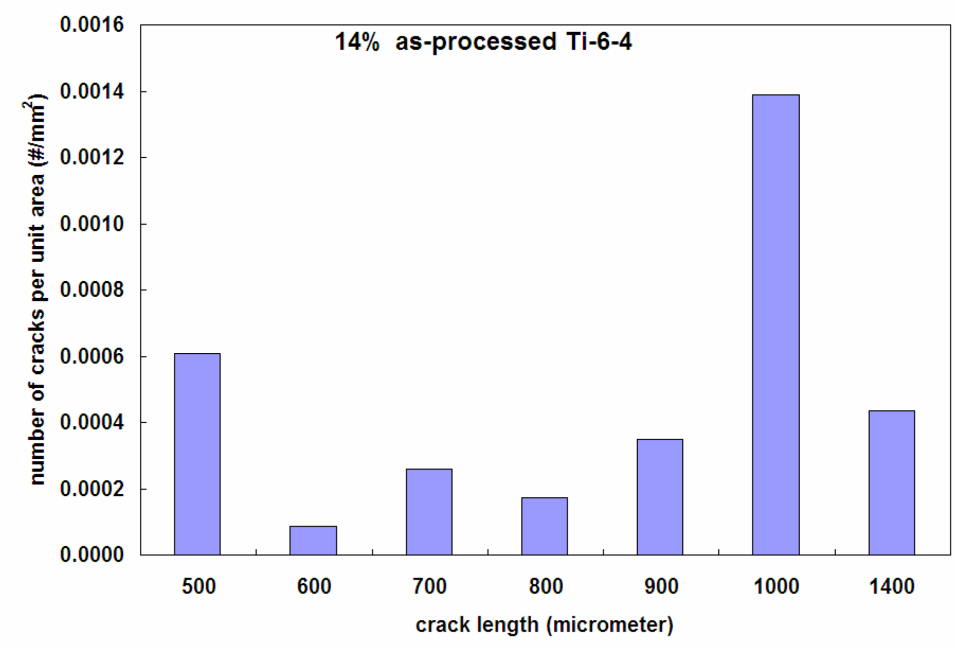

(a)

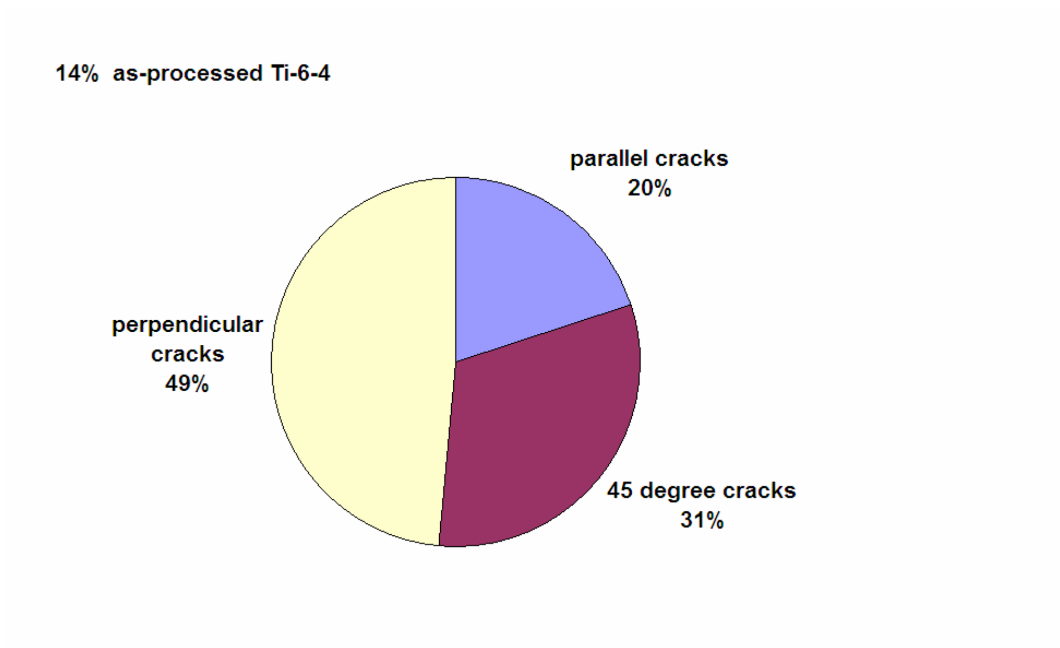

(b)

Figure 5-5 Crack distribution of as-processed 14% Ti6Al4V MIL composite.

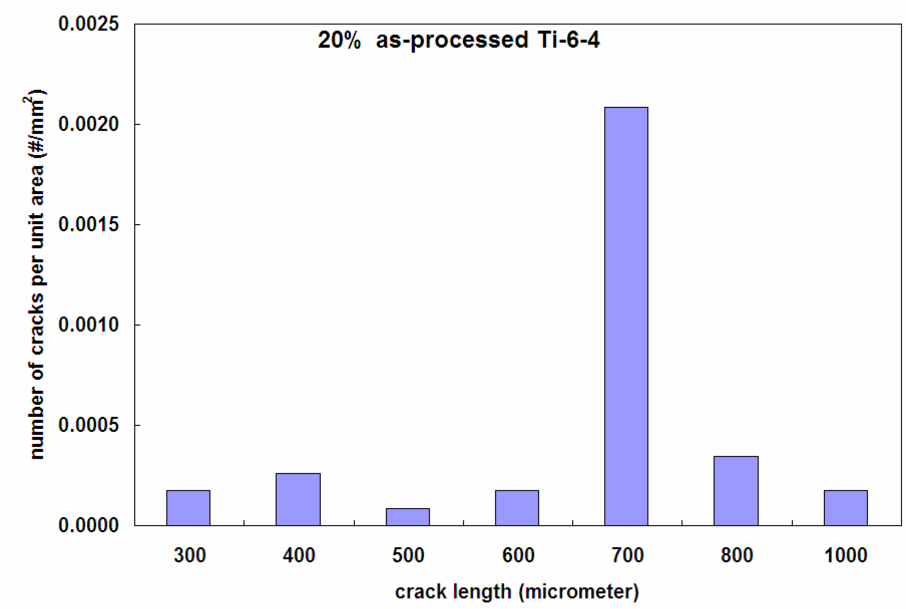

(a)

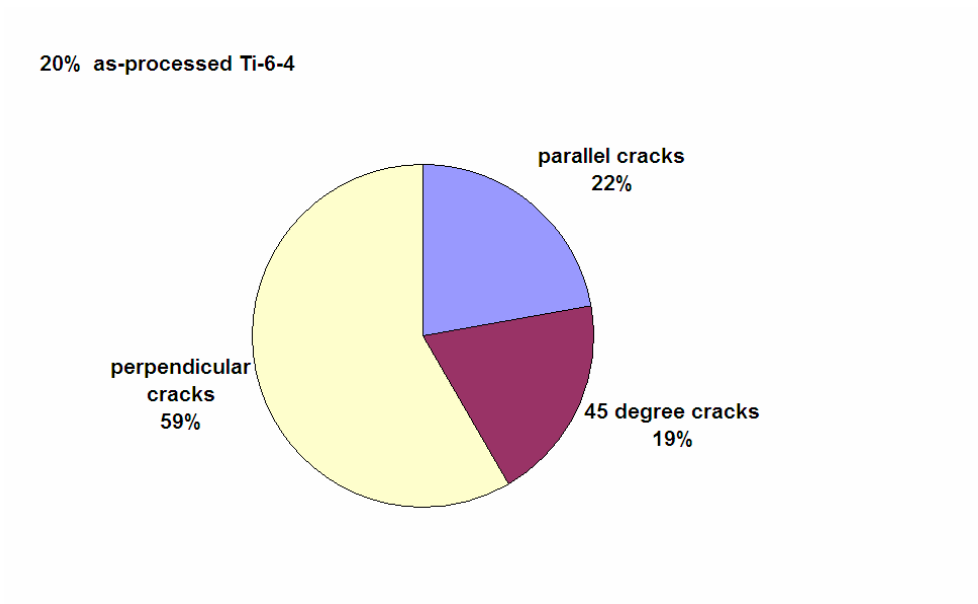

(b)

Figure 5-6 Crack distribution of as-processed 20% Ti6Al4V MIL composite.

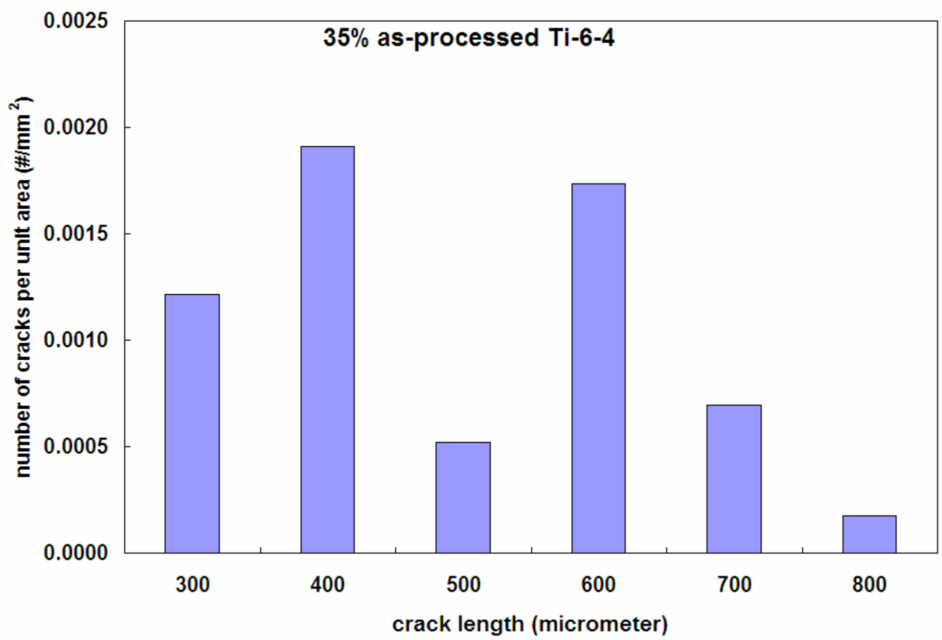

(a)

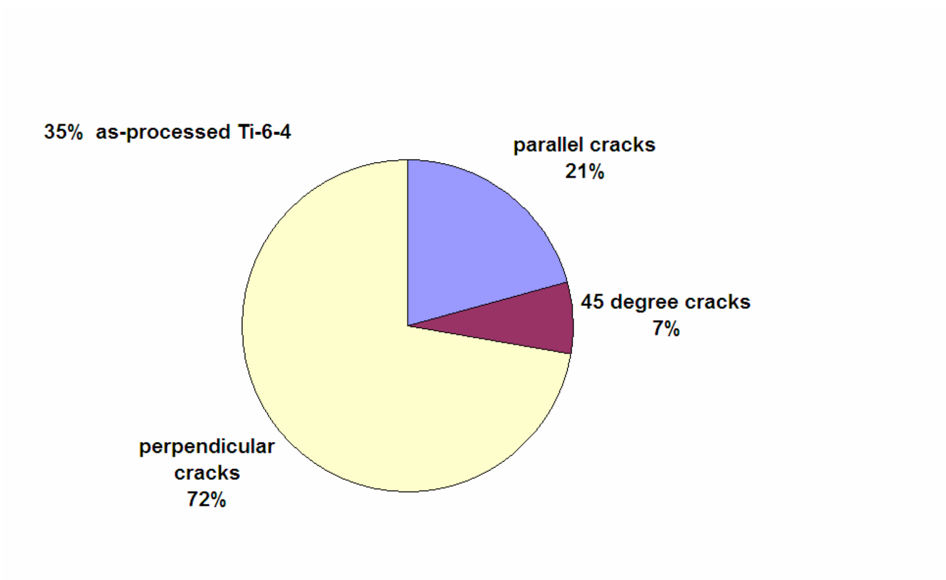

(b)

Figure 5-7 Crack distribution of as-processed 35% Ti6Al4V MIL composite.

Figure 5-8 shows the comparison of crack density and the percentage of different types of crack orientation in 14%, 20% and 35% as-processed composites. With increasing volume fraction of Ti6Al4V, the crack density decreases from 0.321 mm/mm^2 to 0.255 mm/mm^2 to 0.137 mm/mm^2(Figure 5-8 (a)). Because of the thermal mismatch between Ti6Al4V and Al_3Ti, the residual stress accumulates during the cooling process and renders the Al_3Ti layers under tension and Ti6Al4V layers under compression. A smaller volume fraction of Ti6Al4V produces larger residual stress in the brittle Al_3Ti layers, and thus forms more cracks and results in a larger crack density. Figure 5-8 (b) shows the crack distributions. It is seen that while the concentration of parallel cracks tends to be consistent across volume fractions of Ti6Al4V, the concentration of perpendicular cracks increases from 49% (14% Ti6Al4V) to 72% (35% Ti6Al4V), and the concentration of inclined cracks decreases from 31% (14% Ti6Al4V) to 7% (35% Ti6Al4V). This means that although the number of overall cracks decreases with increasing volume fraction of Ti6Al4V, the number of perpendicular cracks decreases relatively less than the number of inclined cracks, and the percentage of perpendicular cracks increases at the expense of the inclined cracks.

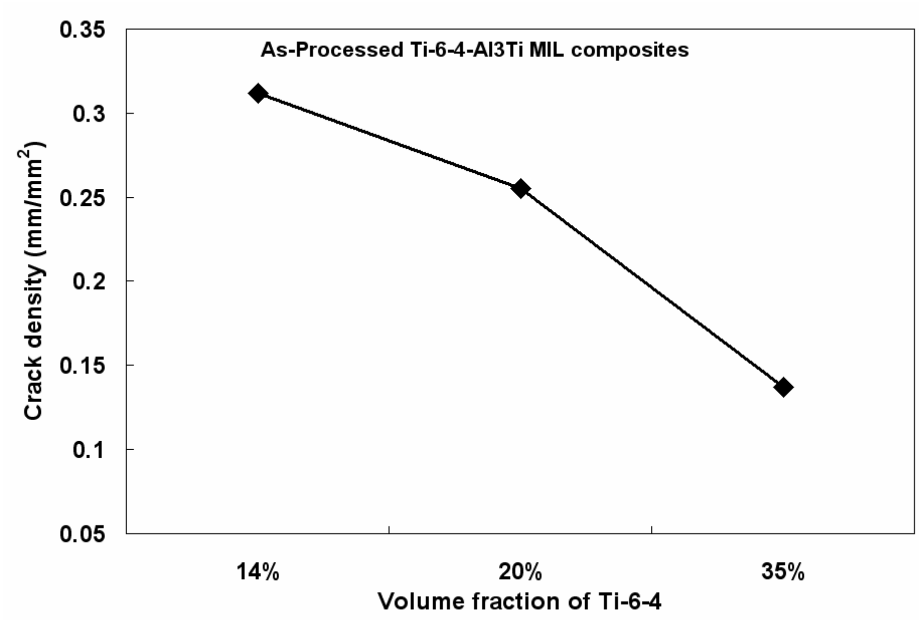

(a)

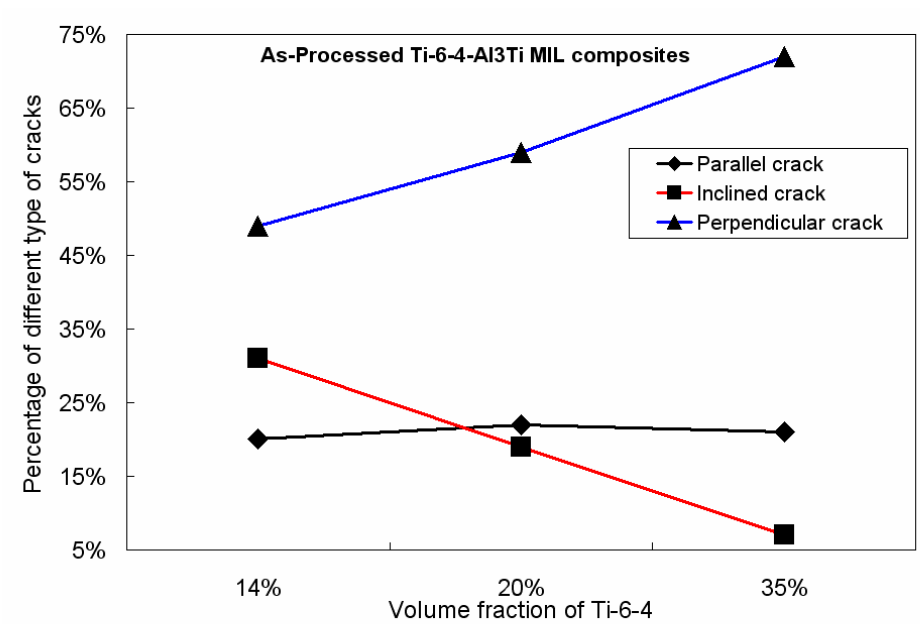

(b)

Figure 5-8 Crack densities and percentage of different types of crack orientations in 14%, 20% and 35% MIL composites.

5.2 Compression tests on pure Al_3Ti

Quasi-static and dynamic compression tests were performed on pure Al_3Ti, which was fabricated in the same manner as the Ti6Al4V-Al_3Ti MIL composites. The thickness of the Ti6Al4V and Al foils were in such a way that Ti6Al4V and Al are all consumed to form Al_3Ti and the final product consists only of Al_3Ti intermetallic compound.

The maximum compressive stresses of pure Al_3Ti were obtained for different strain rate (1000/s, 0.01/s, 0.0001/s). They are listed in Table 6 and compared with the compressive stress of Ti6Al4V-Al_3Ti MIL composites (35% Ti6Al4V) under the same testing conditions.

Table 6 Comparison of maximum compressive stress of pure Al_3Ti and MIL composites (35% Ti6Al4V) at different strain rate.

	Maximum compressive stress of pure Al_3Ti (MPa)	Maximum compressive stress of Ti6Al4V-Al_3Ti (35% Ti6Al4V, perpendicular loading) (MPa)
Dynamic (1000/s)	1285	1370
Quasi-static (0.01/s)	921	1100
Quasi-static (0.0001/s)	890	1000

SEM has been used to characterize pure Al_3Ti after tests, and the results are shown in Figure 5-9. Both intergranular and transgranular cracks were observed, and the strain rates show little influences on the crack modes except that intergranular crack mode seems more popular. Figure 5-10 shows the different crack modes observed found in pure Al_3Ti.

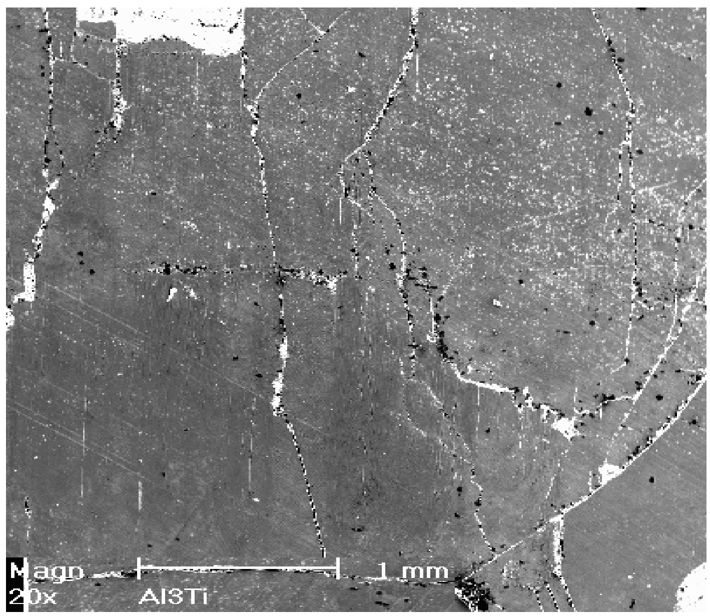

Figure 5-9 SEM, $\dot{\varepsilon}$=0.0001/s, pure Al_3Ti.

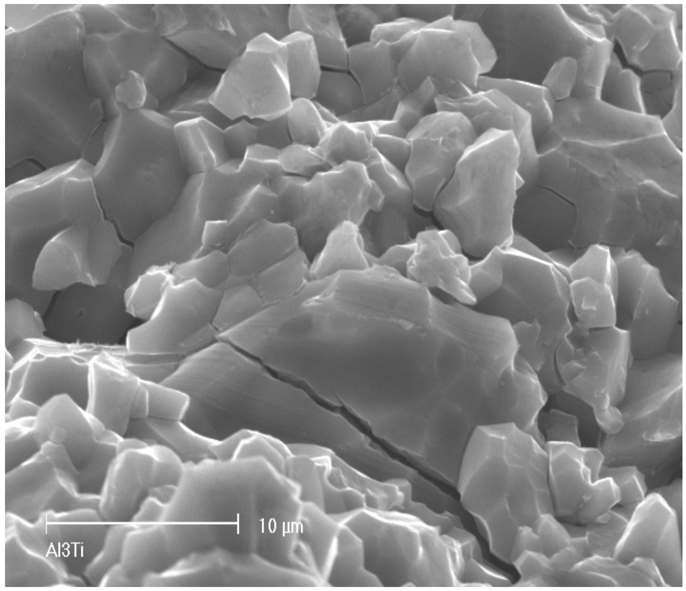

(a)

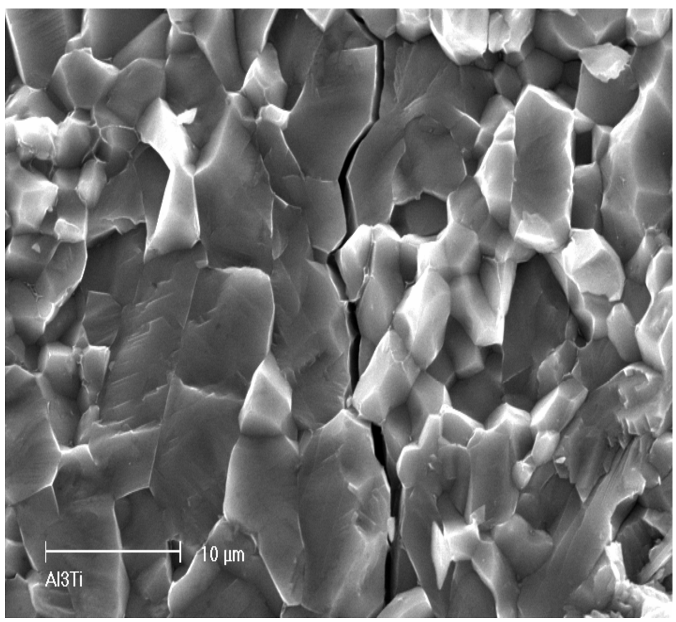

(b)

Figure 5-10 Crack modes in pure Al_3Ti. (a) Transgranular crack; (b) intergranular crack.

5.3 Damage evolution in Ti6Al4V-Al_3Ti MIL composites: observation

A large number of mechanical tests were performed on the Ti6Al4V-Al_3Ti MIL composites. The tested samples were then characterized under SEM and optical microscope to understand how the damage evolves under different conditions, such as strain, strain rate, volume fraction of Ti6Al4V, and the loading direction. A damage parameter, converted from the crack density, is introduced to define the damage in the tested specimens in terms of elastic modulus.

5.3.1 Quasi-static compression tests (0.0001/s): parallel to the interface

Figure 5-11 shows the SEM pictures of 14%, 20% and 35% MIL composites after quasi-static loading in parallel direction. At ~1% strain (Figure 5-11 (a), (c) and (e)), the basic layered structure of Ti6Al4V-Al_3Ti is maintained, while most cracks are parallel cracks in the middle of the Al_3Ti layer. At the failure, (Figure 5-11 (b), (d), (f) and (g)), delamination along the interface, parallel cracks in the middle of the Al_3Ti layers, as well as buckling of Ti6Al4V layers, were observed. The inclined cracks in Al_3Ti are occasionally seen but soon re-align themselves in the loading directions, connecting the cracks along the interfaces and the cracks along the middle of the Al_3Ti or connecting cracks along the interfaces in the opposite side of the Al_3Ti layer (Figure 5-11 (i)).

As Figure 5-11 shows, cracks in Al_3Ti layer develop at ~1% strain and most of the cracks are along the middle of the Al_3Ti layers, where is typical weaker than the rest of composites and usually consists of a combination of voids, impurity and the reaction residue. As the strain increases, these cracks continue to develop and delaminations occur. The inclined cracks are rare, but when they develop, they have the tendency to re-align in the loading direction and connect the other parallel cracks. When the Al_3Ti layers fail, the Ti6Al4V layers take the additional loading and have the tendency to buckle. Because the strength of the composites increases with increasing volume fraction of Ti6Al4V, the composites with higher volume fraction of Ti6Al4V fail at higher strains. However, the major features of failure in parallel loading are similar: delamination along the interfaces, buckling of Ti6Al4V layers, and cracking in the middle of the Al_3Ti layers.

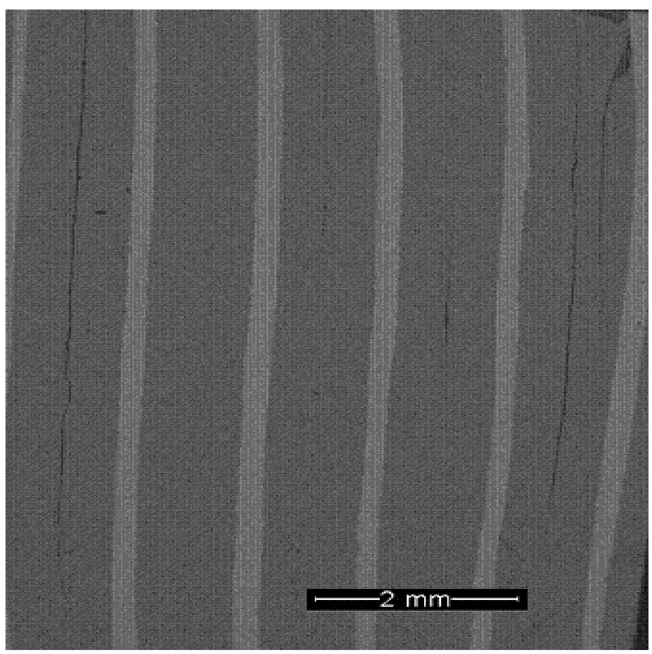

Figure 5-11 SEM of MIL composites after quasi-static compression in parallel loading.

(a) 14% Ti6Al4V, 1% strain.

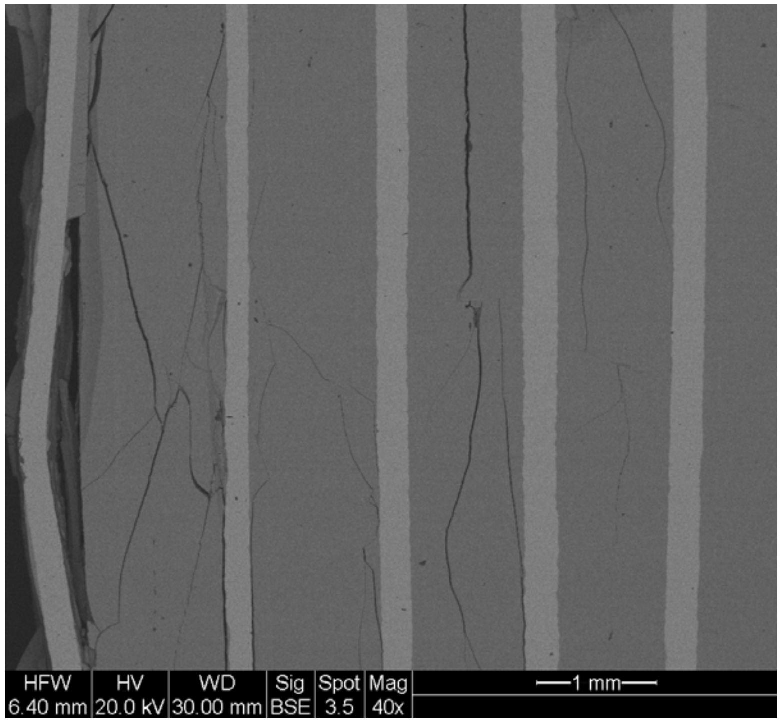

Figure 5-11 continued (b) 14% Ti6Al4V, 1.7% (failure)

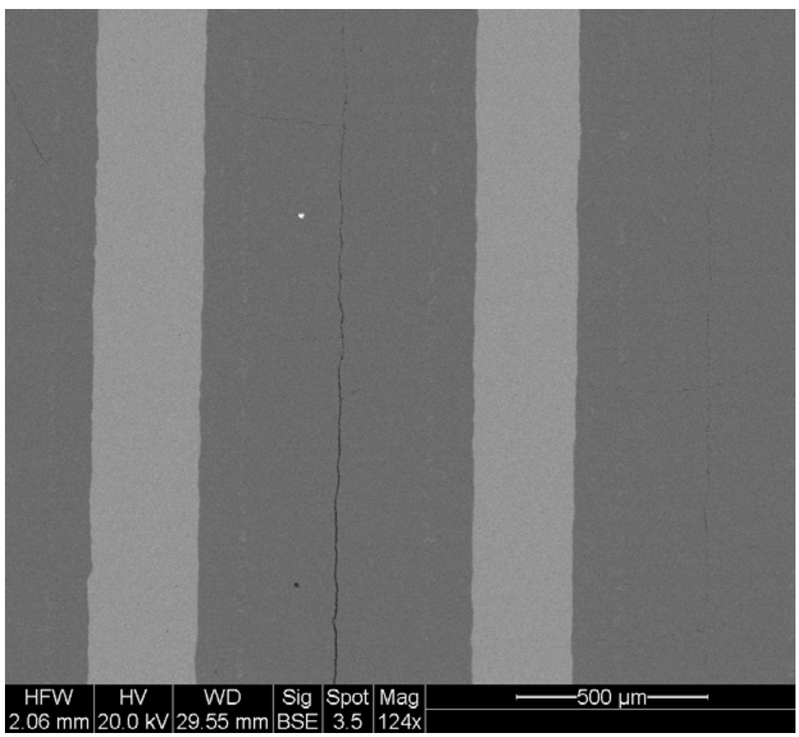

Figure 5-11 continued (c) 20% Ti6Al4V, 1% strain

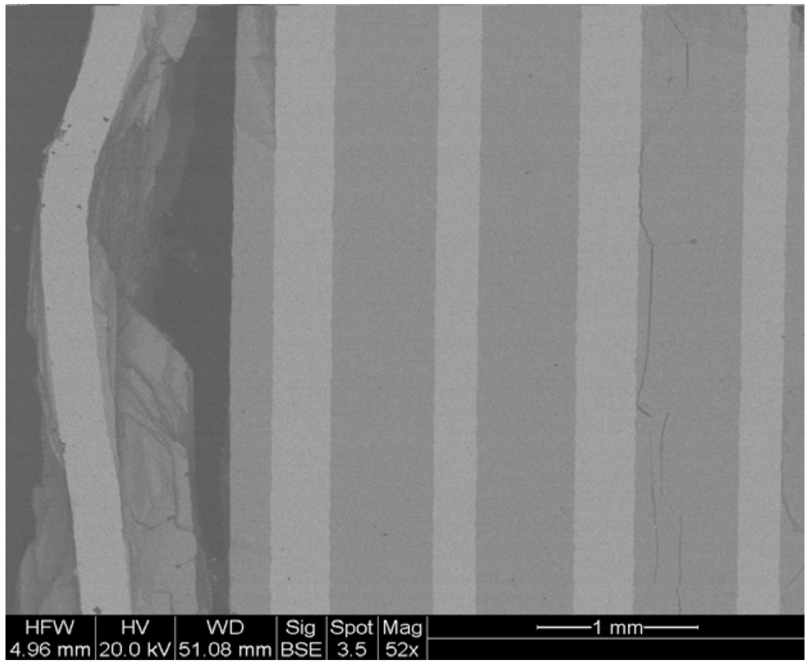

Figure 5-11 continued (d) 20% Ti6Al4V, 2.3% (failure)

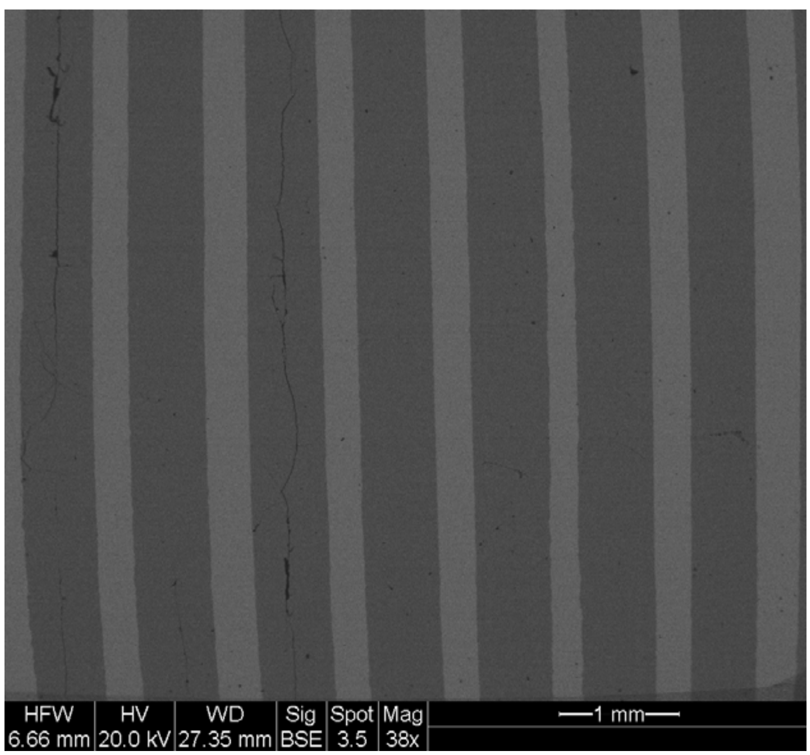

Figure 5-11 continued (e) 35% Ti6Al4V, 1% strain

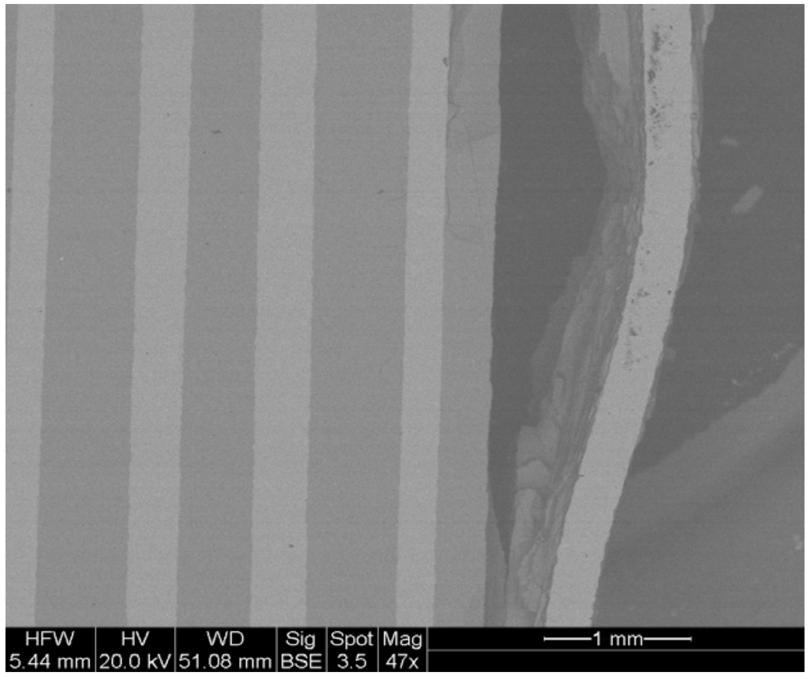

Figure 5-11 continued (f) 35% Ti6Al4V, 2.9% (failure)

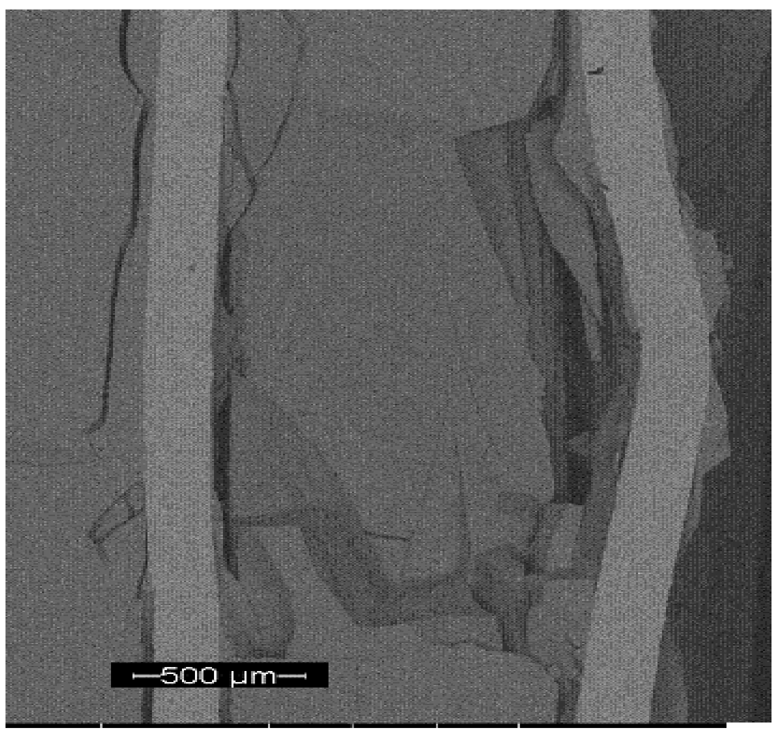

Figure 5-11 continued (g) 14% Ti6Al4V, 1.7% (failure)

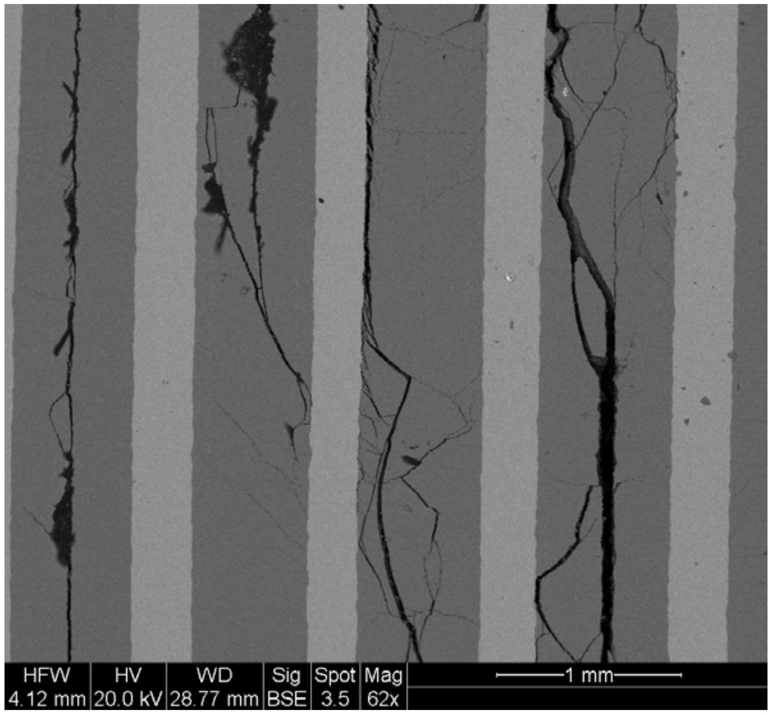

Figure 5-11 continued (h) 20% Ti6Al4V, 2.3% (failure).

The buckling of the Ti6Al4V layers plays a pivotal role in this kind of fracture. The thicker Ti6Al4V layers are more resistant to buckling in accordance with the Euler equation:

$$P_{cr} = \frac{\pi^2 EI}{L^2} \tag{5.3}$$

where E is Young's modulus, I is the moment of inertia, and L is the length of the specimen. The moment of inertia increases with the cube of the thickness of the Ti6Al4V lamella; the thicker the layers, the less tendency for buckling. Buckling of the Ti6Al4V layer is clearly seen in the left hand side of Figure 5-12 (a), which leads to the collapse of the Al_3Ti layer. The right-hand side shows a shear band in the metallic layer, and Figure 5-12 (b) shows a close-up of this feature.

It is possible to convert the crack density into a damage parameter, D, which is defined as a measure of the physical damage in materials. When D=0, one has a material state with no damage; D increases with damage progression until it reaches 1 when the material fails. The advantage of using D is that it is a unitless number, and can be calculated as:

$$D = \frac{A_c}{A} = \frac{m \cdot \pi a^2}{A} = \frac{\pi A \rho_{crack}{}^2}{4m} \tag{5.4}$$

where A_c is the effective damage area assumed to be, in this section, of a region in which the crack is located, A is the total surface area, a is half of the crack length, ρ_{crack} is the crack density defined in Equation (5.1), and m is the total number of cracks.

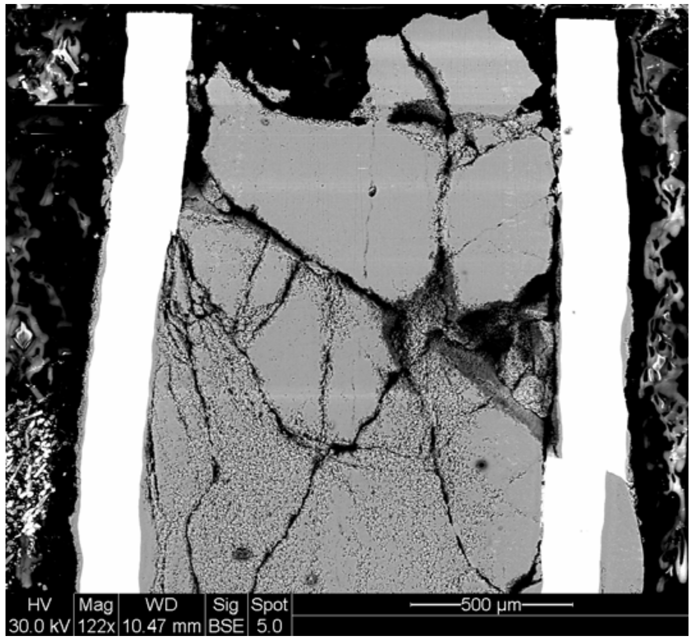

(a)

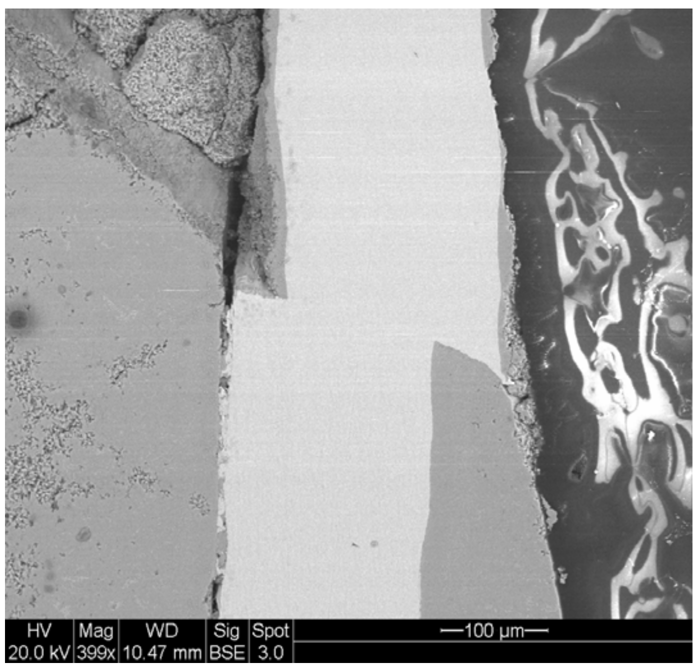

(b)

Figure 5-12 SEM, parallel compression, 14% Ti6Al4V, $\dot{\varepsilon}$ =0.0001/s.

Here we assume that the dimension of the cracks perpendicular to the surface is equal to the thickness of specimen, and that cracks propagate unimpeded through the Al_3Ti. Figure 5-13 shows the damage parameter, D, and crack distribution for 14%, 20% and 35% MIL composites at increasing strains. A power-law relation between D and ε is employed to fit the experimental data:

$$D = D_0 + k\varepsilon^n \tag{5.5}$$

where D_0 , n and k are material parameters. As the strain increases, D increases; at a constant strain, damage increases with decreasing concentration of Ti6Al4V. The damage parameter increases to unity at failure (Figure 5-13 (a)). As the strain increases, the concentration of the parallel cracks overtakes that of the perpendicular and inclined cracks as the major crack morphology. The concentration of parallel cracks increases sharply from zero to 1% strain and then more gradually until failure (Figure 5-13 (b)).

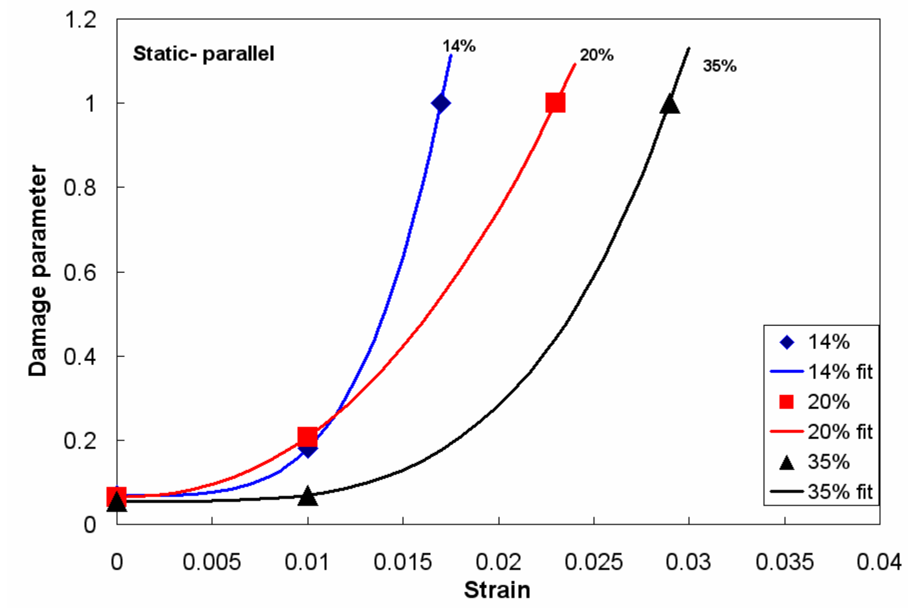

(a)

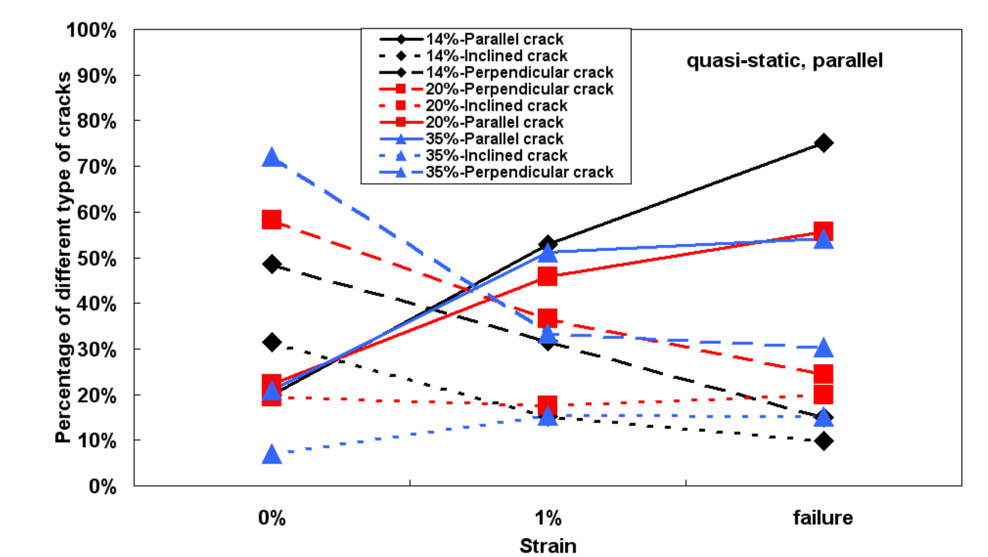

(b)

Figure 5-13 Crack densities and crack distributions for MIL composites after quasi-static compression in parallel loading: (a) damage parameter; (b) crack distribution.

5.3.2 Dynamic compression tests: parallel to the interface

Because of the difficulty of controlling the strains under dynamic loading, only specimens at ~1% strain and failure were obtained.

Figure 5-14 shows the SEM pictures of 14%, 20% and 35% MIL composites after dynamic loading in parallel direction with 800~2000/s strain rates. At ~1% strain (Figure 5-14 (a), (c) and (e)), although the basic layered structure of Ti6Al4V-Al_3Ti is retained, larger damage is observed than in Figure 5-14. Cracks are formed along the middle of the Al_3Ti layer, parallel and perpendicular to the interfaces. At failure (Figure 5-14 (b), (d) and (f)), the cracks developed at ~1% strain continue to grow, leading to the buckling of Ti6Al4V layers, and delamination along the interfaces and along the middle of the Al_3Ti layers. An interesting feature observed in specimens under dynamic loading in parallel direction is that many Al_3Ti are blown away upon impact, even at ~1% strain; at failure, only part of the Al_3Ti layers are retained, with the left Ti6Al4V layers, seen in the secondary electron micrograph (Figure 5-14 (h) and (i)). It is also observed in some specimens that only half of Al_3Ti is left in the through the thickness (Figure 5-14 (b) and (h)).

From Figure 5-14, the cracks along the middle of the Al_3Ti layers are most common at ~1% strain. Because the impact process was completed in such a short period of time, the severely deformed Al_3Ti would not be accommodated in the existing structure, and many were blown away (Figure 5-14 (g)). This significantly weakens the intermetallic phase, and leaves Ti6Al4V layers to take additional loadings instantly. Finally, failure occurs, in the form of delamination along the interface and buckling of Ti6Al4V layers. Comparing with quasi-static tests, the composites after dynamic tests are much more fragmented, and many Al_3Ti are blown away upon impact. This leads to the simultaneous delamination of several interfaces, usually breaking the specimens into fragmented pieces. As this happens, each of those parts suddenly experiences a sharp increase in stress concentration, leading to severely damaged specimens.

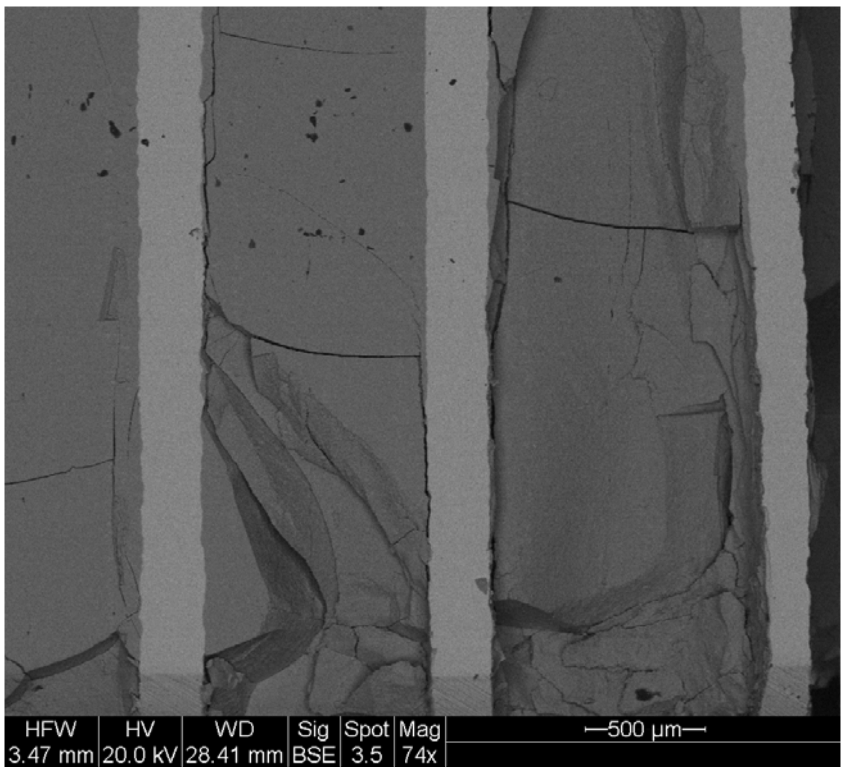

Figure 5-14 SEM of MIL composites after dynamic compression in parallel loading.

(a) 14% Ti6Al4V, ~1% strain

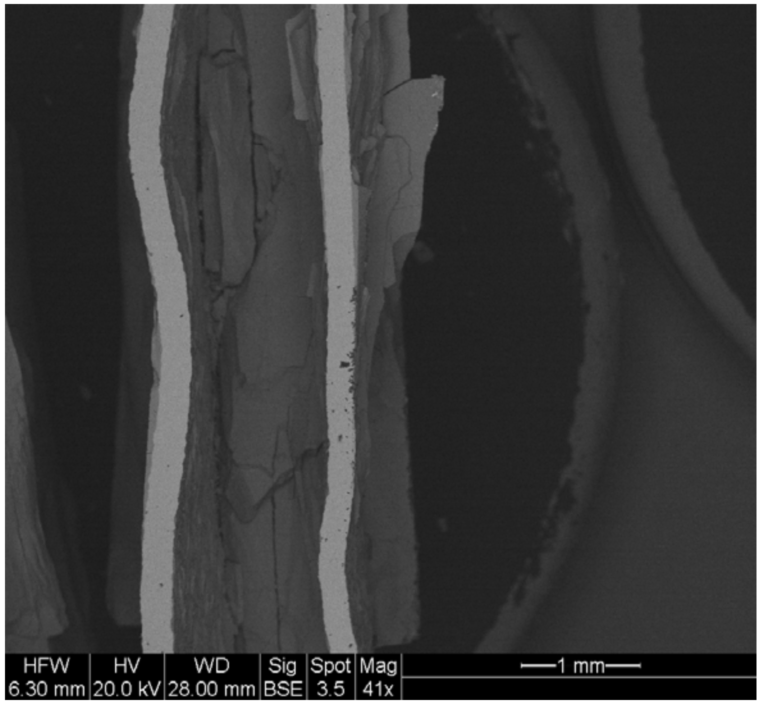

Figure 5-14 continued (b) 14% Ti6Al4V, ~1.9% (failure)

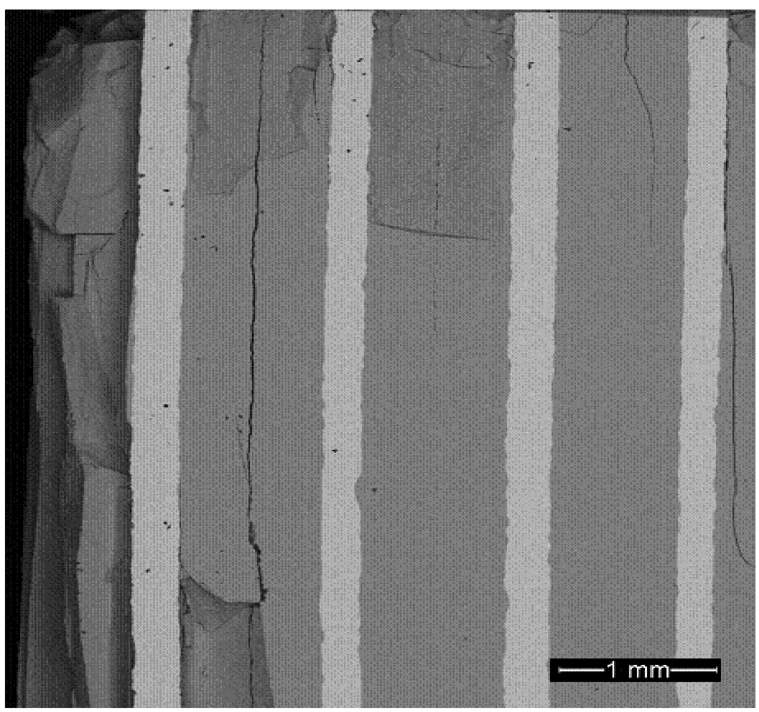

Figure 5-14 continued (c) 20% Ti6Al4V, ~1% strain

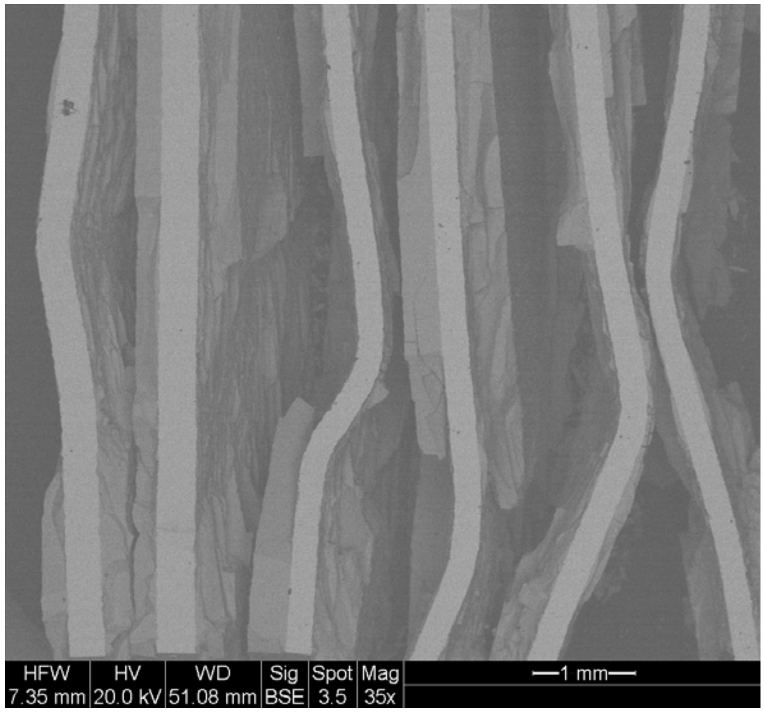

Figure 5-14 continued (d) 20% Ti6Al4V, ~2.5% (failure)

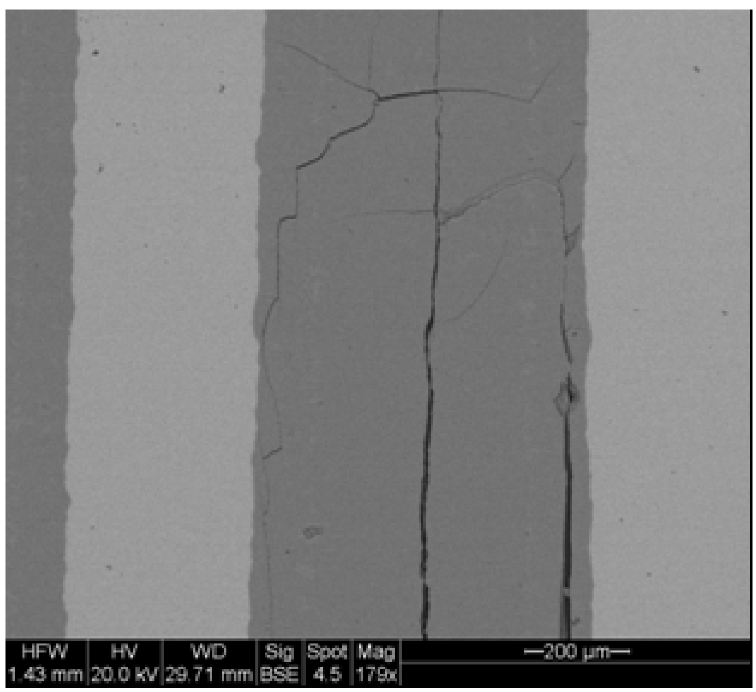

Figure 5-14 continued (e) 35% Ti6Al4V, ~1% strain

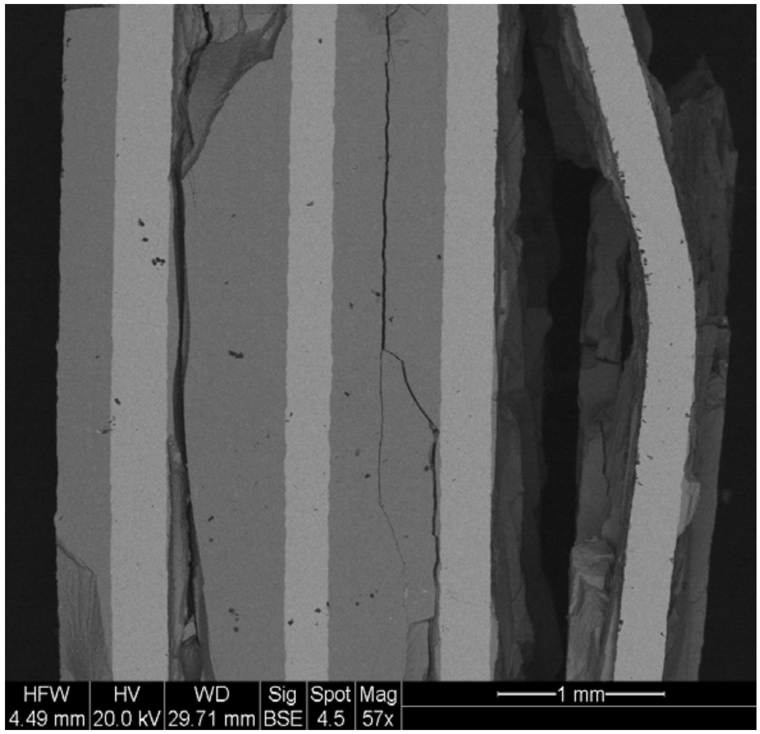

Figure 5-14 continued (f) 35% Ti6Al4V, ~3.3% (failure)

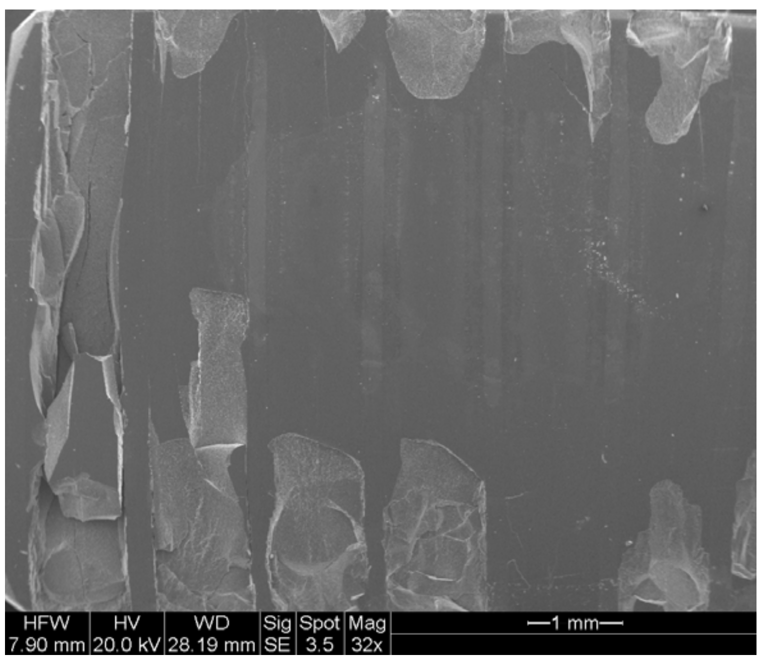

Figure 5-14 (g) 14% Ti6Al4V, ~1%

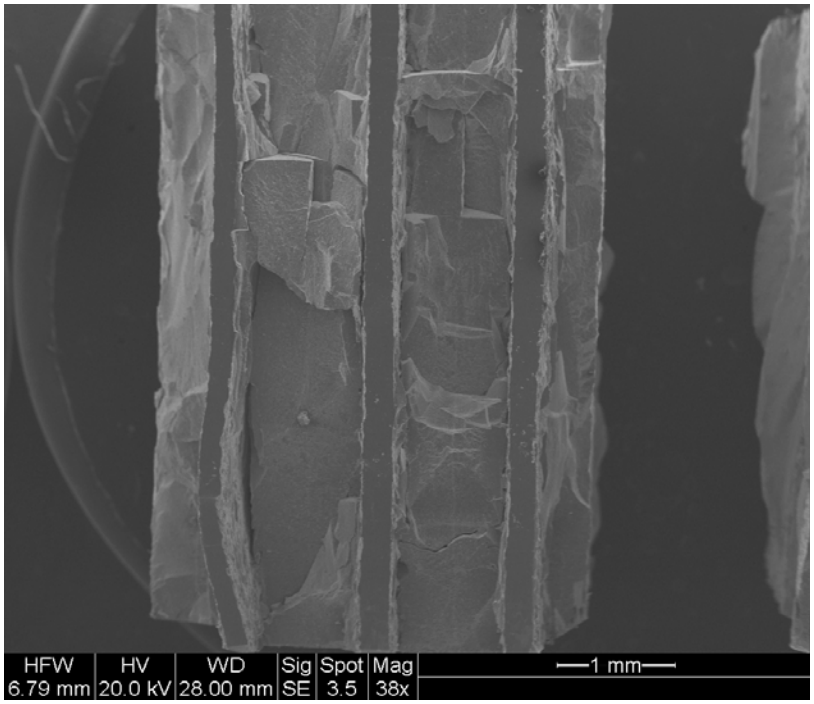

Figure 5-14 continued (h) 14% Ti6Al4V, ~1.9% (failure).

Figure 5-15 shows the damage parameter and crack distribution for 14%, 20% and 35% MIL composites at different strains after dynamic loading in parallel direction. It is seen that, as the strain increases, the damage parameter across volume fractions of Ti6Al4V increases. In comparison with those after quasi-static loading in parallel direction, the damage parameters at ~1% strain are higher, due to the severe damage upon impact. The concentration of the parallel cracks dominates among the different types of cracks, and is also larger than those after quasi-static parallel deformation.

Figure 5-16 compares the crack density at ~1% strain and failure after dynamic and quasi-static loading in parallel direction.

At ~1% strain, the crack densities in dynamic loading are higher than those in quasi-static loading. Because of the higher strength the added Ti6Al4V provides, the crack density decreases as the volume fraction of Ti6Al4V increases. At the failure, however, contrary to our expectation (that the crack densities in the dynamic conditions are higher than those in the quasi-static conditions), the data shows that the crack densities after dynamic parallel loading are lower than those after quasi-static parallel loading. One possible reason is that the specimens after dynamic loading up to failure are very fragmented, and most of time only parts of the specimens could be obtained. The data from those parts thus underestimated the crack density after dynamic parallel loading. The dotted line is the estimate of the real crack density after dynamic loading, which shows a decrease in crack density with increasing concentration of Ti6Al4V and the crack density after dynamic testing higher than that after quasi-static parallel loading.

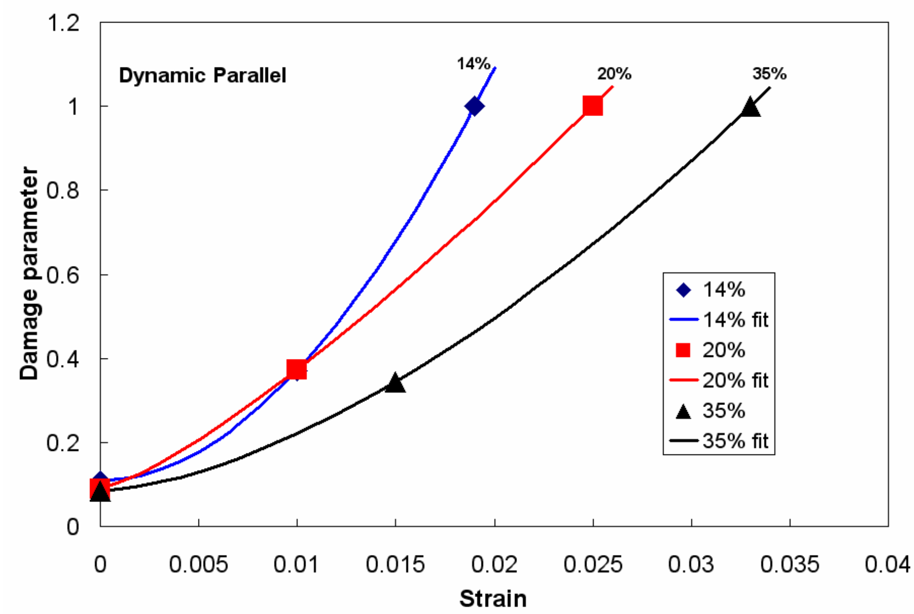

(a)

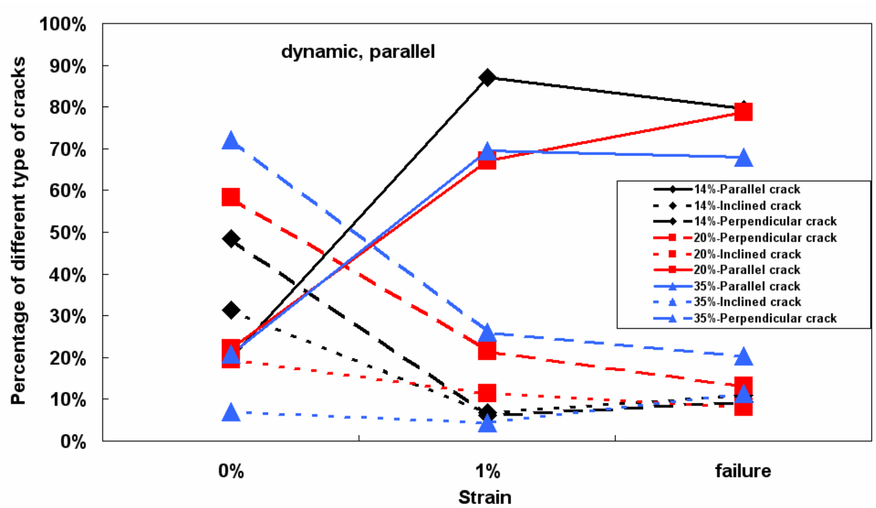

(b)

Figure 5-15 Crack densities and crack distributions for MIL composites after dynamic compression in parallel loading: (a) damage parameter; (b) crack distribution.

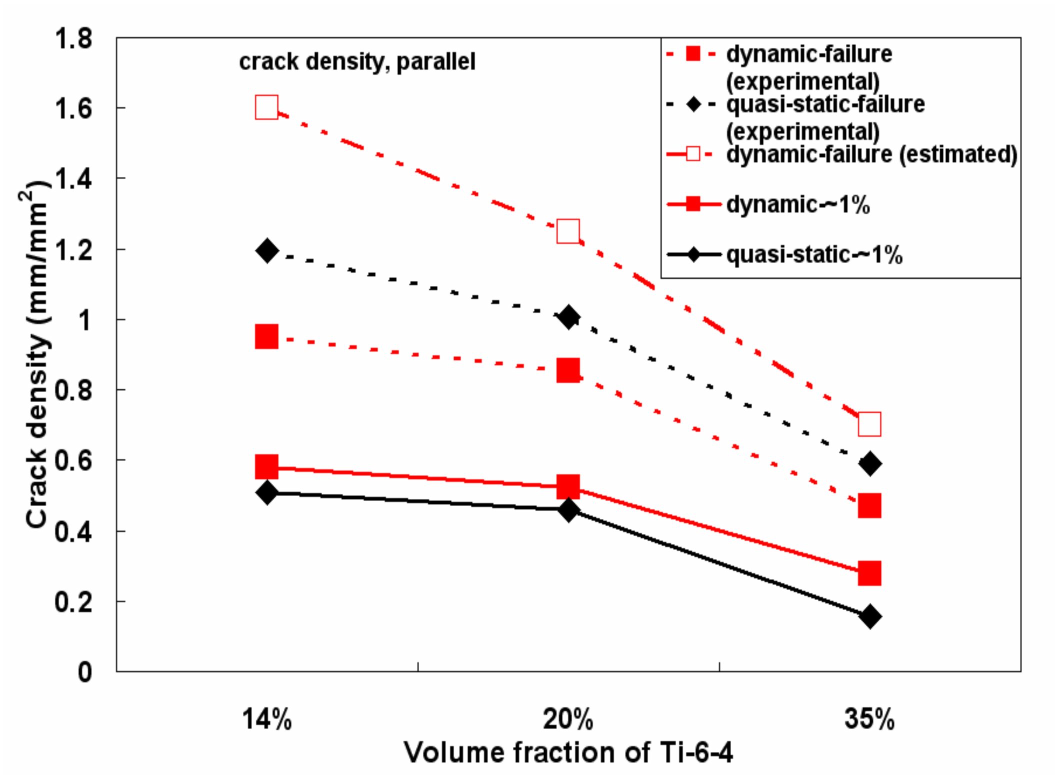

Figure 5-16 Crack density comparison at ~1% and failure strain after the dynamic and quasi-static loading in parallel direction.

5.3.3 Quasi-static compression tests: perpendicular to the interface

Figure 5-17 shows the SEM pictures of 14%, 20% and 35% MIL composites after quasi-static loading in perpendicular direction. At ~1% strain (Figure 5-17 (a), (c) and (e)), the basic layered structure of Ti6Al4V-Al_3Ti is maintained, while cracks are in the form of perpendicular, parallel and inclined directions to the interfaces. At failure (Figure 5-17 (b), (d) and (f)), Ti6Al4V layers fail by the shear cracks, 45^o to the interfaces. Also seen at failure are some parallel cracks along the middle of Al_3Ti layers and delamination along the interfaces. At the intermediate strains, shear band development is observed (Figure 5-17 (g): ~2% strain, and (h): ~2.5% strain). In Figure 5-17 (g), the shear bands are in their early stages, when the inclined cracks reach the interfaces and plastically deform the Al_3Ti layers by squeezing further into Ti6Al4V layers. Figure 5-17 (h) shows the later stage of the shear band development, as the shear bands from the opposite side of the Al_3Ti layers start to reach for each other, forming shear cracks in Ti6Al4V layers. The cracks that reach the interface but do not develop shear bands in Ti6Al4V deviate along the interface and delaminate the Ti6Al4V-Al_3Ti interface.

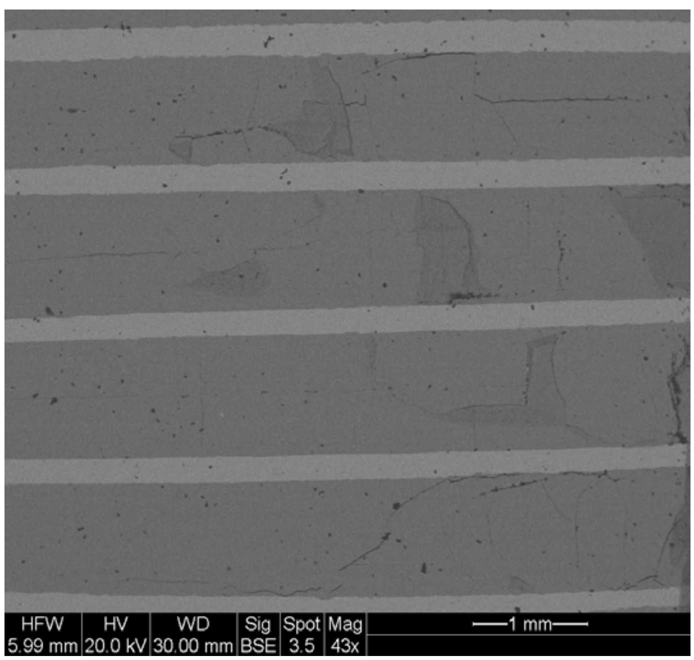

Figure 5-17 SEM of MIL composites after quasi-static compression in perpendicular loading.

(a) 14% Ti6Al4V, ~1% strain

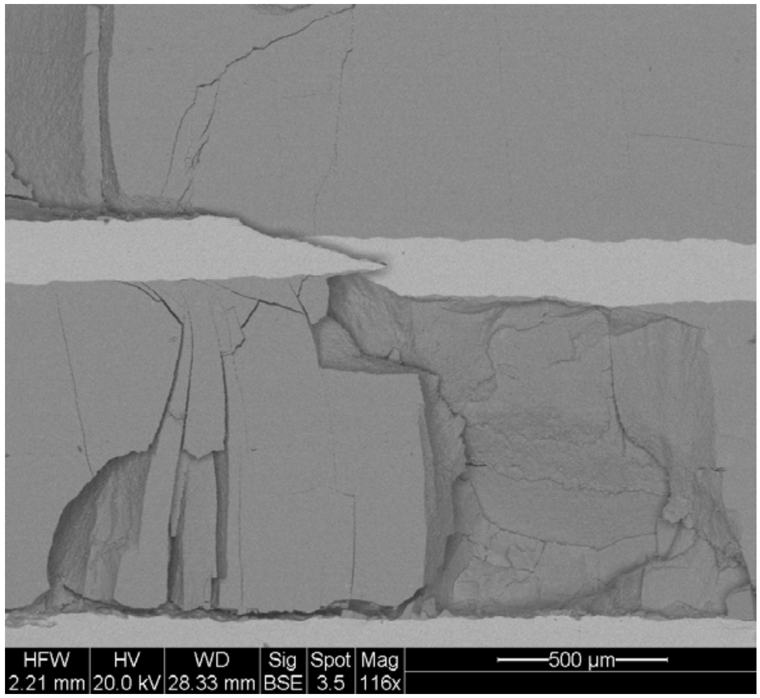

Figure 5-17 continued (b) 14% Ti6Al4V, ~2% (failure)

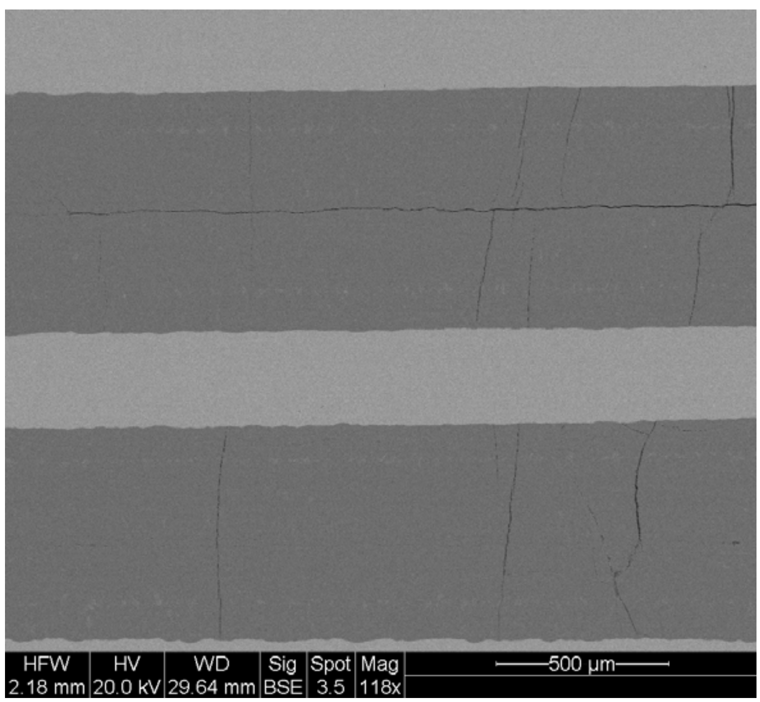

Figure 5-17 continued (c) 20% Ti6Al4V, ~1% strain

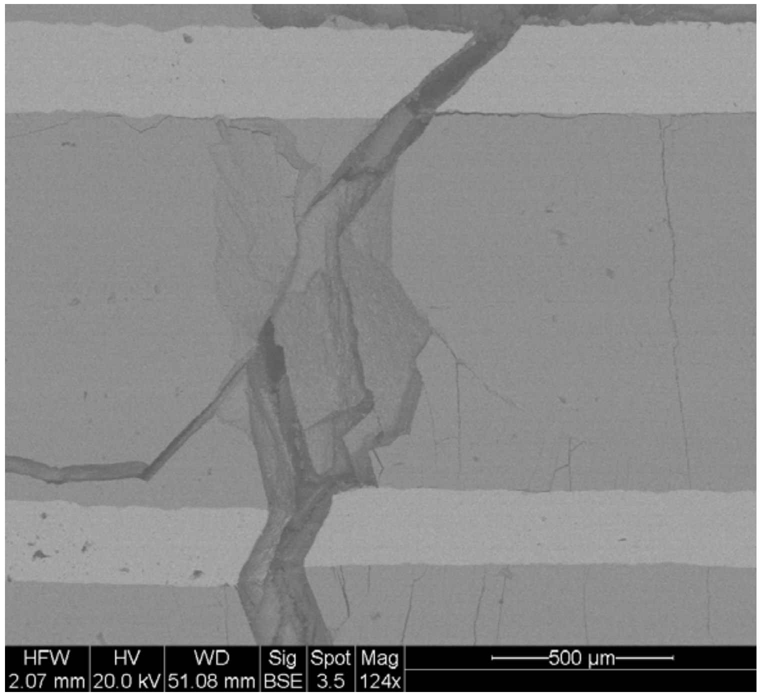

Figure 5-17 continued (d) 20% Ti6Al4V, ~2.8% (failure)

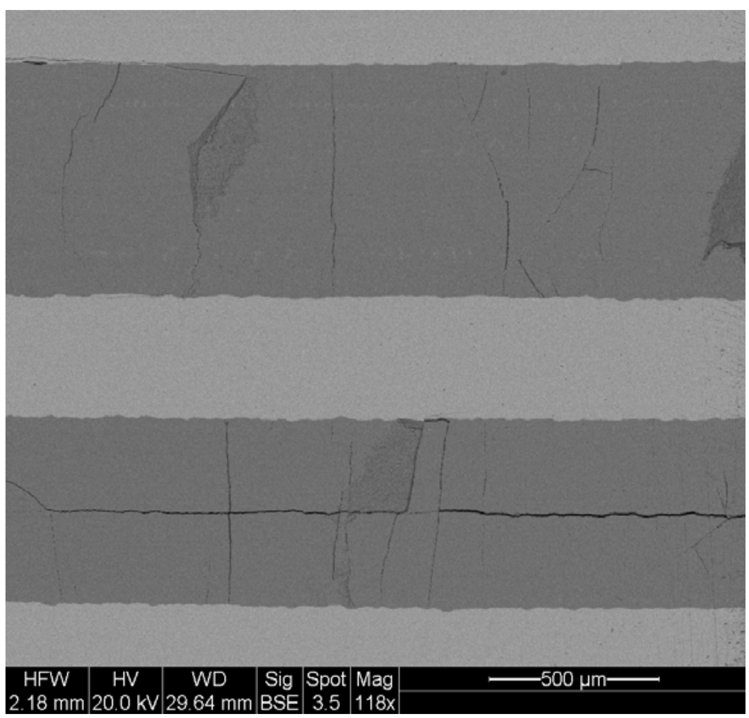

Figure 5-17 continued (e) 35% Ti6Al4V, ~1% strain

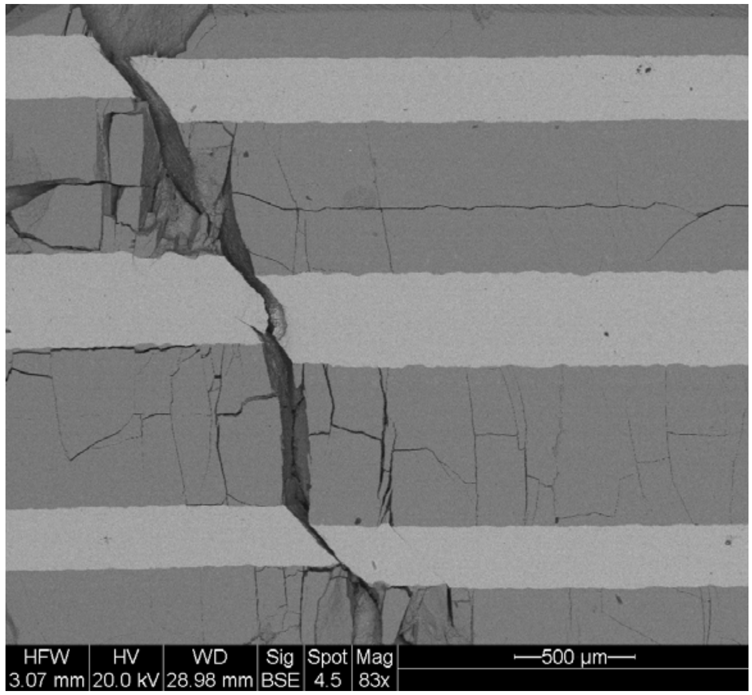

Figure 5-17 continued (f) 35% Ti6Al4V, ~3.4% (failure)

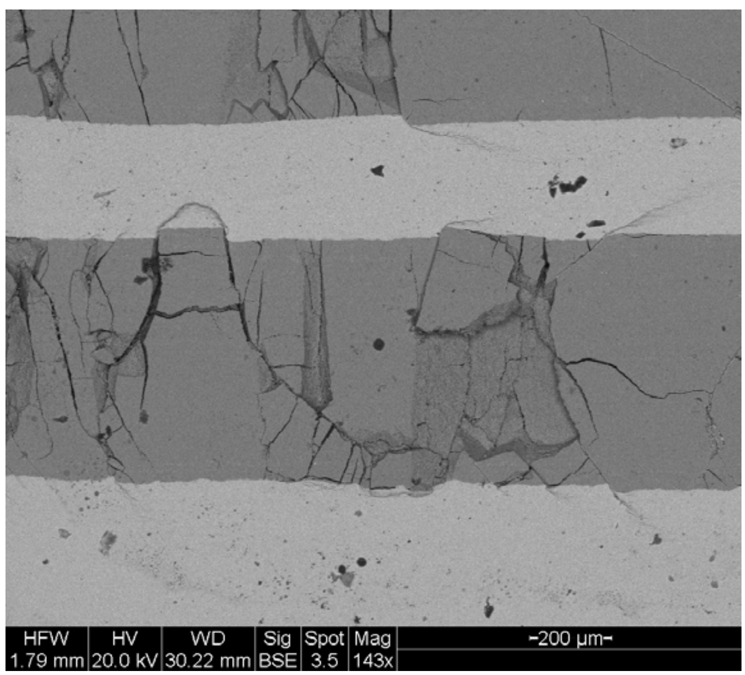

Figure 5-17 continued (g) 35% Ti6Al4V, ~2%

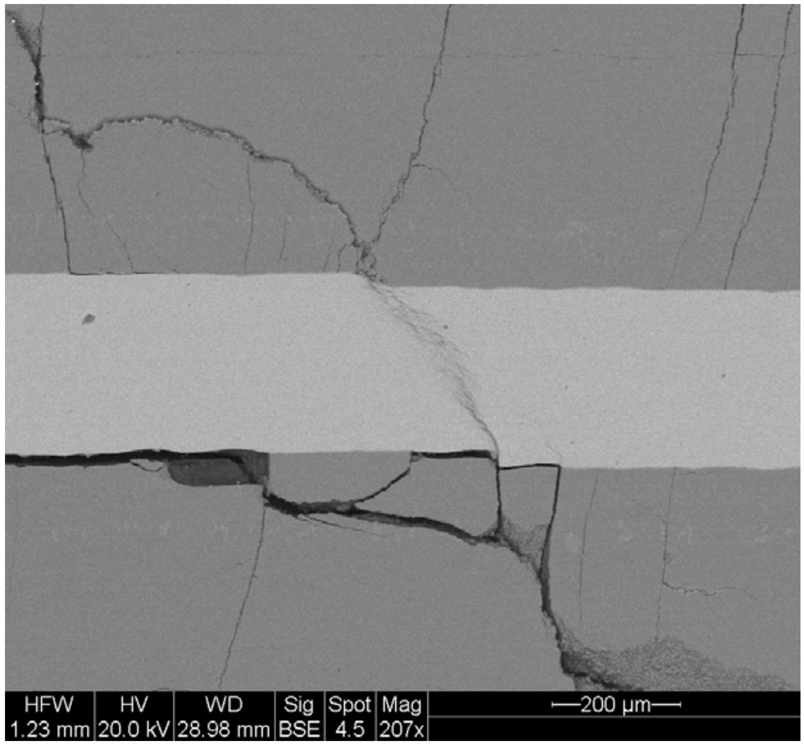

Figure 5-17 continued (h) 20% Ti6Al4V, ~2.5%.

Figure 5-18 shows the damage parameter and crack distribution for 14%, 20% and 35% MIL composites of different strains after quasi-static loading in perpendicular direction. It is found that the damage parameter increases with increasing strains, and the increase accelerates approaching failure (Figure 5-18 (a)). The percentages of different types of cracks are stable with increasing strains, and the concentration of inclined cracks is slightly higher at failure (Figure 5-18 (b)).

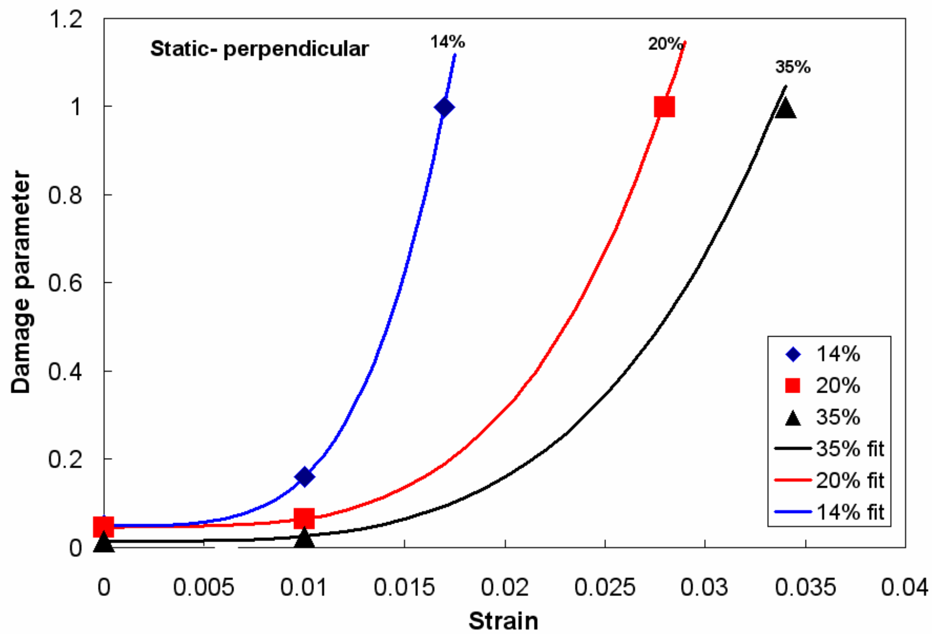

(a)

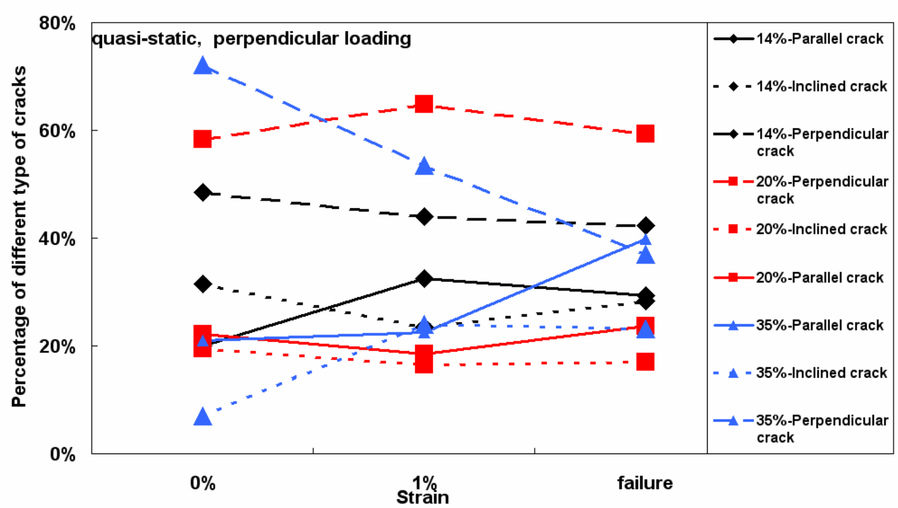

(b)

Figure 5-18 Crack density and crack distribution for MIL composites with different strains after quasi-static compression in perpendicular loading: (a) damage parameter; (b) crack distribution.

5.3.4 Dynamic compression tests: perpendicular to the interface

Figure 5-19 shows the SEM pictures of 14%, 20% and 35% MIL composites after dynamic loading in perpendicular direction with 800~2000/s strain rates. At ~1% strain (Figure 5-19 (a), (c) and (e)), similar to quasi-static tests, most cracks are aligned with the loading direction or along the middle of the Al_3Ti layers. At failure (Figure 5-19 (b), (d) and (f)), the Ti6Al4V layers are failed by the shear cracks, parallel cracks along the middle of the Al_3Ti layers and the delaminations along the interfaces. Comparing with quasi-static deformation, the Al_3Ti layers are much more fragmented and the Ti6Al4V layers are largely segmented. Many parts of Al_3Ti (Figure 5-19 (h)) and even parts of the composites (Figure 5-19 (b)) were blown away upon impact, which makes the stresses concentrate faster in Ti6Al4V layers where the Al_3Ti are absent, and thus accelerates the process from the generation of shear bands to the failure of Ti6Al4V by shear cracks. This is why very few shear bands are observed in dynamic tests. Once one layer of Ti6Al4V fails, the rest Ti6Al4V layers taking even more loadings fail consecutively.

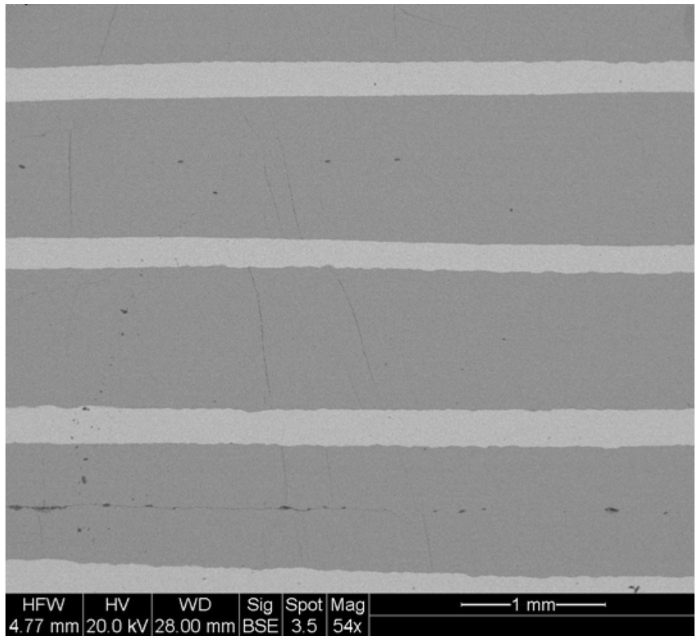

Figure 5-19 SEM of MIL composites after dynamic compression in perpendicular loading.

(a) 14% Ti6Al4V, ~1% strain

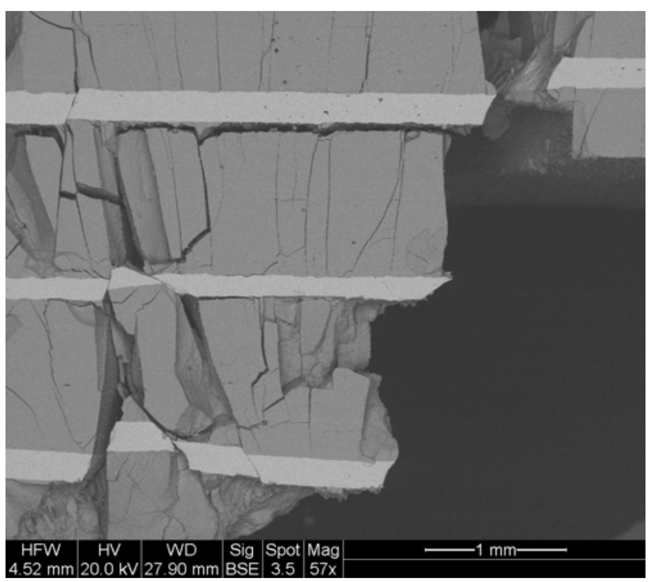

Figure 5-19 continued (b) 14% Ti6Al4V, ~2.2% (failure)

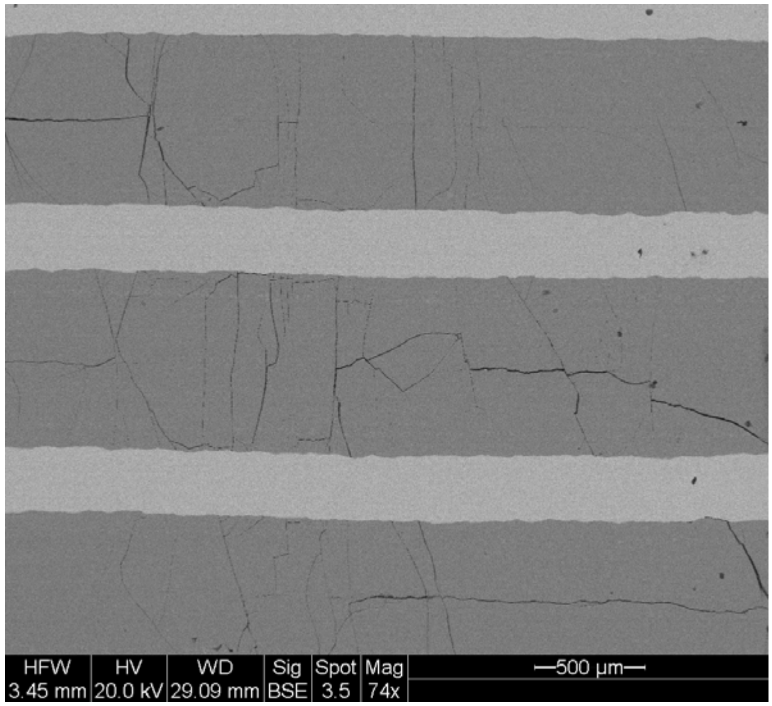

Figure 5-19 continued (c) 20% Ti6Al4V, ~1% strain

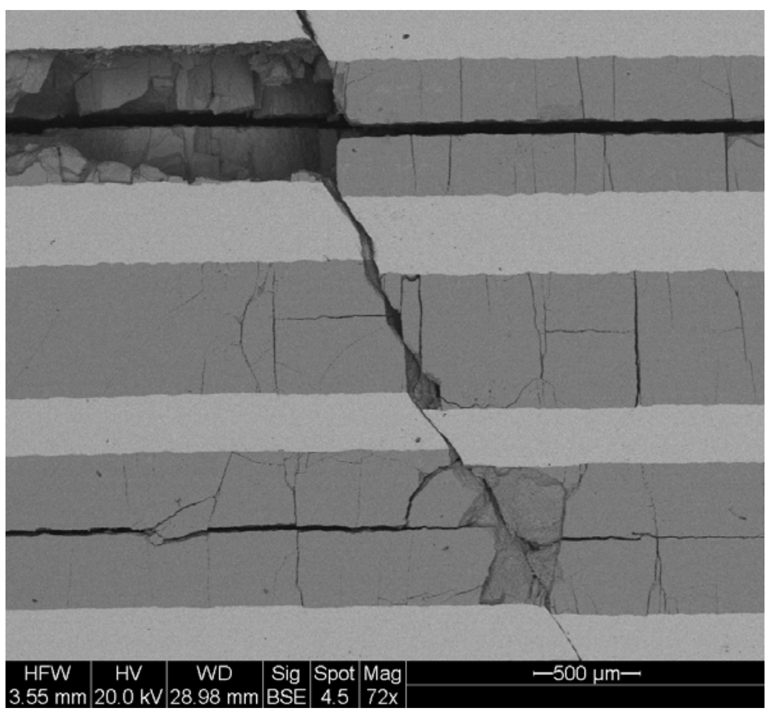

Figure 5-19 continued (d) 20% Ti6Al4V, ~3.1% (failure)

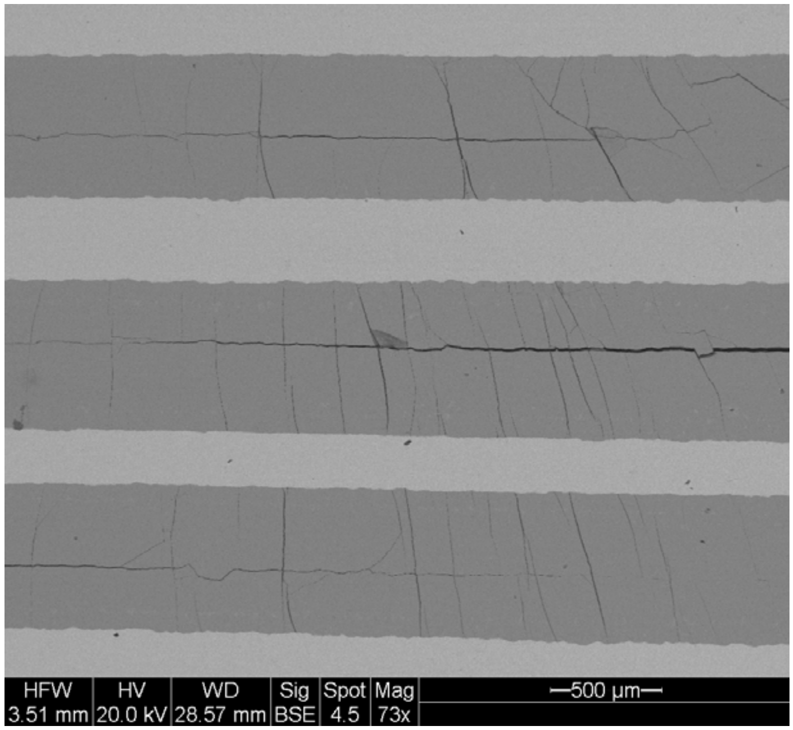

Figure 5-19 continued (e) 35% Ti6Al4V, ~1.4% strain

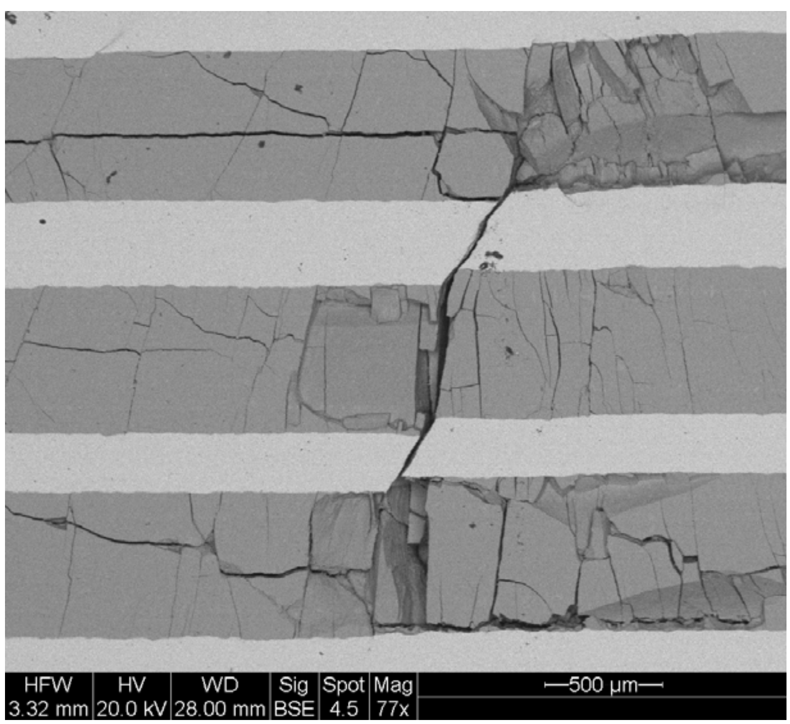

Figure 5-19 continued (f) 35% Ti6Al4V, ~3.5% (failure)

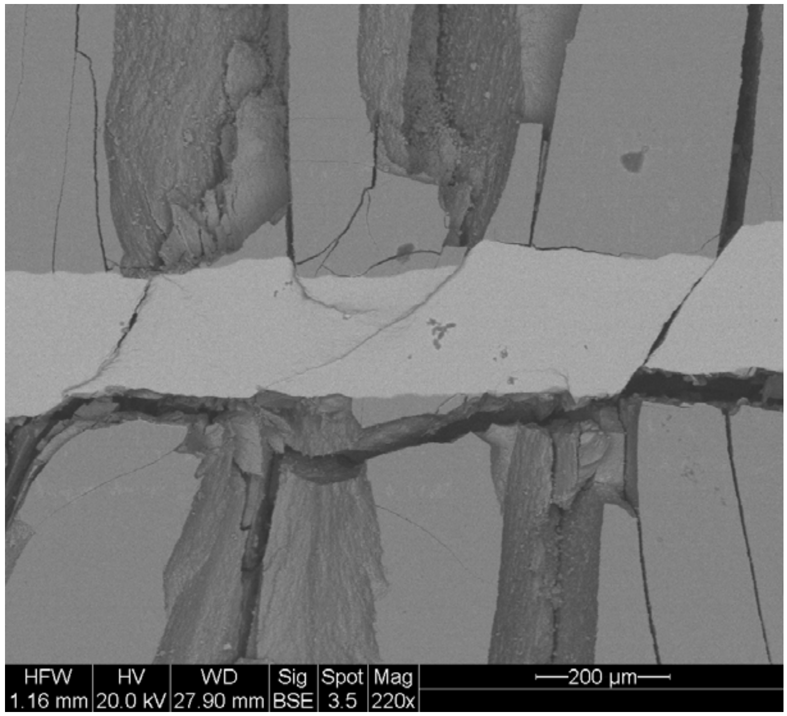

Figure 5-19 continued (g) 14% Ti6Al4V, ~2.2%

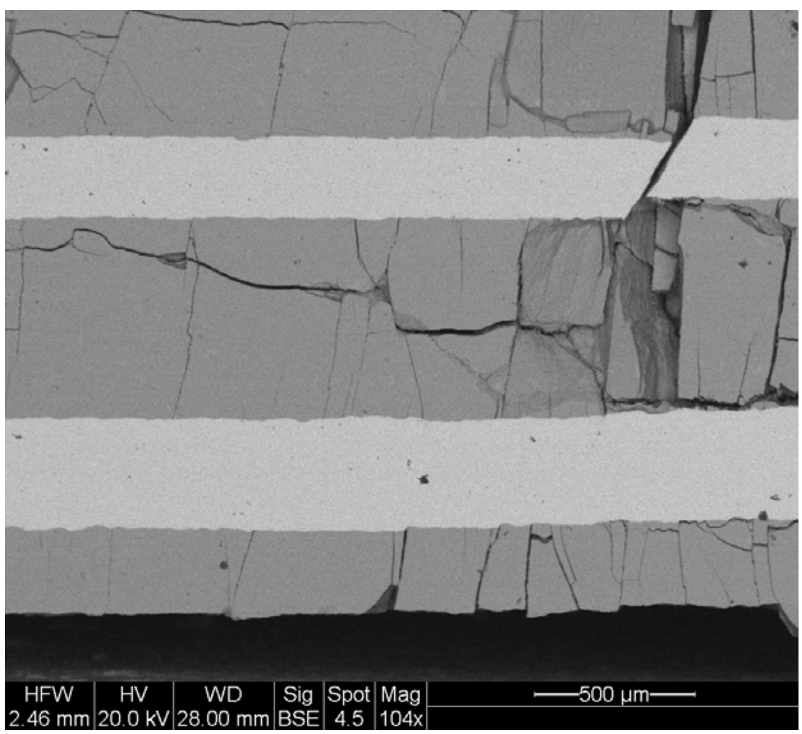

Figure 5-19 continued (h) 35% Ti6Al4V, ~3.5% (failure)

Figure 5-20 shows the damage parameter and crack distribution after dynamic deformation. It is seen that as the strains increase, the damage parameter in different volume fractions of Ti6Al4V increases, and the increase accelerates approaching failure. The trend for 35% MIL composites is unusual because only specimens with ~1.5% strains were obtained and thus overestimated the damage parameter. In percentage terms (Figure 5-20 (b)), it shows that generally the concentrations of the perpendicular cracks decrease, and the concentrations of the parallel cracks increase, while the concentrations of the inclined cracks are stable. This means the parallel cracks along the middle of the Al_3Ti layers and delaminations along the interfaces are more popular in dynamic perpendicular deformation than in quasi-static perpendicular deformation.

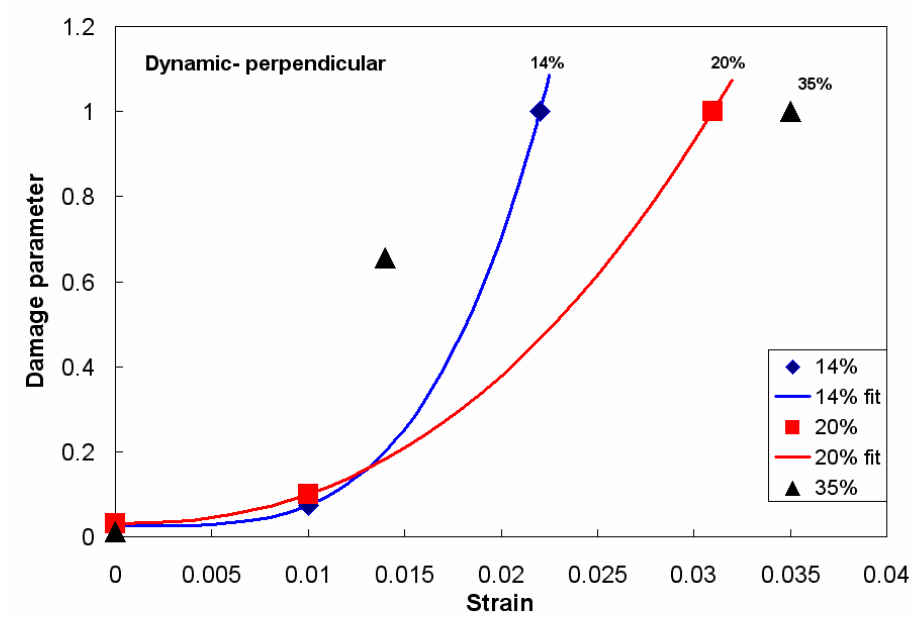

(a)

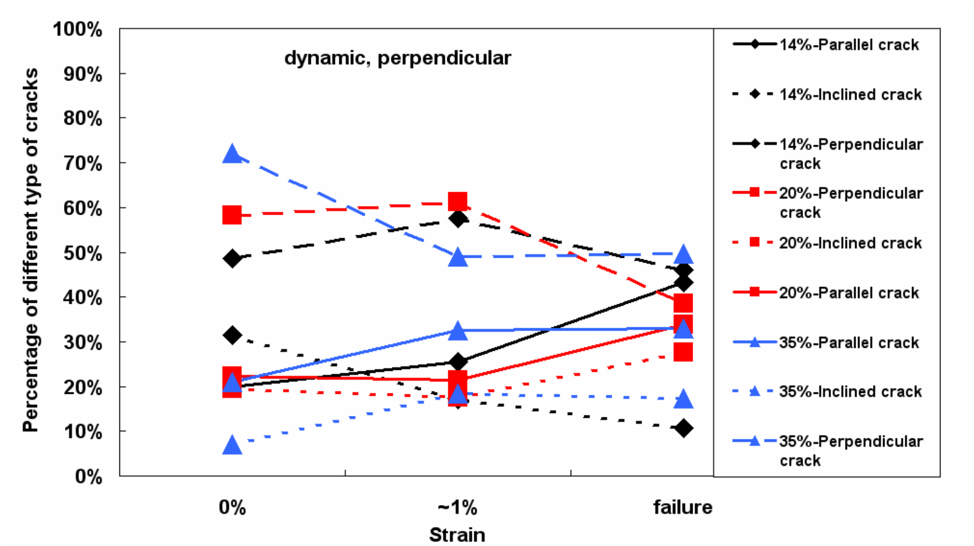

(b)

Figure 5-20 Crack density and crack distribution for MIL composites after dynamic compression in perpendicular loading: (a) damage parameter; (b) crack distribution.

Figure 5-21 compares the crack density at ~1% strain and failure after dynamic and quasi-static loading in perpendicular direction, which shows the similar trend as in parallel direction.

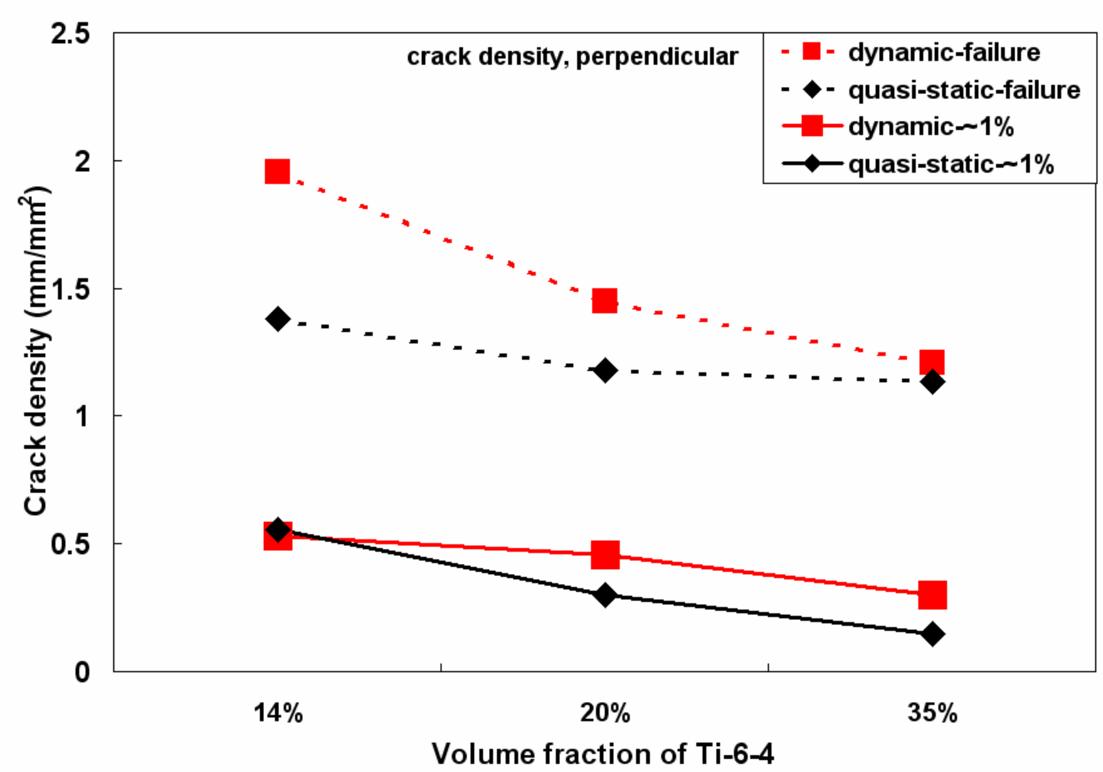

Figure 5-21 Crack density comparison in 1% and failure strain after the dynamic and quasi-static loading in perpendicular direction.

5.4 Effect of damage on elastic modulus

The damage in the MIL composites has a considerable effect on the elastic modulus. An expression developed by O'Connell and Budiansky [84] is used and modified to model the effect:

$$\frac{E}{E_0} = 1 - \frac{16\left(10-3\upsilon\right)\left(1-\upsilon^2\right)}{45\left(45-\upsilon\right)} f_s \approx 1 - 1.63Na^3 \tag{5.6}$$

where N is the number of cracks per unit volume, and a is the radius of a mean crack. E is the effective Young's modulus of the cracked material. E_0 is Young's modulus of uncracked material and for MIL composite, it is equal to

in parallel direction

$$E_0 = V_{Ti}E_{Ti} + V_{Al_3Ti}E_{Al_3Ti} \tag{5.7}$$

and in perpendicular direction

$$\frac{1}{E_0} = \frac{V_{Ti}}{E_{Ti}} + \frac{V_{Al_3Ti}}{E_{Al_3Ti}} \tag{5.8}$$

The definition of cracks used by O'Connell and Budiansky [84] differs from the one in Equation (5.6). O'Connell and Budiansky considered circular crack with radius of a (Figure 5-22 (a)), while we consider rectangular cracks with the smaller side equal to 2a and the larger side equal to the thickness of the specimen (Figure 5-22 (b)). These asymmetric cracks are produced by the unimpeded crack growth in Al_3Ti.

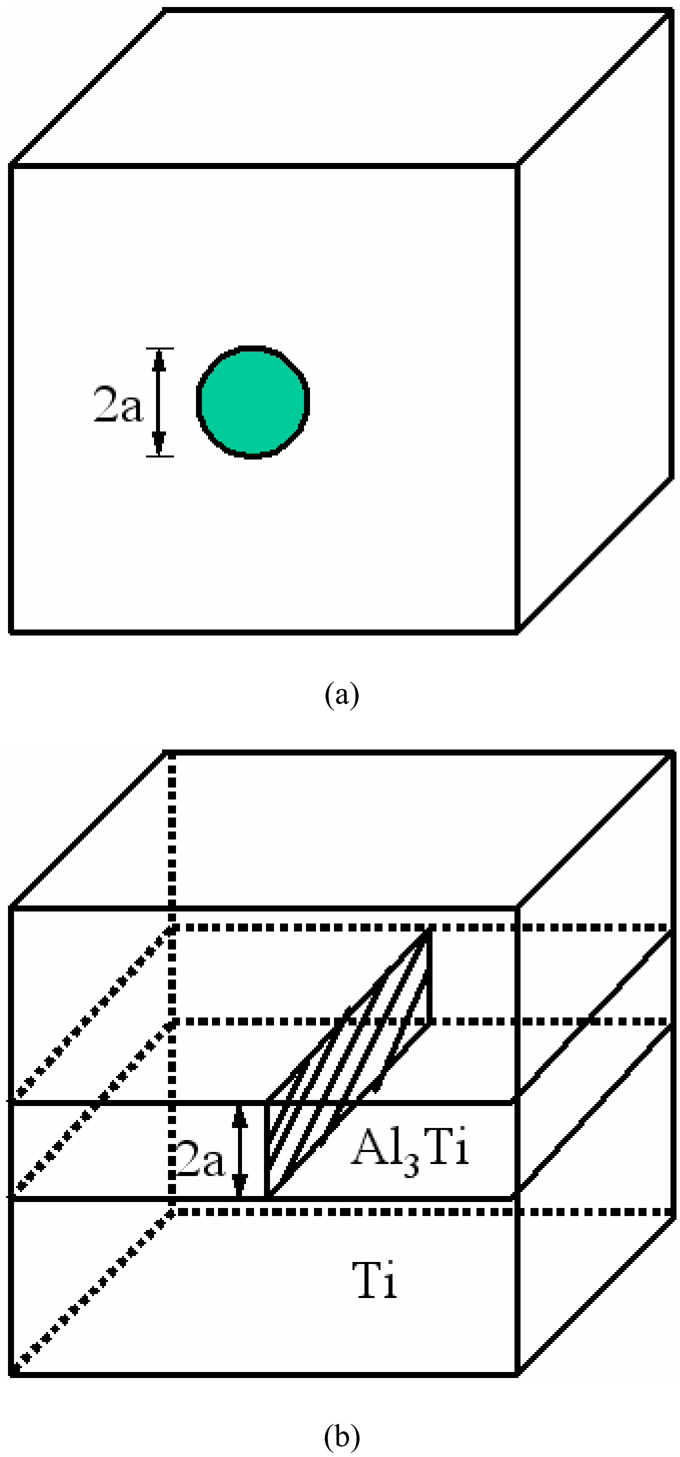

Figure 5-22 Schematics of crack shape: (a) O'Connell and Budiansky crack; (b) MIL crack.

In the O'Connell-Budiansky equation, Na^3 is a measure of the fraction of the material that is under the effect of the cracks, and we modify this equation by replacing Na^3 by the fraction of the material under the effect of rectangular cracks in Al_3Ti:

$$Na^3 = \frac{m\pi a^2 t}{At} = D \tag{5.9}$$

where m is the total number of cracks, a is half of the crack size in Al_3Ti, t is the thickness of Al_3Ti, and A is the surface area of MIL specimen. Substituting Equation (5.9) into Equation (5.6)

$$E = E_0\left[1-1.63D\right] = E_0\left[1-1.63\left(D_0 + k\varepsilon^n\right)\right] \tag{5.10}$$

Since $E = \frac{d\sigma}{d\varepsilon}$, the calculated stress-strain relation can be obtained:

$$\sigma = \int_0^{\varepsilon} E d\varepsilon = \int_0^{\varepsilon} E_0\left[1-1.63\left(D_0 + k\varepsilon^n\right)\right] d\varepsilon = E_0\left[\left(1-1.63D_0\right)\varepsilon - \frac{1.63k\varepsilon^{n+1}}{n+1}\right] \tag{5.11}$$

The failure stress occurs at $\frac{d\sigma}{d\varepsilon} = 0$, i.e., the onset of softening. This corresponds to

$$\frac{d\sigma}{d\varepsilon} = E_0\left[\left(1-1.63D_0\right) - 1.63k\varepsilon^n\right] = 0 \tag{5.12}$$

Thus,

$$\varepsilon_{failure} = \left(\frac{1-1.63D_0}{1.63k}\right)^{1/n} \quad \text{and} \quad \sigma_{failure} = E_0\left[\frac{n\left(1-1.63D_0\right)}{n+1} \bullet \left(\frac{1-1.63D_0}{1.63k}\right)^{1/n}\right] \tag{5.13}$$

Figure 5-23 and Figure 5-24 compare the calculated and experimental elastic relations in parallel and perpendicular directions for quasi-static and dynamic deformation.

In quasi-static deformation, the calculated elastic relation compares well with the experimental data at small strains and only deviates when approaching failure (Figure 5-23 (a) and Figure 5-24 (a)). On the other hand, in dynamic deformation, the calculated values deviate from the experimental data from the beginning and such deviation intensifies as strain increases (Figure 5-23 (b) and Figure 5-24 (b)). Mathematically, in dynamic deformation, the material parameters k and n are larger than those in the quasi-static deformation, and according to Equation (5.12), they decrease the elastic slope. Physically, the materials undergo some extreme situations and therefore, the calculation is less predictable in dynamic loading. One possible reason for this is that cracks continue to grow under unloading, in the dynamic case; therefore, the measured density is higher than the one existing under loading.

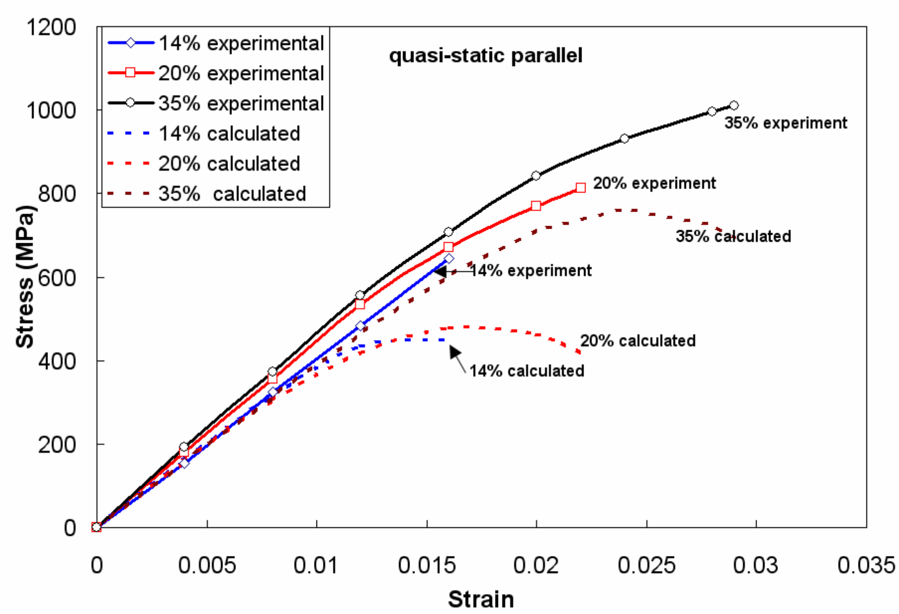

(a)

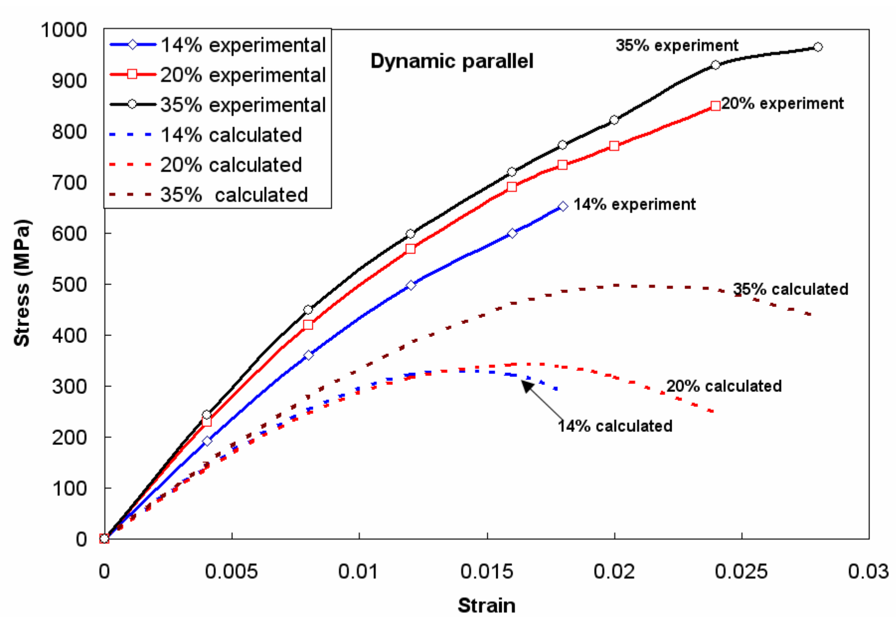

(b)

Figure 5-23 Comparison of calculated and experimental stress-strain relation for MIL composites in parallel loading direction: (a) quasi-static; (b) dynamic.

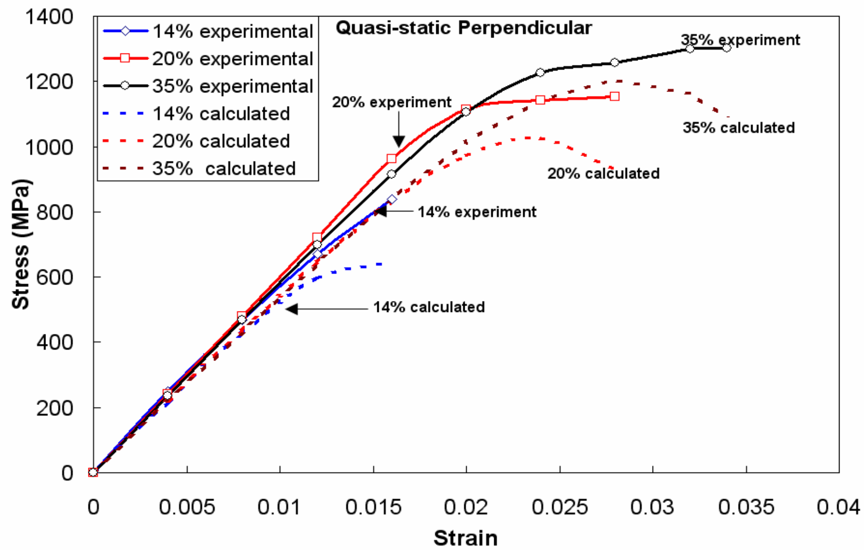

(a)

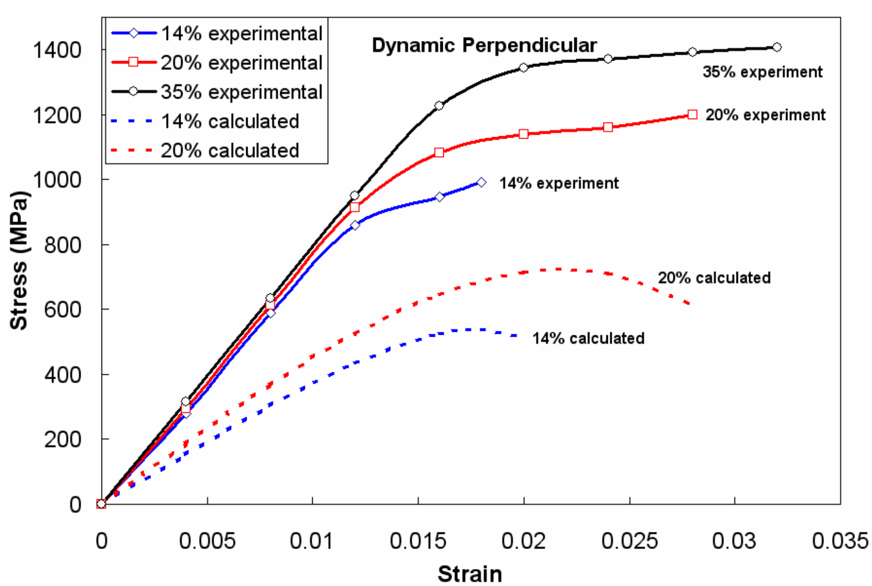

(b)

Figure 5-24 Comparison of calculated and experimental stress-strain relation for MIL composites in perpendicular loading direction: (a) quasi-static; (b) dynamic.

5.5 Damage evolution in the Ti6Al4V-AL_3Ti MIL composites: physical modeling

The establishment of a failure criterion for the intermetallic layers in the Ti6Al4V- Al_3Ti MIL composites requires a fundamental appraisal of the mechanisms of damage under the unique conditions experienced by Al_3Ti. The conventional failure mechanisms including Mohr-Coulomb [85], Johnson-Holmquist [86], Govindjee, Kay, and Simo [87], are only strictly applicable to bulk materials, in which the three dimensions are of the same order. In the laminates, however, one of the dimensions is much smaller.

Damage-failure criterions for laminate composites has been investigated in the past and many researchers have proposed their failure theories for laminate composites of various kinds [88 - 103]. The majority of the failure theories for composite laminates have been developed by extending failure models applicable to homogeneous isotropic materials so as to apply them to heterogeneous anisotropic materials, such as failure theories include non-interactive theories like the maximum-stress [104] and maximum-strain models, and interactive theories where quadratic, fourth and higher order polynomials are used [105].

Hutchinson and Evans [106, 107] have developed micromechanically-based damage mechanisms for multilayered materials. Hashin [108 - 111], Nairn [112, 113], and Hu [114] have derived corresponding solutions for multilayer laminate composites. These solutions lead to lower-bound estimates when used to predict the dependence of axial Young's modulus on crack density. Puck [115] used a layer-by-layer failure analysis to treat the successive failure of different laminates subjected to a variety of loading conditions. Zinoviev [116] presents a theory describing the deformation and failure processes of the laminate composites under plane stress. Others [117 - 122] use stress or energy based criterions to evaluate the failure of the laminate composites.

Some of the concepts studied in those previous researches are applicable to the Ti6Al4V-Al_3Ti MIL composite, and since the interfacial strength is higher than the shear strengths of both metal and intermetallics, interfacial delamination is not a major failure mechanism. Four damage evolution mechanisms are identified from the experiments and are discussed below.

5.5.1 Tension: parallel to laminate plane

Tensile cracks, perpendicular to the loading direction, and with a length equal to the thickness, appear with a decreasing spacing as the load is increased. This is shown schematically in Figure 5-25. The stresses are shown in the right-hand side. The external traction increases from (a) to (d). Each crack unloads the intermetallic, and this load transfer can be calculated [123]. As the spacing of cracks decreases, the load-transfer ability decreases and the metallic component carries a greater fraction of the load, leading to softening.

5.5.2 Compression: parallel to laminate plane

The intermetallic is confined between metallic layers, and therefore Poisson ratio effects can produce confinement stresses that affect the failure mechanism. Poisson's ratios for the intermetallic and metallic components are 0.17 and 0.321, respectively; if the metallic layer undergoes plastic deformation, its Poisson ratio is increased to 0.5. Thus, it is safe to assume that we have the scenario depicted in Figure 5-26, i.e., the intermetallic will fail by shear. Figure 5-26 shows three modes of damage accumulation: vertical cracks forming initially along the intermetallic central plane; buckling of the metallic component (this initiates at the surfaces of specimen and propagates inwards); and shear band formation in Ti6Al4V layer. From the SEM pictures (Figure 5-12 (a) and (b)), we can see clearly that under parallel compression loading, the Ti6Al4V layer fails by buckling and shear localization.

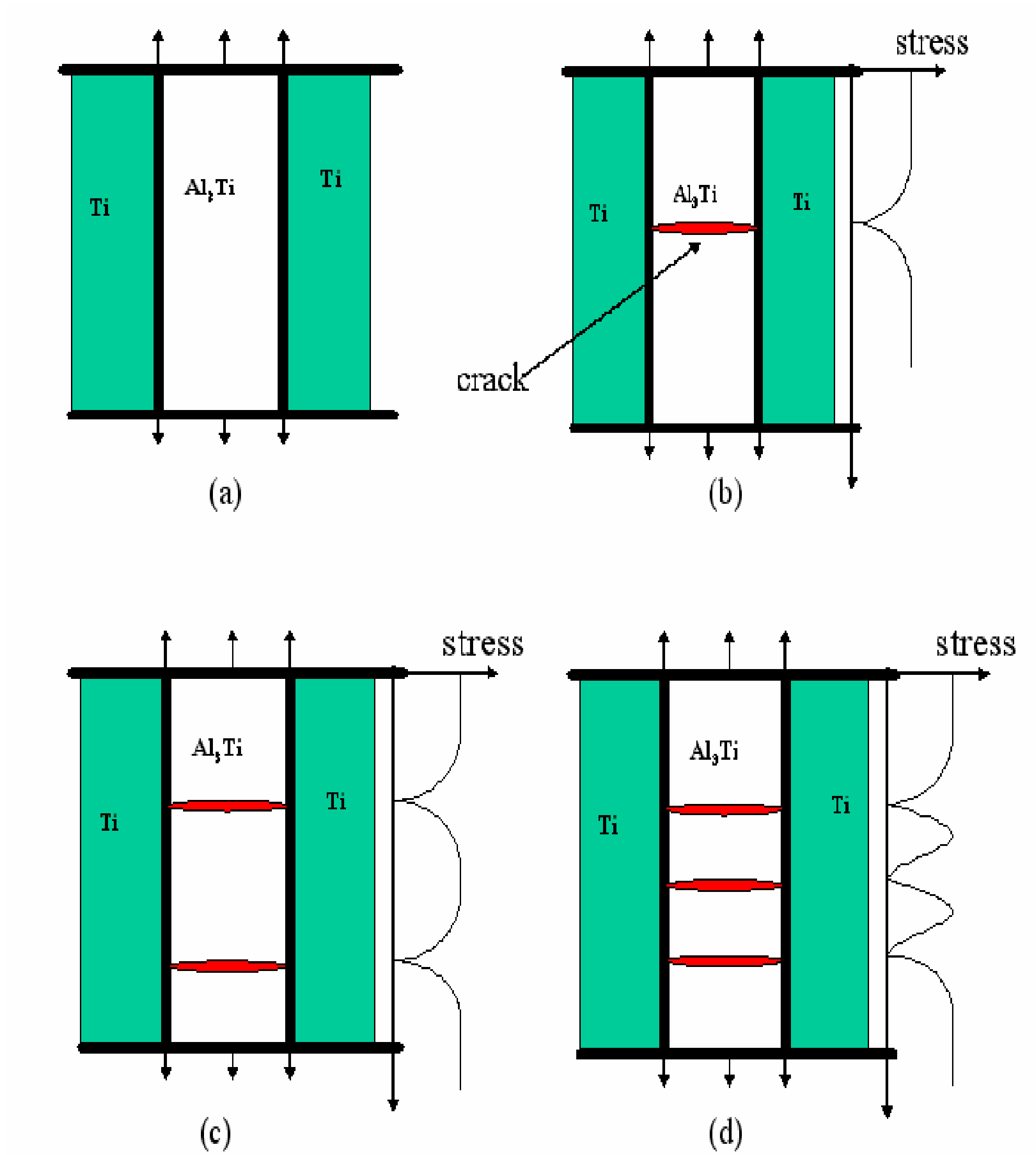

Figure 5-25 Tensile loading parallel to laminate plane; increasing traction from (a) to (d).

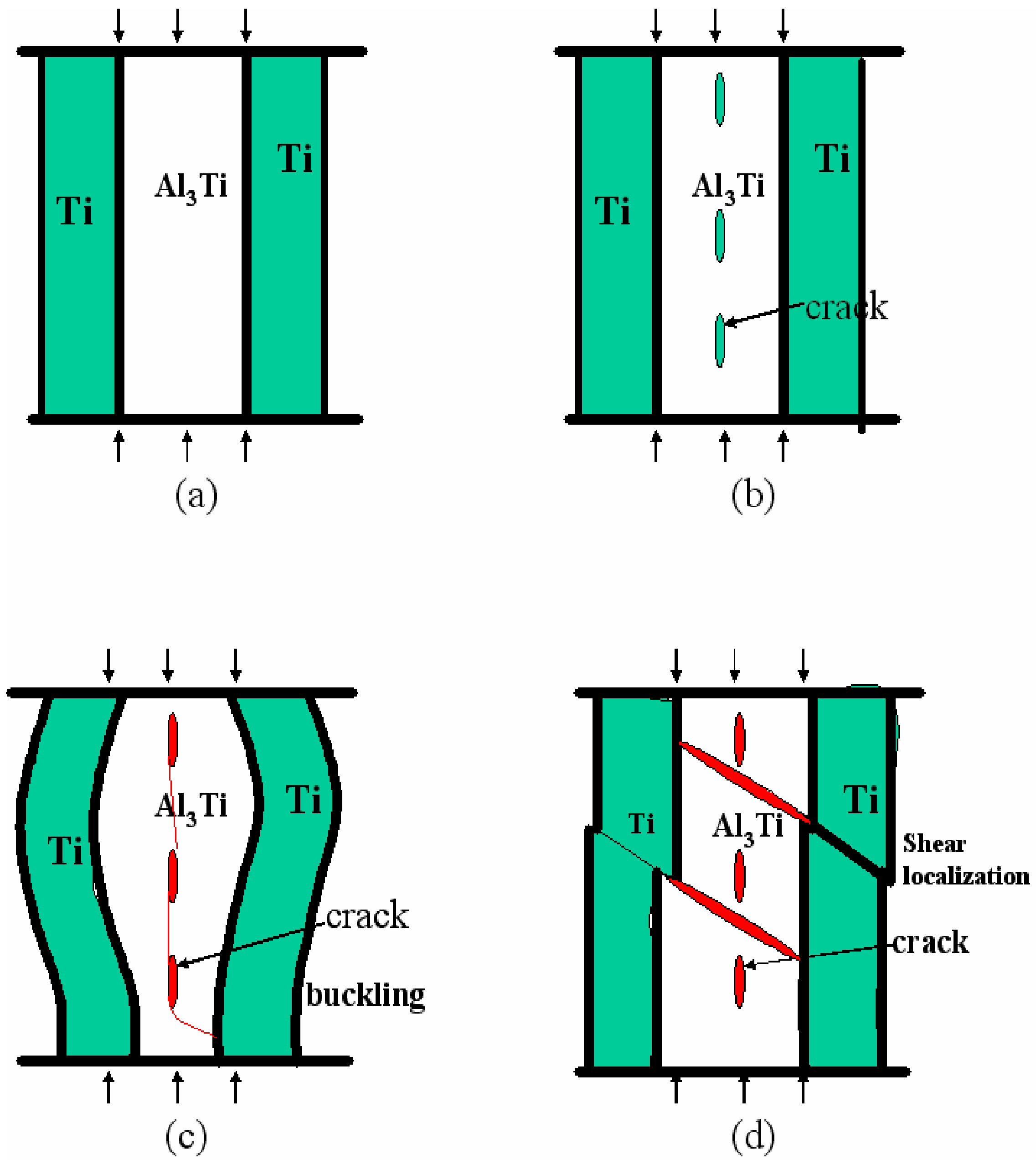

Figure 5-26 Compression loading parallel to the laminate plane without confinement: (a) loading configuration; (b) axial splitting along central plane in Al_3Ti; (c) plastic buckling of Ti6Al4V; (d) shear localization of Ti6Al4V.

If the specimen is confined and axial splitting is inhibited, shear failure establishes itself as the dominant mode of failure. This is shown schematically in Figure 5-27.

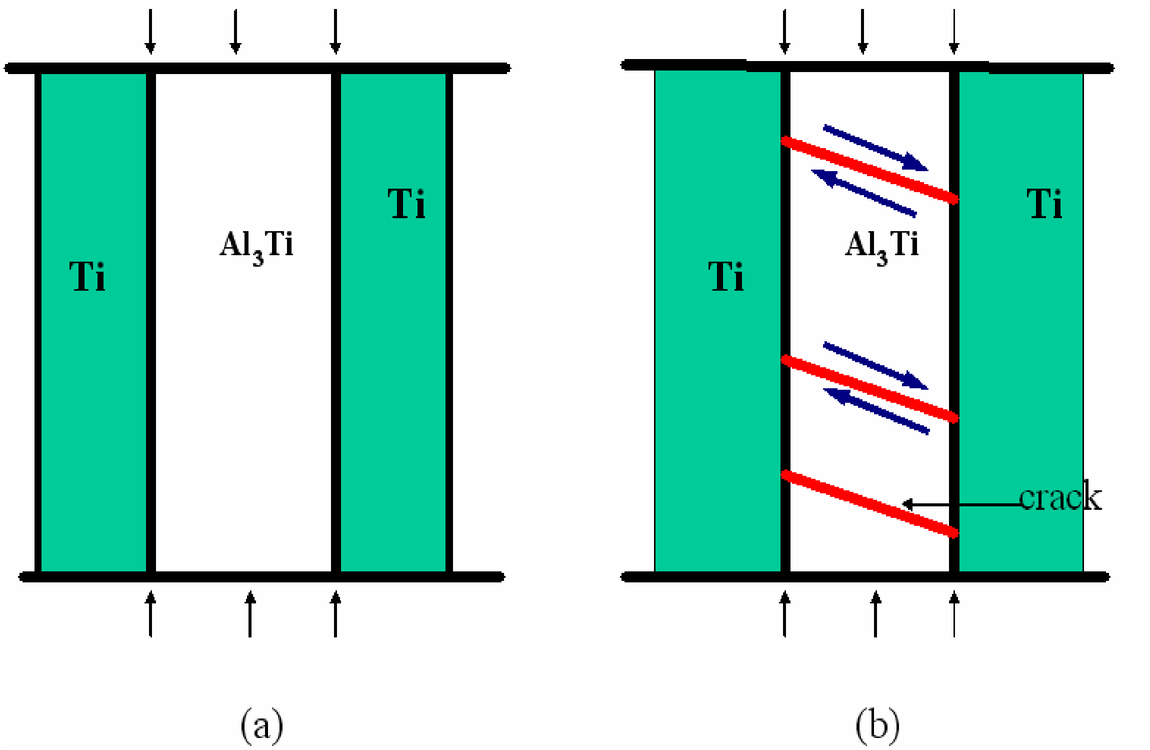

Figure 5-27 Compression loading parallel to the laminate plane with confinement.

5.5.3 Shear

For the shear loading, tensile cracks at 45^0 to the interface should form. These cracks increase in density as the shear stress is increases, and they gradually unload the intermetallic layer. Figure 5-28 (b) shows this damage mechanism. Figure 5-28 (c) shows an alternative mechanism: a shear crack along central plane of Al_3Ti.

5.5.4 Compression: perpendicular to laminate plane

The sequence of damage accumulation that was observed in numerous experiments is shown in Figure 5-29. Damage initiates by the formation of axial splitting cracks in the intermetallic. These cracks are limited in size by the thickness of the intermetallic layer (Figure 5-29 (b) and (c)). Their spacing gradually decreases until they start connecting via shear failure in the Ti6Al4V layer to the axial splitting cracks in adjacent layers. The damage thus evolves into shear failure because of the confinement provided by the Ti6Al4V layers to the brittle intermetallics. This is confirmed by the SEM micrograph of Figure 5-17 (g), where the cracks formed in Al_3Ti layer first develop a small "step" on the interface and then propagate through the Ti6Al4V layer, which will ultimately form the shear band Ti6Al4V layer and lead to the final failure of the MIL (Figure 5-17 (h)).

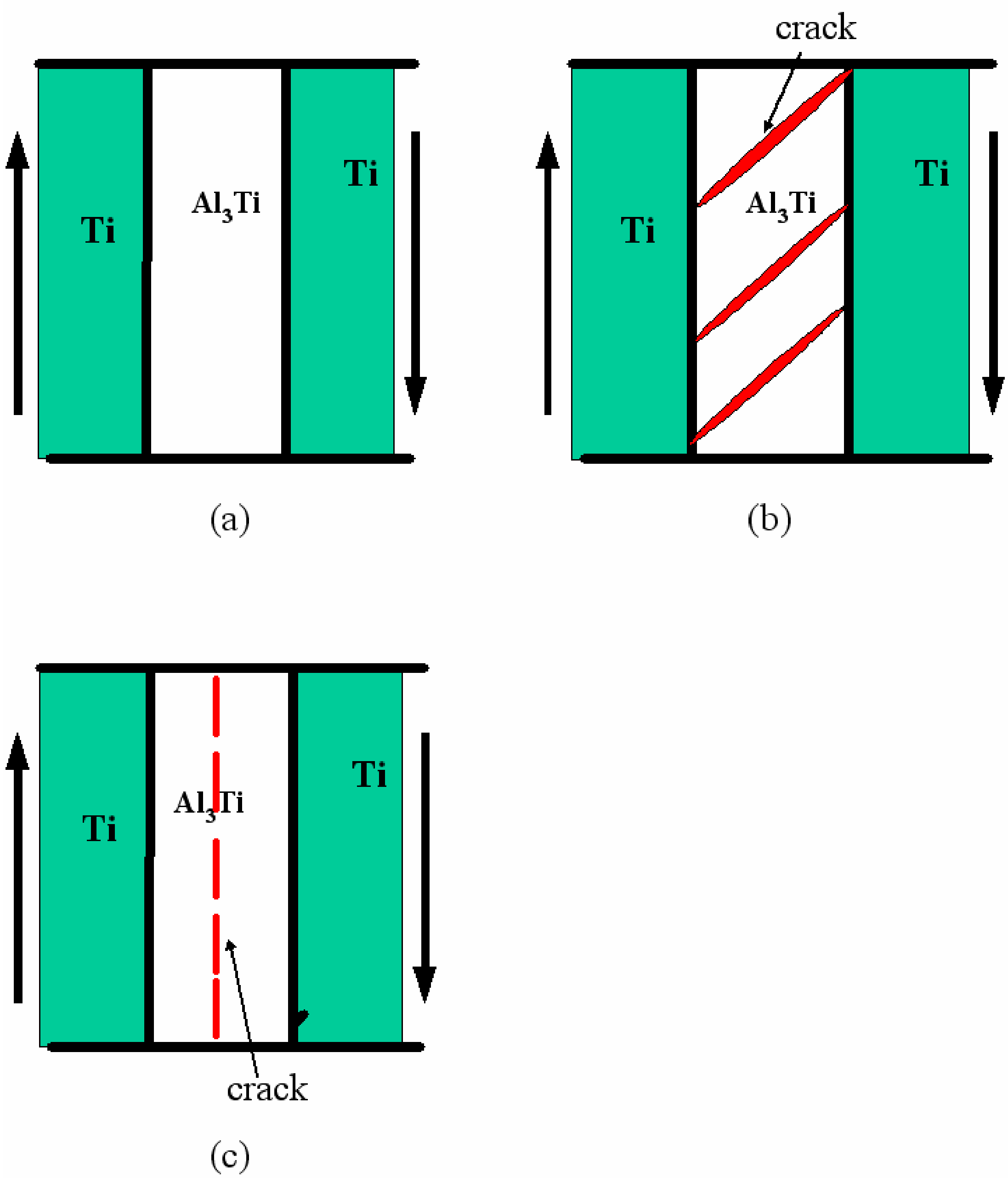

Figure 5-28 Shear loading parallel to laminate plane; loading configuration; (b) tensile cracks at 45^o to interface; (c) shear crack along central plane of Al_3Ti.

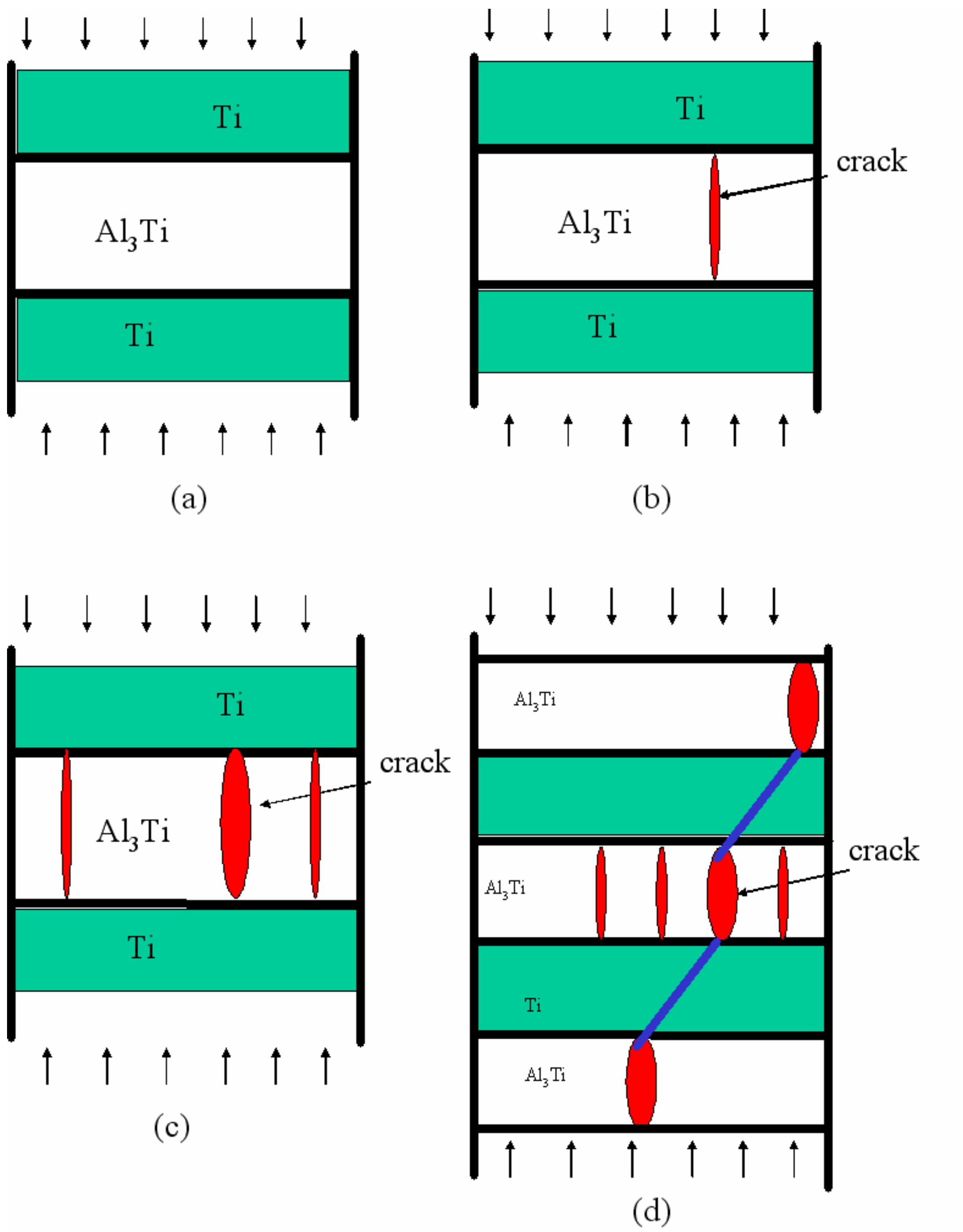

Figure 5-29 Compression loading perpendicular to laminate plane; stress increases from (a) to (d).

CHAPTER 6

MODELING OF MECHANICAL AND FRACTURE PROPERTIES OF THE TI6AL4V-AL$_3$TI MIL COMPOSITES

In this chapter, elastic properties of Ti6Al4V-Al$_3$Ti MIL composites were modeled as a function of volume fraction of Ti6Al4V and orientation. The results were then successfully compared with the experimental measures. Residual stress during cooling is induced in the Ti6Al4V-Al$_3$Ti MIL composites due to the thermal expansion mismatch between Ti6Al4V and Al$_3$Ti, which render Ti6Al4V layer under compression and Al$_3$Ti under tension. Residual stress was analytically modeled, and creep mechanism and crack propagation mechanism were introduced as relaxation mechanisms. Finite element simulation took into consideration of the finite boundary of the composite, showed the distribution as well as evolution of the residual stress. Both analytical modeling and finite element simulation were successfully compared with the experimental measurements. The influence of residual stress on fracture toughness was quantified and the fracture toughness was modeled as a combination of crack initiation toughness and stress intensity due to the designed internal stresses, the later of which is evaluated by a weight function. The calculated fracture toughness agrees well with the experimental measurements.

6.1 Elastic properties of Ti6Al4V-Al_3Ti MIL composites

6.1.1 Elastic properties as a function of volume fraction of Ti6Al4V

Elastic properties, Young's modulus, shear modulus and Poisson's ratio of Ti6Al4V-Al_3Ti MIL composites were evaluated as a function of volume fraction of Ti6Al4V. Figure 6-1 shows the coordinate system for the Ti6Al4V-Al_3Ti MIL composites. The [100] direction is perpendicular to the laminate plane (OX_1). The material is isotropic in the OX_2X_3 plane.

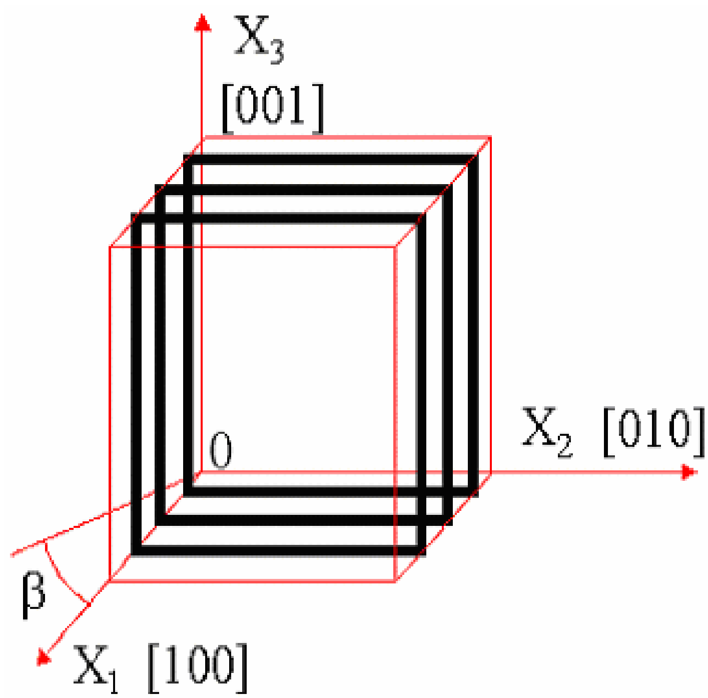

Figure 6-1 Ti6Al4V-Al_3Ti metal-intermetallic laminate composites coordinate system with angle β about the 3-axis.

The following equations [124, 125, 126] describe the relations between elastic properties of Ti6Al4V-Al_3Ti MIL composite and the volume fraction of Ti6Al4V.

$$E_{11} = 2\left(1-\upsilon_m+\left(\upsilon_m-\upsilon_I\right)\cdot\left(1-c\right)\right)\times \left[\begin{array}{l}\left(1-c\right)\cdot\dfrac{K_m\cdot\left(2K_I+G_I\right)-G_I\cdot\left(K_m-K_I\right)\cdot\left(1-c\right)}{2K_I+G_I+2\left(K_m-K_I\right)\cdot\left(1-c\right)}+\\ c\cdot\dfrac{K_m\cdot\left(2K_I+G_m\right)+G_m\cdot\left(K_I-K_m\right)\cdot\left(1-c\right)}{2K_I+G_m-2\left(K_I-K_m\right)\cdot\left(1-c\right)}\end{array}\right] \tag{6.1}$$

$$E_{22} = c\cdot E_m+\left(1-c\right)\cdot E_I+\frac{c\cdot\left(1-c\right)\cdot E_I\cdot E_m\cdot\left(\upsilon_m-\upsilon_I\right)^2}{c\cdot E_m\cdot\left(1-\upsilon_I{}^2\right)+\left(1-c\right)\cdot E_I\cdot\left(1-\upsilon_m{}^2\right)} \tag{6.2}$$

$$G_{12} = \left(1-c\right)\cdot G_I\cdot\frac{2G_m-\left(G_m-G_I\right)\cdot\left(1-c\right)}{2G_I+\left(G_m-G_I\right)\cdot\left(1-c\right)}+c\cdot G_m\cdot\frac{\left(G_m+G_I\right)-\left(G_m-G_I\right)\cdot\left(1-c\right)}{\left(G_m+G_I\right)+\left(G_m-G_I\right)\cdot\left(1-c\right)} \tag{6.3}$$

$$\upsilon_{23} = \frac{c\cdot\upsilon_m\cdot E_m\cdot\left(1-\upsilon_I{}^2\right)+\left(1-c\right)\cdot\upsilon_I\cdot E_I\cdot\left(1-\upsilon_m{}^2\right)}{c\cdot E_m\cdot\left(1-\upsilon_I{}^2\right)+\left(1-c\right)\cdot E_I\cdot\left(1-\upsilon_m{}^2\right)} \tag{6.4}$$

$$\upsilon_{12} = \frac{\left(1-c\right)\cdot K_m\cdot\upsilon_m\cdot\left(2K_I+G_I\right)\cdot c+K_I\cdot\upsilon_I\cdot\left(2K_m+G_I\right)\cdot\left(1-c\right)}{K_m\cdot\left(2K_I+G_I\right)-G_I\cdot\left(K_m-G_I\right)\cdot\left(1-c\right)}+ c\cdot\frac{K_I\cdot\upsilon_I\cdot\left(2K_m+G_m\right)\cdot\left(1-c\right)+K_m\cdot\upsilon_m\cdot\left(2K_I+G_m\right)\cdot c}{K_m\cdot\left(2K_I+G_m\right)+G_m\cdot\left(K_I-K_m\right)\cdot\left(1-c\right)} \tag{6.5}$$

$$G_{23} = \frac{E_{22}}{2\left(1+\upsilon_{23}\right)} \tag{6.6}$$

where E_{jj}, is the Young's modulus in direction j for the composite; G_{ij}, is the shear modulus in the ij plane for the composite; υ_{ij}, is the Poisson's ratio in the ij plane for the composite; υ_m, is the Poisson's ratio of Ti6Al4V; υ_I, is Poisson's ratio of intermetallic Al_3Ti;

$c\left(\mathrm{h_m}/\mathrm{H}\right)$, is the concentrations of Ti6Al4V; E_m, is the Young's modulus of

Ti6Al4V; E_I, is the Young's modulus of intermetallic Al_3Ti; K_m and K_I are the bulk moduli of Ti6Al4V and intermetallic Al_3Ti, respectively; G_m and G_I are the shear moduli.

The corresponding strain-stress relation is:

$$\begin{Bmatrix} \varepsilon_{11} \\ \varepsilon_{22} \\ \varepsilon_{33} \\ 2\varepsilon_{23} \\ 2\varepsilon_{31} \\ 2\varepsilon_{12} \end{Bmatrix} = \begin{bmatrix} \frac{1}{E_{11}} & -\frac{\upsilon_{12}}{E_{11}} & -\frac{\upsilon_{12}}{E_{11}} & 0 & 0 & 0 \\ -\frac{\upsilon_{12}}{E_{11}} & \frac{1}{E_{22}} & -\frac{\upsilon_{23}}{E_{22}} & 0 & 0 & 0 \\ -\frac{\upsilon_{12}}{E_{11}} & -\frac{\upsilon_{23}}{E_{22}} & \frac{1}{E_{22}} & 0 & 0 & 0 \\ 0 & 0 & 0 & \frac{2\cdot(1+\upsilon_{23})}{E_{22}} & 0 & 0 \\ 0 & 0 & 0 & 0 & \frac{1}{G_{12}} & 0 \\ 0 & 0 & 0 & 0 & 0 & \frac{1}{G_{12}} \end{bmatrix} \cdot \begin{Bmatrix} \sigma_{11} \\ \sigma_{22} \\ \sigma_{33} \\ \sigma_{23} \\ \sigma_{31} \\ \sigma_{12} \end{Bmatrix} \tag{6.7}$$

The Young's modulus, shear modulus and Poisson's ratio of Al_3Ti and Ti6Al4V are listed in Table 7.

Table 7 Young's modulus, shear modulus and Poisson's ratio of Al_3Ti and Ti6Al4V.

	Ti	Al_3Ti
$E(GPa)$	115.7	216
$G(GPa)$	43.8	92.3
υ	0.321	0.17

Figure 6-2 shows the calculated Young's moduli (E_{11} and E_{22}) and shear moduli (G_{12} and G_{23}) of the Ti6Al4V-Al_3Ti MIL composites as a function of volume fraction of Ti6Al4V. Figure 6-3 shows Poisson's ratios υ_{12} and υ_{23} of the Ti6Al4V-Al_3Ti MIL composites as a function of volume fraction of Ti6Al4V.

It is seen from Figure 6-2 and Figure 6-3 that Young's moduli and shear moduli of the Ti6Al4V-Al_3Ti MIL composites decrease with increasing volume fraction of Ti6Al4V, and that the Poisson's ratios increase with the increasing volume fraction of Ti6Al4V.

The elastic properties of Ti6Al4V-Al_3Ti metal-intermetallic laminate composites have been experimentally measured by Resonant Ultrasonic Spectroscopy (RUS) for 20% Ti6Al4V, and are listed in Table 8 along with the calculated values, which agree well with the experimental measurements.

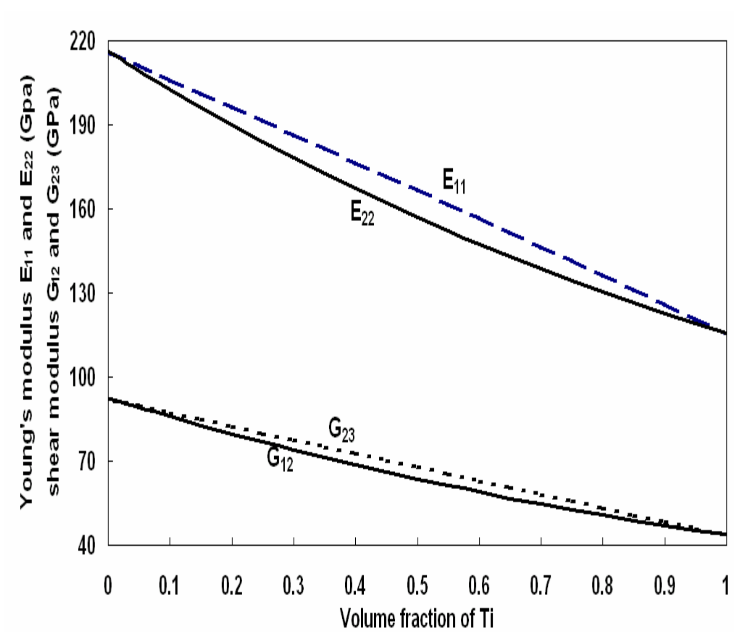

Figure 6-2 Elastic properties, Young's and shear moduli of the laminate composites as a function of volume fraction of Ti6Al4V.

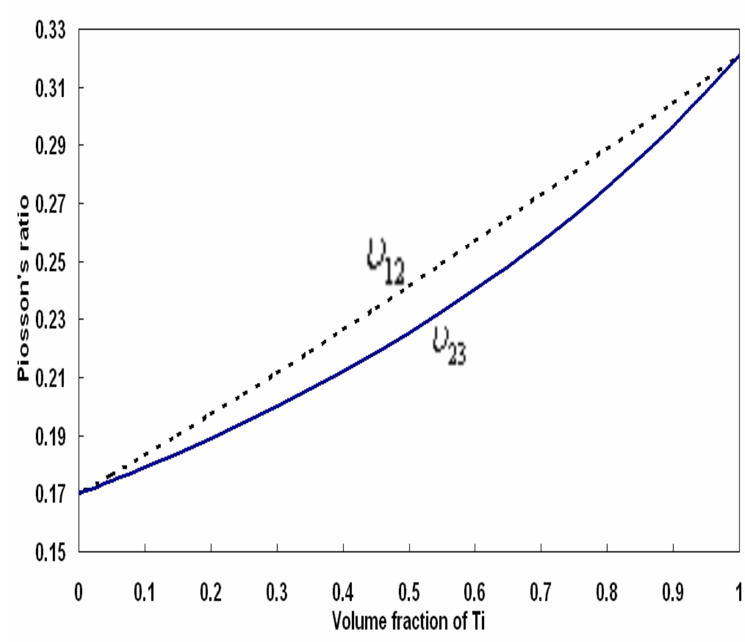

Figure 6-3 Poisson's ratios υ_{12} and υ_{23} of the laminate composites as a function of volume fraction of Ti6Al4V.

Table 8 Comparison of calculated and experimental elastic constants for Ti6Al4V-Al_3Ti metal-intermetallic laminate composites with 20% Ti6Al4V.

	Experimental measurements	Calculated values
$E_{11}(GPa)$	186.98	189.96
$E_{22}(GPa)$	180.92	196.45
$G_{12}(GPa)$	73.94	79.76
$G_{23}(GPa)$	74.50	82.60
υ_{12}	0.1952	0.1974
υ_{23}	0.2145	0.1895

6.1.2 Elastic properties as a function of orientation

Elastic properties of Ti6Al4V-Al_3Ti metal-intermetallic laminate composites were evaluated as a function of orientation. The same coordinate system was used; X_1 [100] is the transverse direction and β is the angle with respect to the 3-axis (transformed [100] axis creates an angle β with the original [100] axis). The elastic properties in different orientations can be calculated by expressing the elastic compliances in the fourth-order tensor notation, and transforming this tensor [127] as

$$S'_{ijkl} = a_{im} \cdot a_{jn} \cdot a_{ko} \cdot a_{lp} \cdot S_{mnop} \tag{6.8}$$

where a_{ij} are the cosines of the orientation angles: $a_{11} = \cos\beta$, $a_{12} = 0$, $a_{13} = \sin\beta$, $a_{21} = -\sin\beta$, $a_{22} = 0$, $a_{23} = \cos\beta$, $a_{31} = 0$, $a_{32} = 1$, and $a_{33} = 0$. In converting the elastic compliances from 2-index notation to the tensorial 4-index notation, one has to carefully consider factors of 2 and 4 arising from the definition of strain. Knowing the elastic compliance tensor in the rotated coordinate system, the elastic moduli can be obtained from

$$E_{11}(\beta) = \frac{1}{S'_{11}(\beta)} \tag{6.9}$$

$$E_{22}(\beta) = \frac{1}{S'_{22}(\beta)} \tag{6.10}$$

$$G_{12}(\beta) = \frac{1}{S'_{66}(\beta)} \tag{6.11}$$

$$G_{23}(\beta) = \frac{1}{S'_{44}(\beta)} \tag{6.12}$$

$$\upsilon_{12}(\beta) = \frac{-S'_{12}(\beta)}{S'_{11}(\beta)} \tag{6.13}$$

$$\upsilon_{23}(\beta) = \frac{-S'_{23}(\beta)}{S'_{22}(\beta)} \tag{6.14}$$

where

$$S'_{11}(\beta) = S_{11} \cdot \cos^4 \beta + S_{33} \cdot \sin^4 \beta + S_{55} \cdot \cos^2 \beta \cdot \sin^2 \beta + 2S_{31} \cdot \cos^2 \beta \cdot \sin^2 \beta \tag{6.15}$$

$$S'_{22}(\beta) = S_{33} \cdot \cos^4 \beta + S_{11} \cdot \sin^4 \beta + S_{55} \cdot \cos^2 \beta \cdot \sin^2 \beta + 2S_{31} \cdot \cos^2 \beta \cdot \sin^2 \beta \tag{6.16}$$

$$\begin{aligned} S'_{12}(\beta) &= S_{13} \cdot \cos^4 \beta + S_{13} \cdot \sin^4 \beta + S_{11} \cdot \cos^2 \beta \cdot \sin^2 \beta + \\ &S_{33} \cdot \cos^2 \beta \cdot \sin^2 \beta - S_{55} \cdot \cos^2 \beta \cdot \sin^2 \beta \end{aligned} \tag{6.17}$$

$$S'_{23}(\beta) = S_{32} \cdot \cos^2 \beta + S_{12} \cdot \sin^2 \beta \tag{6.18}$$

$$S'_{44}(\beta) = S_{44} \cdot \cos^2 \beta + S_{66} \cdot \sin^2 \beta \tag{6.19}$$

$$\begin{aligned} S'_{66}(\beta) &= S_{55} \cdot \cos^4 \beta + S_{55} \cdot \sin^4 \beta + 4S_{33} \cdot \cos^2 \beta \cdot \sin^2 \beta - 4S_{31} \cdot \cos^2 \beta \cdot \sin^2 \beta \\ &-2S_{55} \cdot \cos^2 \beta \cdot \sin^2 \beta \end{aligned} \tag{6.20}$$

The compliance matrix can be calculated from its relationship with the stiffness matrix (C*S=1).

Figure 6-4 shows the elastic properties of Ti6Al4V-Al_3Ti MIL composite as a function of orientation for 20% Ti6Al4V. As seen, the Young's modulus E_{11} is a mirror of E_{22}; they are equal to each other at $\beta = 45^0$. For an increasing β, E_{22} first increases and then rapidly decreases. The results in Figure 6-4 show the anisotropy in the elastic properties of this laminate system, which in turn affect its mechanical properties in a significant manner.

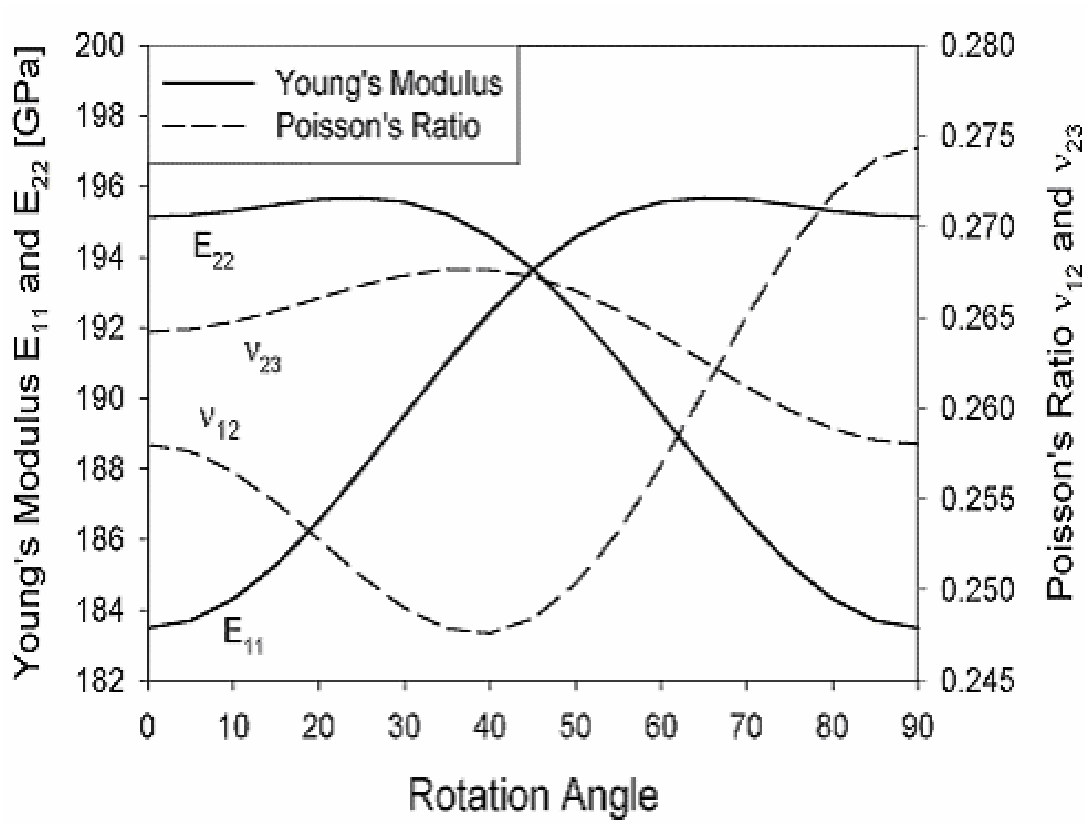

Figure 6-4 Elastic properties of Ti6Al4V-Al_3Ti metal-intermetallic laminate composites as a function of orientation.

6.2 Residual stress in MIL composites

Under uniform temperature change, stresses are induced in a composite due to the thermal expansion mismatch between the matrix and the reinforcing phase. Composite thermal stresses and thermal expansion depend on the following:

1. Reinforcement volume fraction and morphology (i.e., particle, fiber or plate size, shape, orientation distribution, and continuity);

2. Matrix crystallographic texture and porosity;

3. Possible voids or lack of adhesion at matrix-reinforcement interfaces.

4. Cracks.

In principle, as a reversible phenomenon, thermal expansion at a given temperature should be determined only by the elastic constants and thermal expansion coefficients of the matrix and reinforcement, accounting for the possible presence of voids in matrix and/or at interfaces. However, the residual stresses may be large enough to induce nonreversible phenomena such as plastic yielding, reinforcement fracture, void growth in the matrix, interface decohesion, creeping or cracking in the matrix. The nonreversible thermal expansion depends on the plastic or viscoplastic strength of both the matrix and the reinforcement, as well on the damage resistance of the matrix and on the cracking and sliding resistance of matrix-reinforcement interfaces. Generally speaking, nonreversible phenomena tends to reduce the residual stresses, and they are designated as relaxation phenomena because their driving force is the lowering of the internal strain energy of the composite [128].

Several models have proposed to predict the residual stress in composites [129-150]. Cannillo et al. [151] proposed a computational model which applies the finite element method at the microscale, which models the real microstructural details to accurately predict the local stress values and distribution. They also experimentally measured the residual thermal stresses by means of a piezo-spectroscopic technique. Ee et al. [152] employed a thermal elastic-viscoplastic finite element model to evaluate the residual stresses remainingin a machined component. Teixeira-Dias et al.

[153] used a three-dimensional mechanical model to determine the residual stress fields in SiC-Al fiber reinforced composites. The model is based on the thermoelastic reinforcement behavior and the thermoelastic–viscoplastic matrix behavior. They also evaluated the influence of material parameters using two different unit cells representing of continuous and short fiber reinforcement in finite element simulation. Aghdam et al. [154] proposed a finite element micromechanical model to study effects of thermal residual stress bonding on the transverse behavior of a unidirectional SiC/Ti6Al4V metal matrix composite. Dunn et al. [155] used Eshelby's theory to analyze the thermally induced residual stress in metal matrix composites. Teodosiu et al. [156,157] studied the residual stress fields in an aluminium matrix reinforced by spherical SiC particles. A spherical symmetric thermoviscoplastic model was used to calculate the thermal residual stresses, assuming that the particles behave elastically whereas the matrix exhibits an elastoviscoplastic behaviour. Sayman [158] obtained the residual stress distribution along the thickness of aluminum metal-matrix laminated plates by elastic–plastic stress analysis. Hsueh et al. [159] studied the thermal expansion behavior and residual stresses in multilayer capacitor (MLC) systems by including plasticity of the electrodes.

The following sections investigate the residual stress in Ti6Al4V-Al_3Ti MIL composite using both analytical method and finite element simulation. In the analytical model, two stress release mechanisms, creep (section 6.2.2) and crack propagation (section 6.2.3) mechanisms are introduced, and the result obtained from a combination of the two mechanism (section 6.2.4) presents the best solution comparable with the experimental results. Finite element simulation was also performed to investigate the residual stress distribution.

6.2.1 Elastic analysis

When the Ti6Al4V-Al_3Ti MIL composite cools down, Al_3Ti layer shrinks more than Ti6Al4V layer because the coefficient of thermal expansion of Al_3Ti is larger than that of Ti6Al4V. This mismatch of strain will render Ti6Al4V layer under compression and Al_3Ti layer under tension. Table 9 shows the coefficients of thermal expansion of Ti6Al4V and Al_3Ti. Figure 6-5 shows a schematic of residual stress distribution in Ti6Al4V-Al_3Ti MIL composites after cooling.

Table 9 The coefficients of thermal expansion of Ti6Al4V and Al_3Ti.

Materials	Ti ($\times 10^{-6} / {}^{0}C$)	Al_3Ti ($\times 10^{-6} / {}^{0}C$)
Coefficients of thermal expansion	9.5	13

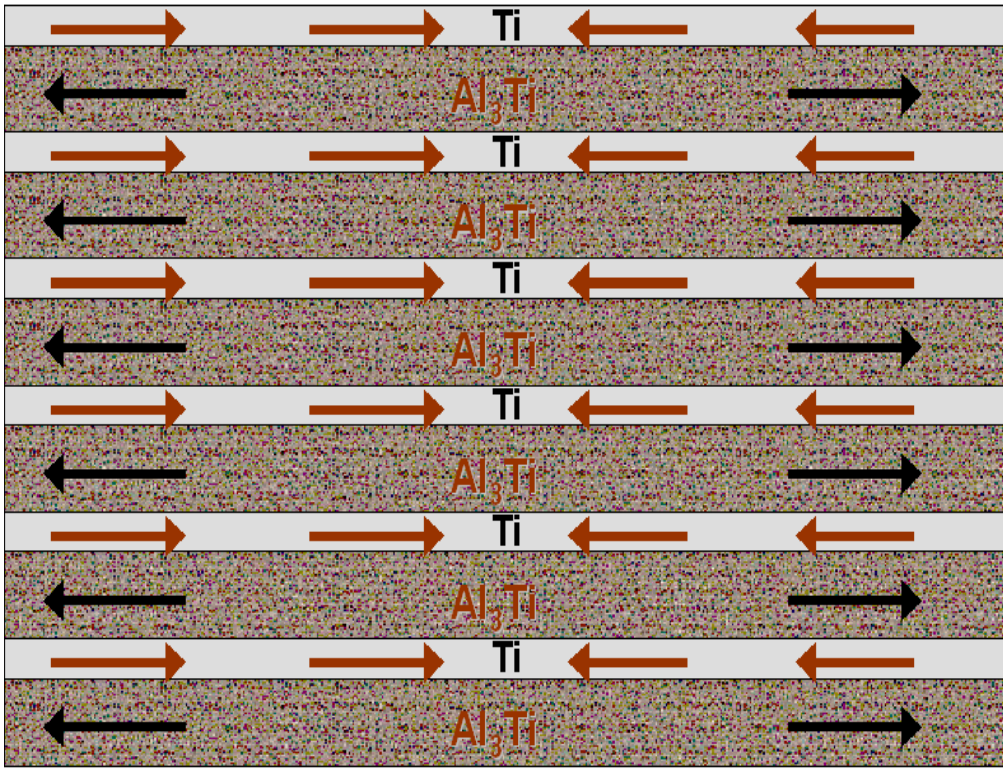

Figure 6-5 The schematics of residual stress distribution in Ti6Al4V-Al_3Ti MIL composites after cooling.

To analytically calculate residual stress in Ti6Al4V-Al_3Ti MIL composite, consider one layer of Ti6Al4V under compression and one layer of Al_3Ti under tension, in a Ti6Al4V-Al_3Ti MIL composite, shown in Figure 6-6.

By force equilibrium in x and y direction

$$\sigma_{Ti\_x} \cdot d_{Ti} \cdot W = \sigma_{Al_3Ti\_x} \cdot d_{Al_3Ti} \cdot W \tag{6.21}$$

$$\sigma_{Ti\_y} \cdot d_{Ti} \cdot W = \sigma_{Al_3Ti\_y} \cdot d_{Al_3Ti} \cdot W \tag{6.22}$$

and

$$\sigma_{Ti\_x} = \sigma_{Ti\_y} \tag{6.23}$$

$$\sigma_{Al_3Ti\_x} = \sigma_{Al_3Ti\_y} \tag{6.24}$$

where W is the width, σ_{Ti_x} is the stress in Ti6Al4V layer at x direction, d_{Ti} is the thickness of Ti6Al4V layer, $\sigma_{Al_3Ti\_x}$ is the stress in Al_3Ti layer at x direction, d_{Al_3Ti} is the thickness of Al_3Ti layer, σ_{Ti_y} is the stress in Ti6Al4V layer at y direction, $\sigma_{Al_3Ti\_y}$ is the stress in Al_3Ti layer at y direction.

The relation between stress and strain in x and y direction is

$$\varepsilon_x = \frac{1}{E} \cdot \left(\sigma_x - \upsilon \cdot \sigma_y \right) \tag{6.25}$$

$$\varepsilon_y = \frac{1}{E} \cdot \left(\sigma_y - \upsilon \cdot \sigma_x \right) \tag{6.26}$$

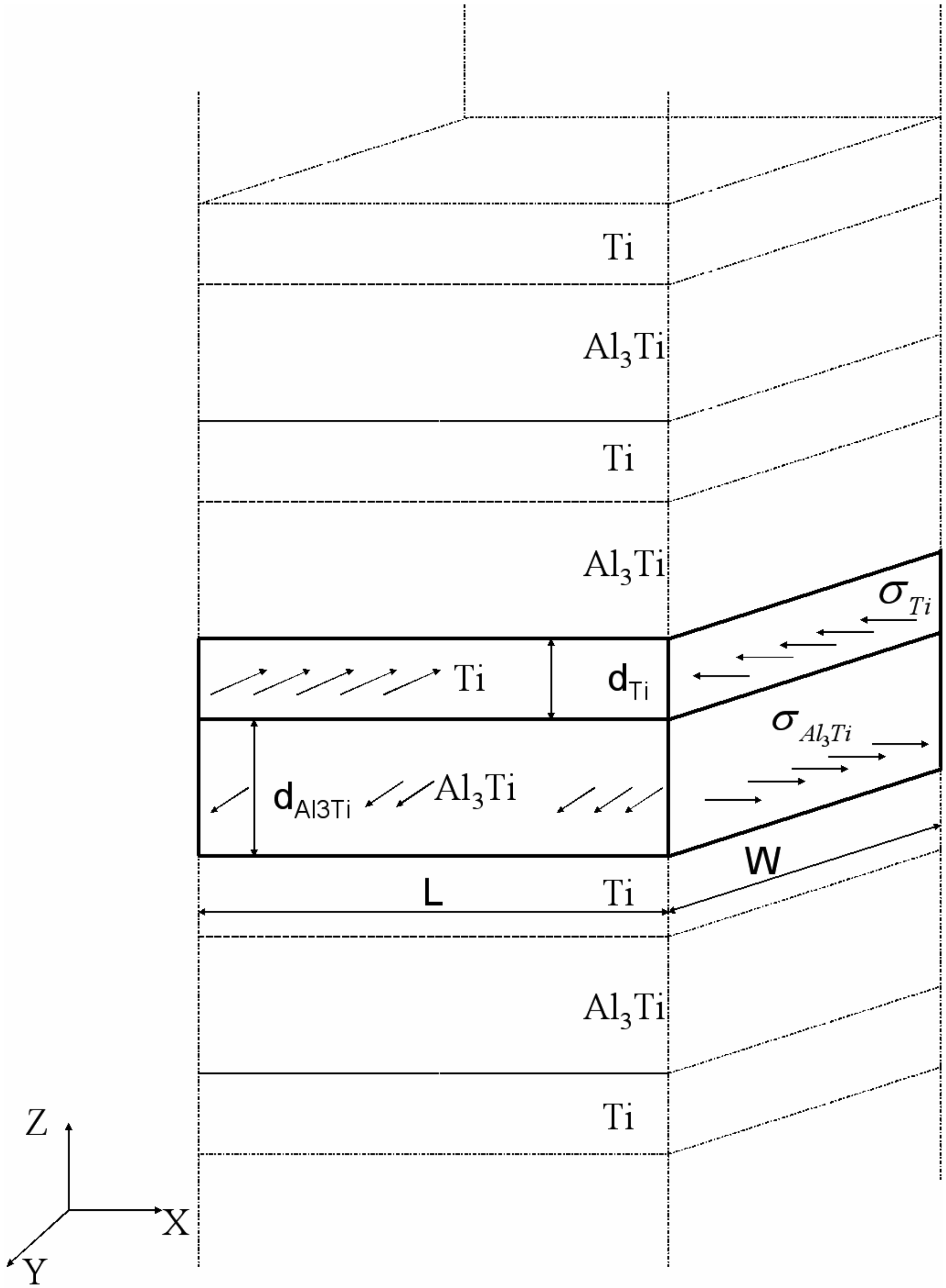

Figure 6-6 The schematics of residual stress in Ti6Al4V-Al_3Ti MIL composites.

By substituting equation (6.25) and equation (6.26) into equation (6.21) and equation (6.22), we obtain

$$\frac{E_{Ti} \cdot d_{Ti}}{1-\upsilon_{Ti}} \cdot \varepsilon_{Ti} = \frac{E_{Al_3Ti} \cdot d_{Al_3Ti}}{1-\upsilon_{Al_3Ti}} \cdot \varepsilon_{Al_3Ti} \tag{6.27}$$

The difference of strains between Ti6Al4V and Al_3Ti is caused by the mismatch of coefficients of thermal expansion, expressed as

$$\varepsilon_{Al_3Ti} - \varepsilon_{Ti} = \Omega \tag{6.28}$$

$$\varepsilon_{Al_3Ti} = \alpha_{Al_3Ti} \cdot \Delta T \tag{6.29}$$

$$\varepsilon_{Ti} = \alpha_{Ti} \cdot \Delta T \tag{6.30}$$

where Ω is the difference of strains and ΔT is the temperature drop.

Substitute the equations (6.28), (6.29) and (6.30) into equation (6.27), we obtain

$$\varepsilon_{Ti} = \frac{E_{Al_3Ti} \cdot d_{Al_3Ti} \cdot (1-\upsilon_{Ti}) \cdot \Omega}{E_{Ti} \cdot d_{Ti} \cdot (1-\upsilon_{Al_3Ti}) + E_{Al_3Ti} \cdot d_{Al_3Ti} \cdot (1-\upsilon_{Ti})} \tag{6.31}$$

$$\sigma_{Ti} = \frac{E_{Al_3Ti} \cdot E_{Ti} \cdot d_{Al_3Ti} \cdot \Omega}{E_{Ti} \cdot d_{Ti} \cdot (1-\upsilon_{Al_3Ti}) + E_{Al_3Ti} \cdot d_{Al_3Ti} \cdot (1-\upsilon_{Ti})} \tag{6.32}$$

The volume fraction of Ti6Al4V, c, is defined as

$$c = \frac{d_{Ti} \cdot W \cdot L}{d_{Ti} \cdot W \cdot L + d_{Al_3Ti} \cdot W \cdot L} = \frac{d_{Ti}}{d_{Ti} + d_{Al_3Ti}} \tag{6.33}$$

where L is the length.

Substitute equation (6.33) into equation (6.32)

$$\sigma_{Ti} = \frac{E_{Ti} \cdot (1-c) \cdot \Omega}{\left[1+(\zeta-1) \cdot c\right] \cdot (1-\upsilon_{Ti})} \tag{6.34}$$

where $\zeta = \frac{1-\upsilon_{Al_3Ti}}{1-\upsilon_{Ti}} \cdot \frac{E_{Ti}}{E_{Al_3Ti}}$

The residual stress in Ti6Al4V layers obtained above has been plotted with temperature for different volume fraction of Ti6Al4V and shown in Figure 6-7. It is shown how the residual stress increases as the temperature decreases.

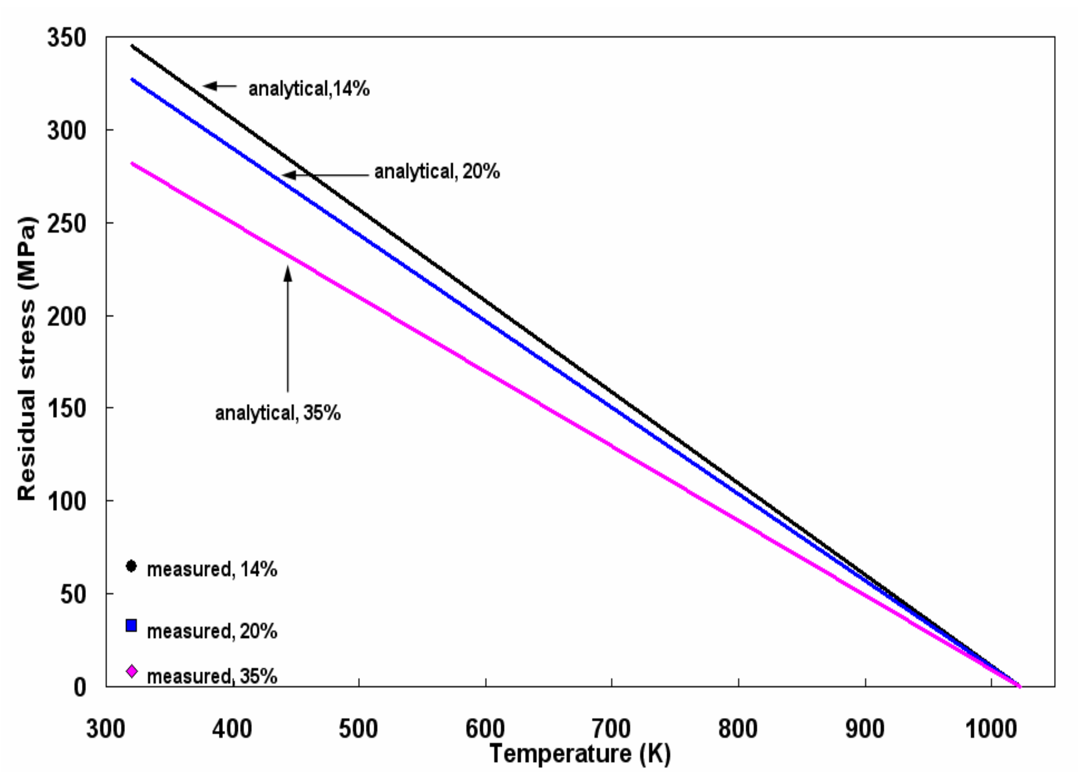

Figure 6-7 Calculated residual stress vs. temperature for different volume fraction of Ti6Al4V and compared with experimental measurements.

Residual stresses in Ti6Al4V-Al_3Ti MIL composites were measured by X-ray diffraction, and they are also plotted in Figure 6-7 and listed in Table 10 along with the calculated residual stresses for different volume fraction of Ti6Al4V. The measured residual stress in slow cooling refers to the slow cooling rate at the final stage of processing. It is seen that the residual stresses decrease with increasing volume fraction of Ti6Al4V and the calculated residual stresses are much higher than the measured ones.

Table 10 The comparison of calculated residual stress by various stress release mechanisms with experimental measurements.

Volume fraction of Ti6Al4V	14%	20%	35%
Calculated residual stress (MPa)	345	327	282
Calculated residual stress with creep in Ti6Al4V only (MPa)	280	260	208
Calculated residual stress with creep in both Ti6Al4V and Al_3Ti (MPa)	257	240	195
Calculated residual stress with creep and crack propagation in infinite size MIL composites (MPa)	86.15	69.33	46.63
Measured residual stress (MPa)	65.01	32.38	8.29

6.2.2 Residual stress release mechanism I: creep

As seen in Table 10, the residual stress at slow cooling rate is smaller than in the standard cooling rate, which implies that certain time dependent stress relaxation mechanism may be active in the cooling process.

Creep known as the anelastic or time-dependent deformation of a material is characterized by a slow flow of the material, which behaves as if it were viscous. If a mechanical component of a structure is subjected to a tensile load, the decrease in cross-sectional area, due to the increase in length resulting from creep, generates an increase in stress. When the stress reaches the ultimate tensile stress of the material, failure occurs. Figure 6-8 shows the characteristic creep curve; the ordinate shows the strain and the abscissa shows time. The creep curves are usually divided into three stages: I, primary or transient; II, secondary, constant rate, or quasi viscous; and III, tertiary. Stage II, in which the creep rate is constant, is the most important [160].

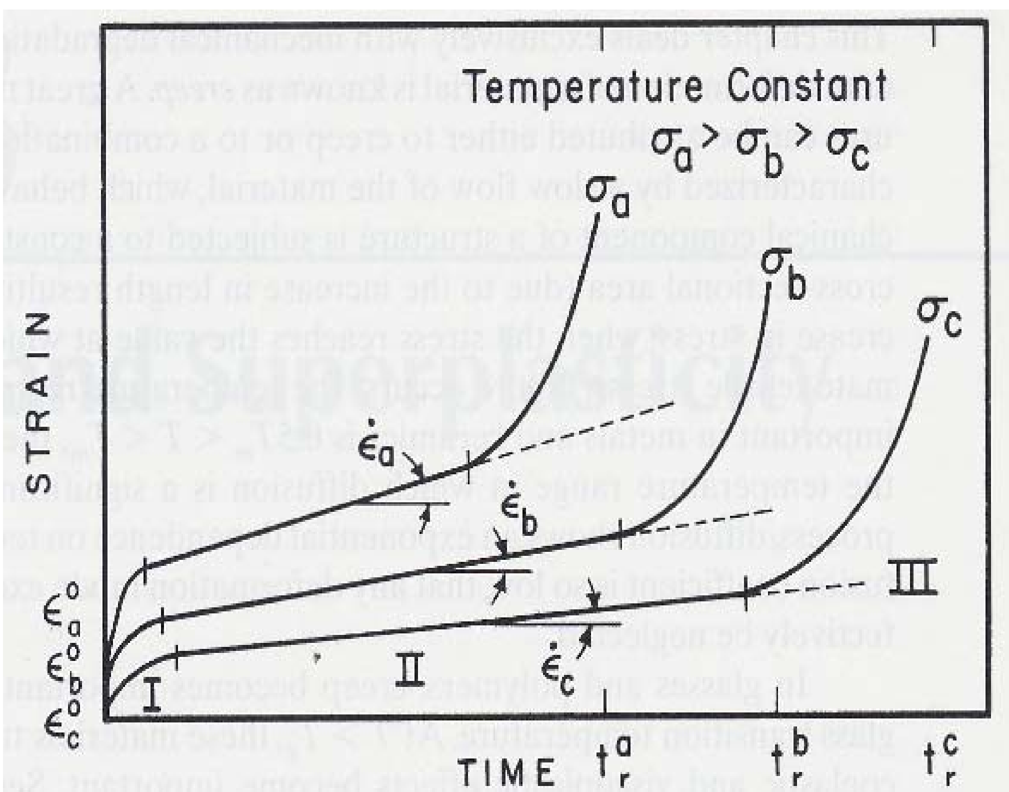

Figure 6-8 The characteristic creep curves(adapted from Meyers [160]).

The second stage, known as steady-state creep is represented by power-law equation.

$$\frac{\dot{\varepsilon}_s\, kT}{D\mu b} = A\left(\frac{\sigma}{\mu}\right)^n \tag{6.35}$$

where $\dot{\varepsilon}_s$ is the steady-state strain rate, μ the shear modulus, D the appropriate diffusivity coefficient, b the Burgers vector, T the temperature, k the Boltzmann's constant and σ the applied stress. A and n are constants.

The original standard cooling curve and the linearized standard cooling curve of MIL are shown in Figure 6-9.

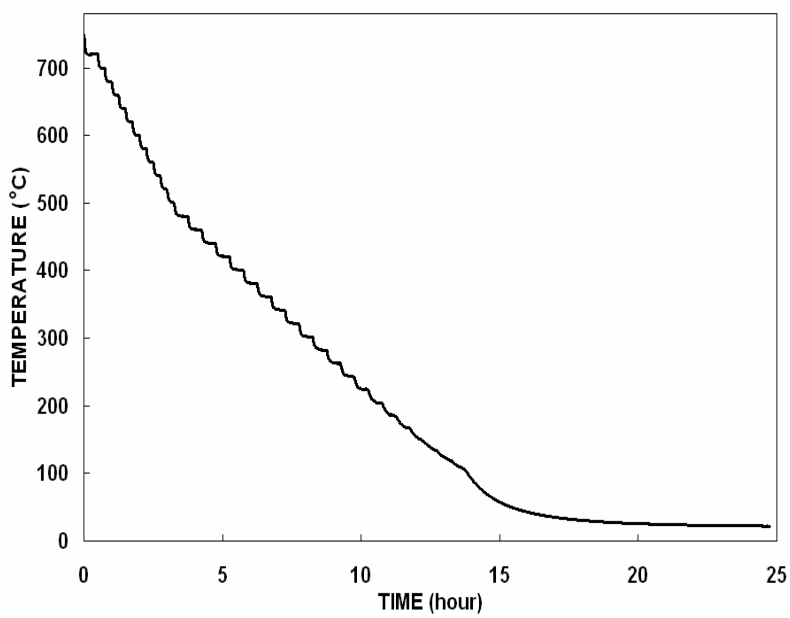

Figure 6-9 (a) Original experimental cooling curve

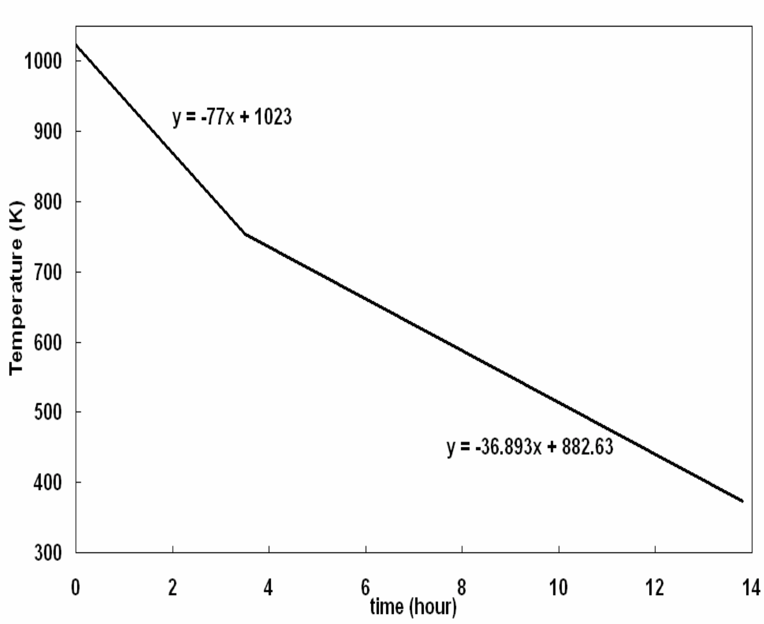

(b)

Figure 6-9 Experimental cooling curve of MIL. (a) Original experimental cooling curve; (b) linearized experimental cooling curve.

6.2.2.1 Creep in Ti6Al4V

To take consideration of creep in Ti6Al4V, Doner-Conrad equation can be rewritten as

$$\dot{\varepsilon}_s = A \cdot \left(\frac{\sigma}{\mu} \right)^n \cdot \frac{D\mu b}{kT} \tag{6.36}$$

$$\mu = 43.8GPa$$

$$b = 0.294nm$$

$$A = 3 \times 10^5$$

$$n = 4.55\,.$$

$$D = 1.0 \times \exp\left(\frac{-57800 \times 4.186\, J/mol}{T \cdot 8.314\, J/mol \cdot K}\right) \times 10^{-4}\, m^2/s$$

Temperature in the cooling curve was segmented into small temperature intervals with corresponding time intervals. A schematic drawing of such segmentation is shown in Figure 6-10.

At time t_1, the strain rate $\dot{\varepsilon}_{s\_1}$, is obtained by equation (6.36), where the initial residual stress in Ti6Al4V σ_{i1} is obtained by equation (6.34). The corresponding strain, ε_{s_1} is then given by

$$\varepsilon_{s\_1} = \dot{\varepsilon}_{s\_1} \cdot (t_1 - 0) \tag{6.37}$$

The change of stress due to the creep in Ti6Al4V is obtained by

$$\Delta\sigma_1 = E_{Ti} \cdot \varepsilon_{s\_1} \tag{6.38}$$

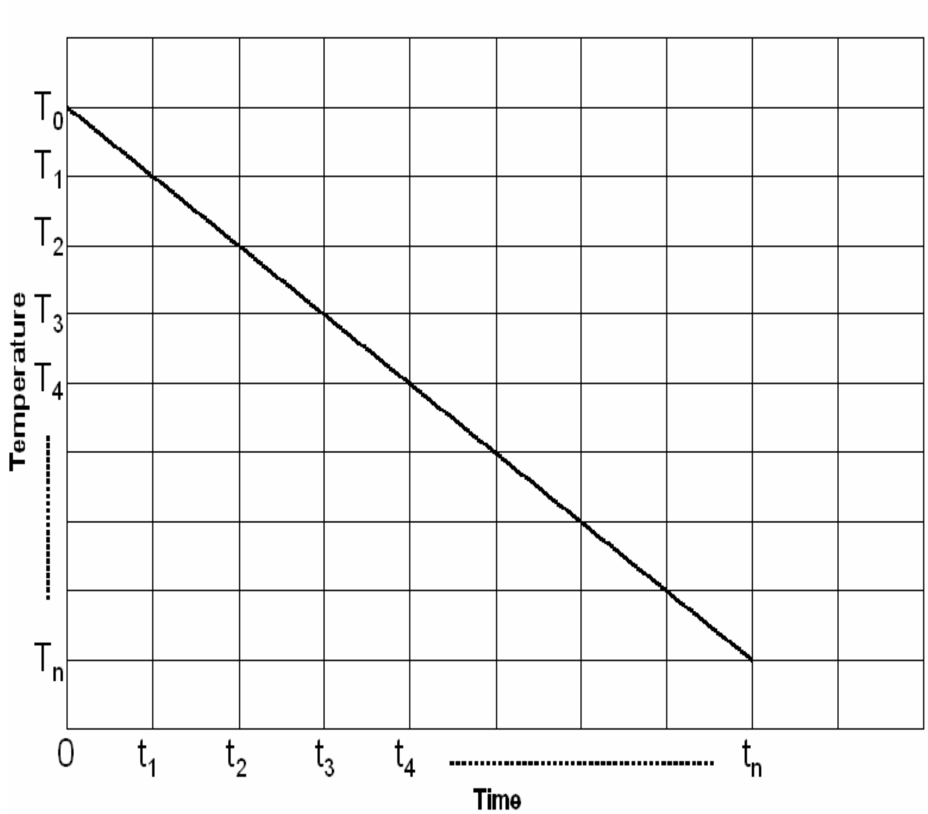

Figure 6-10 The schematic drawing of segment of time in cooling curve for Ti6Al4V-Al_3Ti MIL composites.

The residual stress after creep in Ti6Al4V at time t_1 is the reduction of the change of stress from the initial residual stress:

$$\sigma_{r\_1} = \sigma_1 - \Delta\sigma_1 \tag{6.39}$$

In the next time interval, from t_1 to t_2, the temperature decreases from T_1 to T_2 and the residual stress is built up again. The initial residual stress at t_2 is the sum of the residual stress at t_1 and newly-built-up residual stress $\Delta\sigma_{n\_2}$:

$$\sigma_{i\_2} = \sigma_{r\_1} + \Delta\sigma_{n\_2} \quad (6.40)$$

Substitute equation (6.40) into equation (6.36), strain rate $\dot{\varepsilon}_{s\_2}$ at t_2 can be obtained. The corresponding change of strain, ε_{s_2} is given by

$$\varepsilon_{s\_2} = \dot{\varepsilon}_{s\_2} \cdot (t_2 - t_1) \quad (6.41)$$

The change of stress due to the creep in Ti6Al4V is then obtained by

$$\Delta\sigma_2 = E_{Ti} \cdot \varepsilon_{s\_2} \quad (6.42)$$

The residual stress after creep in Ti6Al4V at t_2 is the reduction of the change of stress from the initial residual stress:

$$\sigma_{r\_2} = \sigma_{i\_2} - \Delta\sigma_2 \quad (6.43)$$

The calculation continues from t_3 to t_4, from t_4 to t_5, until from t_{n-1} to t_n. A series of σ_{r_i} can be obtained and plotted with the corresponding temperature. Figure 6-11 shows a flow chart summarizing the process described above.

Following the flow chart in Figure 6-11, a Matlab program has been developed to calculate the residual stresses (see Appendix A). Residual stresses with creep in Ti6Al4V and those without creep, along with the experimental measurements for different volume fraction of Ti6Al4V, are shown in Figure 6-12.

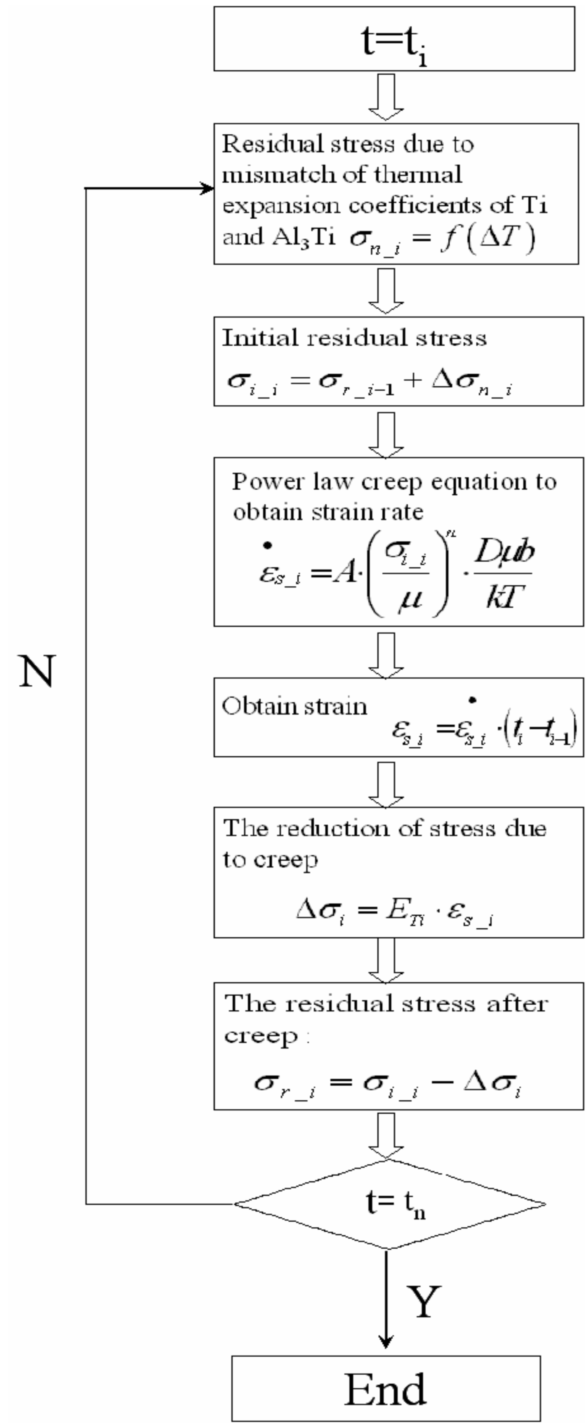

Figure 6-11 A flow chart representing the process used to calculate residual stress in MIL composite after creep.

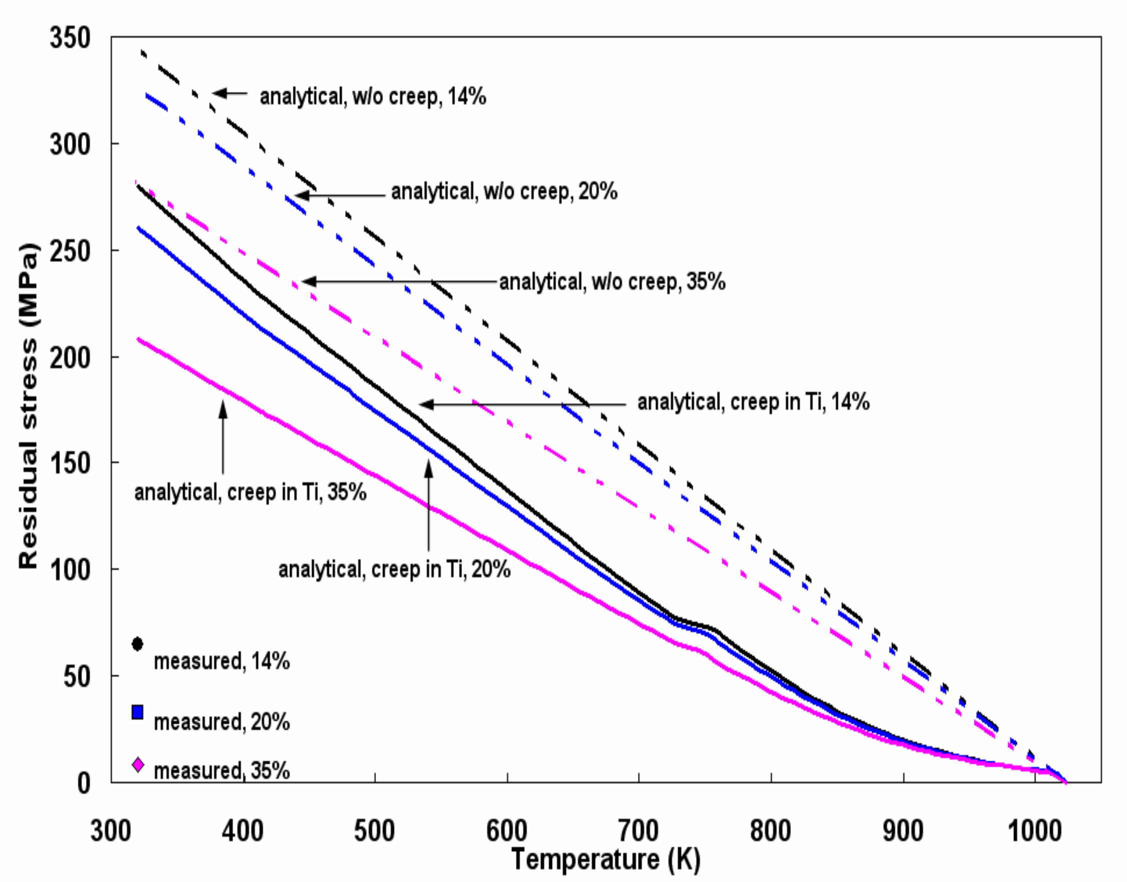

Figure 6-12 Residual stresses with creep in Ti6Al4V, those without creep, and the experimental measurements for different volume fraction of Ti6Al4V.

From Figure 6-12, it is seen that by creeping in Ti6Al4V, the residual stress has been reduced by 40% from 1035K to 780K. However, below 780K, the residual stresses due to the mismatch of thermal expansion coefficients of Ti6Al4V and Al_3Ti are built up and creep in Ti6Al4V is not an effective mechanism to release the residual stresses in Ti6Al4V-Al_3Ti MIL composites. Table 10 shows the residual stresses with creep in Ti6Al4V, those without creep, and the experimental measurements for different volume fraction of Ti6Al4V.

6.2.2.2 Creep in both Ti6Al4V and Al_3Ti

As shown in Table 10, with creeping in Ti6Al4V, the calculated residual stresses are still higher than the measured ones at different volume fraction of Ti6Al4V. Creep in Al_3Ti is also considered to contribute to the relaxation of residual stress in Ti6Al4V-Al_3Ti MIL composites.

Doner-Conrad equation was rewritten to apply for Al_3Ti, as

$$\dot{\varepsilon}_s = \frac{M}{T} \cdot \left(\frac{\sigma}{\mu}\right)^n \cdot \exp\left(-\frac{Q}{RT}\right) \tag{6.44}$$

$$M = 3.275 \times 10^{11} s^{-1}$$

$$\mu = 92.3 GPa$$

$$Q = 67596\, J/mol$$

$$n = 3\,.$$

$$R = 8.314\, J/mol \cdot K$$

The calculation for the effects of creep in Al_3Ti is similar as that in Ti6Al4V and by following the flow chart in Figure 6-11, and the results are shown in Figure 6-13, residual stresses without creep, those with creep in Ti6Al4V only, those with creep in both Ti6Al4V and Al_3Ti, and the experimental measurements for different volume fraction of Ti6Al4V.

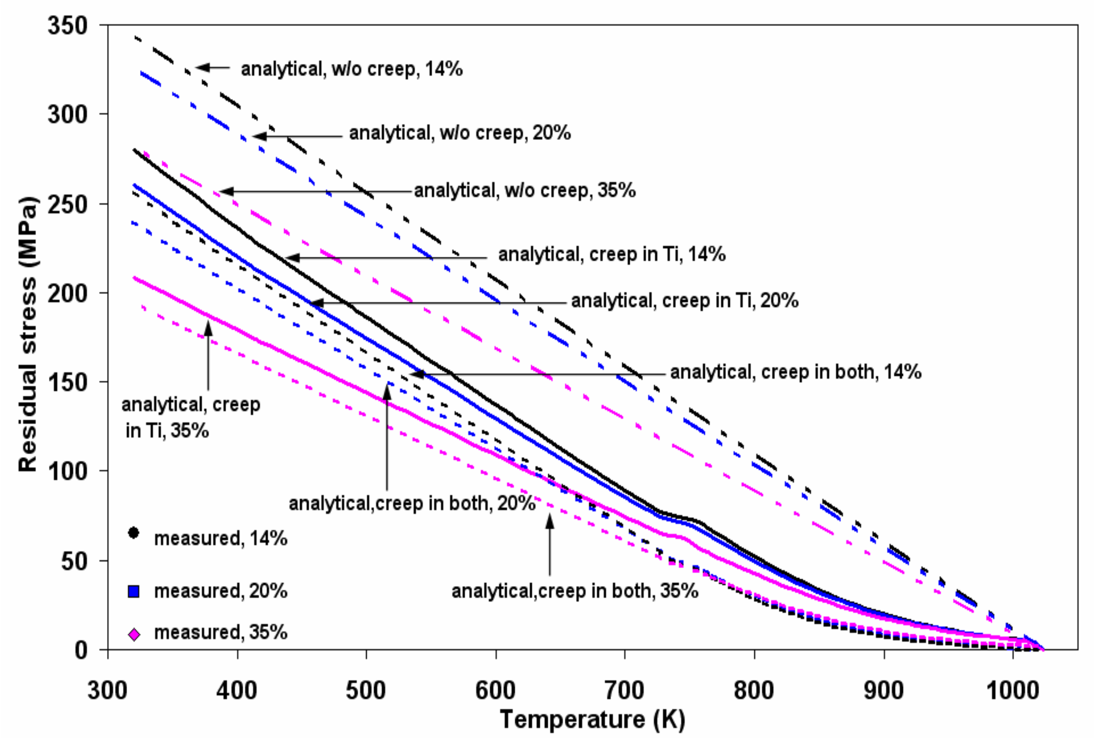

Figure 6-13 Residual stresses with creep in Ti6Al4V only, with creep in both Ti6Al4V and Al_3Ti, without creep, and the experimental measurements for different volume fraction of Ti6Al4V.

As seen from Figure 6-13, after considering creep in both Ti6Al4V and Al_3Ti, the residual stresses decrease even more. However, comparing with the experimental measurements, the calculated residual stresses are still higher at each and every volume fraction of Ti6Al4V. Table 10 compares the residual stresses without creep, those with creep in Ti6Al4V only, those with creep in both Ti6Al4V and Al_3Ti, and the experimental measurements for different volume fraction of Ti6Al4V.

6.2.3 Residual stress release mechanism II: crack propagation

As the residual stresses increase during the cooling process, the brittle Al_3Ti layer under increasing tensile stresses, and when the stresses reach the critical stresses, existing microcracks would begin to propagate in the Al_3Ti layer, which helps to release the residual stresses. Figure 6-14 shows the effect of microcracks on Young's modulus (adapted from Meyers [160]): with more and larger cracks, the Young's modulus decreases.

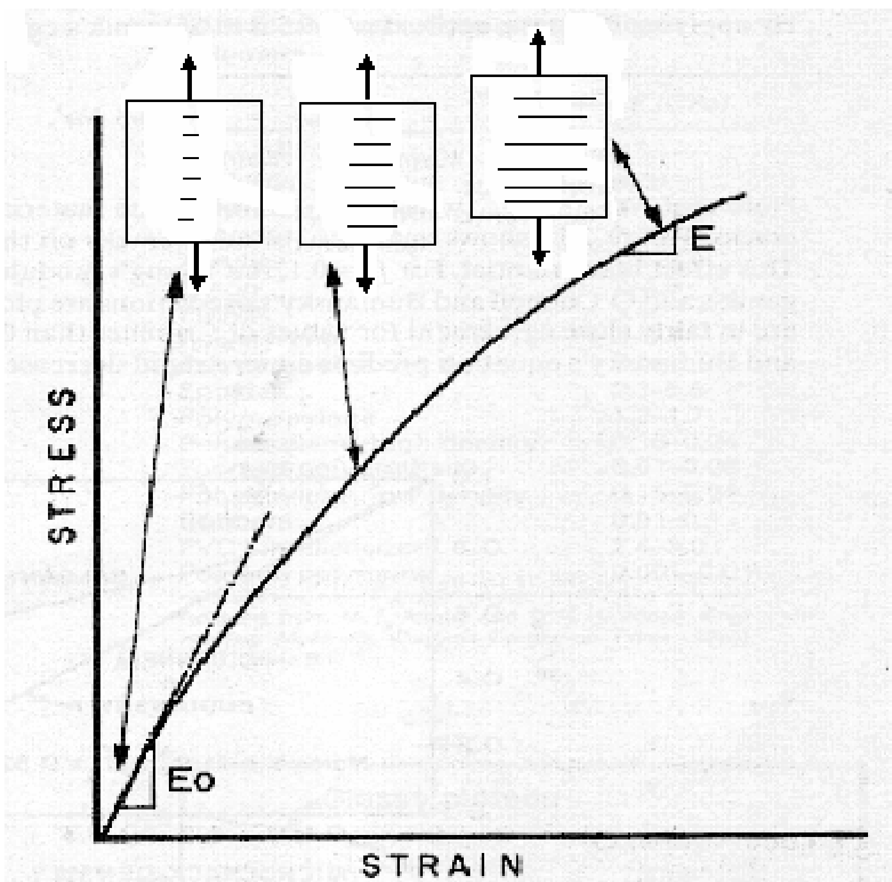

Figure 6-14 Effect of microcracks on Young's modulus (adapted from Meyers [160]).

6.2.3.1 Crack propagation: simple spring model

According to Griffith criterion, two things happen when a crack propagates: elastic strain energy is released in a volume of material, and two new crack surfaces are created which represent a surface-energy term. Thus an existing crack will propagate if the elastic strain energy released by doing so is greater than the surface energy created by the two new crack surfaces. Figure 6-15 shows the schematics when cracks are presence in Al_3Ti under tension. The crack size is assumed to be the thickness of the Al_3Ti layer and perpendicular to the interface.

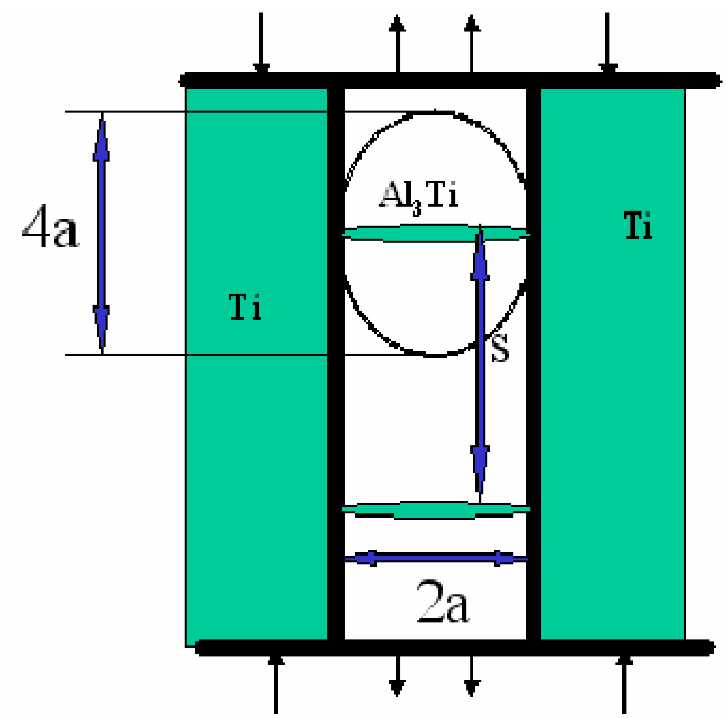

Figure 6-15 The schematics when cracks are presence in Al_3Ti under tension.

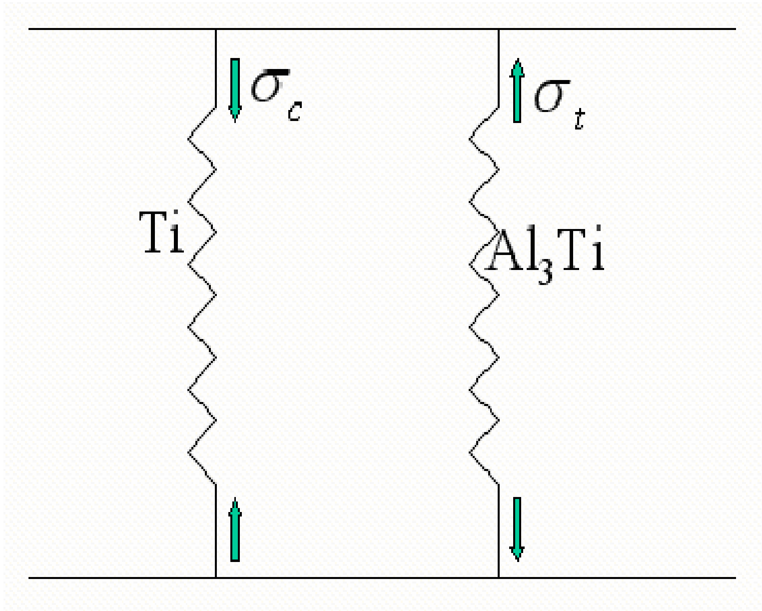

Figure 6-16 A spring system modeling for Ti6Al4V-Al_3Ti MIL composites.

The ellipse region denotes the approximate volume of material in which the stored elastic strain energy is released and the stress in that area decreases to zero. If thickness of Al_3Ti is $2a$, the longest axis of the ellipse will be $4a$ and the area over which elastic energy is released is $2\pi a^2$. Since Ti6Al4V is under compression and Al_3Ti is under tension during the cooling, Ti6Al4V-Al_3Ti MIL composites can be modeled as a spring system, shown in Figure 6-16.

Depending on the distance between two cracks, s, the effective Young's modulus of Al_3Ti, $E^e_{Al_3Ti}$, in the presence of the cracks, is as a function of the normalized distance $\frac{s}{a}$. When there is no crack in Al_3Ti, the normalized distance is infinite and the effective Young's modulus of Al_3Ti is the theoretical Young's modulus. When the distance between two cracks equals 4a, the relaxation areas of the neighboring cracks overlap and the normalized distance is 4. In that case, the Al_3Ti layer is not going to take any load and the effective Young's modulus of Al_3Ti becomes zero. This relation between the effective Young's modulus of Al_3Ti and the theoretical Young's modulus of Al_3Ti is expressed as

$$\frac{E^{e}_{Al_3Ti}}{E_{Al_3Ti}} = 1 - \frac{4}{\frac{s}{a}} \tag{6.45}$$

Substituting equation (6.45) into equation (6.34) , the residual stress in Ti6Al4V- Al_3Ti MIL composites can be obtained as

$$\sigma_c = \frac{E_1 \cdot (1-c) \cdot \Omega}{\frac{E_1}{E_2} \frac{c}{1-4\frac{a}{s}} \cdot (1-\upsilon_2) + (1-c) \cdot (1-\upsilon_1)} \tag{6.46}$$

The subscript 1 and 2 represent Ti6Al4V and Al_3Ti, respectively.

Figure 6-17 shows residual stresses as a function of the normalized distance, $\frac{s}{a}$, for different volume fraction of Ti6Al4V. The residual stress decreases as the normalized distance decreases. When the normalized distance becomes smaller, i.e. as the crack density becomes larger, the residual stress becomes smaller as more stress is released. When the normalized distance approaches 4, i.e. the distance between two cracks approach twice the thickness of Al_3Ti layer, the residual stress tends to be zero, because the relaxation areas of the neighboring cracks have overlapped and all stresses have been released.

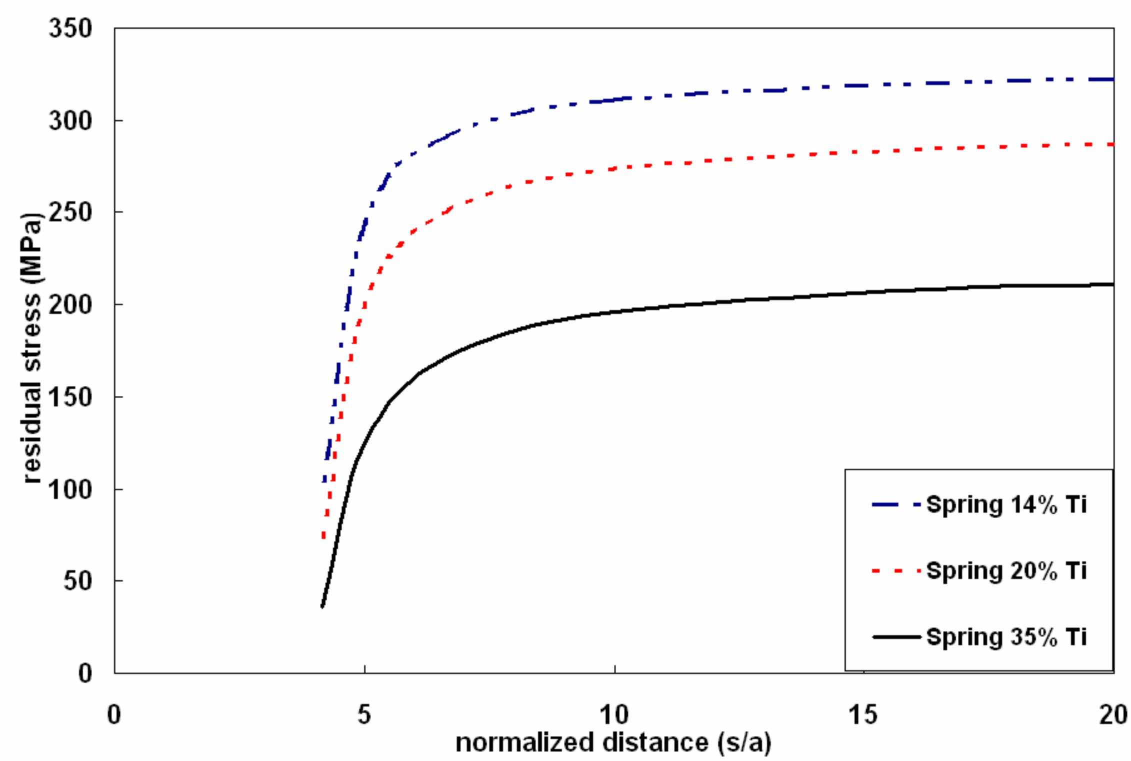

Figure 6-17 Residual stresses as a function of normalized distance for different volume fractions of Ti6Al4V (Spring model).

6.2.3.2 Crack propagation: Salganik model

Another suggestion by Salganik [161] predicted the effect of microcracks on Young's modulus as

$$E_2^e = \frac{E_2}{\left(1 + \dfrac{16 \cdot (10 - 3\upsilon_2) \cdot (1 - \upsilon_2^{\,2})}{45 \cdot (2 - \upsilon_2)} \cdot N\left(a, \dfrac{s}{a}\right) \cdot a^3\right)} \tag{6.47}$$

E_2^e is the effective Young's modulus of Al_3Ti, E_2 is the Young's modulus of the uncracked Al_3Ti, υ_2 is the Poisson's ratio of Al_3Ti, $N\left(a,\frac{s}{a}\right)$ is the number of cracks per unit volume, a is the radius of a mean crack, s is the distance between two cracks.

Figure 6-18 (a) shows a schematic of the single model used to estimate the effective Young's modulus of Al_3Ti. The crack is assumed to be perpendicular to the interface.

We can express the product of Na^3 in terms of $\frac{s}{a}$. Considering that each crack is a square ($2a \times 2a$) and the length of the crack is equal to the thickness of Al_3Ti layer. The volume between two cracks is $V = 4sa^2$. The number of cracks per unit volume is $N = \frac{1}{V} = \frac{1}{4sa^2}$. The product Na^3 is

$$Na^3 = \frac{a}{4s} = \frac{1}{4\frac{s}{a}} \tag{6.48}$$

By substituting equation (6.48) into equation (6.47), the degradation of Young's modulus of Al_3Ti by virtue of the existence of cracks can be established. E_2^e is obtained as a function of $\frac{s}{a}$, shown in Figure 6-18 (b).

Substituting equation (6.47) into the equation (6.34), residual stress can be predicted by Salganik model as

$$\sigma_c = \frac{E_1 \cdot (1-c) \cdot \Omega}{\frac{E_1 \cdot c}{E_2} \cdot (1-\upsilon_2) \cdot \left(1 + \frac{16 \cdot (10 - 3\upsilon_2) \cdot (1-\upsilon_2^{\,2})}{45 \cdot (2-\upsilon_2)} \cdot N\left(a, \frac{s}{a}\right) \cdot a^3\right) + (1-c) \cdot (1-\upsilon_1)} \tag{6.49}$$

Figure 6-19 shows the residual stress as a function of normalized distance by Salganik model for different volume fractions of Ti6Al4V. The residual stress decreases as the normalized distance decreases. When the normalized distance is smaller, i.e. the crack density in Al_3Ti is higher, the residual stress in Ti6Al4V-Al_3Ti MIL composite is lower as more stress is released.

Both models, Spring and Salganik models, predict that residual stress tends to be higher when the normalized distance is larger, i.e. when the crack density in Al_3Ti is lower, and the residual stress is lower when more cracks are present in Al_3Ti. However, the Spring model is more conservative than the Salganik model, as it predicts smaller residual stress than the Salganik model at every normalized distance.

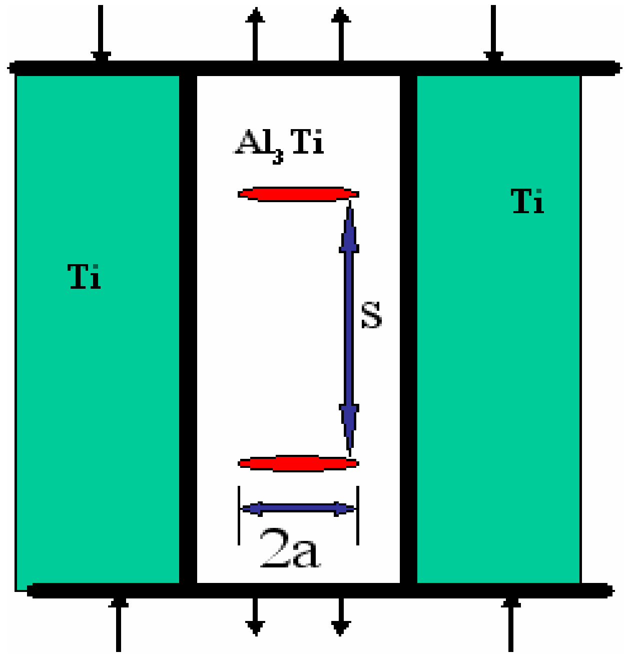

(a)

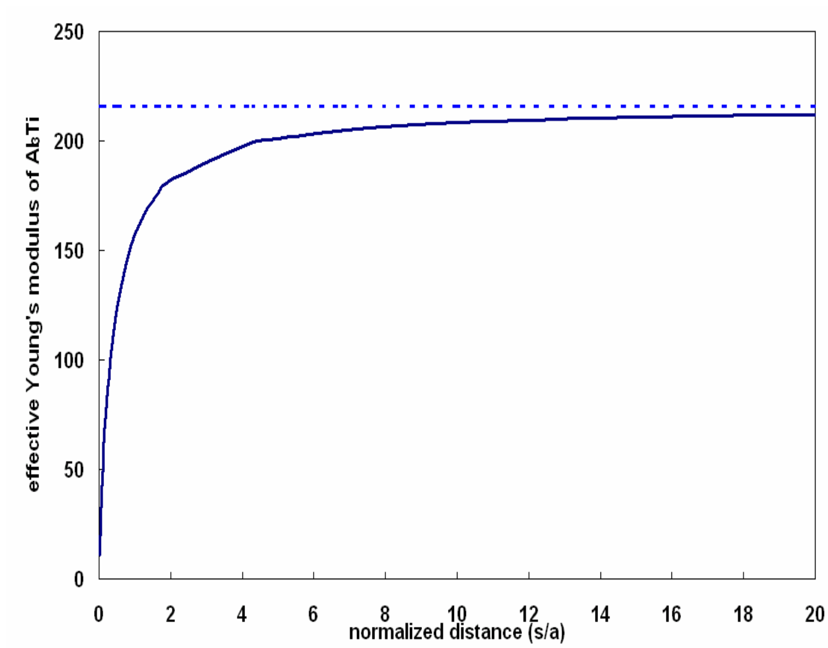

(b)

Figure 6-18 (a) A schematic drawing of Salganik model; (b) effective Young's modulus of Al_3Ti as a function of normalized distance.

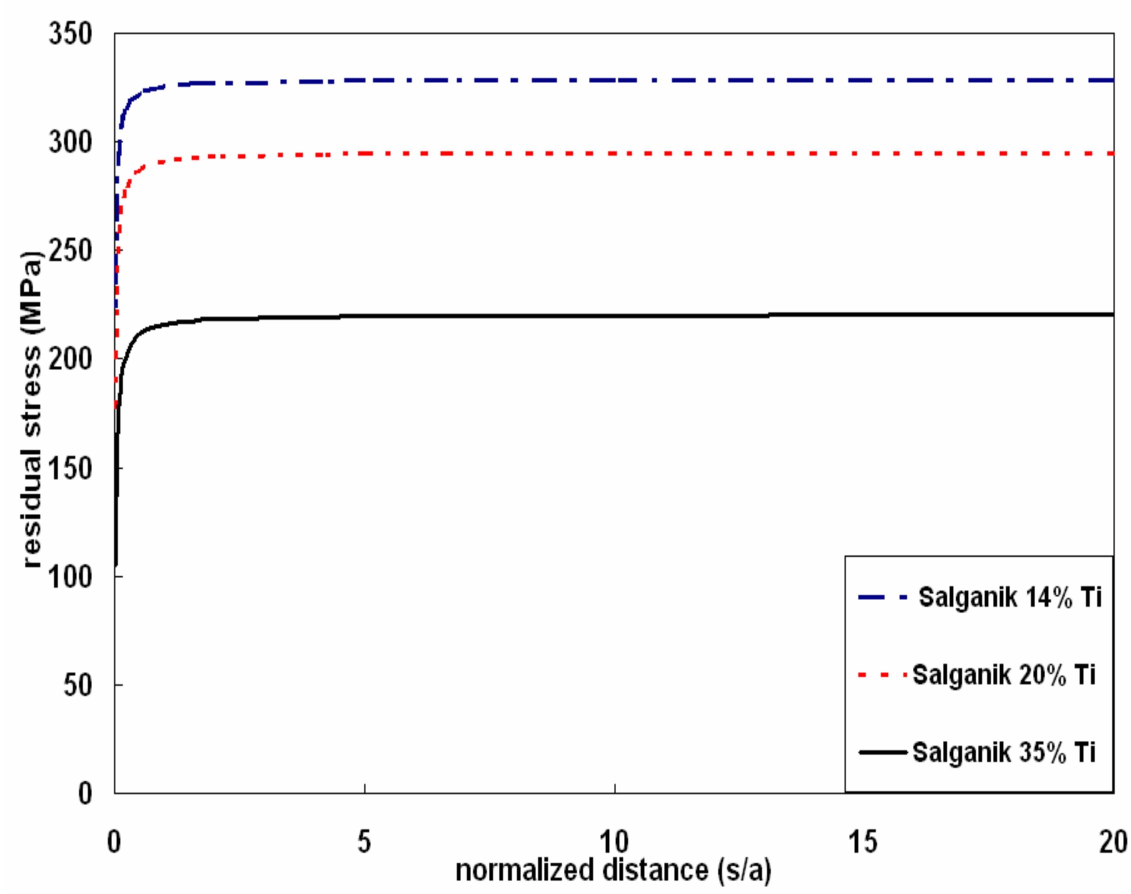

Figure 6-19 Residual stress as a function of normalized distance for different volume fractions of Ti6Al4V (Salganik model).

6.2.4 Combining creep and crack propagation mechanisms

As have been observed from the optical and SEM pictures, cracks have developed during the cooling process in MIL composites; therefore, combining the creep mechanism and crack propagation mechanism should help us understand how the residual stress evolutes during cooling.

As the residual stress increases during the cooling process, the Al_3Ti layer is under growing tensile stress. Due to the brittleness of intermetallics, existing cracks in Al_3Ti would start to propagate, when the residual stress exceeds the critical stress. The residual stress, σ_r, is a function of crack size, crack density and temperature.

$$\sigma_r = \sigma_r\left(a, \frac{s}{a}, T\right) \tag{6.50}$$

The critical stress, σ_c^*, is a function of the effective fracture toughness of Al_3Ti, which is the combination of the intrinsic fracture toughness of Al_3Ti and the extrinsic fracture toughness, determined by the residual stress in Al_3Ti layer, crack size and crack density (the effect of residual stress on fracture toughness is quantified and discussed in details in section 6.4).

$$K_{effective} = K_{ixtransic}\left(T\right) + K_{extransic}\left(a, \frac{s}{a}, \sigma_r\right) \tag{6.51}$$

$$\sigma_c^* = \frac{K_{effective}}{\sqrt{\pi a}} \tag{6.52}$$

As the existing cracks start to propagate, the residual stress is released, which negatively affects the effective toughness and thus decreases the critical stress. The cracks will continue to grow until the released residual stress is smaller than the decreased critical stress. As the temperature decreases, the residual stress will continue to increase and when it is larger than the decreased critical stress, the cracks begin to grow again. This process will continue as the temperature decrease to room temperature or when the crack size reaches the length of the Al_3Ti layer. The process is summarized in a flow chart (Figure 6-20).

Assuming the initial crack size is a quarter of the thickness of Al_3Ti layer and the Ti6Al4V-Al_3Ti MIL composites are infinitely long. In addition, the initial intrinsic fracture toughness of Al_3Ti at 1023K is assumed to be 0.5 $MPa\sqrt{m}$ and the final intrinsic fracture toughness at room temperature is 1.5 $MPa\sqrt{m}$.

A Matlab code (see Appendix) is developed to carry out the calculation and the residual stress evolution, the comparison of the critical stress and residual stress evolution in Al3Ti and the crack propagation are shown in Figure 6-21, Figure 6-22, and Figure 6-23.

It is observed, in Figure 6-23, that the crack remains "sleeping" at high temperature, when the critical stress is sufficiently higher than the residual stress (see Figure 6-22). The maximization of the critical stress (see Figure 6-22), reflects the competing effect of increasing intrinsic fracture toughness and increasing residual stress due to the decreasing temperature on the fracture toughness. The decreasing critical stress in the lower temperature reflects the dominating effect of the residual stress on the effective fracture toughness, despite an increasing intrinsic fracture toughness of Al_3Ti. As the residual stress eventually exceeds the critical stress, crack starts to propagate, and the mechanism described above takes into place. Both residual stress and critical stress decreases due to the crack growth, however to different magnitude. The crack continues to grow whenever the residual stress exceeds the critical stress, and stops growing when it does not, until the temperature drops to room temperature or the crack size reaches the thickness of the Al_3Ti layer.

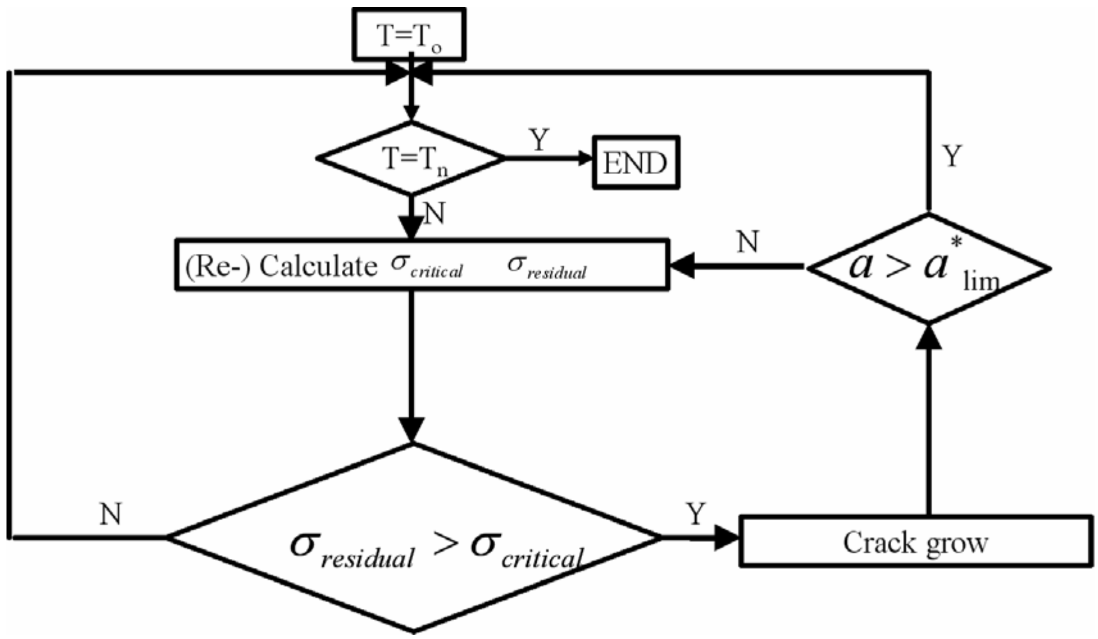

Figure 6-20 A flow chart of calculating residual stress combining the creep and crack propagation mechanisms.

From Figure 6-21, it is seen that the residual stresses in different concentration of Ti6Al4V have all increased steadily before the critical stresses in Al_3Ti are exceeded, during which time, the creep in Ti6Al4V and Al_3Ti is the dominate mechanism in releasing the residual stresses. After that, the crack growth dominates the residual stress release process, as demonstrated by the steady decrease in residual stress in Ti6Al4V. The sharpest decrease in residual stress is observed in 14% MIL, followed by 20% and 35% MIL. This attributes to the higher residual stress level and larger initial crack size in 14% MIL composites, and it implies that the effective fracture toughness in 14% MIL is more negatively affected by the crack growth, as does the corresponding critical stress, which is verified in Figure 6-22.

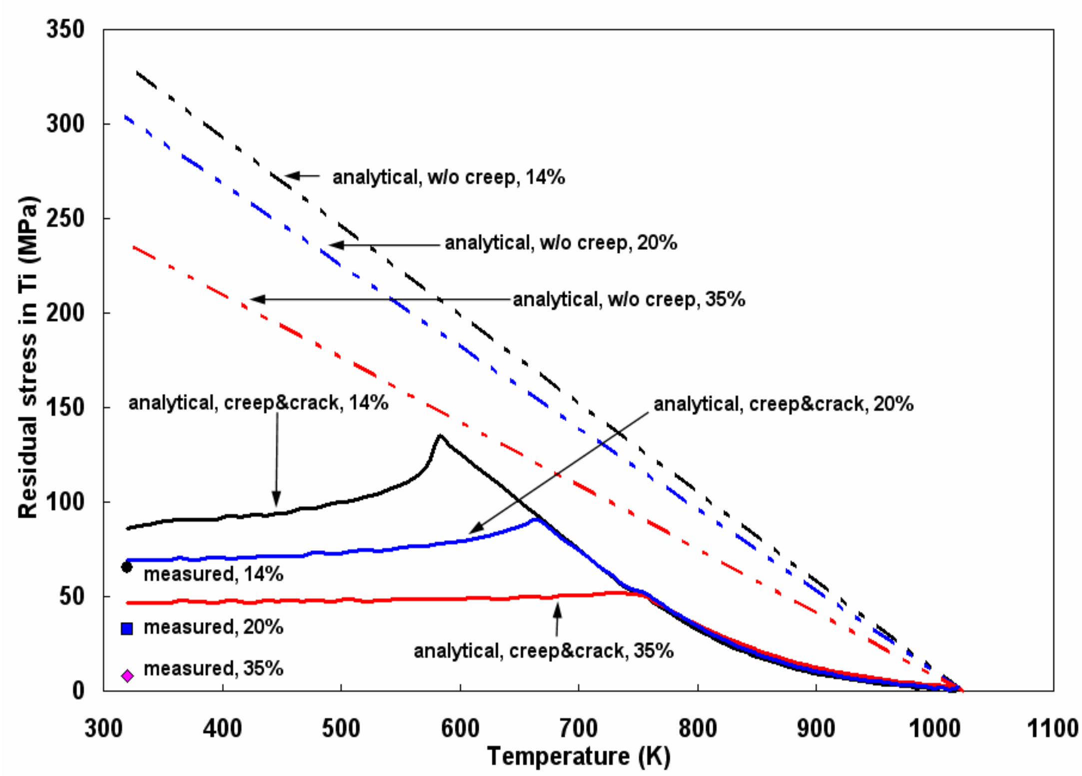

Figure 6-21 The residual stress in infinite dimensional Ti6Al4V-Al_3Ti MIL composites with creep and crack propagation mechanisms.

Shown in Figure 6-22 is the evolution of critical stress and residual stress in Al_3Ti during cooling. As the residual stress increases in Ti6Al4V, the corresponding residual stress in Al_3Ti also increases, and its negative effect on the apparent fracture toughness of Al_3Ti is demonstrated by the decreasing critical stress in Al_3Ti that resists the crack growth. When the critical stress is exceeded by the residual stress in Al_3Ti, those two stresses compete with each other to determine whether the crack would further grow, and the results were recorded by the Matlab code (Appendix A).

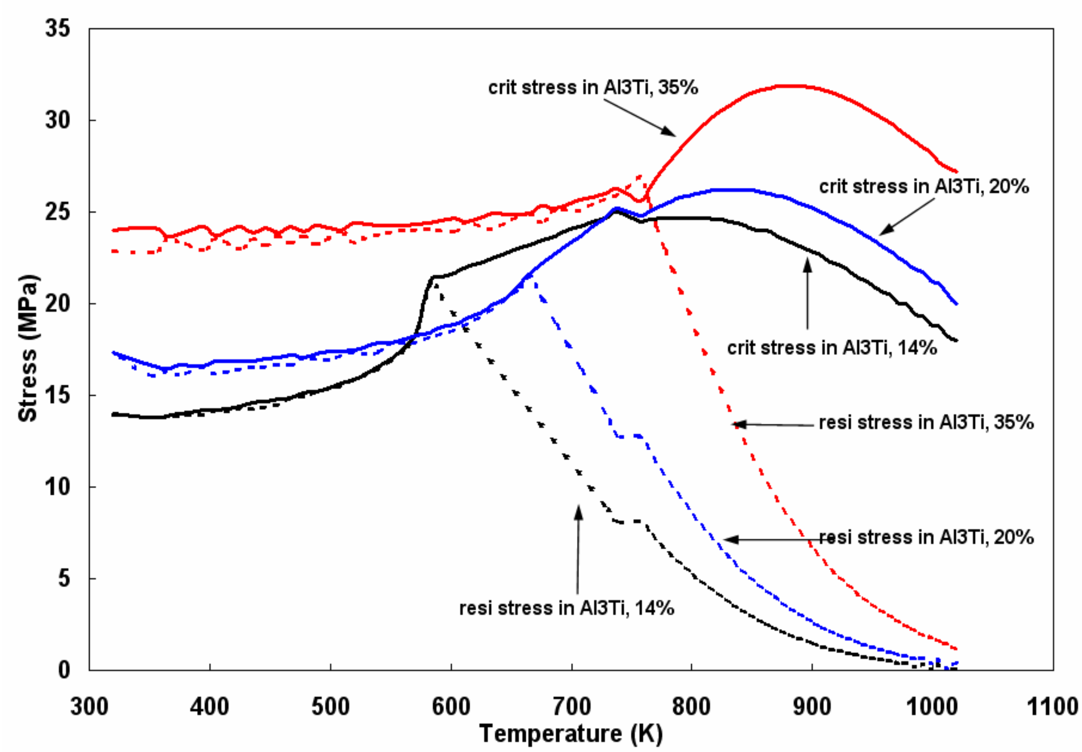

Figure 6-22 The evolution of critical stress and residual stress in Al_3Ti.

Figure 6-23 shows the evolution of crack size in the MIL composites during cooling. The steeper slope of crack length evolution in the 14% MIL suggests that lower residual stress in Al_3Ti erodes the apparent fracture toughness slower, which enables Al_3Ti to resist crack growth for a longer period of time. The crack length is eventually constrained by the size of the Al_3Ti layers, and the crack stops growing at the interface, verified by the experiments and demonstrated by the plateau close to room temperature in Figure 6-23.

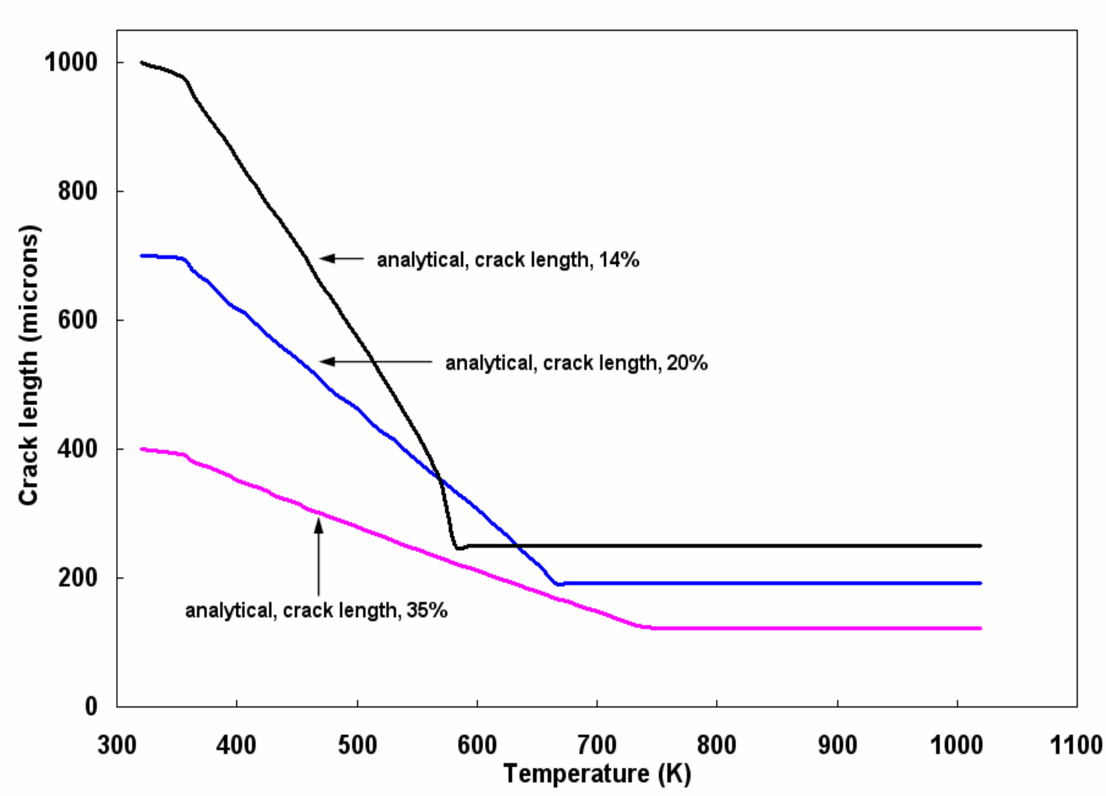

Figure 6-23 The evolution of crack growth in 14%, 20% and 35% MIL composites during cooling.

6.3 Finite element simulation of residual stress in Ti6Al4V-Al_3Ti MIL composites

Analytical modeling of residual stress evolution discussed in section 6.2 assumes an infinite length of Ti6Al4V and intermetallic layers, and the results reflect the average stress level in Ti6Al4V. In reality, the MIL composites have finite size and the distribution of residual stress in Ti6Al4V is uneven. Since the residual stress measurement was an average value, and was conducted only on small samples, it is very likely that the local residual stress level in that tested specimen does not reflect the real residual stress in the larger MIL piece. Finite element simulation thus provides a means to include the boundary conditions to obtain more realistic residual stress, and more importantly, its distribution.

Commercially finite element software, ABAQUS, was used to conduct the residual stress simulation during the cooling in 3D formulation. Because of the symmetry, only one eighth of the specimen was simulated. Section 6.3.1 shows the results of the FE simulation of residual stress with creep and cracking, and section 6.3.2 shows the FE simulation of residual stress with creep and crack propagation.

6.3.1 FE simulation of residual stress with creep and cracking

A 3-D 17 layer body, was created to model the real MIL sample, and three faces of the sample were confined in x, y and z global directions as implied by the symmetric boundary conditions. Initial conditions include an initial temperature of 1023K, and the predefined field simulates the real cooling curve (see Figure 6-9 (b)). Creep in both Ti6Al4V and Al_3Ti was considered. The meshed model is shown in Figure 6-24.

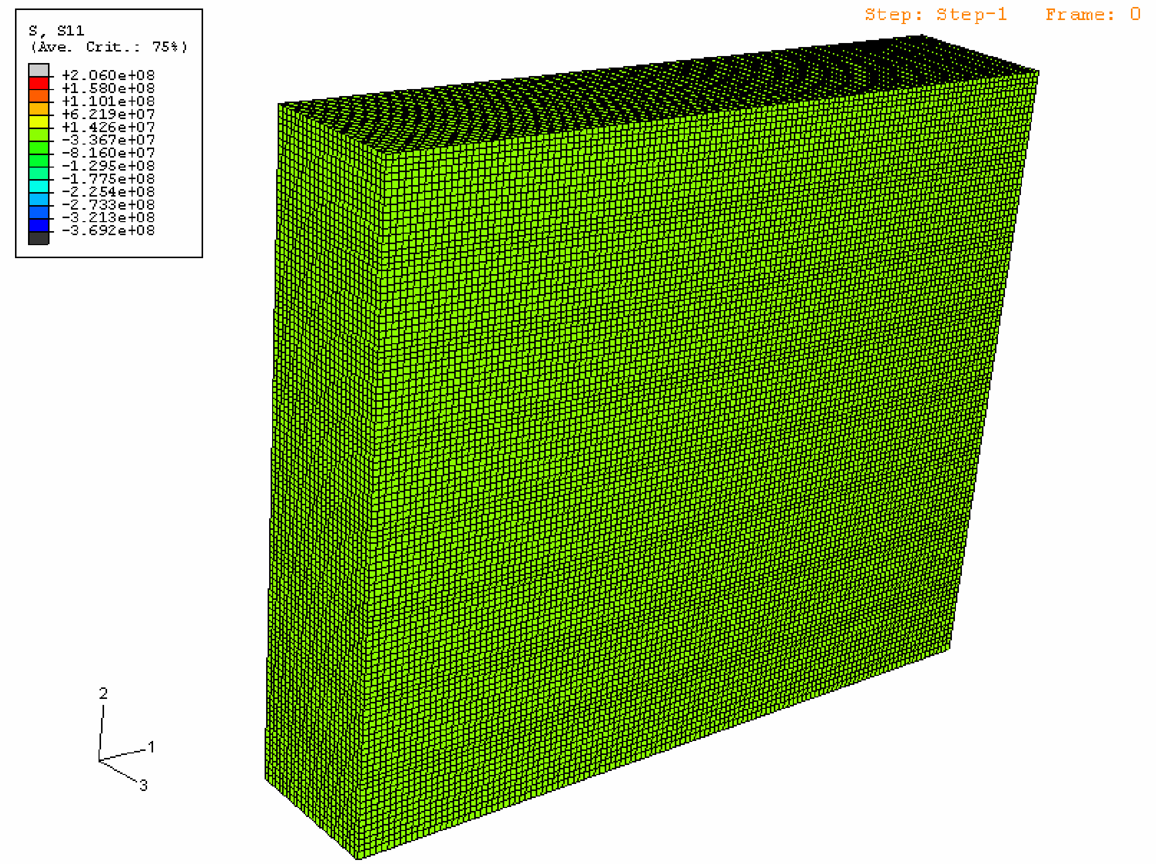

Figure 6-24 FE models for MIL composites at the initial stage.

8 node brick element is used in the simulation, and the results with creep in both Ti6Al4V and Al_3Ti are shown in Figure 6-25, at different stages. The development of residual stress was clearly observed, with compressive stress in Ti6Al4V and tensile stress in Al_3Ti. The stress increases in magnitude as temperature decreases, and the stress concentrates more on the confined side, which correspond to the specimen's center and is constrained by symmetry. While there is variation in stress magnitude towards boundary and interfaces, most Ti6Al4V layers experience relative constant stress levels. Residual stress in Ti6Al4V was calculated by averaging the stresses in

different Ti6Al4V layers, and the results are shown and compared with the analytical solutions in Figure 6-26. Comparing with the analytical solution, the FE results predict a similar trend in the residual stress evolution. However, in FE simulation, creep is effective for a longer period of time during cooling, and as a result, a smaller stress than that in the analytical modeling in Ti6Al4V layers is observed.

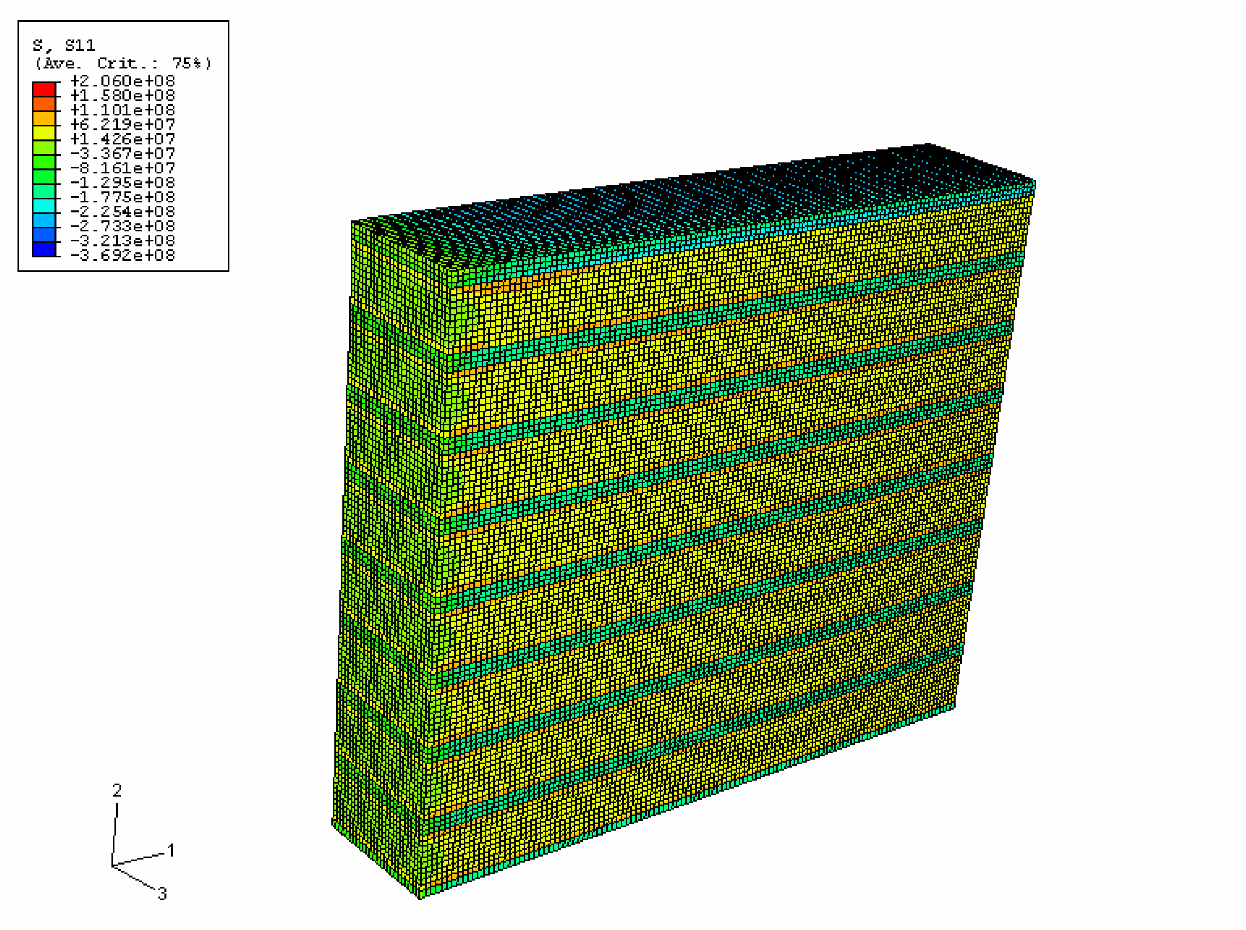

Figure 6-25 (a) T=753.5K

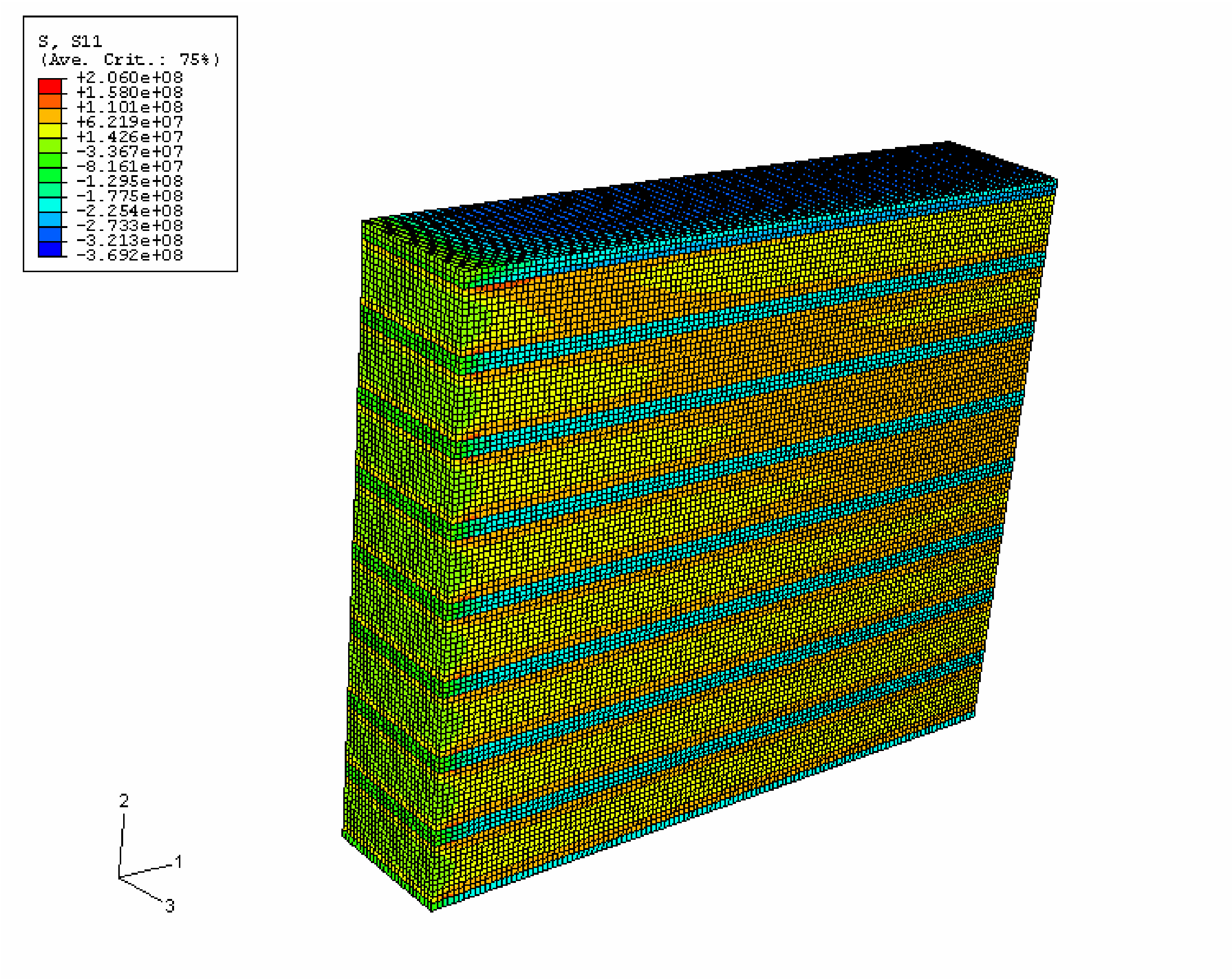

Figure 6-25 (b) T=503.7K

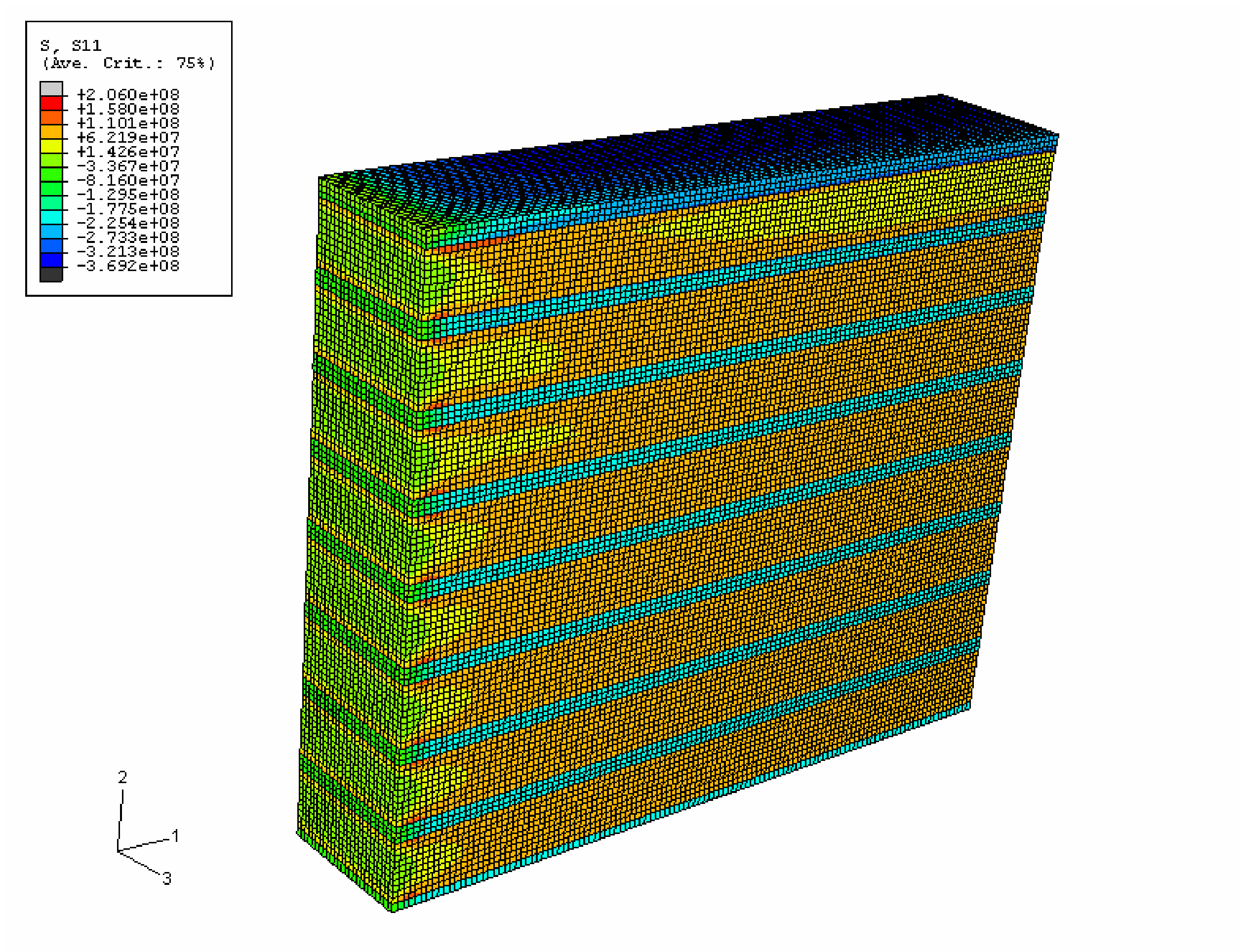

(c) T=320K

Figure 6-25 Magnitude and distribution of residual stress during cooling.

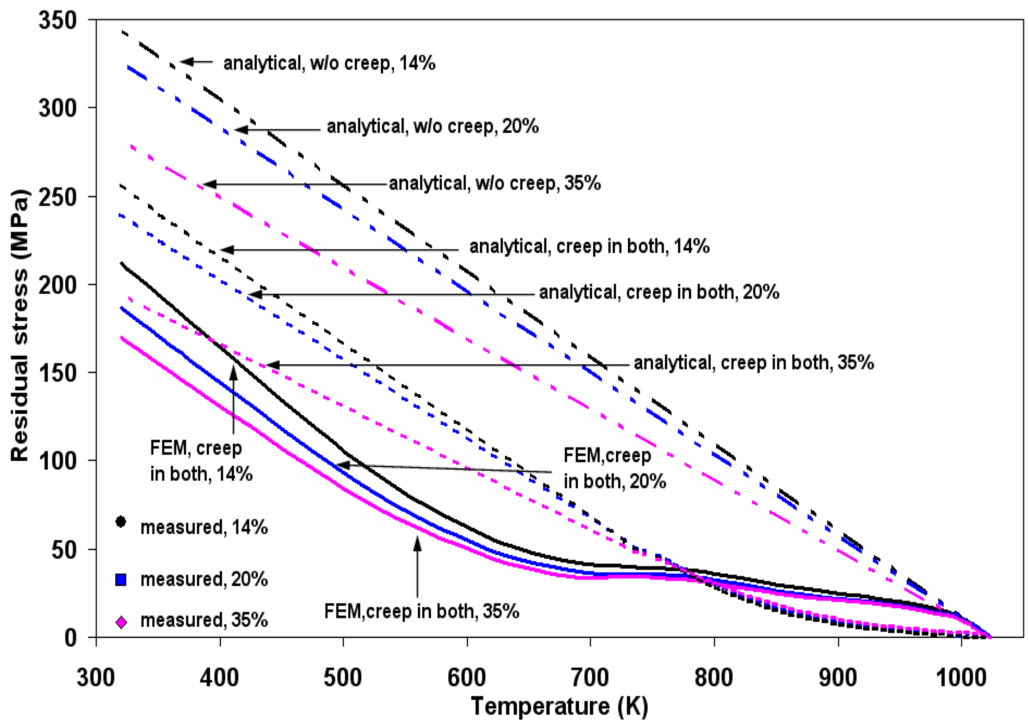

Figure 6-26 FE results of residual stress during cooling, in comparison with analytical modeling.

Cracking as another mechanism discussed in section 6.2.3 was also introduced in the simulation. Only perpendicular cracks were used in the simulation, as they are the main crack morphology observed under microscopes. Data from experiments, such as the sizing and crack locations as observed in Figure 5-2, Figure 5-3 and Figure 5-4, were reproduced in the same fashion to simulate the real cooling process. The crack was simulated by introducing far smaller material properties in comparison with Ti6Al4V and Al_3Ti, to bypass the difficulty rising from numerical calculation, meshing and distortion. The properties of the individual component were also adjusted with the existence of cracks according to Salganik model. The simulation results are shown in Figure 6-27, at different stages.

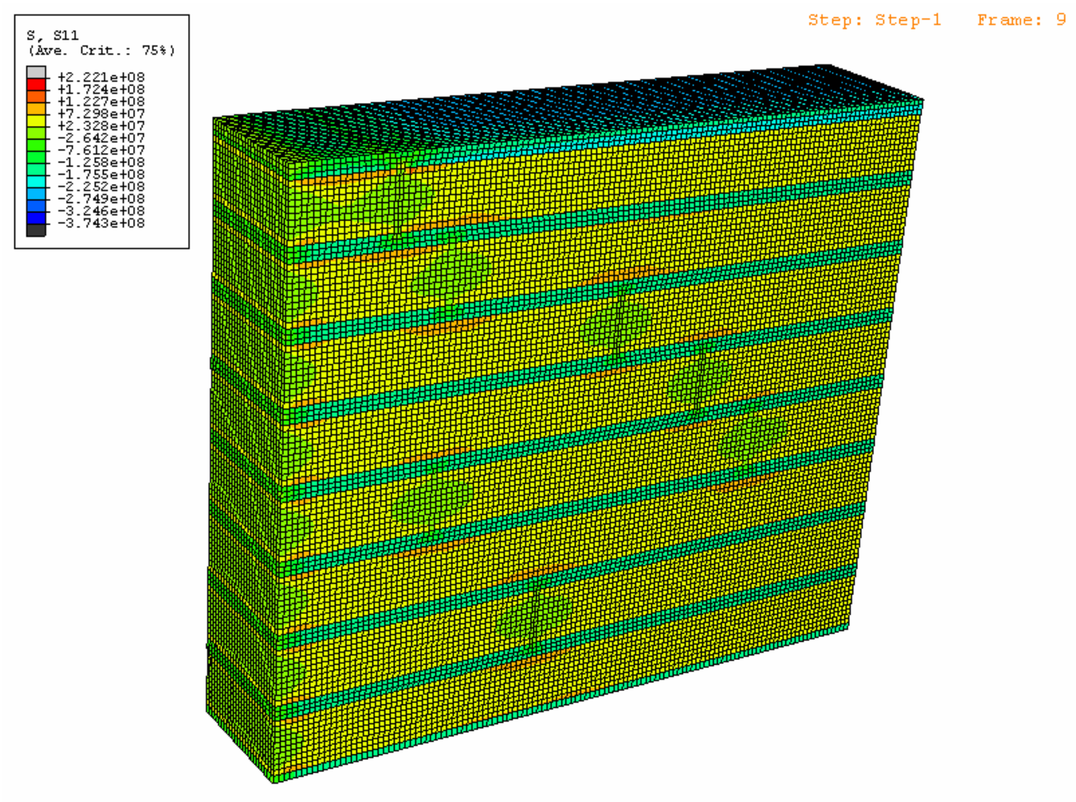

Figure 6-27 (a) T=753.5K

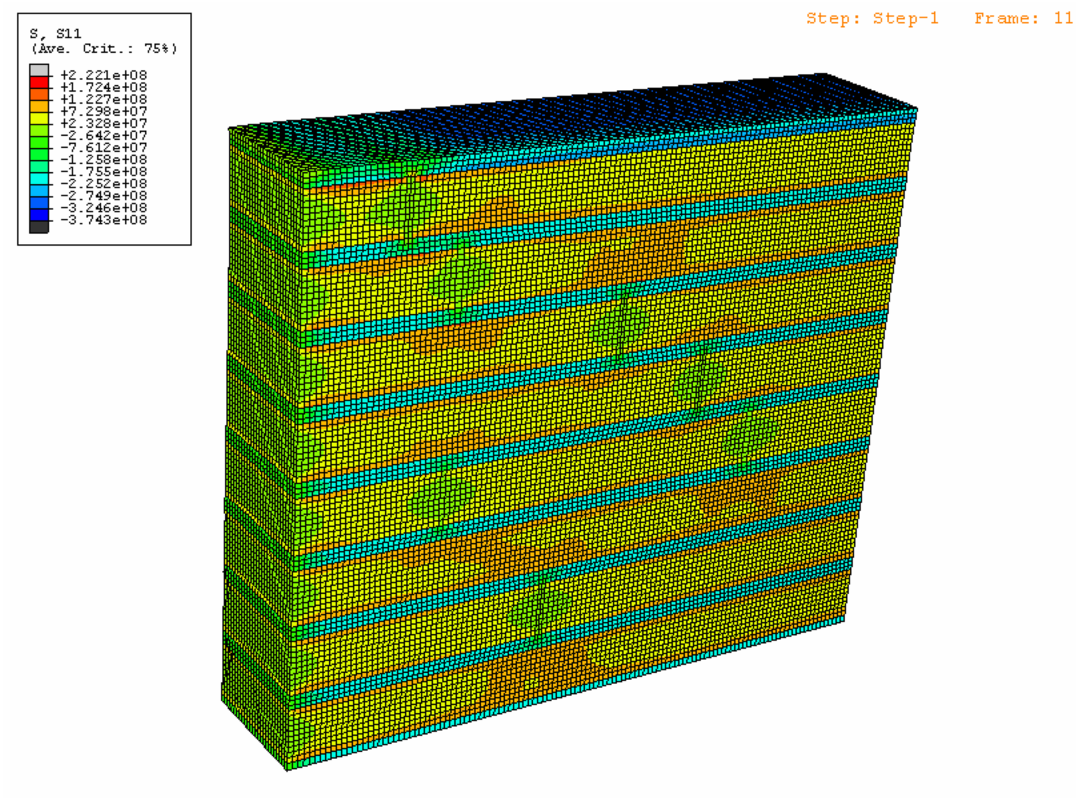

Figure 6-27 (b) T=503.7K

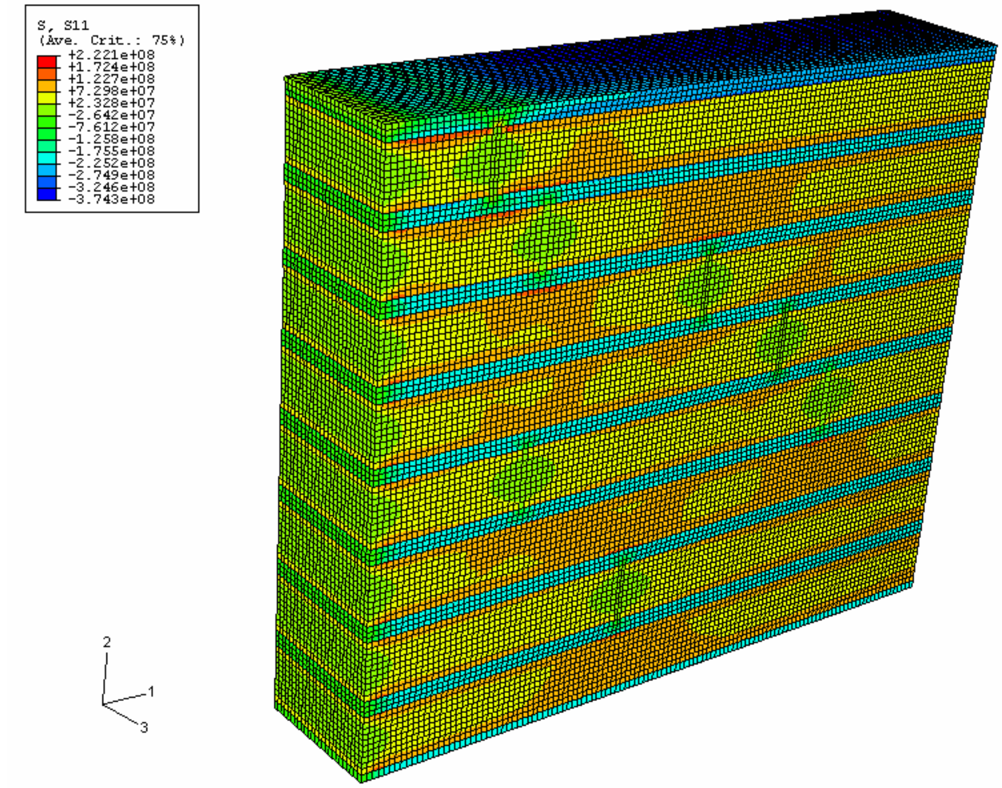

(c) T=320K

Figure 6-27 Magnitude and distribution of residual stress during cooling, with presence of cracking.

Comparing with Figure 6-25, the simulation results with the presence of cracks show a dramatic decrease in the stress levels around cracks, in both Ti6Al4V and Al_3Ti layers. It is also observed that from the start of cooling, there exists an elliptical area of stress relaxation in Al_3Ti, which by and large confirms the Spring model used in section 6.2.3.1. Since there is not enough stress concentration in the nearby areas to initiate additional cracks, the existence of this stress relaxation area also explains why the cracking spacing between cracks observed in the specimens is usually more than 10 times larger than the thickness of the same Al_3Ti layer. This relaxation area even extends into the neighboring Ti6Al4V layers and thus attributes to the release of stress levels in Ti6Al4V. However, such areas in both Ti6Al4V and Al_3Ti do render other areas with greater stress concentration, noticeably in the neighboring Al_3Ti layers, as observed in Figure 6-27 (a). This stress concentration at the early stage of cooling is detrimental, as it would potentially initiate a new cracking site or develop "sleeping" microcracks in those areas, especially when those areas contain defects, like voids or impurity.

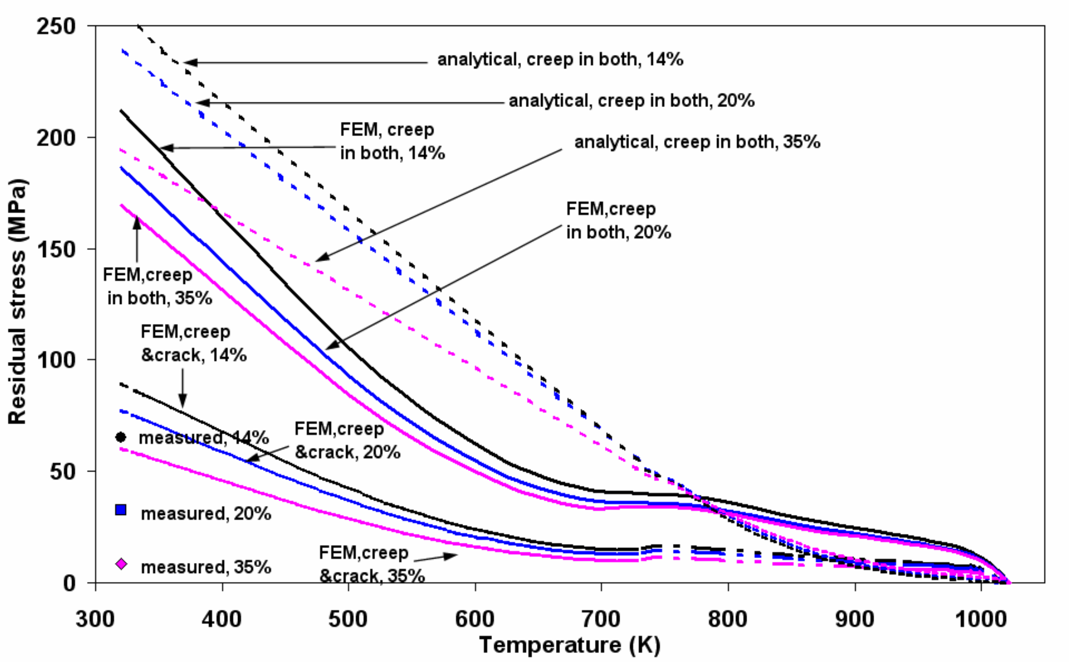

Figure 6-28 FE results of residual stress during cooling, in comparison with analytical modeling.

Figure 6-28 shows the FE simulation results of residual stress evolution during cooling with the existence of cracks, in comparison with analytical solutions. It is seen that the residual stress level has dramatically been reduced with the presence of cracks in Al_3Ti, and it is more or less comparable with the experimental measurements.

6.3.2 FE simulation of residual stress with crack propagation

There are two routes to simulate the crack propagation in MIL composites: one is to simulate how crack size evolves during cooling; the other is how the spacing between cracks evolves. The first route was chosen in this study, because the crack spacing observed in experiments is usually more than 10 times greater than the crack size itself and at that distance, interactions among cracks are considered negligible.

The initial crack sizes are assumed to be a quarter of the thickness of Al_3Ti layers, located in the middle of the layers. The initial condition and boundary conditions are the same as described in section 6.3.1. The FE model with initial condition is shown in Figure 6-29 (notice the existing of the microcracks in Al_3Ti).

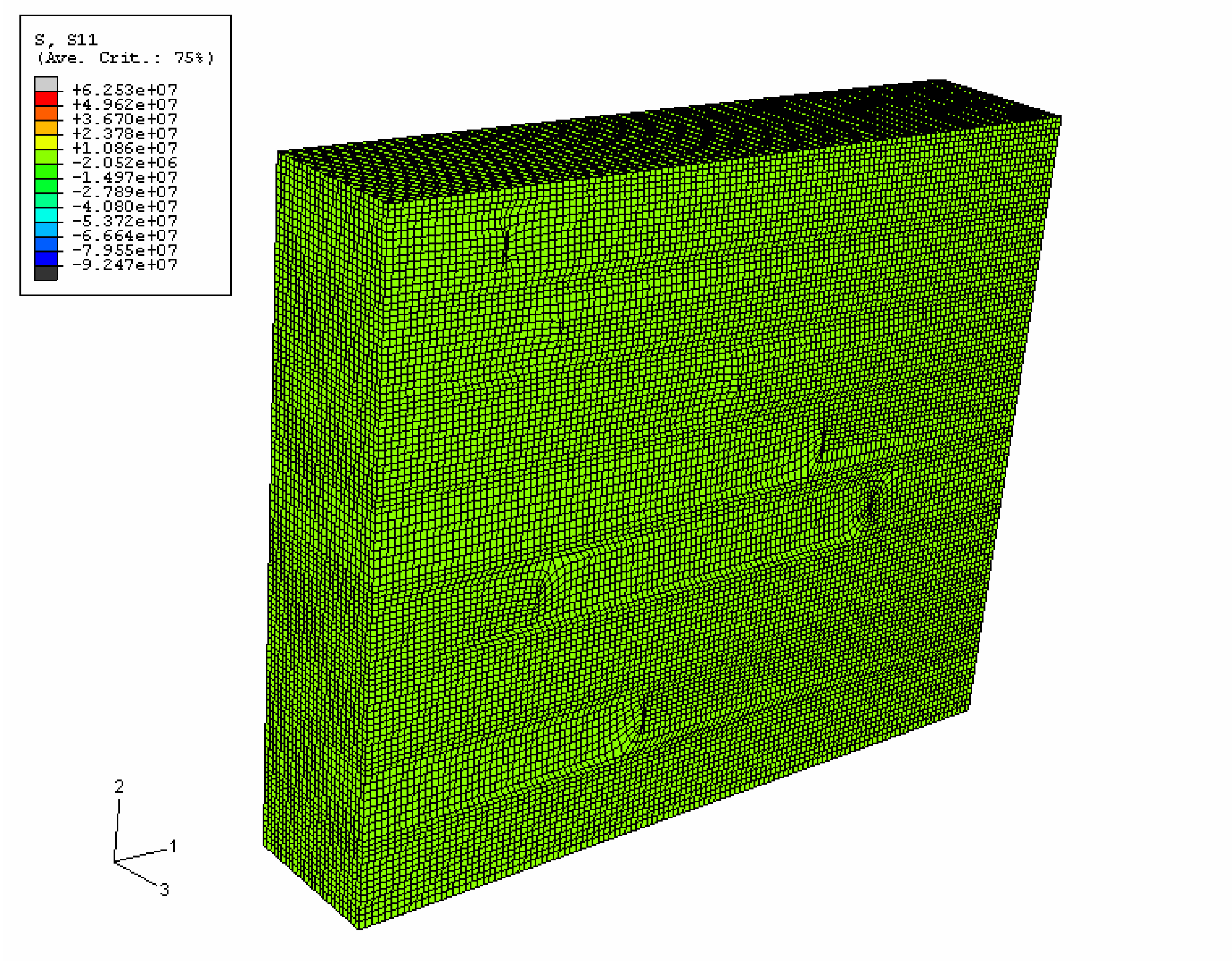

Figure 6-29 Crack propagation simulation, initial condition.

The J-integral, which represents the energy required to propagate a crack, was calculated around crack tip and compared with the critical value to determine whether the cracks would further propagate. J-integral is calculated in ABAQUS as

$$J = \int_A \lambda(s) n \cdot H \cdot q dA \tag{6.53}$$

where $\lambda(s)$ is a virtual crack advance in the plane of a three-dimensional fracture; dA is a surface element along a vanishing small tubular surface enclosing the crack tip; n is the outward normal to dA; and q is the local direction of virtual crack extension. H is given by

$$H = W\,I - \sigma \cdot \frac{\partial u}{\partial x} \tag{6.54}$$

where for elasto-viscoplastic material behavior, W is defined as the elastic strain energy density plus the plastic dissipation, thus representing the strain energy in an “equivalent elastic material.”

Although in theory, J integral is path independent, experience has shown that the first contour calculated in ABAQUS is of significantly lower accuracy, therefore at least 10 J-integrals around crack tip were requested for each crack. If the J-integral exceeds the critical value, crack length is extended and the elastic modulus is accordingly reduced; otherwise, it stays the same for the next simulation. The process is summarized in Figure 6-30. Since ABAQUS does not have the capability to simulate crack propagation in 3D automatically, the simulation was interrupted periodically, and comparison and the necessary adjustments were made manually.

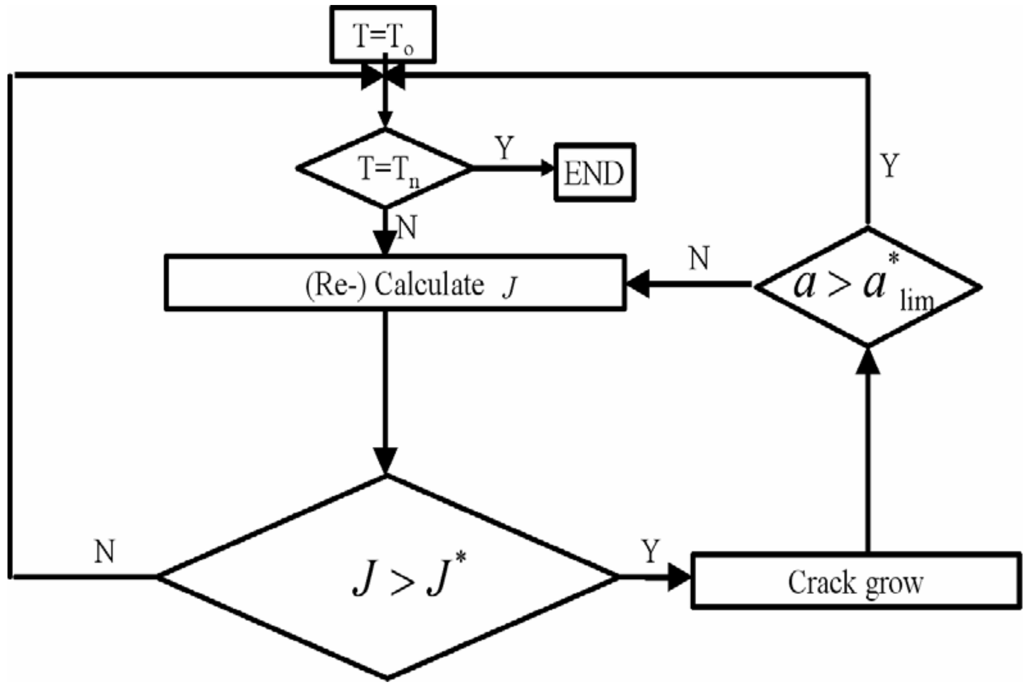

Figure 6-30 Schematics of crack propagation in FE simulation.

Figure 6-31 shows the intermediate steps as the cracks grow; here a is the crack size and t is the thickness of the Al_3Ti layer.

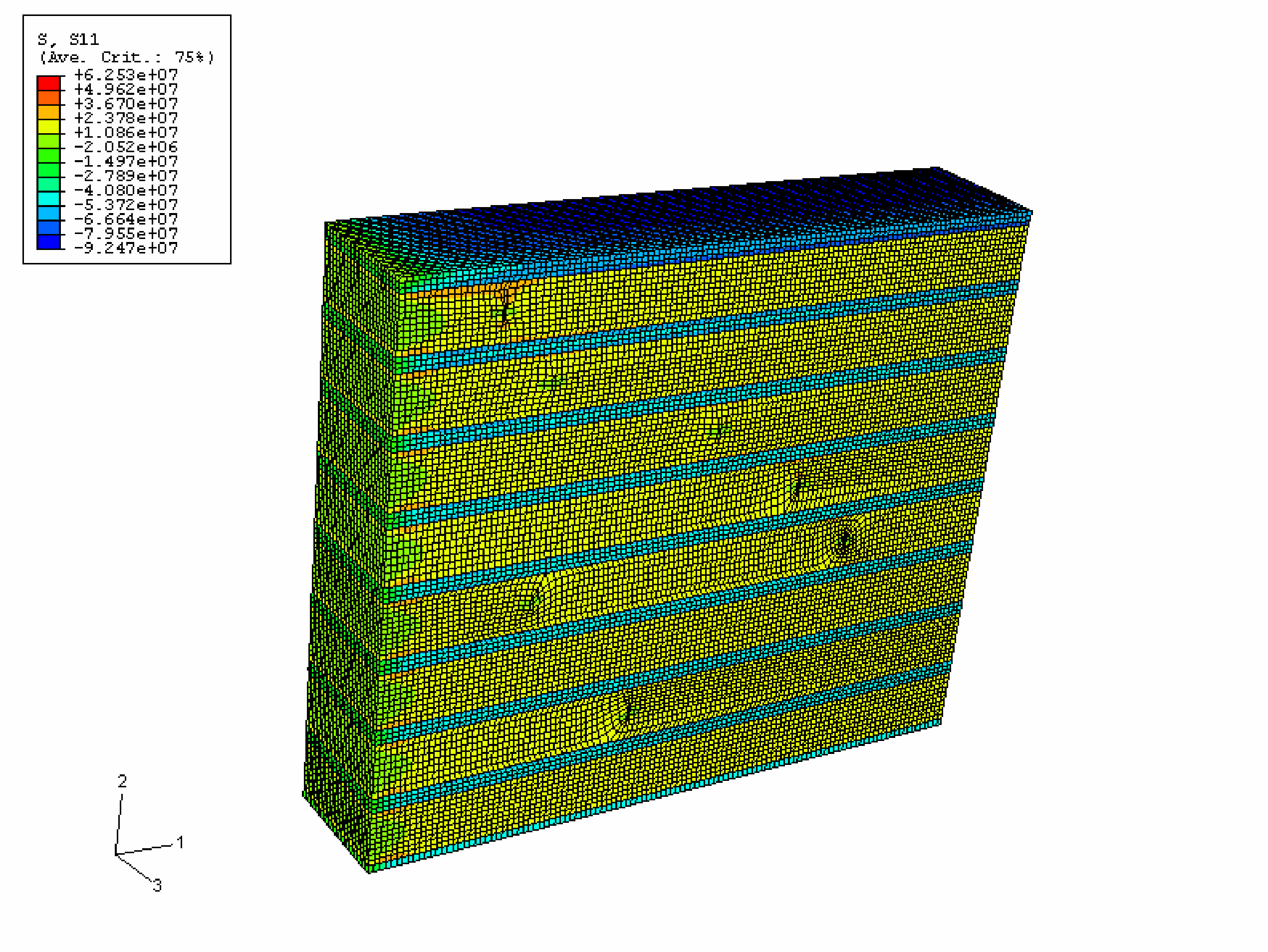

Figure 6-31 (a) T=915.2K, a = 0.25t.

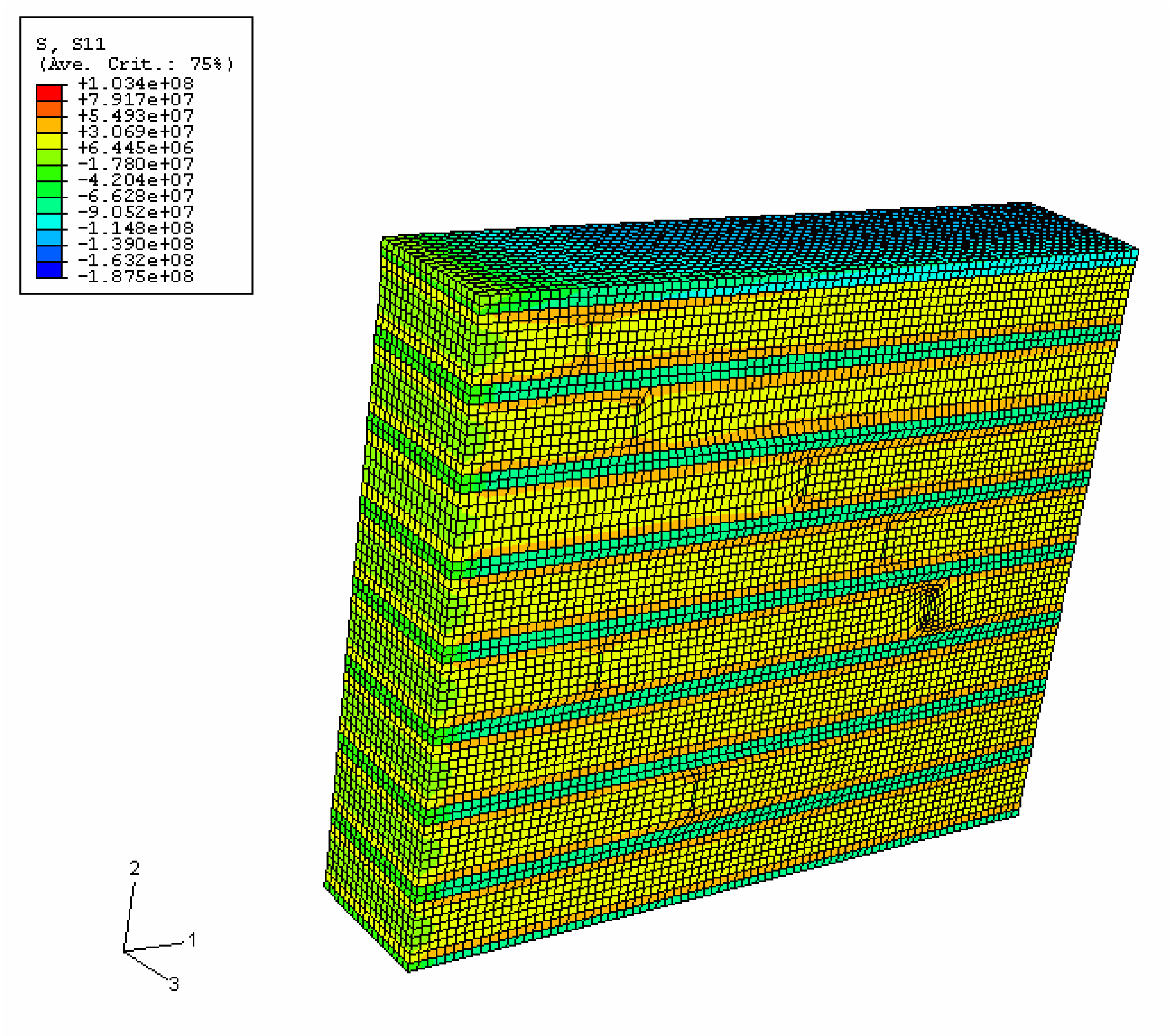

Figure 6-31 (b) T= 788.2K, a = 0.25t.

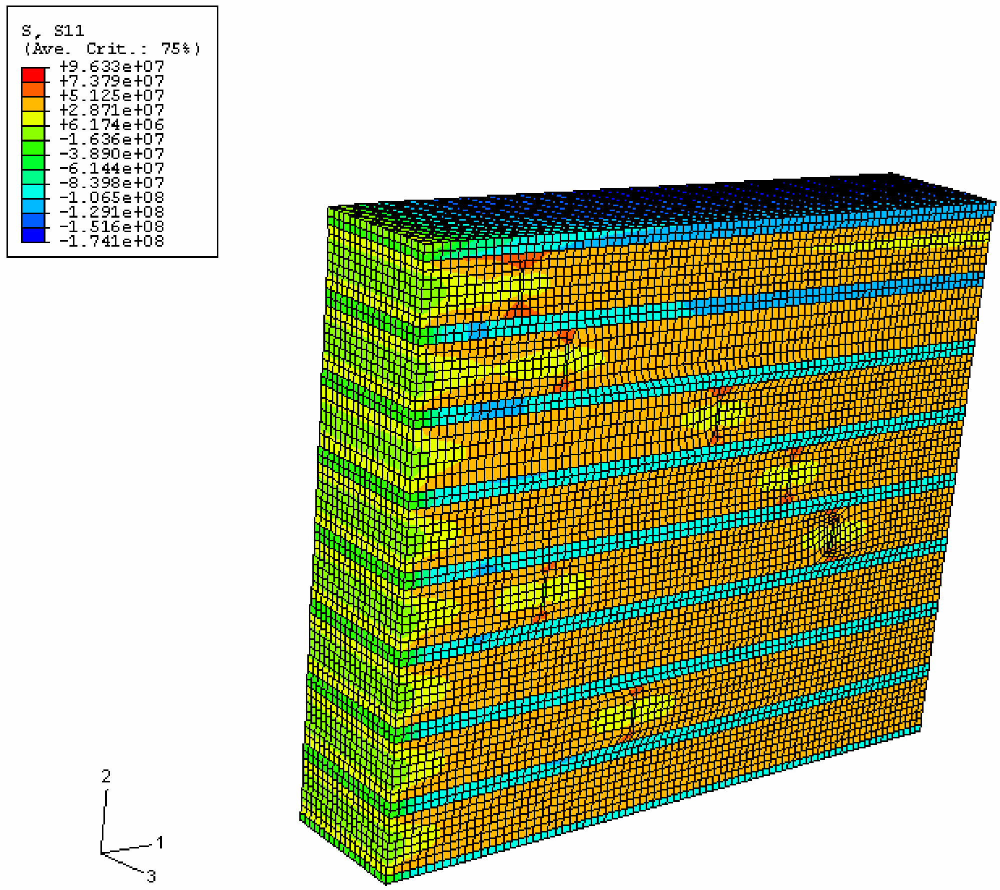

(c) T= 551.7K, a = 0.5t.

Figure 6-31 Crack propagation simulation, intermediate steps.

Figure 6-32 shows the FE results of residual stress, in comparison with the analytical solutions, which show the residual stress with creep and with creep and cracking.

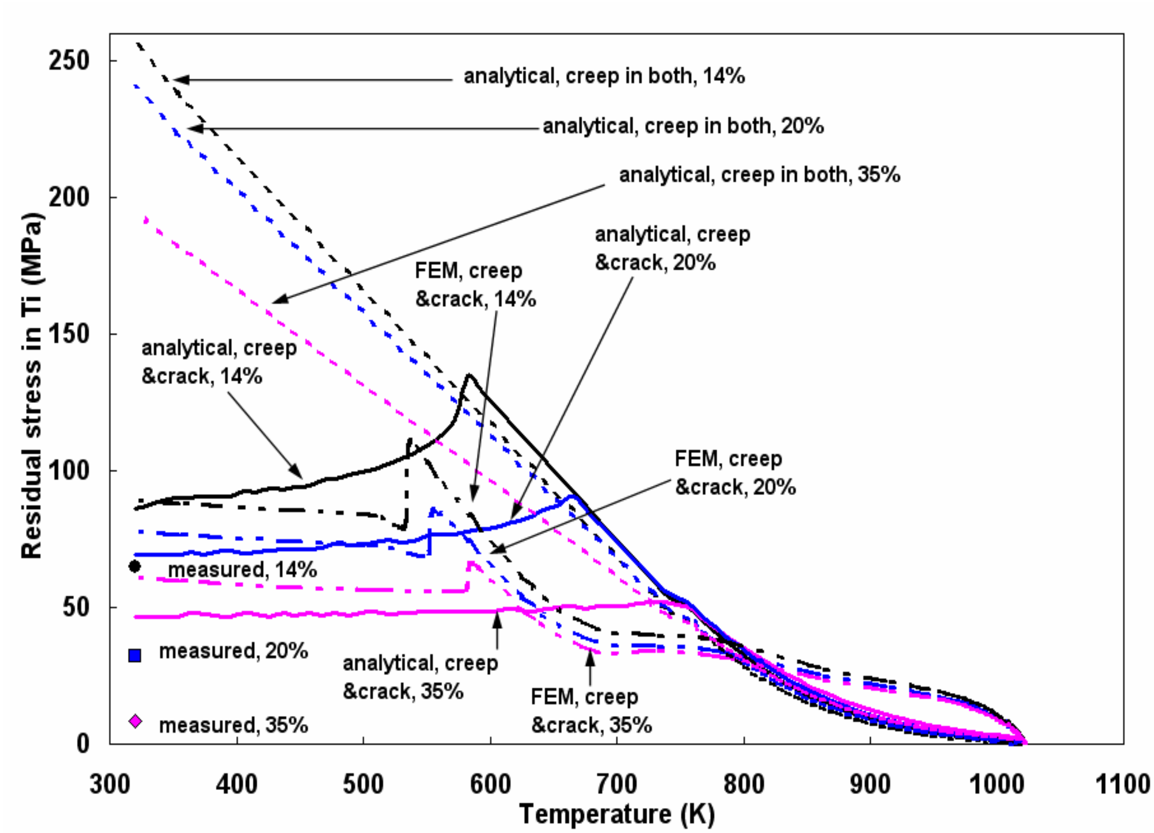

Figure 6-32 FE results of residual stress, in comparison with analytical solutions.

The residual stress obtained by FE simulation at room temperature is comparable with the analytical solutions and the experimental measurements. However, the evolution of the residual stress itself is very different. The creep effect on the residual stress obtained by FE simulation is much more prominent than that in the analytical solutions, as the creep very effectively prevents the residual stress build-up in the early stage. In the later part of the cooling process, as the residual stress increases, so does the J-integral around the crack tips. When the J-integral exceeds the critical value, the cracks grow, but unlike the analytical solution, the FE simulation predicts a sudden eruption and the cracks keep growing in an unstable fashion until reaching the interfaces, while the residual stress experiences a sharp decrease, shown in Figure 6-33. The residual stress after that does not increase much, because of the relaxation the crack propagation provides and the erosion of elastic modulus in Al_3Ti. Given the brittleness of the Al_3Ti layers, the scenario obtained from FE simulation is likely to be what has actually happened. One explanation that analytical solution gives a more gradual increase of cracking is that it uses the critical stress criterion, which compares the far-field stress in general. Another reason is that the nature of this finite element simulation restricted the minimum size of the crack increment confined by the finite size of the element, which may not capture the changes within that minimum increment. In that sense, the finite element simulation provides a more accurate solution for residual stress evolution and distribution by taking into consideration of the finite size of MIL composites on the one hand, but on the other hand, it is less accurate by increasing crack size in a finite fashion. Table 11 shows the comparison of residual stress obtained by analytical modeling, FE simulation and experimental measurements.

Table 11 The comparison of residual stress obtained by analytical modeling, FE simulation and experimental measurements.

Volume fraction of Ti6Al4V	14%	20%	35%
FE simulation (MPa)	89.53	77.86	60.73
Analytical modeling (MPa)	86.15	69.33	46.63
Measured residual stress (MPa)	65.01	32.38	8.29

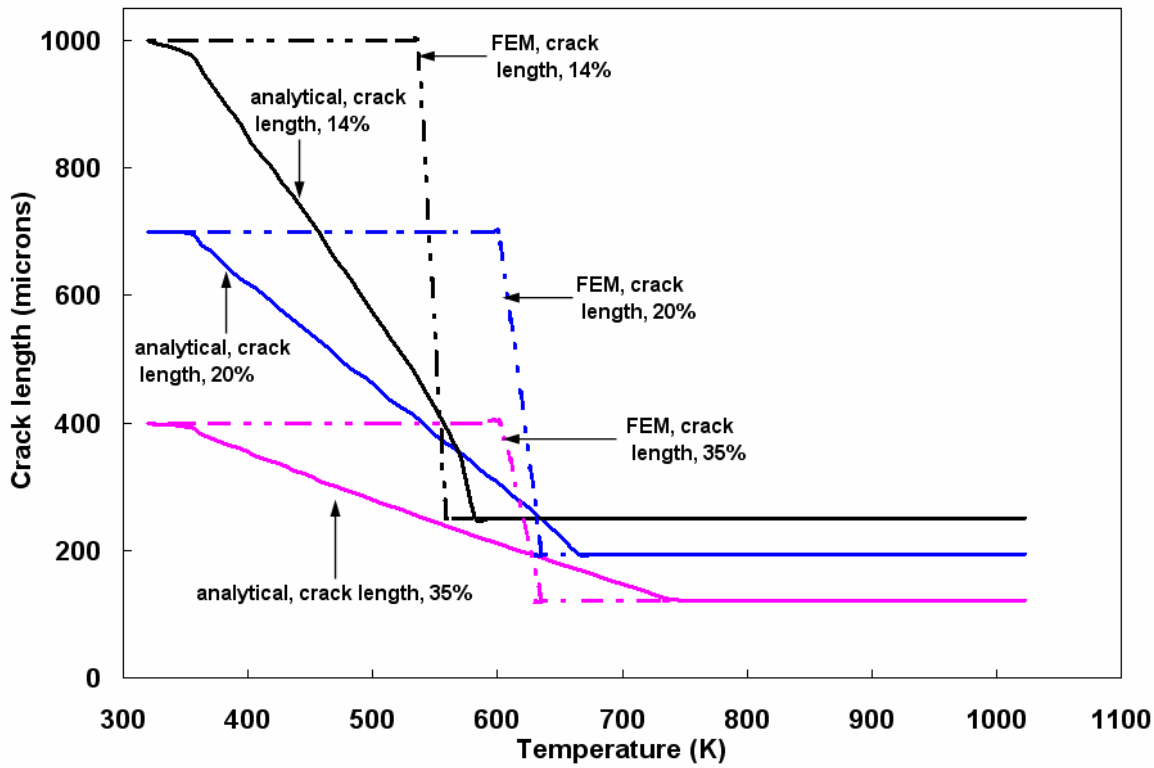

Figure 6-33 FE results of crack length, in comparison with analytical solutions.

6.4 Fracture toughness of Ti6Al4V-Al_3Ti MIL composites

The existence of residual stress in MIL composites has an important effect on the fracture toughness. As it is known, imposing a distribution of internal stresses to improve the fracture toughness is a global materials design principle, which has been implicitly applied in a number of previous studies [162-165]. From the modeling viewpoint, the effect of the residual stresses can be interpreted in one of two ways. In one interpretation, the effect of the macroscopic residual stress can be treated entirely as a correction to the crack-driving force, and the intrinsic fracture toughness of the material is considered unchanged from that of a monolithic material. This approach was used by Sherman and Green et al. [166] to treat the fracture of compression-strengthened glass and three-layer alumina-zirconia composites, respectively. Alternatively, the surface-compression-strengthened materials are toughened since the resistance to fracture from a surface crack is enhanced by the presence of the surface compression [167]. In this case, the enhanced fracture toughness must be viewed as apparent fracture toughness since the higher resistance to fracture is derived from a reduction of the crack-driving force rather than an increase in the intrinsic resistance to crack extension.

The apparent toughness $K_{c,app}$ is considered the sum of the crack-initiation toughness and stress intensity due to the designed internal stresses

$$K_{c,app} = K_0 + K_T \tag{6.55}$$

where K_0 is the crack-initiation toughness and K_T is the stress intensity due to the designed internal stresses, obtained by integrating the product of the stress distribution and a weight function over the crack length [168, 169]. A weight function method is used to calculate K_T

$$K_T = \int_0^a h(\frac{x}{a},\alpha) \cdot \sigma_r(x) dx \tag{6.56}$$

where a is the crack length, α is the crack length normalized by specimen's width W, h $(x/a, \alpha)$ is the weight function and can be calculated for a known crack and laminate geometry [170], and $\sigma_r(x)$ is the residual stress. h $(x/a, \alpha)$ is given as

$$h\left(\frac{x}{a},\alpha\right)=\sqrt{\frac{2}{\pi a}}\frac{1}{\left(1-\frac{x}{a}\right)^{\frac{1}{2}}\cdot\left(1-\alpha\right)^{\frac{3}{2}}}\cdot\left\{\left(1-\alpha\right)^{\frac{3}{2}}+\sum A_{\upsilon\mu}\cdot\left(1-\frac{x}{a}\right)^{\upsilon+1}\alpha^{\mu}\right\} \quad (6.57)$$

$A_{\upsilon\mu}$ is given in Table 12.

Table 12 The value $A_{\upsilon\mu}$ of in the weight function.

	$\mu=0$	$\mu=1$	$\mu=2$	$\mu=3$	$\mu=4$
$\upsilon=0$	0.498	2.4463	0.07	1.3187	-3.067
$\upsilon=1$	0.5416	-5.0806	24.3447	-32.721	18.1214
$\upsilon=2$	-0.1928	2.55863	-12.642	19.763	-10.986

Since the components of the composites have different thermal expansion coefficients, one of the components is under compression and the other is under tension and the thickness of the compression layer is d_c, while the thickness of the tension layer is d_t.

For a symmetric three-layer Ti6Al4V-Al_3Ti MIL composite with Ti6Al4V on the top and bottom, the stress intensity was calculated following the equation (6.56). The dependence of stress intensity on the volume fraction of Ti6Al4V is obtained in Figure 6-34. It shows how the stress intensity changes as a function of volume fraction of Ti6Al4V. The maximum value of the stress intensity occurs at the

Ti6Al4V volume fraction of 57%. The initial toughness varied from 23 $MPa\sqrt{m}$ to 29 $MPa\sqrt{m}$ for 20% Ti6Al4V and 35% Ti6Al4V. From Figure 6-34, the stress intensity K_T is 53 $MPa\sqrt{m}$ and 80 $MPa\sqrt{m}$ for 20% Ti6Al4V and 35% Ti6Al4V, and the calculated apparent fracture toughness is 76 $MPa\sqrt{m}$ and 109 $MPa\sqrt{m}$ for 20% Ti6Al4V and 35% Ti6Al4V.

The steady state fracture toughness for 20% Ti6Al4V and 35% Ti6Al4V has been experimentally obtained as 80 $MPa\sqrt{m}$ and 115 $MPa\sqrt{m}$ respectively for divider orientations in Ti6Al4V-Al_3Ti MIL composites [2]. Although experimental steady state fracture toughness for arrester orientations is not available, it has been shown that the steady state fracture toughness for arrester orientations is generally higher than that in the divider orientations, because it needs more work for the crack to advance in the arrester orientation than in the divider orientation. Therefore, the experimental obtained values of 80 $MPa\sqrt{m}$ and 115 $MPa\sqrt{m}$ can be taken as the low limits of steady state fracture toughness for the arrester orientation, and they agree well with the calculated apparent fracture toughness of 76 $MPa\sqrt{m}$ and 109 $MPa\sqrt{m}$ for 20% Ti6Al4V and 35% Ti6Al4V.

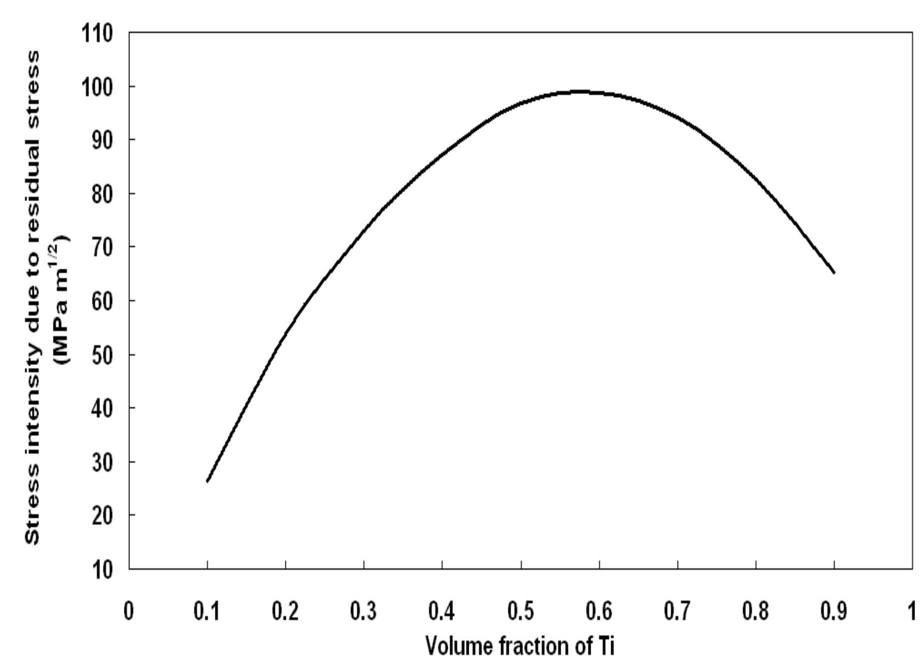

Figure 6-34 Stress intensity of Ti6Al4V-Al_3Ti MIL composite due to the residual stresses as a function of fraction of Ti.

CHAPTER 7

CONCLUSIONS AND FUTURE PLAN

7.1 Conclusions

Based on the experimental and modeling results, the following conclusions can be made:

1. The cracks in the as-processed MIL composites were characterized under optical microscope and cracks can be classified into three categories: parallel to the interface, perpendicular to the interface and 45^0 inclined to the interface.
2. The crack densities measured for the as-processed 14%, 20% and 35% MIL composite are 0.321 mm/mm^2, 0.255 mm/mm^2, and 0.137 mm/mm^2, respectively.
3. The concentrations of parallel cracks for MIL composites with different composition vary consistently: the concentration of perpendicular cracks increases from 49% (14% Ti6Al4V) to 72% (35% Ti6Al4V), while the concentration of inclined cracks decreases from 31% (14% Ti6Al4V) to 7% (35% Ti6Al4V).
4. Quasi-static and dynamic compression tests were conducted on pure Al_3Ti. Transgranular and intergranular cracks were characterized under SEM. The strain rates have shown little effects on the formation of the

two different crack morphologies.

5. The specimens tested in the parallel direction failed by delamination along the interfaces, cracking along the middle of the Al_3Ti layers, and buckling of Ti6Al4V. After dynamic deformation, the specimens were much more fragmented than after quasi-static deformation, and most Al_3Ti is comminuted and blown away upon impact.
6. The specimens tested in the perpendicular direction failed by shear, delamination along interface, and cracking along the middle the Al_3Ti layers. As in the parallel direction, the specimens after dynamic deformation are much more fragmented than those after quasi-static deformation.
7. The crack density was measured using optical microscopy for all testing conditions and converted to a damage parameter, D. Generally, the damage parameter under dynamic deformation is higher than that in quasi-static deformation, for the same strain. The damage parameter increases with increasing strain, but decreases with increasing volume fraction of Ti6Al4V. D was found to increase from ~0.018 in the as-processed condition (D_0) to ~1 at failure.
8. The evolution of the elastic modulus was calculated and compared with the experimental results. It is found that the calculated elastic modulus in quasi-static deformation matches the experimental results well using the increase in microcracking through a modified O'Connell-Budiansky

equation. The equation also enables the estimate of the compressive strength, which is the stress when $\frac{d\sigma}{d\varepsilon}=0$. The results are in good agreement with experiments for quasi-static deformation. For dynamic deformation, the predicted elastic modulus is considerably lower than the measured values. This is interpreted as follows: microcrack growth is proceeding during and after compressive loading, so that the measured values reflect post-deformation growth during specimen unloading.

9. Based on the experiment observation, four different damage evolution mechanisms have been identified, including axial splitting, shear localization in Ti6Al4V layers, crack propagation along the central plane of weakness in Al_3Ti, and delamination at Ti6Al4V-Al_3Ti interface.

10. The elastic anisotropy of the Ti6Al4V-Al_3Ti MIL composite is of the orthotropic kind, and the elastic properties, Young's modulus, shear modulus and Poisson's ratio, have been assessed as a function of volume fraction of Ti6Al4V and orientation. Those calculated values have been successfully compared with the experimental measurements.

11. The residual stresses in Ti6Al4V-Al_3Ti MIL composites were analytically evaluated for different volume fraction of Ti6Al4V. Two stress release mechanisms, the creep and crack propagation mechanisms were proposed in the analysis. The calculated residual stress after each mechanism was compared with the experimental measurements and the combination of all stress release mechanisms render the best results with

the experimental measurements.

12. Finite element simulation was conducted using ABAQUS, including both creep and crack propagation. The FE results were compared with the analytical solutions and the experimental measurements. FE simulation has confirmed the analytical assessment of the stress level on average, and demonstrated the stress local distribution locally, verified by experiments. FE simulation predicts an unstable crack growth, as the cracks keep growing until reaching the interfaces, and the corresponding residual stress experiences a sharp decrease.

13. The effect of residual stress on fracture toughness was evaluated, and apparent fracture toughness was evaluated as a combination of the crack initiation toughness and the stress intensity due to the residual stress, the latter of which is calculated by a weight function method. The calculation predicts the maximum stress intensity at 57% volume fraction of Ti6Al4V.

7.2 Achieved goals

This research has successfully achieved the objectives of investigating the evolution of damage and residual stress in the MIL composites, through both the experimental methods and theoretical modeling. The series of experiments conducted in a controlled manner and characterized under optical microscope and SEM have identified the damage evolution patterns in the MIL composites. The crack density has also provided important insights on the effects of the damage on the elastic modulus and stress strain relations. The theoretical modeling focused on the evolution and distribution of residual stress during the cooling process and its effect on the fracture toughness of MIL composites. The proposed stress release mechanisms were successfully implemented by analytical calculation and finite element simulation, and the results yielded good agreements with the experimental measurements.

Overall, this research provided deep insights on one promising type of engineering materials, the metal-intermetallic laminate composite, by understanding its behaviors under and normal and extreme conditions and by anticipating its residual stress level during fabrication which may have important effects during its service.

The goals that have been achieved and the corresponding sections are shown in Figure 7-1.

7.3 Future work

Investigation of other stress release mechanisms during cooling, such as visco-plastic, and their incorporation into the analytical and finite element simulation of residual stresses.

Introduction of crack initiation in the analysis of residual stresses, with different crack initiation criterions.

Automation of damage evolution in the finite element simulation.

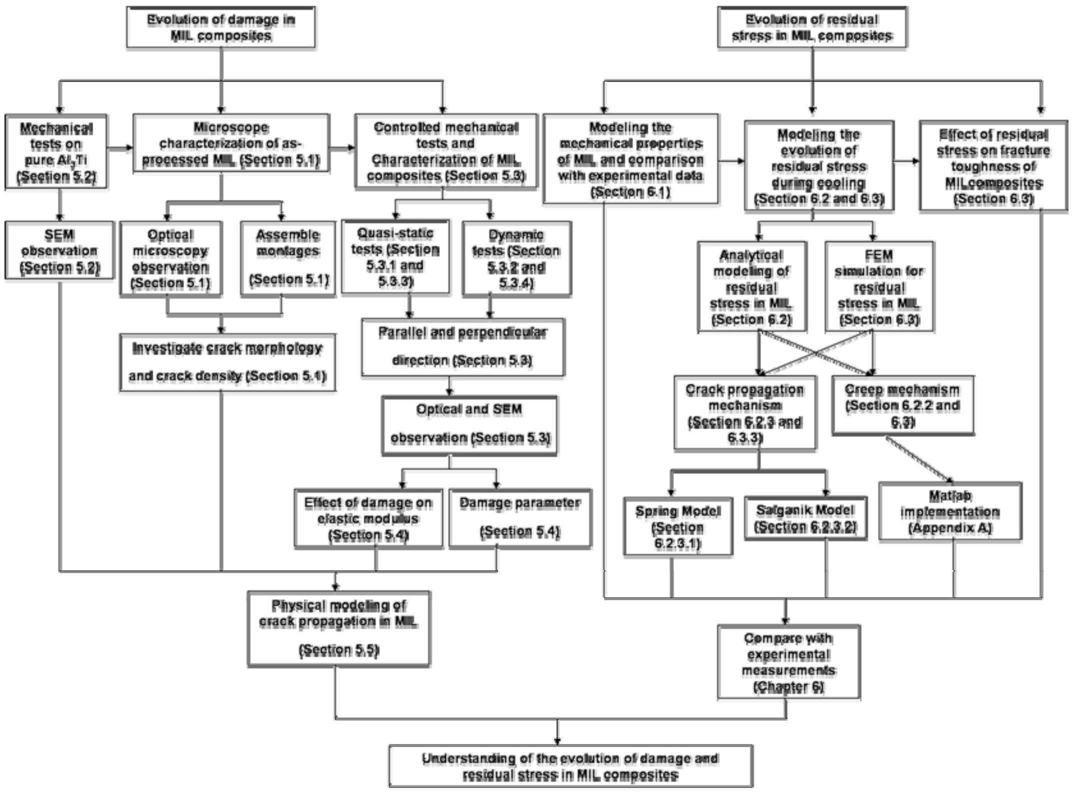

Figure 7-1 The schematics of the research progress.

APPENDIX A
SOURCE CODE FOR CALCULATING RESIDUAL STRESSES OF TI6AL4V-AL_3TI METAL INTERMETALLIC LAMINATE COMPOSITES WITH CREEP IN TI6AL4V AND AL3TI AND/OR CRACK PROPAGATION

```
function []=main()
diary 1.txt
delete 1.txt

%calculation on creep in both Ti and Al3Ti layer with the crack growth in MIL during the cooling to obtain the compressive residual stress in Ti
%MIL creeps during cooling, so the residual stress in Ti after cooling will not be as high as the one without cooling
%residual_stress=E * |thermal expansion coefficence of Ti - thermal expansion coefficence of Al3Ti | * delta_T
%----------------------------------------------------------------------------------------
%                                    For creep in Ti layer
%----------------------------------------------------------------------------------------
%Step I:
%--------
%using Doner-Conrad equation to calculate the strain rate of the creep in Ti:
%strain rate_Ti=(residual_stress/G)^m_Ti*(A*D*G*b/kT)-----------(1)
%where A and m are constants which depend on the particular operating mechanism; strain rate is th esteady-state tensile strain rate;
%G is the shear modulus; D is the diffusivity coefficent; b is the burgers vector; stress is the applied tensile stress;
%--------
%Step II:
```

```
%--------
%after getting the strain rate of the creep,  by multiplying the time steps, stain can be obtained:
%strain=strain rate*delta_t-----------(2)
%--------

%Step III:
%--------
%multiplied the strain by Young's modulus, the change in stress can be obtained
%delta_stress_Ti=strain_Ti*E---------------(3)
%------------------------------------------------------------------------------------------
%                                  For creep in Al3Ti layer
%------------------------------------------------------------------------------------------
%Step IV:
%--------
%using power law equation to calculate the strain rate of the creep in Al3Ti:
%strain_rate_Al3Ti=M/T * (stress_Al3Ti/G_Al3Ti)^n_Al3Ti*exp(-Q/RT)-- (1)
%where stress_Al3Ti is obtained from
%stress_Al3Ti=stress*con/(1-con)
%where M and n are constants which depend on the particular operating mechanism; strain rate is th esteady-state tensile strain rate;
%G is the shear modulus; stress is the applied tensile stress; Q is activation energy of Al3Ti; con is the concentration of Ti
%--------
%Step V:
%--------

%after getting the strain rate of the creep,  by multiplying the time steps, stain can be obtained:
%strain_Al3Ti=strain rate_Al3Ti*delta_t-----------(2)
%--------
%Step VI:
%--------
```

%multiplied the strain by Young's modulus, the change in stress can be obtained

%Young's modulus of Al3Ti is a function of crack length, crack spacing, and is calculated as

%E_Al3Ti=216*10^9/(1+16*(10-3*poisson_Al3Ti)*(1-poisson_Al3Ti^2)/(45*(2-poisson_Al3Ti))*pi*num_crack*crack_size_origin/space_origin)

%where the initial crack length is assumed for different concentration of MIL, while the ultimate crack length, which limits

%the length of the crack growth, is obtained from experiements and enforced whenever the developing crack reaches it.

%delta_stress_Al3Ti=strain_Al3Ti*E_Al3Ti---------------(3)

%--------

%Step VII:

%--------

%convert the change of residual stress in TiAl3 into the corresponding change of residual stress in Ti by

%delta_stress_Ti_from_Al3Ti=delta_stress_Al3Ti*(1-con)/con

%--------

%Step VIII:

%--------

%add the delta_stress_Ti_from_Al3Ti and delta_stress_Ti together to obtain the total change in residual stress in Ti

%delta_stress = delta_stress_Ti + delta_stress_Ti_from_Al3Ti

%--------

%Step IX:

%--------

%substract delta_stress_total from the initial stress in Ti, the modified stress in Ti is obtained for the next step to Step I

%modi_stress = residual_stress - delta_stress-----------(4)

%--------

%Step X:

%--------

%compare the stress after creep in both Ti and Al3Ti with the critical stress, which is a function of crack length, crack spacing and effective fracture toughness of Al3Ti.

%stress_intensity_Al3Ti = integral (h*modi_stress_Al3Ti)-----------(5)

%effe_fract_tough_Al3Ti=fracture_toughness_Al3Ti-stress_intensity_Al3Ti-(6)

%crit_stress_Al3Ti = effe_fract_tough_Al3Ti/(pi*crack_size_origin)^0.5----(7)

%modi_stress_Al3Ti=modi_stress*con/(1-con)-------------------(8)

% case I: modi_stress_Al3Ti < crit_stress_Al3Ti

% go to step I

% case II: modi_stress_Al3Ti > crit_stress_Al3Ti

% crack growth, then recalculate (7), then compare again

%If crack_size_origin >= crack_size_ultimate

% go to Step I

%If crack_size_origin < crack_size_ultimate

% the stress decreases due to the crack growth

%stress_decrease=650*((E*(1-con)/(1+(E*1.22/E_Al3Ti_old)*con)*(1-0.321))*strain_0_2-(E*(1-con)/(1+(E*1.22/E_Al3Ti_new)*con)*(1-0.321))*strain_0_2);

% stress=stress-stress_decrease;

% modi_stress_Al3Ti_2=stress*con/(1-con);

% go to Step X, and compare the modi_stress with crit_stress again

%--

%redo all the above steps along the cooling curve will give a modi_stress-temperature and modi_stress-time plot

%--

%variables:

%G_Ti: shear modulus of Ti

%E_Ti: Young's modulus of Ti

%poisson_Al3Ti: Poisson's ratio of Al3Ti;

%k: Boltzmann's constant

%R: gas constant

%D: diffusivity coefficient of Ti

%b_Ti: burgers vector of Ti

%A, m: constants depending on the particular operating mechanism of Ti

%alpha_Ti: thermal expansion coefficence of Ti

%alpha_Al3Ti: thermal expansion coefficence of Al3Ti

%G_Al3Ti: shear modulus of Al3Ti

%E_Al3Ti_origin: Young's modulus of Al3Ti in the beginning;

%E_Al3Ti: current Young's modulus of Al3Ti

%M, n: constants depending on the particular operating mechanism of Al3Ti

%Q: activation energy of Al3Ti

%con: concentration of Ti

%coeffi: the spacing between two cracks

%num_crack: number of cracks in the sample specimen

%percentage: the percentage increase of crack from previous one

%t_n_1: the ending time of the first cooling curve

%t_n_2: the ending time of the second cooling curve

%t_0: the starting time

%T_1: the higher temperature in a time step

%T_2: the lower temperature in a time step

%T: the average temperature in a time step

%stress_1: beginning stress of the first cooling curve w/o considering creep

%stress_2: beginning stress of the second cooling curve w/o considering creep

%T=f(t): Temperature is a function of time

%init_stress: the stress without creep

%modi_stress: the stress considering creep

%delta_stress: the difference between init_stress and modi_stress

%stress_inter: the sum of stress with creep and stress with different CTE

%stress_intensity_Al3Ti: stress intensity of Al3Ti with crack

%effe_fract_tough_Al3Ti: effective fracture toughness of Al3Ti, combination of original fracture toughness and stress intensity

%fract_toughness_orgin_Al3Ti: original fracture toughness of Al3Ti at 1023C

%fract_toughness_Al3Ti_room_temp:Al3Ti fract tough at room temperature

%crit_stress_Al3Ti: stress beyond which crack in Al3Ti will propagate

%crack_size_origin_Al3Ti: half of the original crack size in Al3Ti

%crack_size_Al3Ti: half of the developing/current crack size in Al3Ti

```
%final_stress: final stress in Ti
%modi_stress_Al3Ti: the equavalent stress in Al3Ti
%strain_rate: the strain rate of creep
%strain: the strain in time delta_t
%delta_t: the time interval
%n: steps
%[modi_stress_Al3Ti,crit_stress_Al3Ti,crack_size_origin,stress,stress_inter,E_Al3Ti]=stat(modi_stress_Al3Ti,crit_stress_Al3Ti,crack_size_origin,stress,space_origin,E_Al3Ti,stress_inter)
%a subroutine function which compares the residual stress in Al3Ti with the current critical stress
%-----------------------------------------------------------------------------------------
%          Notice: ALL VARIABLES THAT DO NOT COME WITH "_Al3Ti" ARE FOR Ti, EXCEPT THOSE VARIABLES THAT
%                  ARE ONLY USED FOR Al3Ti
%-----------------------------------------------------------------------------------------
%Global variables
%-----------------------------------------------------------------------------------------
global alpha_Ti alpha_Al3Ti con percentage G R k E b G_Al3Ti poisson_Al3Ti a c p q Q m n M A AA mm stress_0_2 con crack_size_ultimate
global stress_0 coeffi strain_0_2 strain_0 delta_t_2 delta_t fract_toughness_orgin_Al3Ti fract_toughness_Al3Ti_room_temp num_crack
alpha_Ti=9.5*10^(-6);
alpha_Al3Ti=13*10^(-6);
con=0.35;
percentage=0.01;
coeffi=10;
num_crack=1;
%---------------------
%For Ti
G=43.8*10^9;
R=8.314;
k=1.38*10^(-23);
E=115.7*10^9;
```

```
b=0.294*10^(-9);
fract_toughness_orgin_Al3Ti=0.5*10^6;
fract_toughness_Al3Ti_room_temp=1.5*10^6;
%---------------------
%For Al3Ti
G_Al3Ti=92.3*10^9;
poisson_Al3Ti=0.17;
concentration = con;
switch lower(concentration)
  case 0.14
    crack_size_origin=250*10^(-6);
    space_origin=coeffi*crack_size_origin;
    crack_size_ultimate=1000*10^(-6);
  case 0.2
    crack_size_origin=193*10^(-6);
    space_origin=coeffi*crack_size_origin;
    crack_size_ultimate=700*10^(-6);
  case 0.35
    crack_size_origin=104*10^(-6);
    space_origin=coeffi*crack_size_origin;
    crack_size_ultimate=400*10^(-6);
end
E_Al3Ti_origin=216*10^9/(1+16*(10-3*poisson_Al3Ti)*(1-
poisson_Al3Ti^2)/(45*(2-
poisson_Al3Ti))*pi*num_crack*crack_size_origin/space_origin);
E_Al3Ti=E_Al3Ti_origin;
Q=67596;
M=3.275*10^11;
n=3;
%-----------------------------------------------------------------------------------------
% First cooling stage
%-----------------------------------------------------------------------------------------
A=5*10^(-1);
m=3;
```

```
t_n_2=3.5;
t_n_1=0;
p=40;
delta_t=(t_n_2-t_n_1)/p;
stress_store_1=zeros(p,1);
T_store_1=zeros(p,1);
delta_stress_store_1=zeros(p,1);
stress_original_store_1=zeros(p,1);
modi_stress_Al3Ti_store_1=zeros(p,1);
crit_stress_Al3Ti_store_1=zeros(p,1);
crack_size_origin_store_1=zeros(p,1);
delta_T=77*delta_t;
strain_0=(alpha_Al3Ti-alpha_Ti)*delta_T;
   stress_0=E*(1-con)/((1+(E*1.22/E_Al3Ti-1)*con)*(1-0.321))*strain_0;
   T_1=-77*0*delta_t+1023;
   T_2=-77*(0+1)*delta_t+1023;
   T=(T_1+T_2)/2;
   %T,T_1,T_2,T
   D=(10^(-4))*exp(-58000*4.186/(R*T));
   strain_rate=(A*D*G*b/(k*T))*(stress_0/G)^m;
   strain=strain_rate*delta_t*3600;
   delta_stress_Ti=strain*E;
   stress_0_Al3Ti=stress_0*con/(1-con);
   strain_rate_Al3Ti=(M/T)*exp(-Q/(R*T))*(stress_0_Al3Ti/G_Al3Ti)^n;
   strain_Al3Ti=strain_rate_Al3Ti*delta_t*3600;
   delta_stress_Al3Ti=strain*E_Al3Ti_origin;
   delta_stress_Ti_from_Al3Ti=delta_stress_Al3Ti*(1-con)/con;
   delta_stress=delta_stress_Ti+delta_stress_Ti_from_Al3Ti;
   stress=stress_0-delta_stress;
   stress_original_store_1(1,1)=stress_0-delta_stress_Ti;
   stress_store_1(1,1)=stress;
   modi_stress_Al3Ti_store_1(1,1)=stress*con/(1-con);
   crit_stress_Al3Ti_store_1(1,1)=stress*con/(1-con)*10;
   T_store_1(1,1)=T;
```

```
        delta_stress_store_1(1,1)=delta_stress;
        crack_size_origin_store_1(1,1)=crack_size_origin;
      for c=1:p-1
      E_Al3Ti=216*10^9/(1+16*(10-3*poisson_Al3Ti)*(1-
poisson_Al3Ti^2)/(45*(2-
poisson_Al3Ti))*pi*num_crack*crack_size_origin/space_origin);
        if  crack_size_origin>=crack_size_ultimate
            stress_inter=stress+stress_0_2;
            %stress_inter
            T_1=-77*c*delta_t+1023;
            T_2=-77*(c+1)*delta_t+1023;
            T=(T_1+T_2)/2;
            D=(10^(-4))*exp(-58000*4.186/(R*T));
            strain_rate=(stress_inter/G)^m*A*D*G*b/(k*T);
            strain=strain_rate*delta_t*3600;
            delta_stress_Ti=strain*E;
            stress_inter_Al3Ti=stress_inter*con/(1-con);
            strain_rate_Al3Ti=(M/T)*exp(-
      Q/(R*T))*(stress_inter_Al3Ti/G_Al3Ti)^n;
            strain_Al3Ti=strain_rate_Al3Ti*delta_t*3600;
            delta_stress_Al3Ti=strain*E_Al3Ti;
            delta_stress_Ti_from_Al3Ti=delta_stress_Al3Ti*(1-con)/con;
            delta_stress=delta_stress_Ti+delta_stress_Ti_from_Al3Ti;
            stress=stress_inter-delta_stress;
        else
          modi_stress_Al3Ti=stress*con/(1-con);
          %c,modi_stress_Al3Ti
          %crack_size_origin
          x=0:crack_size_origin/1e6:crack_size_origin*0.999999;
          h=(2/(pi*crack_size_origin))^0.5*(1-x/crack_size_origin).^(-
0.5)*modi_stress_Al3Ti;
          stress_intensity_Al3Ti = trapz(x,h);
            T_1=-77*c*delta_t+1023;
            T_2=-77*(c+1)*delta_t+1023;
```

```
                    T=(T_1+T_2)/2;
                    fracture_toughness_Al3Ti=((T-320)
*fract_toughness_orgin_Al3Ti+(1023-T)*fract_toughness_Al3Ti_room_temp)/703;
                  effe_fract_tough_Al3Ti=fracture_toughness_Al3Ti-
stress_intensity_Al3Ti;
                  crit_stress_Al3Ti = effe_fract_tough_Al3Ti/(pi*crack_size_origin)^0.5;
                    if modi_stress_Al3Ti<crit_stress_Al3Ti
                      stress_inter=stress+stress_0;
                      T_1=-77*c*delta_t+1023;
                      T_2=-77*(c+1)*delta_t+1023;
                      T=(T_1+T_2)/2;
                      D=(10^(-4))*exp(-58000*4.186/(R*T));
                      strain_rate=(stress_inter/G)^m*A*D*G*b/(k*T);
                      strain=strain_rate*delta_t*3600;
                      delta_stress_Ti=strain*E;
                      stress_inter_Al3Ti=stress_inter*con/(1-con);
                      strain_rate_Al3Ti=(M/T)*exp(-
Q/(R*T))*(stress_inter_Al3Ti/G_Al3Ti)^n;
                      strain_Al3Ti=strain_rate_Al3Ti*delta_t*3600;
                      delta_stress_Al3Ti=strain*E_Al3Ti;
                      delta_stress_Ti_from_Al3Ti=delta_stress_Al3Ti*(1-con)/con;
                      delta_stress=delta_stress_Ti+delta_stress_Ti_from_Al3Ti;
                      stress=stress_inter-delta_stress;
                      modi_stress_Al3Ti=stress*con/(1-con);
                    else
            [modi_stress_Al3Ti,crit_stress_Al3Ti,crack_size_origin,stress,stress_inter,E_
Al3Ti]=stat(modi_stress_Al3Ti,crit_stress_Al3Ti,crack_size_origin,stress,space_origi
n,E_Al3Ti,stress_inter);
                    end
                end
                stress_original_store_1(c+1,1)=stress_inter-delta_stress_Ti;
                stress_store_1(c+1,1)=stress;
                modi_stress_Al3Ti_store_1(c+1,1)=modi_stress_Al3Ti;
                crit_stress_Al3Ti_store_1(c+1,1)=crit_stress_Al3Ti;
```

```
        crack_size_origin_store_1(c+1,1)=crack_size_origin;
        T_store_1(c+1,1)=T;
    end
    %-----------------------------------------------------------------------------------------
    % Second cooling stage
    %-----------------------------------------------------------------------------------------
    AA=5*10^(5);
    mm=4.5;
    t_n_2=14.8;
    t_n_1=3.5;
    q=40;
    delta_t_2=(t_n_2-t_n_1)/q;
    delta_T_2=36.8*delta_t_2;
    strain_0_2=(alpha_Al3Ti-alpha_Ti)*delta_T_2;
    stress_0_2=E*(1-con)/((1+(E*1.22/E_Al3Ti-1)*con)*(1-0.321))*strain_0_2;
    stress_store_2=zeros(q-1,1);
    T_store_2=zeros(q-1,1);
    delta_stress_store_2=zeros(q-1,1);
    stress_original_store_2=zeros(q-1,1);
    modi_stress_Al3Ti_store_2=zeros(q-1,1);
    crit_stress_Al3Ti_store_2=zeros(q-1,1);
    crack_size_origin_store_2=zeros(q-1,1);
    for a=1:q-1
            crack_size_origin=crack_size_origin;
            E_Al3Ti=216*10^9/(1+16*(10-3*poisson_Al3Ti)*(1-
poisson_Al3Ti^2)/(45*(2-
poisson_Al3Ti))*pi*num_crack*crack_size_origin/space_origin);
        if  crack_size_origin>=crack_size_ultimate
            stress_inter=stress+stress_0_2;
                T_1=-36.8*(3.5+a*delta_t_2)+882.6;
                T_2=-36.8*(3.5+(a+1)*delta_t_2)+882.6;
                T=(T_1+T_2)/2;
                D=(10^(-4))*exp(-58000*4.186/(R*T));
                strain_rate=(stress_inter/G)^mm*AA*D*G*b/(k*T);
```

```
                        strain=strain_rate*delta_t*3600;
                        delta_stress_Ti=strain*E;
                        stress_inter_Al3Ti=stress_inter*con/(1-con);
                        strain_rate_Al3Ti=(M/T)*exp(-
Q/(R*T))*(stress_inter_Al3Ti/G_Al3Ti)^n;
                        strain_Al3Ti=strain_rate_Al3Ti*delta_t*3600;
                        delta_stress_Al3Ti=strain*E_Al3Ti;
                        delta_stress_Ti_from_Al3Ti=delta_stress_Al3Ti*(1-con)/con;
                        delta_stress=delta_stress_Ti+delta_stress_Ti_from_Al3Ti;
                        stress=stress_inter-delta_stress;
                else
                      x=0:crack_size_origin/1e6:crack_size_origin*0.999999;
                      h=(2/(pi*crack_size_origin))^0.5*(1-x/crack_size_origin).^(-
0.5)*modi_stress_Al3Ti_2;
                      stress_intensity_Al3Ti_2 = trapz(x,h);
                        T_1=-36.8*(3.5+a*delta_t_2)+882.6;
                        T_2=-36.8*(3.5+(a+1)*delta_t_2)+882.6;
                        T=(T_1+T_2)/2;
            fracture_toughness_Al3Ti=((T-320)*fract_toughness_orgin_Al3Ti+(1023-
T)*fract_toughness_Al3Ti_room_temp)/703;
effe_fract_tough_Al3Ti_2=fracture_toughness_Al3Ti-stress_intensity_Al3Ti_2;
crit_stress_Al3Ti_2=effe_fract_tough_Al3Ti_2/(pi*crack_size_origin)^0.5;
                      if modi_stress_Al3Ti_2<crit_stress_Al3Ti_2
                        modi_stress_Al3Ti_2=modi_stress_Al3Ti_2;
                        stress=modi_stress_Al3Ti_2*(1-con)/con;
                        stress_inter=stress+stress_0_2;
                        T_1=-36.8*(3.5+a*delta_t_2)+882.6;
                        T_2=-36.8*(3.5+(a+1)*delta_t_2)+882.6;
                        T=(T_1+T_2)/2;
                        D=(10^(-4))*exp(-58000*4.186/(R*T));
                        strain_rate=(stress_inter/G)^mm*AA*D*G*b/(k*T);
                        strain=strain_rate*delta_t*3600;
                        delta_stress_Ti=strain*E;
                        stress_inter_Al3Ti=stress_inter*con/(1-con);
```

```
strain_rate_Al3Ti=(M/T)*exp(-Q/(R*T))*(stress_inter_Al3Ti/G_Al3Ti)^n;
            strain_Al3Ti=strain_rate_Al3Ti*delta_t*3600;
            delta_stress_Al3Ti=strain*E_Al3Ti;
            delta_stress_Ti_from_Al3Ti=delta_stress_Al3Ti*(1-con)/con;
            delta_stress=delta_stress_Ti+delta_stress_Ti_from_Al3Ti;
            stress=stress_inter-delta_stress;
          else
      [modi_stress_Al3Ti_2,crit_stress_Al3Ti_2,crack_size_origin,stress,stress_inte
r,E_Al3Ti]=stat2(modi_stress_Al3Ti_2,crit_stress_Al3Ti_2,crack_size_origin,stress,s
pace_origin,E_Al3Ti,stress_inter);
          end
      end
        if stress < stress_inter
          stress=stress_inter;
        else
          stress=stress;
        end
        modi_stress_Al3Ti_store_2(a,1)=modi_stress_Al3Ti_2;
        crit_stress_Al3Ti_store_2(a,1)=crit_stress_Al3Ti_2;
        crack_size_origin_store_2(a,1)=crack_size_origin;
        stress_store_2(a,1)=stress;
        T_store_2(a,1)=T;
        delta_stress_store_2(a,1)=delta_stress;
        stress_original_store_2(a,1)=stress_inter-delta_stress_Ti;
      end
      T_store=zeros(p+q-1,1);
      stress_store=zeros(p+q-1,1);
      modi_stress_Al3Ti_store=zeros(p+q-1,1);
      crit_stress_Al3Ti_store=zeros(p+q-1,1);
      crack_size_origin_store=zeros(p+q-1,1);
      delta_stress_store=zeros(p+q-1,1);
      stress_with_Ti_creep_only=zeros(p+q-1,1);
      for i=1:p
        T_store(i,1)=T_store_1(i,1);
```

```
    stress_store(i,1)=stress_store_1(i,1);
    modi_stress_Al3Ti_store(i,1)=modi_stress_Al3Ti_store_1(i,1);
    crit_stress_Al3Ti_store(i,1)=crit_stress_Al3Ti_store_1(i,1);
    crack_size_origin_store(i,1)=crack_size_origin_store_1(i,1);
    delta_stress_store(i,1)=delta_stress_store_1(i,1);
    stress_with_Ti_creep_only(i,1)=stress_original_store_1(i,1);
end

for j=p+1:p+q-1
    T_store(j,1)=T_store_2(j-p,1);
    stress_store(j,1)=stress_store_2(j-p,1);
    modi_stress_Al3Ti_store(j,1)=modi_stress_Al3Ti_store_2(j-p,1);
    crit_stress_Al3Ti_store(j,1)=crit_stress_Al3Ti_store_2(j-p,1);
    crack_size_origin_store(j,1)=crack_size_origin_store_2(j-p,1);
    delta_stress_store(j,1)=delta_stress_store_2(j-p,1);
    stress_with_Ti_creep_only(j,1)=stress_original_store_2(j-p,1);
end

%-------------------------------------------------------------------------------------
%calculating the stress-Temperature relation without any creep or crack in
either Ti %or Al3Ti
%-------------------------------------------------------------------------------------

stress_without_creep=zeros(2,1);
T_without_creep=zeros(2,1);
T_without_creep(1,1)=1019.6;
T_without_creep(2,1)=343;
stress_without_creep(1,1)=0;
strain_without_creep=(alpha_Al3Ti-alpha_Ti)*(T_without_creep(1,1)-
T_without_creep(2,1));
concentration = con;
switch lower(concentration)
  case 0.14
    stress_without_creep(2,1)=140.5*10^9*strain_without_creep;
```

```
  case 0.2
    stress_without_creep(2,1)=128.5*10^9*strain_without_creep;
  case 0.35
    stress_without_creep(2,1)=100.5*10^9*strain_without_creep;
end

modi_stress_Al3Ti_store,crit_stress_Al3Ti_store,crack_size_origin_store,con

%-------------------------------------------------------------------------------
% Plotting the results
%-------------------------------------------------------------------------------

%plot(T_store,stress_store/10^6,T_store,stress_original/10^6)
%plot(T_store,delta_stress_store/10^6)
%plot(T_store,crack_size_origin_store,'-.k')
xlabel('Temperature (K)')
ylabel('Stress (MPa)')

concentration = con;
switch lower(concentration)
  case 0.14
     text(500,200,'stress vs temperature for 14%Ti')
     text(950,15,' \leftarrow stress before creep')
     text(875,10,' stress after creep and crack\rightarrow')
  case 0.2
     text(500,200,'stress vs temperature for 20%Ti')
     text(950,15,' \leftarrow stress before creep')
     text(480,50,' stress after creep and crack\rightarrow')

  case 0.35
     text(500,200,'stress vs temperature for 35%Ti')
     text(950,15,' \leftarrow stress before creep')
     text(875,10,' stress after creep and crack\rightarrow')
end
```

```
diary off
%end
return


%--------------------------------------------------------------------------------------------
%subroutine for the first stage
%--------------------------------------------------------------------------------------------
function
[modi_stress_Al3Ti,crit_stress_Al3Ti,crack_size_origin,stress,stress_inter,E_Al3Ti]=
stat(modi_stress_Al3Ti,crit_stress_Al3Ti,crack_size_origin,stress,space_origin,E_Al3
Ti,stress_inter)
global alpha_Ti alpha_Al3Ti con percentage G R k E b G_Al3Ti
poisson_Al3Ti a c p q Q m n M A AA mm stress_0_2 con crack_size_ultimate
global stress_0 coeffi strain_0_2 strain_0 delta_t_2 delta_t
fract_toughness_orgin_Al3Ti fract_toughness_Al3Ti_room_temp num_crack
c
  if modi_stress_Al3Ti<crit_stress_Al3Ti
      modi_stress_Al3Ti=modi_stress_Al3Ti;
      crit_stress_Al3Ti=crit_stress_Al3Ti;
      stress=modi_stress_Al3Ti*(1-con)/con;
      stress_inter=stress+stress_0;
  else
%--------------------------------
%the crack grows
%--------------------------------
      crack_size_origin=crack_size_origin*(1+percentage);
    if crack_size_origin>=crack_size_ultimate
      crack_size_origin=crack_size_ultimate;
      modi_stress_Al3Ti_1=modi_stress_Al3Ti_1;
      crit_stress_Al3Ti_1=100*modi_stress_Al3Ti_1;
      stress=stress;
```

```
stress_inter=stress;
E_Al3Ti=E_Al3Ti;
return
else
crack_size_origin
%--------------------------------
%recalculate the residual stress
%--------------------------------
E_Al3Ti_old=E_Al3Ti;
E_Al3Ti=216*10^9/(1+16*(10-3*poisson_Al3Ti)*(1-
poisson_Al3Ti^2)/(45*(2-
poisson_Al3Ti))*pi*num_crack*crack_size_origin/space_origin);
E_Al3Ti_new=E_Al3Ti;
E_Al3Ti_old,E_Al3Ti_new
stress_decrease=100*((E*(1-con)/(1+(E*1.22/E_Al3Ti_old)*con)*(1-
0.321))*strain_0-(E*(1-con)/(1+(E*1.22/E_Al3Ti_new)*con)*(1-0.321))*strain_0);
stress=stress-stress_decrease;
modi_stress_Al3Ti=stress*con/(1-con);
%--------------------------------
%recalculate the critical stress
%--------------------------------
x=0:crack_size_origin/1e6:crack_size_origin*0.999999;
h=(2/(pi*crack_size_origin))^0.5*(1-x/crack_size_origin).^(-
0.5)*modi_stress_Al3Ti;
stress_intensity_Al3Ti = trapz(x,h);
stress_intensity_Al3Ti
T_1=-77*c*delta_t+1023;
T_2=-77*(c+1)*delta_t+1023;
T=(T_1+T_2)/2;
fracture_toughness_Al3Ti=((T-320)*fract_toughness_orgin_Al3Ti+(1023-
T)*fract_toughness_Al3Ti_room_temp)/703;
effe_fract_tough_Al3Ti=fracture_toughness_Al3Ti-stress_intensity_Al3Ti;
crit_stress_Al3Ti = effe_fract_tough_Al3Ti/(pi*crack_size_origin)^0.5;
modi_stress_Al3Ti,crit_stress_Al3Ti
```

```
%-----------------------------------------------
%compare the critical stress with residual stress
%-----------------------------------------------
[modi_stress_Al3Ti,crit_stress_Al3Ti,crack_size_origin,stress,stress_inter,E_Al3Ti]=stat(modi_stress_Al3Ti,crit_stress_Al3Ti,crack_size_origin,stress,space_origin,E_Al3Ti,stress_inter);
        stress=modi_stress_Al3Ti*(1-con)/con;
        stress
        end
    end
return


%------------------------------------------------------------------------------------------
%subroutine for the second stage
%------------------------------------------------------------------------------------------
function
[modi_stress_Al3Ti_2,crit_stress_Al3Ti_2,crack_size_origin,stress,stress_inter,E_Al3Ti]=stat2(modi_stress_Al3Ti_2,crit_stress_Al3Ti_2,crack_size_origin,stress,space_origin,E_Al3Ti,stress_inter)
global alpha_Ti alpha_Al3Ti con percentage G R k E b G_Al3Ti poisson_Al3Ti a c p q Q m n M A AA mm stress_0_2 con crack_size_ultimate
global stress_0 coeffi strain_0_2 strain_0 delta_t_2 delta_t fract_toughness_orgin_Al3Ti fract_toughness_Al3Ti_room_temp num_crack
a
    if modi_stress_Al3Ti_2<crit_stress_Al3Ti_2
        modi_stress_Al3Ti_2=modi_stress_Al3Ti_2;
        crit_stress_Al3Ti_2=crit_stress_Al3Ti_2;
        stress=modi_stress_Al3Ti_2*(1-con)/con;
        stress_inter=stress+stress_0_2;
    else
%--------------------------------
%the crack grows
%--------------------------------
```

```
            crack_size_origin=crack_size_origin*(1+percentage);
            if crack_size_origin>=crack_size_ultimate
              crack_size_origin=crack_size_ultimate;
              modi_stress_Al3Ti_2=modi_stress_Al3Ti_2;
              crit_stress_Al3Ti_2=100*modi_stress_Al3Ti_2;
              stress=stress;
              stress_inter=stress;
              E_Al3Ti=E_Al3Ti;
              return
            else
            crack_size_origin
        %--------------------------------
        %recalculate the residual stress
        %--------------------------------
             E_Al3Ti_old=E_Al3Ti;
        E_Al3Ti=216*10^9/(1+16*(10-3*poisson_Al3Ti)*(1-
        poisson_Al3Ti^2)/(45*(2-
        poisson_Al3Ti))*pi*num_crack*crack_size_origin/space_origin);
             E_Al3Ti_new=E_Al3Ti;
             E_Al3Ti_old,E_Al3Ti_new
        stress_decrease=650*((E*(1-con)/(1+(E*1.22/E_Al3Ti_old)*con)*(1-
0.321))*strain_0_2-(E*(1-con)/(1+(E*1.22/E_Al3Ti_new)*con)*(1-
0.321))*strain_0_2);
             stress=stress-stress_decrease;
              modi_stress_Al3Ti_2=stress*con/(1-con);
        %--------------------------------
        %recalculate the critical stress
        %--------------------------------
            x=0:crack_size_origin/1e6:crack_size_origin*0.999999;
        h=(2/(pi*crack_size_origin))^0.5*(1-x/crack_size_origin).^(-
0.5)*modi_stress_Al3Ti_2;
            stress_intensity_Al3Ti_2 = trapz(x,h);
            stress_intensity_Al3Ti_2
              T_1=-36.8*(3.5+a*delta_t_2)+882.6;
```

```
T_2=-36.8*(3.5+(a+1)*delta_t_2)+882.6;
T=(T_1+T_2)/2;
fracture_toughness_Al3Ti=((T-320)*fract_toughness_orgin_Al3Ti+(1023-T)*fract_toughness_Al3Ti_room_temp)/703;
fracture_toughness_Al3Ti
effe_fract_tough_Al3Ti_2=fracture_toughness_Al3Ti-stress_intensity_Al3Ti_2;
effe_fract_tough_Al3Ti_2/(pi*crack_size_origin)^0.5;
modi_stress_Al3Ti_2,crit_stress_Al3Ti_2
%-------------------------------------------------
%compare the critical stress with residual stress
%-------------------------------------------------

[modi_stress_Al3Ti_2,crit_stress_Al3Ti_2,crack_size_origin,stress,stress_inter,E_Al3Ti]=stat2(modi_stress_Al3Ti_2,crit_stress_Al3Ti_2,crack_size_origin,stress,space_origin,E_Al3Ti,stress_inter);
stress=modi_stress_Al3Ti_2*(1-con)/con;
stress
end
end
return

%END OF THE CODE
```

REFERENCES

1 Harach, D.J., Vecchio, K.S., Microstructure evolution in metal intermetallic laminate (MIL) composites synthesized by reactive foil sintering in air, Metallurgical and Materials Transactions A, 2001, 32A: 1493-1505.

2 Rohatgi, A., Harach, D.J., Vecchio, K.S., Harvey, K.P., Resistance-curve and fracture behavior of Ti–Al_3Ti metallic–intermetallic laminate (MIL) composites, Acta Materialia, 2003, 51: 2933–2957.

3 Alman, D.E., Rawers, J.C., Hawk, J.A., Microstructual and failure characteristics of metal-intermetallic layed sheet composites, Metallurgical and Materials Transactions A, 1995, 26: 589-599.

4 Alman, D.E., Dogan, C.P., Hawk, J.A., Rawers, J.C., Processing, structure and properties of metal-intermetallic layered composites, Material Science and Engineering, 1995, A192-293: 624-632.

5 Rawers, J.C., Alman, D.E. Hawk, J.A., Int. J. Self prop. High. Temp. Syn., 1993, 2 (1): 12-24.

6 Sigl, L.S., Mataga, P.A., Dalgleish, B.J., McMeeking, R.M., Evans, A.G., On the toughness of brittle materials reinforced with a ductile phase, Acta Metallurgica 1988;36 (4):945-953.

7 Mataga, P.A., Deformation of crack-bridging ductile reinforcements in toughened brittle materials, Acta Metallurgica 1989; 37 (12):3349-3359.

8 Rao, K.T.V., Soboyejo, W.O., Ritchie, R.O., Ductile-phase toughening and fatigue-crack growth in niobium-reinforced molybdenum disilicide intermetallic composites, Metallurgical Transactions A: Physical Metallurgy and Materials Science, 1992;23A (8):2249-2257.

9 Ashby, M.F., Blunt, F.J., Bannister, M., Flow characteristics of highly constrained metal wires, Acta Metallurgica 1989;37 (7):1847-1857.

10 Zok, F., Hom, C.L., Large-scale bridging in brittle matrix composites, Acta Metallurgica et Materialia 1990; 38 (10):1895-1904.

11 Flinn, B.D., Lo, C.S., Zok, F.W., Evans, A.G., Fracture resistance characteristics of a metal-toughened ceramic, Journal of the American Ceramic Society 1993;76 (2):369-375.

12 Dalgleish, B.J., Trumble, K.P., Evans, A.G., The strength and fracture of alumina bonded with aluminum alloys, Acta Metallurgica 1989;37 (7):1923-1931.

13 Deve, H.E., Evans, A.G., Odette, G.R., Mehrabian, R., Emiliani, M.L., Hecht, R.J., Ductile reinforcement toughening of titanium aluminide: effects of debonding and ductility, Acta Metallurgica et Materialia 1990;38:1491-1502.

14 Rao, K.T.V., Odette, G.R., Ritchie, R.O., On the contrasting role of ductile-phase reinforcements in the fracture toughness and fatigue-crack propagation behavior of TiNb/γ-TiAl intermetallic matrix composites, Acta Metallurgica et Materialia, 1992; 40 (2):353-361.

15 Shaw, M.C., Marshall, D.B., Dadkhah, M.S., Evans, A.G., Cracking and damage mechanisms in ceramic/metal multilayers, Acta Metallurgica et Materialia 1993; 41: 3311-3322.

16 Heathcote, J., Odette, G.R., Lucas, G.E., Rowe, R.G., Skelly, D.W., On the micromechanics of low temperature strength and toughness of intermetallic/metallic microlaminate composites, Acta Materialia, 1996; 44 (11): 4289-4299.

17 Bloyer, D.R., Rao, K.T.V., Ritchie, R.O., Resistance-curve toughening in ductile/brittle layered structures: Behavior in Nb/Nb3Al laminates, Materials Science and Engineering A, 1996; 216 (1-2): 80-90.

18 Cao, H.C., Evans, A.G., On crack extension in ductile/brittle laminates, Acta Metallurgica et Materialia 1991; 39 (12):2997-3005.

19 Petrovic, J.J., Bhattacharya, A.K., Honnell, R.E., Mitchell, T.E., Wade, R.., McClellan, K.J., ZrO2 and ZrO2---SiC particle reinforced MoSi2 matrix composites, Materials Science and Engineering A, 1992, 155 (1-2): 259-266.

20 Bloyer, D.R., Venkateswara Rao, K.T., Ritchie, R.O., Resistance-curve toughening in ductile-phase reinforced intermetallic laminates, Joannes Weertman Symposium, Proceedings of a Symposium held during the TMS Annual Meeting, Anaheim, California, February 4-8, 1996, 1996: 261-266.

21 Bloyer, D.R., Venkateswara Rao, K.T., Ritchie, R.O., Fracture toughness and R-curve behavior of laminated brittle-matrix composites, Metallurgical and Materials Transactions A: Physical Metallurgy and Materials Science, 1998, 29A (10): 2483-2496.

22 Bloyer, D.R., Venkateswara Rao, K.T., Ritchie, R.O., Laminated Nb/Nb3Al composites: effect fo layer thickness on fatigue and fracture behavior, Materials Science and Engineering A: Structural Materials: Properties, Microstructure and Processing, 1997, A239-240: 393-398.

23 Bloyer, D.R., Venkateswara Rao, K.T., Ritchie, R.O., Toughness and subcritical crack growth in Nb/Nb3Al layered materials, Materials Research Scitety Symposium Proceedings, 1996, 434: 243-248.

24 Hwu, K.L., Derby., Fracture of metal/ceramic laminates I: Transition from single to multiple cracking, Acta Materialia, 1999, 47 (2): 529-543.

25 Hwu, K.L., Derby., Fracture of metal/ceramic laminates II: Crack growth resistance and toughness, Acta Maerialia, 1999, 47 (2): 545-563.

26 Rawers, J., Perry, K., Crack initiation in laminated metal-intermetallic composites, Journal of Materials Science, 1996, 31 (13): 3501-3506.

27 Walters, J.H., Cline, H.E., The effect of solidification rate on structure and high temperature strength of the eutectic NiAl-Cr, Metallurgical and Materials Transactions A, 1970, 1: 1221-1229.

28 Mendiratta, M.G., Lewandowski, J.J., Dimiduk, D.M., Strength and ductile-phase toughening in the two-phase Nb/Nb5Si3 alloys, Metallurgical and Materials Transactions A, 1991, 22A: 1573-1583.

29 Deve, H.E., Evans, A.G., Odette, G.R., Mehrabian, R., Emilliani, M.L., Hecht, R.J., Ductile reinforcement toughening of γ-TiAl: Effects of debonding and ductility, Acta Metallurgica et Materialia, 1990, 38 (8): 1491-1502.

30 Kajuch, J., Digney, J.D., Lewandowski, J.J., Processing and properties of Nb5Si3 and tough Nb5Si3/Nb laminates, Materials Science and Engineering A, 1992, 155: 59-65.

31 Lu, L., Gohkale, A.B., Abbaschian, R., Insitu formation of an alumina interface coating in reactively synthesized NbAl3-Nb composites, Materials Science and Engineering A, 1991, 144: 11-23.

32 Maupin, H.E., Rawers, J.C., Metal-intermetallics composites formed by reaction-sintering element powders, Journal of Materials Science Letters, 1993, 12: 540-541.

33 Chung, D.S., Enoki, M., Kishi, T., Microstructural analysis and mechanical properties of in situ Nb/Nb-aluminide layered materials, Science and Technology of Advanced Materials, 2002, 3 (2): 129-135.

34 Krstic, V.V., Nicholson, P.S., Toughening of glasses by metallic particles, Journal of the American Ceramic Society, 1981, 64 (9): 499-504.

35 Clyne, T.W., Withers, P.J., An introduction to metal matrix composites, Cambridge University Press, Cambridge, UK, 1993.

36 Graves, J.A., Rowman, R.R., Lewandowski, J.J., MRS, Pittsburgh, PA, 1994, 350: 111-118.

37 C. H. Shang, D. Van Heerden, A. J. Gavens, T. P. Weihs, An X-ray study of residual stresses and bending stresses in free-standing Nb/Nb_5Si_3 microlaminates, Acta Materialia, 2000, 48 (13): 3533-3543.

38 Miracle, D.B., Intermetallic matrix composites, Compressive Composite Materials, MRS, Pittsburgh, PA, 1990, volume 3: 741-778.

39 Ward-Close, C.M., Minor, R., Doorbar, P.J., Intermetallic-matrix composites – a review, Intermetallics, 1996, 4: 217-229.

40 Whang, S.H., Liu, C.T., Pope, D.P., Stiegler, J.O., TMS, Warrendale, PA, 1990, 133-151.

41 Darolia, R., Lewandowski, J.J., Liu, C.T., Martin, P.L., Mairale, D.B., Nathal, N.V., TMS, Warrendale, PA, 1993, 717-726.

42 Clegg, W. J., Kendall, K., Alford, N. M., Birchall, J. D., Button, T. W., A simple way to make tough ceramics, Nature, 1990, 347, 455-457.

43 Soboyejo, W. O., Yea, F., Chena, L-C., Bahtishia, N., Schwartz, D. S. and Lederich, R. J., Effects of reinforcement morphology on the fatigue and fracture behavior of $MoSi_2/Nb$ composites, Acta Materialia, 1996, 44 (5): 2027-2041.

44 Lesuer, D.R., Syn, C.K., Sherby, O.D., Wadsworth, J., Lewandowski, J.J., Hunt, W.H., Mechanical behavior of laminated metal composites, International Materials Reviews, 1996, 41 (5): 169-197.

45 Dalgleish, B.J., Trumble, K.P., Evans, A.G., The strength and fracture of alumina bonded with aluminum alloyes, Acta Metallurgica, 1989, 37 (7): 1923-1931.

46 Lesuer, D.R., Wadswoth, J., Materials Research Society Symposium Proceedings, 1996, 434: 205-211.

47 Bloyer, D.R., Rao, K.T.V., Ritchie, R.O., Fracture tougheness and R-curve behavior of laminated brittle-matrix composites, Metallurgical and Materials Transactions 1998; 29A: 2483-2496.

48 Odette, G.R., Chao, B.L., Sheckherd, J.W., Lucas, G.E., Ductile phase toughening mechanisms in a TiAl---TiNb laminate composite, Acta Metallurgica et Materialia 1992; 40 (9):2381-2389.

49 Subramanian, R., Schneibel, J.H., FeAl–TiC and FeAl–WC composites—melt infiltration processing, microstructure and mechanical properties, Materials Science and Engineering, 1998, A244, 103–112.

50 Imbeni, V., Hutchings, I. M., and Breslin, M. C., Abrasive wear behavior of an Al2O3–Al co-continuous composite, Wear, 1999, 233-235: 462-467.

51 McNaney, J. M., Cannon, R. M., and Ritchie, R. O., Fracture and fatigue-crack growth along aluminum-alumina interfaces, Acta Materialia, 1996, 44 (12): 4713-4728.

52 Huang, Y., Zhang, H.W., The role of metal plasticity and interfacial strength in the cracking of metal/ceramic laminates, Acta Metallurgica et Materialia, 1995,

43 (4): 1523-1530.

53 Rawers J.C., and Alman, D.E., Fracture characteristics of metal/intermetallic laminar composites produced by reaction sintering and hot pressing, Composites Science and Technology, 1995, 54 (4): 379-384.

54 Hwu, K.L., Derby, B., Fracture of metal/ceramic laminates—II. Crack growth resistance and toughness, Acta Materialia 1999; 47 (2):545-563.

55 Hwu, K.L., Derby, B., F Fracture of metal/ceramic laminates—I. Transition from single to multiple cracking, Acta Materialia 1999; 47 (2): 529-543.

56 Rawers, J., Perry, K., Crack initiation in laminated metal-intermetallic composites, Journal of Material Science, 1996, 31 (13): 3501-3506.

57 Fox, M.R., Ghosh, A.K., Structure, strength and fracture resistance of interfaces in NiAl/Mo model laminates, Materials Science and Engineering A, 1999, 259 (2): 261-268.

58 Chung, D.S., Manabu, Enoki, M., Kishi, T., Formation behavior of aluminide layers during the fabrication of Nb/Nb-aluminide laminate materials from Nb and Al foil, J. Japan Inst. Metals, 1999, 63 (8): 1043-1052.

59 Odette, G.R., Chao, B.L., Sheckherd, J.W., Lucas, G.E., Ductile phase toughening mechanisms in a TiAl---TiNb laminate composite, Acta Metallurgica et Materialia, 1992, 40 (9): 2381-2389.

60 Kajuch, J., Short, J., Lewandowski, J.J., Deformation and fracture behavior of Nb in Nb_5Si_3/Nb laminates and its effect on laminate toughness, Acta Metallurgica et Materialia, 1995, 43 (4): 1523-1530.

61 Rigney, J.D., Fracture of laminated and in situ niobium silicide-niobium composites, Materials Research Society Symposium Proceedings, 1996, 434:

227-241.

62 Pickard, S.M., Zhang, H., and Ghosh, A.K., Interface shear properties and toughness of NiAl/Mo laminates, Acta Materialia, 1997, 45 (10): 4333-4350.

63 Xiao, L., and Abbaschian, R., Interfacial modification of Nb/MoSi2 composites and its effects on fracture toughness, Materials Science and Engineering A, 1992, 155 (1-2): 135-145.

64 Li, T., Grignon, F., Benson, D.J., Vecchio, K.S., Olevsky, E.A., Jiang, F.C., Meyers, M.A., Modeling the elastic properties and damage evolution in Ti–Al_3Ti metal–intermetallic laminate (MIL) composites, Materials Science and Engineering, 2004, A374: 10–26.

65 Alman, D.E., Rawers, J.C., Fracture characteristics of metal/intermetallic laminar composites produced by reaction sintering and hot pressing, Composites Science and Technology, 1995, 54 (4): 379-384.

66 Maupin, H.E., Rawers, J.C., Hawk, J.A., In: Proceedings of the 1st International Conference on Advanced Synthesis of Engineered Materials, San Francisco, CA, USA, 1992.

67 Alman, D.E., Dogan, C.P., Hawk, J.A., Rawers, J.C., Processing, structure and properties of metal-intermetallic layered composites, Material Science and Engineering, 1995, A192-293: 624-632.

68 Rawers, J.C., Hansen, J.S., Alman, D.E., Hawk, J.A., Formation of sheet metal-intermetallic composites by self-propagting high-temperature reaction, Journal of Materials Science Letters, 1994; 13:1357-1360.

69 Isobe, S., Noda, T., Structural Intermetallics, The Minerals, Metals and Materials Society, TMS, Warrendale, PA, 1997: 427.

70 Schneider, D., Jewett, T., Gent, C., Segtrop, K., Dahms, M., Structural Intermetallics, The Minerals, Metals and Materials Society, TMS, Warrendale, PA, 1997: 453.

71 Maki, K., Ehira, A., Sayashi, M., Sasaki, T., Noda, T., Okabe, M., Isobe, S., SAE Technical Paper Series, 1996, 96030:117.

72 Dimiduk, D.M., Gamma titanium aluminide alloys—an assessment within the competition of aerospace structural materials, Materials Science and Engineering A, 1999, 263 (2): 281-288.

73 Tetsui, T., Ono, S., Endurance and composition and microstructure effects on endurance of TiAl used in turbochargers, Intermetallics, 1999; 7 (6):689-697.

74 Tetsui, T., Effects of high niobium addition on the mechanical properties and high-temperature deformability of gamma TiAl alloy, Intermetallics, 2002, 10 (3): 239-245.

75 Tetsui, T., Effects of brazing filler on properties of brazed joints between TiAl and metallic materials, Intermetallics, 2001, 9(3): 253-260.

76 Tetsui, T., A newly developed hot worked TiAl alloy for blades and structural components, Scripta Materialia, 2002, 47 (6): 399-403.

77 Tetsui, T., Development of a TiAl turbocharger for passenger vehicles, Materials Science and Engineering A, 2002, 329-331: 582-588.

78 Tetsui, T., Ono, S., Rotating strength of forged TiAl alloys, Intermetallics, 1999; 7 (2): 193-199.

79 Guédou, J.Y., Les Matériaux pour turboréacteurs aéronautiques undéfi á la mécanique thermique, 14ème Congrès de écanique Organized by Assocaition Française de Mécanique, Toulouse, France, 1999.

80 Brunet, A., Valle, R., and Vassel, A., Intermetallic TiAl-based matrix composites: Investigation of the chemical and mechanical compatibility of a protective coating adapted to an alumina fibre, Acta Materialia, 2000, 48 (20): 4763-4774.

81 Vassel, A., Continuous fibre reinforced titanium and aluminium composites: a comparison , Materials Science and Engineering A, 1999, 263: 305-313.

82 Riddle, R., Lesuer, D., Syn, C., Gogolewski, R., Cunningham, B., Application of metal laminates to aircraft structures: Prediction of penetration performance, Finite Element in Analysis and Design, 1996, 23: 173-192.

83 Vasudevan, A.K., Petrovic, J.J., comparative overview of molybdenum disilicide composites, Materials Science and Engineering A, 1992, 155 (1-2): 1-17.

84 O'Connell, R.J., Budiansky, B., Journal of Geology Research, 79 (1974) 5412.

85 Meyers, M.A., Chawla, K.K., Mechanical Behavior of Materials, Prentice Hall, 1998, p.154.

86 Johnson, G.R., Holmquist, T.J., American Institute of Physics, 1994, p. 981-984.

87 Govindjee, S., Kay, G.J., Simo, J.C., Anisotropic modeling and numerical siulation of brittle damage in concrete, International Journal for Numerical Methods in Engineering, 1995, 38(21): 3611-3633.

88 Franklin, H.G., Classical theories of failure of anisotropic materials, Fiber Science and Technology, 1968, 1: 137-150.

89 Sandhu, R.S., A survey of failure theories of isotropic and anisotropic

materials, AFFDL-TR-72-71, AD 756889, Air Force Flight Dynamics Laboratory, Wright-Patter-son Air Force Base, OH, 1972.

90 Sendeckyj, G.P., A brief survey of empirical multiaxial strength criteria for composites. In ASTM STP 497, 1972, 41-51.

91 Wu, E.M., Strength and fracture of composites, In Composite Materials, Vol. 5: Fatigue and Fracture, ed. L.J. Broutman. Academic Press, 1974, 191-248.

92 Wu, E.M., Phenomenological anisotropic failure criteria, In Treatise on Composite Materials, ed. L. J. Broutman, R. H. Kroch and G. P. Sendeckyj. Academic Press, 1973, 353-432.

93 Vicario, A.A., and Toland, R.H., Failure criteria and failure analysis of composite structural components, In Composite Materials, Vol. 7: Structural Design and Analysis, Part I, ed. C. C. Chamis. Academic Press, 1975, 52-97.

94 Hart-Smith, L.J., The role of biaxial stresses in discriminating between meaningful and illusory composite failure theories, Composite Structure, 1993, 25: 3-20.

95 Rowlands, R.E., Strength (failure) theories and their experimental correlation. In Handbook of Composites, Vol. 3: Failure Mechanics of Composites, ed. G. C. Sihand A. M. Skudra. North-Holland, 1984, 71-125.

96 Eckold, G.C., Failure criteria for use in the design environment, Composite Science and Technology, 1998; 58:1095–1106.

97 Edge, E.C., Stress based Grant-Sanders method for predicting failure of composite laminates. Composite Science and Technology, 1998; 58:1043–1044.

98 Rotem, A., Prediction of laminate failure with Rotem failure criterion,

Composite Science and Technology, 1998; 58:1083–1094.

99 Sun, C.T., Tao, J.X., Prediction of failure envelopes and stress strain behaviors of composite laminates, Composite Science and Technology, 1998; 58: 1125–1136.

100 Hart-Smith, L.J., Predictions of the original and truncated maximum strain failure models for certain fibrous composite laminates, Composite Science and Technology, 1998; 58:1151–1178.

101 Hinton, M.J., Kaddour, A.S., Soden, P.D., A comparison of the predictive capabilities of current failure theories for composite laminates, judged against experimental evidence, Composite Science and Technology, 2002; 62:1725–1797.

102 McCartney, L.N., Predicting transverse crack formation in crossply laminate, Composite Science and Technology, 1998; 58:1069–1082.

103 Liu, K-S, Tsai, S.W., A progressive quadratic failure criterion of a laminate, Composite Science and Technology, 1998; 58 (7):1023–1032.

104 Jenkins, C.F., Materials of construction used in aircraft and aircraft engines, Report to Great Britain Aeronautical Research Committee, 1920.

105 Sandhu, R.S., Nonlinear behavior of unidirectional and angle ply laminates, Journal of Aircraft, 1976, 13: 104-111.

106 Hutchinson, J.W., Evans, A.G., Mechanics of materials: top-down approaches to fracture, Acta Materialia, 2000, 48(1): 125-135.

107 Hutchinson, J.W., Evans, A.G., He, M.Y., Micromechanics model for the detachment of residually compressed brittle films and coatings, Acta Materialia, 1999, 47(5): 1513-1522.

108 Hashin, Z., Analysis of cracked laminates: a variational approach, Mechanics of Materials, 1985, 4, 121-136.

109 Hashin, Z., Analysis of stiffness reduction of cracked cross-ply laminates, Engineering Fracture Mechanics, 1986, 25, 771-778.

110 Hashin, Z., Analysis of orthogonally cracked laminates under tension, Journal of Applied Mechanics., 1987, 54, 872-879.

111 Hashin, Z., Thermal expansion coefficient of cracked laminates, Composites Science and Technology, 1988, 31, 247-260.

112 Nairn, J.A., Some new variational mechanics results on composite microcracking, In Proc. 10th Int. Conf. on Composite Materials, Whistler, BC, Canada, 14-18, August 1995.

113 Nairn, J.A., Strain energy release rate for composite mcirocracking: a variational approach, Journal of Composite Materials, 1989, 23, 1106-1129.

114 Nairn, J.A. and Hu, S., The formation and effect of outer-ply microcracks in cross-ply laminates: a variational approach, Engineering Fracture Mechanics, 1992, 41, 203-221.

115 Puck A, Schürmann H. Failure analysis of FRP laminates by means of physically based phenomenological models. Composites Science and Technology, 2002, 62 (12-13): 1633-1662.

116 Zinoviev, P, Grigoriev, S.V., Labedeva, O.V., Tairova, L.R., Strength of multilayered composites under plane stress state. Composites Science and Technology, 1998;58:1209–24.

117 Gotsis, P.K., Chamis, C.C., Minnetyan, L., Prediction of composite laminate

fracture: micromechanics and progressive fracture, Composites Science and Technology, 1998 (58): 1137-1150.

118 Wolfe, W.E., Butalia, T.S., A strain energy based failure criterion for nonlinear analysis of composite laminates subjected to biaxial loading, Composites Science and Technology, 1998; 58 (7):1107–24.

119 Bogetti, T.A., Hoppel, C.P.R., Harik, V.M., Newill, J.F., Burns, B.P., Predicting the nonlinear response and progressive failure of composite laminates, Composites Science and Technology, 2004; 64: 329-342.

120 Cuntze, R.G., Freund, A., The predictive capability of failure mode concept-based strength criteria for multidirectional laminates, Composites Science and Technology, 2004; 64: 343-377.

121 Huang, Z., A bridging model prediction of the tensile strength of composite laminates subjected to biaxial loads, Composites Science and Technology, 2004; 64: 395-448.

122 Mayes, S., Hansen, A.C., Composite laminate failure analysis using multicontinuum theory, Composites Science and Technology, 2004; 64: 379-394.

123 Meyers, M.A., Chawla, K.K., Mechanical Behavior of Materials, Prentice Hall, 1998, 656-663.

124 Christensen, R.M., Mechanics of Composite Materials, John Wiley & Sons, New York, 1990

125 Calcote, L.R., The Analysis of Laminated Composite Structures, Van Nostrand Reinhold Company, New York, 1984

126 Fu, C.L., Electronic, elastic and fracture properties of trialaminide alloys:

Al3Sc and Al3Ti, Journal of Material Research, 1990, 5: 971-979.

127 Vuorinen, J.E., Schwarz, R.B., Resonant ultrasound spectroscopy: applications, current status and limitations, Journal of Alloys and Compounds, 2000, 310 (1-2): 243-250.

128 Clyne, T.W., and Withers, P.J., An Introduction to Metal Matrix Composites, Cambridge University Press, Cambridge, UK, 1993

129 Solti, J. P., Robertson, D.D., Mall, S., Modeling damage in unidirectional ceramic-matrix composites, Composites Science and Technology, 1995, 54 (1):55-66.

130 Bednarcyk, B.A., Arnold, S.M., Transverse tensile and creep modeling of continuously reinforced titanium composites with local debonding, International Journal of Solids and Structures, 2002, 39(7):1987–2017.

131 Wisnom, M.R., Li, D.S., Finite element micromechanical modelling of unidirectional fibre-reinforced metal-matrix composites, Composites Science and Technology, 1994, 51(4):545–563.

132 Nimmer, R.P., Bankert, R.J., Russell, E.S., Smith, G.A., Wright, P.K., Micromechanical modeling of fiber/matrix interface effects in transversely loaded SiC/Ti-6-4 metal matrix composites, J. Comp. Technol. Res., 1991, 13(1):3–13.

133 Aghdam, M.M., Smith, D.J., Pavier, M.J., Finite element micromechanical modelling of yield and collapse behaviour of metal matrix composites, Journal of the Mechanics and Physics of Solids, 2000, 48(3):499– 528.

134 Foringer, M. A., Robertson, D.D., Mall, S., A micromechanistic-based approach to fatigue life modeling of titanium-matrix composites, Composites Part B: Engineering, 1997, 28 (5-6): 507-521.

135 Ismar, H., Schroter, F., Streicher, F., Effects of interfacial debonding on the transverse loading behaviour of continuous fibre-reinforced metal matrix composites , Computers & Structures, 2001:1713–1722.

136 Iyer, S.K., Lissenden, C.J., and Arnold, S.M., Local and overall flow in composites predicted by micromechanics, Composites Part B: Engineering, 2000, 31 (4): 327-343.

137 Lissenden, C.J., Fiber–matrix interfacial constitutive relations for metal matrix composites, Composites Part B: Engineering, 1999, 30:267–278.

138 Herakovich, C.T., Aboudi, J., Lee, S.W., and Strauss, E.A., Damage in composite laminates: Effects of transverse cracks, Mechanics of Materials, 1988, 7 (2): 91-107.

139 Trende, A., Astrom, B.T., and Nilsson, G., Modelling of residual stresses in compression moulded glass-mat reinforced thermoplastics, Composites Part A: Applied Science and Manufacturing, 2000, 31 (11): 1241-1254.

140 Robertson, D.D., Mall, S., A non-linear micromechanics-based analysis of metal-matrix composite laminates, Composites Science and Technology, 1994, 52 (3): 319-331.

141 Buchmann, M., Gadow, R., and Tabellion, J., Experimental and numerical residual stress analysis of layer coated composites, Materials Science and Engineering A, 2000, 288 (2): 154-159.

142 Sarkani, S., Tritchkov, V., and Michaelov, G., An efficient approach for computing residual stresses in welded joints, Finite Elements in Analysis and Design, 2000, 35 (3): 247-268.

143 Hsueh, C-H, and Fuller, E.R., Residual stresses in thermal barrier coatings:

effects of interface asperity curvature/height and oxide thickness, Materials Science and Engineering A, 2000, 283 (1-2): 46-55.

144 Zhang, X.C., Xu, B.S., Wang, H.D., and Wu, Y.X., Modeling of the residual stresses in plasma-spraying functionally graded ZrO2/NiCoCrAlY coatings using finite element method, Materials & Design, 2006, 27 (4): 308-315.

145 Ghafouri-Azar, R., Mostaghimi, J., and Chandra, S., Modeling development of residual stresses in thermal spray coatings, Computational Materials Science, 2006, 35 (1): 13-26.

146 Outeiro, J.C., Umbrello, D., and M'Saoubi, R., Experimental and numerical modelling of the residual stresses induced in orthogonal cutting of AISI 316L steel, International Journal of Machine Tools and Manufacture, In Press, Corrected Proof.

147 Zhang, X.C., Xu, B.S., Wang, H.D., Jiang, Y., and Wu, Y.X., Prediction of three-dimensional residual stresses in the multilayer coating-based systems with cylindrical geometry, Composites Science and Technology, In Press, Corrected Proof.

148 Zhang, X.C., Xu, B.S., Wang, H.D., Jiang, Y., and Wu, Y.X., Modeling of thermal residual stresses in multilayer coatings with graded properties and compositions, Thin Solid Films, 2006, 497 (1-2): 223-231.

149 Anssi Laukkanen, Kenneth Holmberg, Jari Koskinen, Helena Ronkainen, Kim Wallin and Simo Varjus, Tribological contact analysis of a rigid ball sliding on a hard coated surface, Part III: Fracture toughness calculation and influence of residual stresses, Surface and Coatings Technology, 2006, 200 (12-13): 3824-3844.

150 Robertson, D.D., Mall, S., Micromechanical analysis for thermoviscoplastic behavior of unidirectional fibrous composites, Composites Science and

Technology, 1994, 50 (4): 483-496.

151 Cannillo, V., Montorsi, M., Siligardi, C., Sola, A., de Portu, G., Micele, L. and Pezzotti, G., Microscale computational simulation and experimental measurement of thermal residual stresses in glass–alumina functionally graded materials, Journal of the European Ceramic Society, 2006, 26 (8): 1411-1419.

152 Ee, K.C., Dillon, Jr. O.W., and Jawahir, I.S., Finite element modeling of residual stresses in machining induced by cutting using a tool with finite edge radius, International Journal of Mechanical Sciences, 2005, 47 (10): 1611-1628.

153 Teixeira-Dias, F., Menezes, L.F., Numerical determination of the influence of the cooling rate and reinforcement volume fraction on the levels of residual stresses in Al–SiC composites, Computational Materials Science, 2001, 21: 26-36.

154 Aghdam, M.M., Falahatgar, S.R., Micromechanical modeling of interface damage of metal matrix composites subjected to transverse loading, Composite Structures, 2004, 66: 415-420.

155 M.L. Dunn, M. Taya, Elastic-plastic thermal stresses and deformation of short-fibre composites, Journal of Materials Science, 1994, 29: 2053-2062.

156 Surry, M., Teodosiu, C., Menezes, L.F., Thermal residual stresses in particle-reinforced viscoplastic metal matrix composites, Materials Science and Engineering A, 1993, 167: 97-105.

157 Teodosiu, C., Menezes, L.F., Thermal residual stresses in particle-reinforced viscoplastic metal matrix composites, Materials Science and Engineering A, 1993, 167 (1-2): 97-105.

158 Sayman, O., Elastic–plastic stress analysis of symmetric aluminum metal-matrix composite laminated plates under thermal loads varying linearly,

Composites Part B: Engineering, 2005, 36: 61-72.

159 Hsueh, C-H, Ferber, M.K., Apparent coefficient of thermal expansion and residual stresses in multilayer capacitors, Composites Part A: Applied Science and Manufacturing, 2002, 33: 1115-1121.

160 Meyers, M.A., Chawla, K.K., Mechanical Behavior of Materials, Prentice Hall, 1998, p. 95

161 Salganik, R.L., Akad, Izv., Nauk SSR Mekh. Tverd. Tela, 1973, 8: 149.

162 Green, D.J., Critical microstructures for microcracking in Al3O3-ZrO2 composites, Journal of the American Ceramics Society, 1982, 65(12): 610-614.

163 Green, D.J., Compressive surface strengthening of brittle materials by a residual stress distribution, Journal of the American Ceramics Society, 1982, 66(11): 807-810.

164 Virkar, V., Huang, J.L., Cutler, R.A., Strengthening of oxide ceramics by transformation-induced stresses, Journal of the American Ceramics Society, 1987, 70(3): 164-170.

165 Sherman, D., Gong, X., Statistical behavior and misfit stress in ceramic and metal laminated system, Journal of Materials Research, 16(3) (2001) 721-727.

166 Lamon, J., Evans, A.G., Statistical analysis of bending strengths for brittle solids: a multiaxial fracture problem, Journal of the American Ceramics Society, 1983, 66(9): 178-179.

167 Lakshminarayanan, R., Shetty, D.K., Cutler, R.A., Toughening of layed composites with residual surface compression, Journal of the American Ceramics Society, 1996, 79(1): 79-87.

168 Fett, T., Munz, D., Discussion: "Determination of weight functions from reference stress intensity factors", by G. Shen and G. Glinka, Theoretical and Applied Fracture Mechanics, 1992, 17 (3): 239-240.

169 Fett, T., Munz, D., Local stress intensity factors for small semi-elliptical cracks under exponentially distributed stresses, Engineering Fracture Mechanics, 1999, 64 (1): 105-116

170 Fett, T., Munz, D., On the evaluation of crack opening displacement form the stress intensity factor, Engineering Fracture Mechanics, 1987, 27: 697-715.